Environmental
Studies
Research
Funds

099 Comparison of Directional Wave Spectra

Canada

July 1988

Environmental Studies Revolving Funds
Report No. 099
July 1988

COMPARISON OF DIRECTIONAL WAVE SPECTRA

by:

B.-A. Juszko

Seakem Oceanography Ltd.
2045 Mills Road,
Sidney, B.C. V8l 3S1

Scientific Advisers: Dr. J.R. Buckley and Dr. J.R. Wilson.

The correct citation for this report is:

Juszko, B.-A. 1988. Comparison of Directional Wave Spectra. Environmental Studies Revolving Funds, Report Series No. 099. Ottawa. 227 p.

Published under the auspices of the

Environmental Studies Revolving Funds

ISBN 0-920783-98-9

TABLE OF CONTENTS

TABLE OF CONTENTS (continued)

TABLE OF CONTENTS (continued)

LIST OF TABLES

LIST OF ILLUSTRATIONS

LIST OF ILLUSTRATIONS, cont'd.

LIST OF ILLUSTRATIONS, cont'd.

LIST OF ILLUSTRATIONS, cont'd.

LIST OF ILLUSTRATIONS, cont'd.

LIST OF ILLUSTRATIONS, cont'd.

LIST OF ILLUSTRATIONS, cont'd.

LIST OF ILLUSTRATIONS, cont'd.

LIST OF ILLUSTRATIONS, cont'd.

PREFACE

In recent years, it has become apparent that for many ocean engineering applications, a knowledge of the direction of wave propagation would not only be useful but essential. The technology to perform the necessary measurements has evolved from arrays of individual heave sensors, to single instruments capable of measuring a minimum of three independent signals, generally heave and two surface slopes, to sophisticated radar imaging processes. A concurrent development in wave hindcast modelling has occurred due to the requirement for long-term statistics. However, these models still require calibration using directly measured wave parameters. For engineering purposes, knowledge of the performance, applicability and replicability of the different instruments and methods is necessary. Cost effectiveness versus relative performance is also important when choosing the best approach for a given application.

The directional wave spectrum intercomparison study was designed to address these concerns. Two directional buoys, a Datawell WAVEC slope-following buoy, and an Endeco type 956 WAVE-TRACK orbital-following buoy were chosen for examination due to their quite different approaches in obtaining the necessary three independent wave signals, and as operational experience and the required data handling software existed in the scientific community. A wave hindcast model, developed by D.T. Resio at the U.S. Army Waterways Experiment Station in Vicksburg, Mississippi was the one chosen to be incorporated into this study. Synthetic aperture radar imagery (SAR) was also attempted to obtain estimates of directional spreads. Some ground-truthing was supplied, for the heave estimates, by nearby Datawell Waveriders, in use for many years, and for direction by direct visual observations of wave direction and corresponding wind direction measurements. The study extended from February 15, 1984 to April 11, 1984 at a site in the Hibernia area on Newfoundland's Grand Banks.

The study was composed of three phases: phase one consisting of field work, data collection and processing; phase two of wave hindcast modelling of specific time periods; and phase three of a comparison between the various data sets. This final report reflects such a breakdown. Section one will discuss the field

operation and data collection, the data processing techniques used, the relative performance of the directional wave buoys in terms of data return and the results obtained. Section two will detail the selection of the hindcast model, the choice of events, the wind field used as input and the spectra produced. Section three, in effect, pulls all the information together for comparison. It includes a discussion on the assumptions and limitations behind each data set which provides the necessary foundation for the analyses. The data sets are then compared, not only in a bulk statistical sense for spectral properties, but record by record when necessary. An examination of analyses specific to directional wave buoy data illustrates their potential usefulness for trouble-shooting and for studies ranging from the assessment of the direction of group travel to changes in wave surface shape. A final discussion on the applicability and performance of the instruments and methods leads to conclusions and recommendations for future use.

ACKNOWLEDGEMENTS

The success of the field component of this study was a result of input from numerous sources. We gratefully acknowledge the assistance and support of Mobil Oil Canada Ltd. for providing transportation, space and equipment operators on board the mobile drilling unit West Venture. The Marine Environmental Data Service (MEDS) supplied a WAVEC buoy system and Petro-Canada Inc. provided a WAVEC and a WAVE-TRACK buoy system. Assistance in instrument deployment was also provided by MEDS.

We would also like to thank the following organizations who provided the necessary meteorological data for the modelling phase of this study conducted by F.G. Bercha and Associates Ltd. in St. John's, Nfld. These are:

Atmospheric Environment Service, Atlantic Weather Centre, Scientific Services, Atlantic Region, Bedford, N.S.

Atmospheric Environment Service, Canadian Meteorological Centre, Montreal, Quebec.

Atmospheric Environment Service, Newfoundland Weather Office, Gander, Nfld.

Canadian Forces METOC Centre, Dartmouth, N.S.

Husky/Bow Valley East Coast Project, St. John's, Nfld.

Mobil Oil Canada Ltd., St. John's, Nfld.

Petro-Canada Exploration, St. John's, Nfld.

Petro-Canada Resources, Calgary, Alberta

Additional wave data was supplied by Mobil Oil Canada Ltd. through the MANMAR data logs from the West Venture Mobile drilling unit. MEDS forwarded to us, without delay, the Waverider data from Station 169 and the internally recorded data from the WRIPS buoy at Station 501.

Certain individuals deserve special mention. These include Mr. J. Ransom and M. Hassel of Mobil Oil Canada Ltd., J. Murphy and R. Pajunen of MEDS, Dr. R.F. Marsden of Royal Roads Military College for his helpful criticisms and, particularly, Dr. J.R. Buckley, Petro-Canada Ltd., (and later Dr. J.R. Wilson, MEDS) who, as the Scientific Authority, co-ordinated the project. Of the key Seakem personnel, B.R. de Lange Boom successfully co-ordinated the buoy measurement program, designed the buoy moorings, installed the buoy systems, and reviewed the report while R.M. Brown was instrumental in the success of the data collection component of the project and P. Wainwright proofread and edited the report.

GLOSSARY

1. Moments of the heave spectrum - $(M_0, M_1, M_2 \ldots M_n)$

$$M_n = \sum_{i=a}^{b} f_i^n P(f_i) \Delta f \qquad \text{units of m**2/sec**n}$$

where P(f) is the spectral density (m**2/hz) at frequency f and the sum is performed over the range a = lowest frequency spectral estimate to b = highest

2. Significant wave height (or characteristic) wave height - H_{sig}

$$H_{sig} = 4*(M_0)^{1/2}$$

or Average height of the highest one-third waves from a zero-crossing analysis

3. Spectral peakedness parameter - Q_p

$$Q_p = 2 \sum_{i=a}^{b} f_i P^2(f_i) \Delta f / M_0^2$$

4. Spectral width parameter - ϵ

$$\epsilon = (1-M_2^2/(M_0*M_4))^{1/2}$$

5. Spectral narrowness parameter - ν

$$\nu = ((M2*M0-M1^2)/M1^2)^{1/2}$$

6. Peak period (period of spectral maximum)

7. Average period - TM_{01} (i.e. weighted average)

$$TM_{01} = M_0/M_1$$

8. Average apparent period - TM_{02}

$$TM_{02} = (M_0/M_2)^{1/2}$$

9. Apparent crest period - TM_{24}

$$TM_{24} = (M_2/M_4)^{1/2}$$

10. Mean direction at each frequency

$$\theta_m(f_i) = \text{Arctan}\left(\frac{-QD_{13}(f_i)}{QD_{12}(f_i)}\right) \quad \text{or} \quad \overline{\theta(f_i)} = \sum_{i=1}^{N} \theta_N D(f_i,\theta)\Delta\theta$$

where QD_{13}, QD_{12} are the quadrature spectral values for each frequency obtained from a cross-spectral analysis between the heave signal (1) and the two slope signals (2,3) of a directional buoy. $D(f_i,\theta)$ = directional distribution of energy, N = no. of directional bands.

11. Peak direction defined as mean direction at the spectral peak

12. Angular spread (or long-crestedness parameter)

$$S_1(f_i) = \left(\frac{CO_{11}(f_i) - \frac{1}{K_i^2}\sqrt{(CO_{22}(f_i) - CO_{33}(f_i))^2 + (2CO_{23}(f_i))^2}}{CO_{11}(f_i) + \frac{1}{K_i^2}\sqrt{(CO_{22}(f_i) - CO_{33}(f_i))^2 + (2CO_{23}(f_i))^2}} \right)^{\frac{1}{2}}$$

were $Co_{x\,y}$ are the co-spectral values obtained from a cross-spectral analysis and K_i is the wavenumber at frequency f_i.

13. Cosine spread

$$S_2(f_i) = \frac{2 * \frac{1}{K_i}\sqrt{QD_{12}(f_i)^2 + QD_{13}(f_i)^2}}{CO_{11}(f_i) - \frac{1}{K_i}\sqrt{QD_{12}(f_i)^2 + QD_{13}(f_i)^2}}$$

14. Average or apparent direction

$$\text{DIRAV} = \sum_{i=a}^{b} \theta_m(f_i) * P(f_i)\Delta f_i / M_0$$

$$\text{or} \quad \sum_{i=a}^{b} \theta_m(f_i) * \text{Spread}(f_i)\Delta f_i / \sum_{i=a}^{b} \text{Spread}(f_i)\Delta f_i$$

where $\text{Spread}(f_i)$ is some value of directional spread at each frequency

15. Moments of the directional distribution

$$MDpq = \sum_{|k|}\sum_{|\theta|} E(|k|,\theta)\left[|k|\cos\theta\right]^p\left[|k|\sin\theta\right]^q \Delta|k|\Delta\theta$$

(equivalent through the dispersion relation to Longuet-Higgins (1957) formulation)

k= wavenumber
θ = angle

Sum is performed through wavenumber and direction space.

16. Principal direction of the wave field

$$\text{Principal Direction} = \theta p = 1/2 * \text{Arctan}\left(\frac{2MD11}{MD20-MD02}\right)$$

17. Principal direction of the envelope

$$\text{Envelope Direction} = \theta E = 1/2 * \text{Arctan}\left(\frac{2ME11}{ME20-ME02}\right)$$

here:
ME11 = (MD11*MD00 - MD10*MD01)/MD00
ME20 = (MD20*MD00 - MD10*MD10)/MD00
ME02 = (MD02*MD00 - MD01*MD01)/MD00

18. Skewness of the waves = $\theta_E - \theta_p$

19. Mean wave front slope

Mean of all slope values measured on the forward face of a wave determined through a zero-upcrossing analysis (i.e. trough to crest).

20. Mean crest front slope

Mean of all slope values measured between the zero-upcrossing and crest of a wave.

21. Mean trough front slope

Mean of all slope values measured between the trough and zero-upcrossing of a wave.

22. Mean wave back slope

Mean of all slope values measured on the back face of a wave determined through a zero-downcrossing analysis (i.e. crest to following trough).

23. Mean crest back slope

Mean of all slope values measured between the crest of a wave and the following zero-downcrossing.

24. Mean trough back slope

Mean of all slope values measured between the zero-downcrossing of a wave and the trough.

25. RMS slope

$$\sum = \left[\frac{1}{N} \sum_{i=1}^{N} (S_{EW}^2 + S_{NS}^2) \right]^{1/2}$$

26. Significant slope

RMS elevation / wavelength at the spectral peak

EXECUTIVE SUMMARY

A study was conducted from February 15, 1984 to April 11, 1984 at the Hibernia site on Newfoundland's Grand Banks, to assess the performance of various instruments and techniques which measure heave and directional wave climate. Two Datawell WAVEC and one Endeco Type 956 WAVE-TRACK directional buoys were deployed with receiving equipment installed aboard the Mobil Canada Ltd. operated West Venture mobile drilling unit. Present in or near the study area were a Datawell Waverider and a Waverider modified for satellite transmission (WRIPS) operated by the Marine Environmental Data Service (MEDS). As part of the study, overflights with synthetic aperture radar (SAR) were conducted in early April by Intera Technologies Ltd. and hindcasts of directional wave spectra for two storm events were produced by F.G. Bercha and Associates (Nfld.) Ltd.

The WAVE-TRACK buoy was in operation until March 1, when receiver failure occurred. As a result of numerous problems only a 56.7% data recovery was obtained. The first WAVEC buoy operated throughout the study though, during February, some data loss was attributed to receiving antenna problems and in March, from physical problems with the receiver installation. There was an overall 75% data recovery with a 94% recovery after replacement of the antenna. The second WAVEC buoy had a 97% data recovery for scheduled transmissions with no operation or processing problems encountered.

The Datawell Waverider went adrift on March 10. The data were processed and supplied by MEDS. The data from the internal cassette of the satellite transmitting WRIPS buoy were also made available by MEDS.

Due to problems with low wave energies and improper application of the chosen synthetic aperture radar parameters, there were limited results from the SAR study.

The WAVEC and WAVE-TRACK data underwent a standard processing procedure. Assignment of record times proved difficult, especially for the WAVE-TRACK, as time indicators were often absent in the raw records. The data were

calibrated, despiked and cross-spectral analysis were performed on the heave and slope channels with the co- and quadrature spectral estimates ensemble averaged. A Longuet-Higgins directional calculation was then applied. Each heave spectrum was checked visually for data quality. Various data displays for the three directional buoys, the Waverider and MANMAR statistics obtained from the West Venture mobile drilling unit were generated.

Two storm events were chosen for wave hindcasting. The first, two-day event was characterized by a rapid development of winds up to a maximum of 39 knots and an equally rapid and smooth decay. The second event, lasting seven days, contained periods of relatively steady winds. The hindcasts were prepared using a version of a discrete spectrum model originally developed by D.T. Resio at the U.S. Army Waterways Experiment Station.

Prior to examining the results, sources of error were determined by means of a statistical error analysis, by observation of physical problems such as icing of the WAVE-TRACK buoy and through a linearity analysis. The latter showed, for the WAVE-TRACK buoy, that the transfer functions supplied by the manufacturer were insufficient to correct for buoy response and that the buoy response at frequencies greater than 0.3 Hz was poor. Non-linearity increased for all buoys during storm conditions possibly resulting from a Doppler shift due to wind induced surface currents though other non-linear effects cannot be ruled out.

Bulk analyses of heave spectral statistics showed general agreement between all the buoy data sets. There was considerably more scatter when examining the directional statistics. An average apparent direction was calculated and significantly improved the agreement between the respective data sets. These were also shown to correspond well with wind directions. The peak directions from the Endeco buoy did not agree well with those from the WAVEC nor with those calculated using a Band-Pass analysis designed by Endeco.

Selected spectra were examined and shown to be similar although those of the WAVE-TRACK tended to contain increased noise throughout and higher energy at very low frequencies. The directional spectra were improved by correcting with the linearity analysis results but the WAVE-TRACK buoy still showed greater directional spread than the WAVEC. The physical problems of the WAVE-TRACK

buoy preclude any strong conclusions, however similar behaviour was also observed for a buoy moored on the West Coast of Canada (Juszko et al., 1985).

Hindcast model results were examined and shown to predict well the significant wave height, peak period and mean directions during all phases of the storms. The model was capable of separating two directional peaks at a single frequency. However, the spectra appeared to develop too quickly, to be smoothed in frequency and often to have significant energy at frequencies lower than observed or expected.

Corrected slope time series were used to calculate various wave shape statistics. It was found that mean surface slopes were directly related to wind speed with a response time-lag less than that of significant wave height. The waves were also shown to increase in asymmetry with wind speed. There was little correlation with steepness and asymmetry parameters obtained from the heave signal.

Treating wave slopes as accelerations, it was shown that the mean direction of wave travel can be obtained solely from the slope values by minimizing the error associated with the major axis of an ellipse described by a scatter plot of slope coordinates. The directional spread can be examined qualitatively through the ratio of the major and minor axes.

It was concluded that the information return from a directional buoy, such as the Datawell WAVEC, and its apparently consistent operation, provides significant advantages over a standard Waverider system. Its only drawback is the necessity for mooring close to a manned station (no longer a requirement for the WRIPS buoys). Wave hindcast modelling is necessary as it is still the only method available for generation of the long time series needed for proper extreme-wave analysis. Some modifications, however, would be required if applied to the Hibernia site. SAR imaging is very expensive and would not be useful for any long-term monitoring though it could be used when resolving wave directions with high accuracy, for ground-truthing buoy or model observations, or when specific details of refraction patterns are needed.

RÉSUMÉ

Du 15 février au 11 avril 1984, nous avons effectué une étude sur l'emplacement du projet Hibernia, sur les Grands bancs de Terre-Neuve, en vue d'évaluer divers instruments et techniques de mesure des conditions de pilonnement et de direction des vagues. Nous avons largué deux bouées directionnelles Datawell WAVEC et une bouée directionnelle WAVE-TRACK 956 de type Endeco; les instruments de réception étaient installés à bord de la plate-forme de forage mobile West Venture exploitée par Mobil Canada Ltd. Il y avait dans la zone d'étude ou près de cette zone un houlographe Datawell et un houlographe modifié pour la transmission satellite (WRIPS) utilisés par le Service des données sur le milieu marin (SDMM). Dans le cadre de l'étude, la société Intera Technologies Ltd. a effectué des survols au début d'avril avec un radar à antenne synthétique (RAS), et F.G. Bercha and Associates (Nfld.) Ltd. a préparé des rétrospections des spectres de directions des vagues au cours de deux tempêtes.

La bouée WAVE-TRACK a été utilisée jusqu'au 1er mars, jusqu'à ce qu'une panne du récepteur se produise. Suite à de nombreux problèmes, seulement 56,7 % des données ont été récupérés. La première bouée WAVEC a été utilisée pendant toute l'étude, mais il s'est produit en février des pertes de données attribuées à des défectuosités de l'antenne réceptrice et, en mars, du matériel de réception. Le taux de récupération global des données a été de 75%, et de 94% après le remplacement de l'antenne. Ce taux a été de 97% pour ce qui est des transmissions prévues de la deuxième bouée WAVEC, qui n'a pas posé de problèmes d'utilisation ou de traitement des données.

Le 10 mars, le houlographe Datawell a été lancé à la dérive. Les données recueillies ont été traitées et fournies par le SDMM. Ce dernier a également mis à notre disposition les données provenant de la cassette interne de la bouée WRIPS pour la transmission satellite.

En raison de problèmes dus à la faible énergie des vagues et à un mauvais choix des paramètres pour le radar à antenne synthétique (RAS), l'étude menée à l'aide de ce dernier a fourni peu de résultats.

Les données obtenues des bouées WAVEC et WAVE-TRACK ont été soumises à une méthode de traitement classique. L'attribution des temps d'enregistrement s'est révélée difficile, en particulier pour la bouée WAVE-TRACK, car les données brutes ne comprenaient souvent aucun indicateur du temps

d'enregistrement. Nous avons étalonné les données, éliminé les valeurs aberrantes, effectué une analyse inter-spectrale des canaux de pilonnement et de pente et fait la moyenne de l'ensemble des estimations cospectrales et des estimations spectrales de quadrature. Nous avons ensuite appliqué le calcul directionnel de Longuet-Higgins. Nous avons vérifié visuellement la qualité de chaque spectre de pilonnement. Nous avons en outre divers affichages des données provenant des trois bouées directionnelles, du houlographe et des statistiques MANMAR obtenues de la plate-forme de forage mobile West Venture.

Nous avons choisi deux tempêtes pour faire des prévisions à posteriori des vagues. La première, qui a durée deux jours, était caractérisée par un accroissement rapid de la vitesse des vents jusqu'à un maximum de 39 noeuds et une diminution aussi rapide et douce. La deuxième tempête, qui a durée sept jours, a comporté des périodes de vents relativement stables. Les prévisions à posteriori ont été préparées à l'aide d'une version d'un modèle à spectre discret mis au point à l'origine par D.T. Resio, à la U.S. Army Waterways Experiment Station.

Avant d'examiner les résultats, nous avons déterminé les sources d'erreur en effectuant une analyse statistique des erreurs, en observant les problèmes physiques qui se sont posés tels que le givrage des bouées WAVE-TRACK et en effectuant une analyse de linéarité. Cette dernière a montré que, dans le cas de la bouée WAVE-TRACK, les fonctions de transfert prévues par le fabricant étaient insuffisantes pour corriger la réponse de la bouée et que cette réponse était faible à des fréquences supérieures à 0,3 Hz. La non-linéarité a augmenté pour toutes les bouées au cours des tempêtes, peut-être à cause d'un décalage Doppler dû aux courants de surface induits par le vent, mais il est possible que d'autres effets de non-linéarite soient en cause.

D'après les analyses globales des statistiques sur les spectres du pilonnement, toutes les séries de données provenant des bouées correspondent généralement entre elles. Les écarts étaient considérablement plus grands pour ce qui est des statistiques sur les directions. En calculant une direction apparente moyenne, nous avons beaucoup amélioré la correspondance entre les différentes séries de données. Ces dernières correspondaient également bien pour ce qui est des directions des vents. Les directions dominantes indiquées par la bouée Endeco ne correspondent pas bien avec celles obtenues à l'aide de la bouée WAVEC, ni à celles qui ont été calculées à l'aide d'une analyse passe-bande conçue par Endeco.

Nous avons examiné certains spectres qui se sont avérés semblables, même si ceux de la bouée WAVE-TRACK semblaient comporter davantage de bruit en général et une plus grande énergie aux très basses fréquences. Nous avons amélioré les spectres de directions en apportant une correction à l'aide des résultats de l'analyse de linéarité, mais les données de la bouée WAVE-TRACK présentaient toujours une variabilité en direction supérieure à celles de la bouée WAVEC. En raison des problèmes physiques subis par la bouée WAVE-TRACK, nous n'avons pu tirer de grandes conclusions, mais cela a été également le cas pour une bouée amarrée sur la côte ouest du Canada (Juszko et coll., 1985).

Nous avons examiné les résultats du modèle de prévision à posteriori qui s'est révélé représentatif de la hauteur, de la période maximale et de la direction moyenne des vagues au cours de toutes les étapes des tempêtes. Le modèle a permis de distinguer deux pics directionnels à une même fréquence. Toutefois, les spectres ont semblé se développer trop rapidement, se lisser en fréquence et, souvent, avoir une énergie importante à des fréquences plus faibles que celles observées ou attendues.

Nous avons utilisé des séries chronologiques de pentes corrigées pour calculer diverses statistiques sur la forme des vagues. Nous avons trouvé que les pentes moyennes de surface étaient directement liées à la vitesse du vent, avec un retard inférieur à celui de la hauteur des vagues. Nous avons également observé que l'asymétrie des vagues augmentait avec la vitesse du vent. Les paramètres de raideur de pente et d'asymétrie obtenus à partir des signaux de pilonnement étaient peu corrélés.

En traitant les pentes des vagues comme des accélérations, nous avons montré que la direction moyenne de propagation des vagues peut être obtenue à partir des seules valeurs des pentes en minimisant l'erreur associée au grand axe de l'ellipse décrite par le nuage de points dans le diagramme de dispersion coordonnées des pentes. Le rapport du petit au grand axe est un indice de la dispersion des directions.

Nous avons conclu que, par l'information qu'elles fournissent et par la constance apparente de leur fonctionnement, les bouées directionnelles comme la bouée Datawell WAVEC offrent des avantages importants par rapport au houlographe classique. Leur seul désavantage est qu'il faut les amarrer près d'une station habitée (ce qui n'est plus nécessaire pour les bouées WRIPS). Il faut procéder à la modélisation à posteriori des vagues, car elle est encore la seule

méthode qui permette la production des longues séries chronologiques nécessaires à une bonne analyse des vagues d'amplitude extrême. Il faudrait toutefois apporter certaines modifications si on envisage de les utiliser à l'emplacement du projet Hibernia. L'imagerie des radars à antenne synthétique est très coûteuse et ne serait pas utile pour une surveillance à long terme; toutefois, elle pourrait être utilisée pour calculer avec grande précision la direction des vagues, pour vérifier au sol des observations faites à l'aide de bouées ou de modèles ou pour obtenir des détails de réfraction particuliers.

INTRODUCTION

The mobilization and deployment of the directional wave buoys for the Environmental Studies Revolving Funds (ESRF) Directional Wave Spectra Intercomparison Study was performed by Seakem Oceanography Ltd. (under a contract to Petro-Canada Inc.) and the Wave Climate Group of the Marine Environmental Data Service (MEDS), Fisheries and Oceans Canada. The preliminary work of mooring design and construction took place in early January of 1984 when Seakem and MEDS personnel prepared, tested and deployed the buoys and installed the receiving stations. This was completed by the middle of February.

Three directional wave measuring systems were installed as part of the ESRF study: two Datawell WAVEC buoys (one each owned by MEDS and Petro-Canada (PEX)) and a leased Endeco type 956 WAVE-TRACK buoy. A Coastal Climate MINIMET buoy, leased by Petro-Canada, was also installed at the study site as part of a separate experiment. This was performed by Coastal Climate Company personnel with assistance by personnel from this project. In addition, as the deployment vessel was under a joint charter between Mobil Oil Canada Ltd. and Petro-Canada, the geological survey instrument package, RALPH, was prepared and deployed by Dobrocky Seatech personnel for Mobil.

The study was undertaken near the Hibernia C-96 drill site on the Grand Banks of Newfoundland over a period extending from February 15, 1984 to April 11, 1984. Figure 1 shows the location of the experiment, with the insert detailing the moored buoy positions. This site was convenient as it provided relatively uniform water depths, between 80 and 85 meters, freedom from nearshore influences, and a nearby manned platform, the West Venture mobile drilling unit operated by Mobil Oil Canada Ltd., to house receiving and data logging equipment. The presence of the drilling unit had the added benefit of supplying two extra data sets to the study: visual observations of meteorological and sea conditions and heave spectral estimates from a nearby Datawell Waverider. A satellite transmitting (WRIPS) Waverider was also operating in the vicinity of the drilling unit. The site is generally open to all wave directions with perhaps some sheltering from 270 to 300° (true) due to the Island of Newfoundland. During the study, sea ice

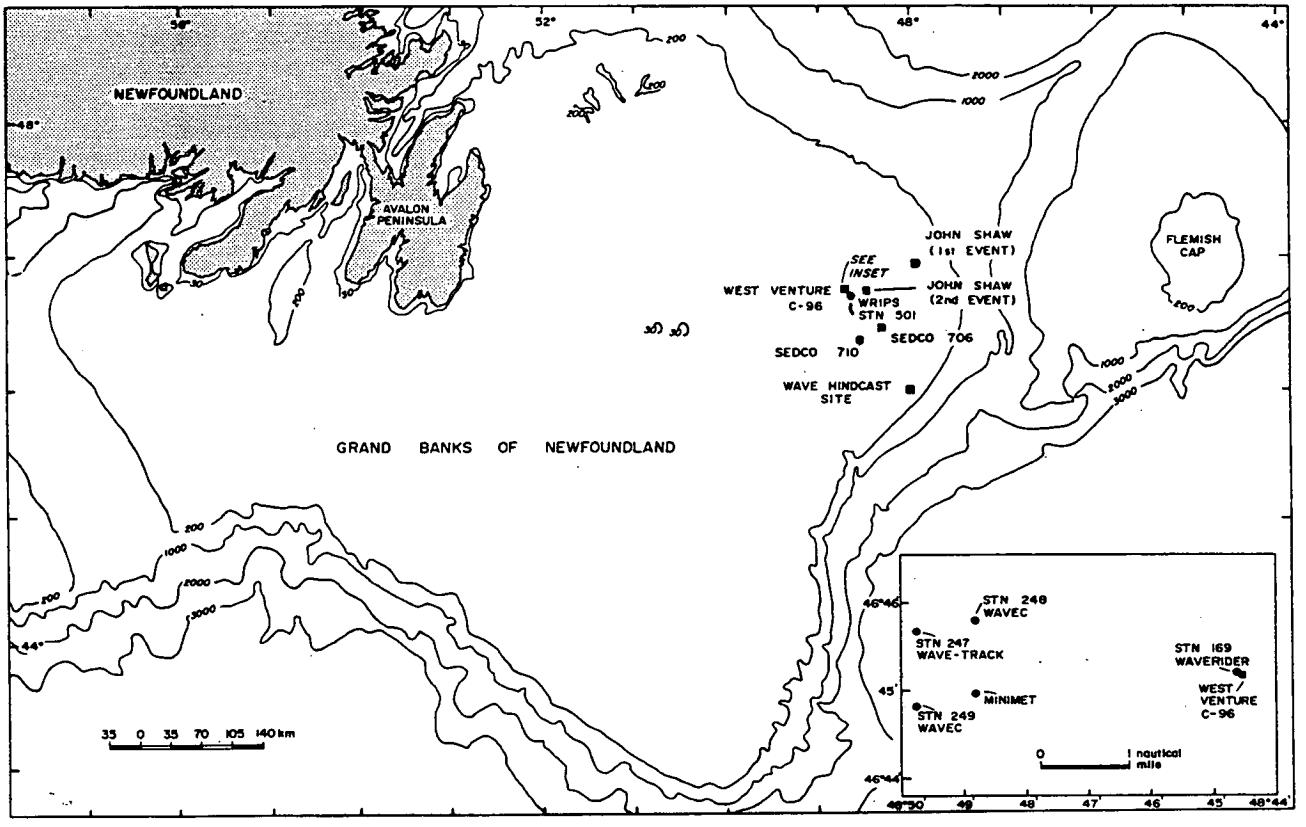

Figure 1. Location Map.

approached and retreated from the north-northwest several times, potentially limiting fetch from these directions as well. Table 1 details the ownership of the instrumentation, their mooring location, the parameters measured and the source of the processed data.

TABLE 1.

INSTRUMENTS AND METHODS - SUMMARY

INSTRUMENT OR METHOD	OWNER	LOCATION	STN. NO.	AVAILABLE PARAMETERS	DATA PROCESSING PERFORMED BY
DATAWELL WAVERIDER	MEDS[1]	46° 45.20' N 48° 44.60' W	169	- Heave Spectral Estimates	MEDS
DATAWELL WAVERIDER[2] (WRIPS)	MEDS	46° 41.00' N 48° 40.00' W	501	- Heave Spectral Estimates	INTERNAL
DATAWELL WAVEC	PETRO-CANADA INC.	46° 45.80' N 48° 48.80' W	248	- Heave, North-South and East-West Slope - Heave and Direction Spectral Estimates	SEAKEM OCEANOGRAPHY LTD.
DATAWELL WAVEC[2]	MEDS	46° 44.83' N 48° 49.75' W	249	- As above	SEAKEM OCEANOGRAPHY LTD.
ENDECO WAVE-TRACK TYPE 956	ENDECO INC.	46° 45.67' N 48° 45.75' W	247	- Heave, North-South and East-West Wave Tilts - Heave and Direction Spectral Estimates	SEAKEM OCEANOGRAPHY LTD.
MINIMET	COASTAL CLIMATE CO.	46° 44.97' N 48° 48.80' W	-	- Heave Spectral Estimates - Meteorological Data	COASTAL CLIMATE
VISUAL OBSERVATION (On West Venture)	MOBIL OIL CANADA LTD.	46° 45.17' N 48° 44.59' W	-	- Sea and Swell Estimates - Meteorological Data	
SYNTHETIC APERTURE RADAR	INTERA ENVIRONMENTAL CONSULTANTS LTD.	Over the buoy locations	-	- Wavelength, Wave Speed and Direction	INTERA ENVIRONMENTAL CONSULTANTS LTD.
WAVE HINDCAST MODELLING	F.G.BERCHA LTD.	46° N 48° W		- Heave and Direction Spectral Estimates	F.G. BERCHA LTD.

1 - MEDS - Marine Environmental Data Service, Department of Fisheries and Oceans, Ottawa
2 - Additions to initial experimental design

DATA COLLECTION AND PROCESSING

INSTRUMENTATION

Datawell Waverider

There were two Datawell Waverider buoys in the study area. One was a standard heave measuring buoy which transmitted to the drilling unit. The other was modified by Adamo Rupp Assoc. for internal data processing and satellite transmission (WRIPS). The Waveriders report heave by means of double integration of a measured acceleration. The accelerometer is mounted on a stabilized platform which reduces the contamination of the vertical signal by any horizontal acceleration.

For the standard Waverider, the analog wave height signal is transmitted to a shore station where it is recorded on tape. In addition, a reference signal, of constant amplitude and frequency, is recorded which aids in the diagnosis of tape speed variation and stretching which would otherwise affect the accuracy of the results. These data tapes were digitized and processed at MEDS, who supplied the spectral information.

The satellite transmitting WRIPS buoy processes, internally, the heave signal into a heave spectrum and transmits 43 statistics (35 frequencies) to the GOES satellite. The signal in turn is relayed to a receiving station in the United States and put on computer which can be accessed by the MEDS computer in Ottawa. These transmissions are recorded on an internal tape as well as, during storms, a raw time series every three hours. These data allow for the filling of any transmission gaps and for the possibility of further analysis of the original time series. These data were also provided by MEDS for this study.

Datawell WAVEC

The Datawell WAVEC buoy is a surface following heave and slope measuring buoy. Figure 2 contains a schematic of the WAVEC buoy and Figure 3

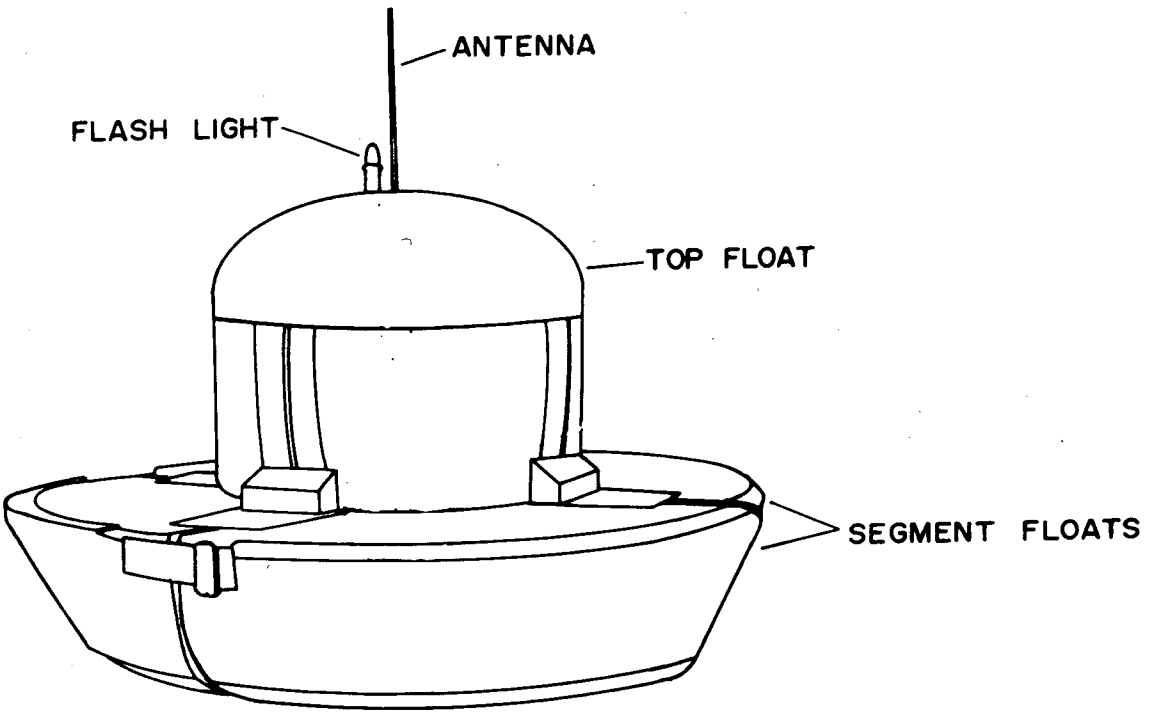

Figure 2. Schematic of a Datawell WAVEC Buoy.

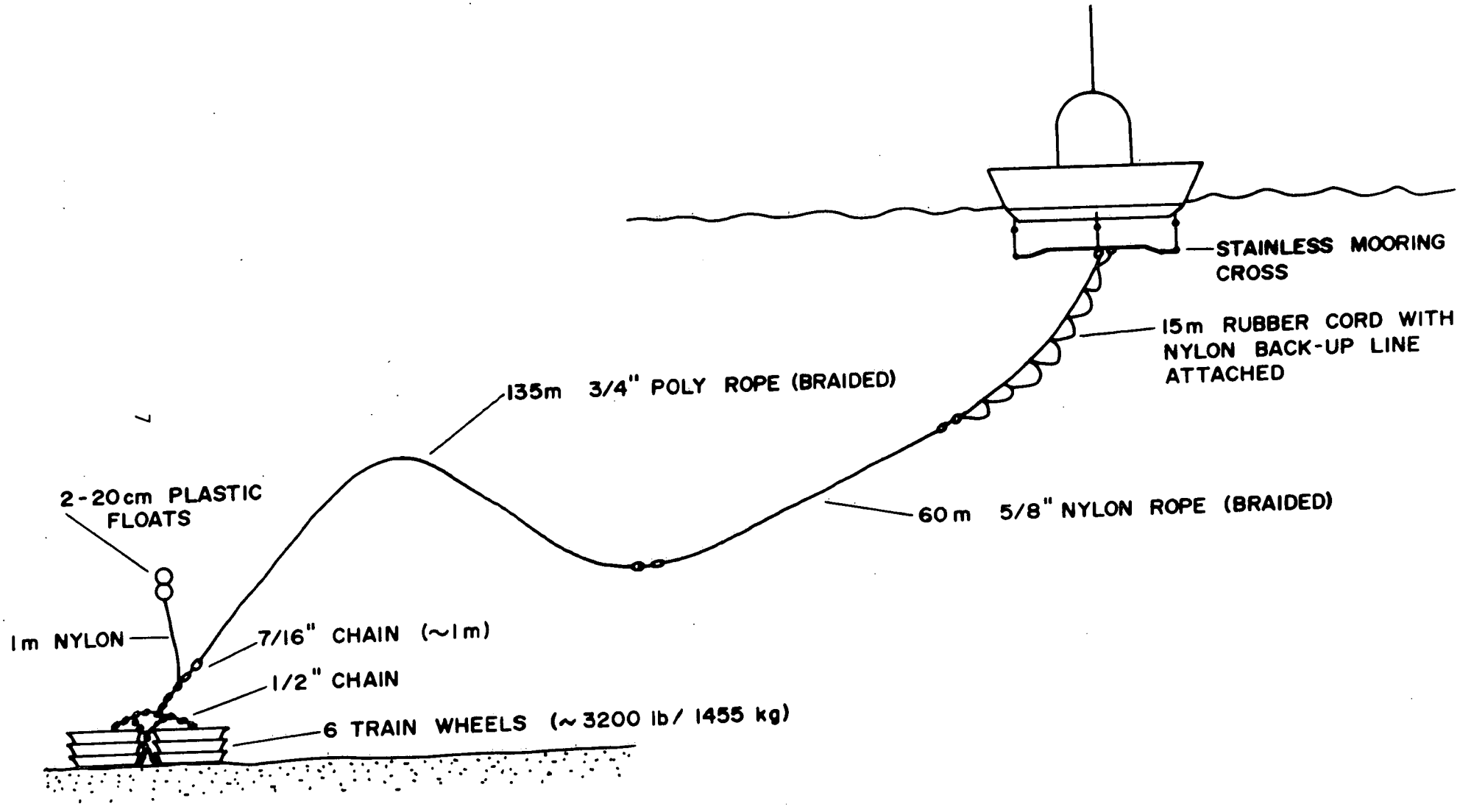

Figure 3. Schematic of WAVEC mooring.

that of the mooring used in this study. The buoy design consists of a central instrument canister containing the HIPPY sensor to which are strapped five flotation segments.

The HIPPY sensor measures heave by measuring acceleration then double integrating. Pitch and roll measurements are obtained from the induced voltages in a pick-up coil, mounted on a gravity stabilized platform, as it crosses two alternating magnetic fields which have been generated parallel to the pitch and roll axis. A three-axis (x, y, and down) fluxgate compass measures the earth's local magnetic field. These six analog signals are filtered with anti-aliasing filters, sampled every .78125 seconds and transmitted to a DIREC receiver on the drilling unit. Within the receiver, the pitch, roll, and magnetic field measurements are used to calculate the buoys orientation and the two surface slope components with respect to magnetic north and east. The receiver also performs an initial error check on signal transmission quality and rapid orientation changes. An operator can control the recording duration and interval, obtain real-time output using an attached computer terminal, and select optional continuous recording during periods of higher wave heights (i.e., above a given threshold value).

A Columbia Data Products 300D cartridge recorder was used to write, in ASCII characters, the digitized (12-bit) heave and slope measurements, a scan counter to check for any missing data, and a quality code (values 0 to 9), the latter two being generated by the DIREC receiver. A time header is also written at the start of each new recording period. The data logging system resulted in the least amount of data loss due to time ambiguities or missing data.

Endeco 956 WAVE-TRACK

The Endeco 956 WAVE-TRACK buoy does not follow surface slope but responds to the associated shear in the wave orbital velocities which induce a buoy tilt relative to the vertical by asserting a drag on the shaft of the buoy (see Figure 4). The resulting tilt signals are in phase with that of the heave and 90° out of phase with a corresponding surface slope signal. The impetus for this "inverted pendulum" design was to allow for maximum buoy response at wave peaks and

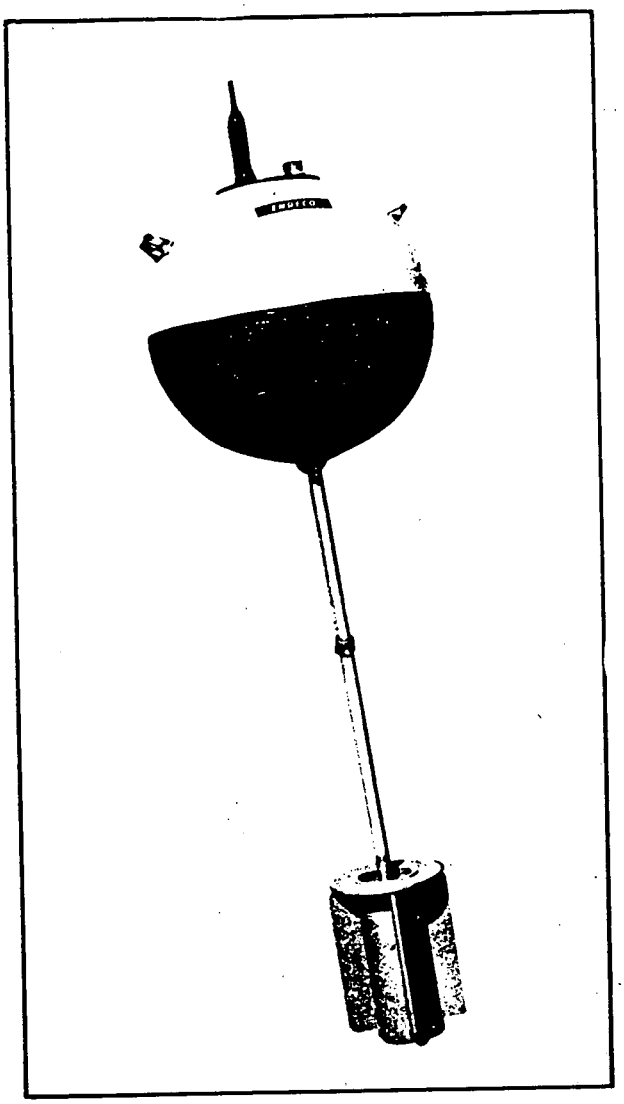

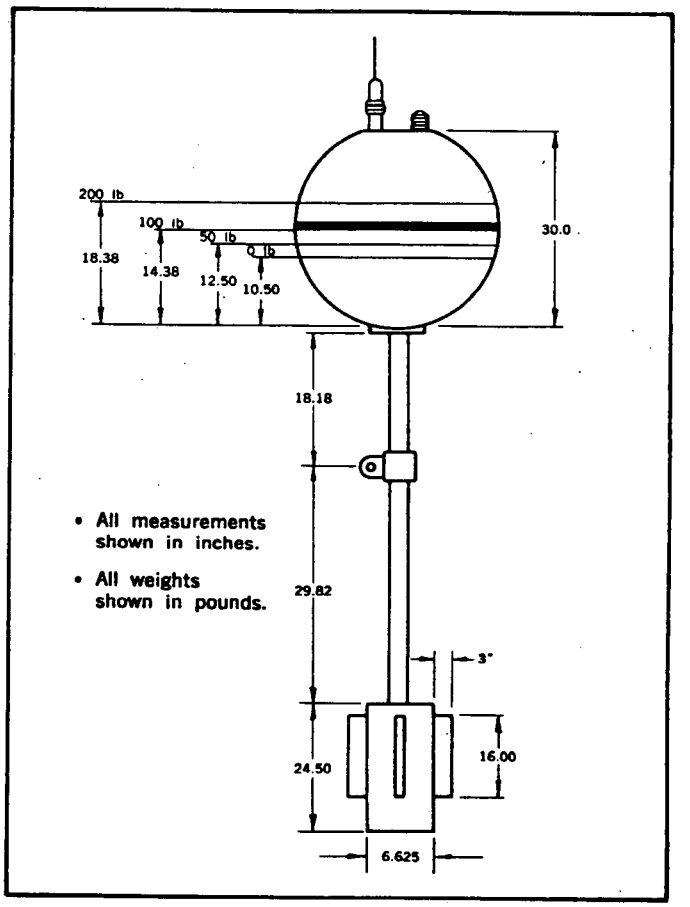

Figure 4. Schematic of an Endeco WAVE-TRACK buoy.

troughs thereby reducing errors due to horizontal accelerations associated with breaking waves. Moving in phase with orbital velocities was also believed to reduce high frequency surface noise. Figure 5 contains a schematic of the mooring used in this study.

The sensor package is located in the pressure case at the lower end of the shaft while the transmitting electronics and batteries are contained within the surface sphere. Heave is again measured using an accelerometer. The pitch and roll sensors consist of small reservoirs, mounted perpendicularly to each other in the horizontal plane, within which mercury moves up and down when the sensor is tilted. Capacitance sensors are mounted on the reservoir housing and respond to any movement of the mercury. A two-axis fluxgate compass provides the buoy orientation needed to convert the pitch and roll information to north-south and east-west tilts. The analog information from the three channels (heave, N-S and E-W tilt) are telemetered to the receiver where the signals are filtered and sampled by a sample and hold circuit into eight bit digital data. The data are then transferred to a data logger for storage. The receiver also supplies three zero values every 128 scans (one scan consisting of three measurements, one value for each channel) and a time mark for each start of a transmission. If the signal is temporarily interrupted, the hour mark will again be written out when transmission resumes. By counting the number of points between each indicator scan, any missing data will be noticed. If so, the entire block has to be rejected as there is no way of knowing from which channel or scan the data points were lost. The receiver does not supply explicit time headers, individual scan counters or quality codes. The Endeco receiver does have the option of providing analog output, in which case a different, more versatile data logging system (e.g. a Sea Data Model 1236 Data Logger) could be used.

The data logger used in this experiment was a Techtran Logger, which, like the Columbia Data logger, only transcribes that information sent to it by the receiver. The data in this case are written in binary.

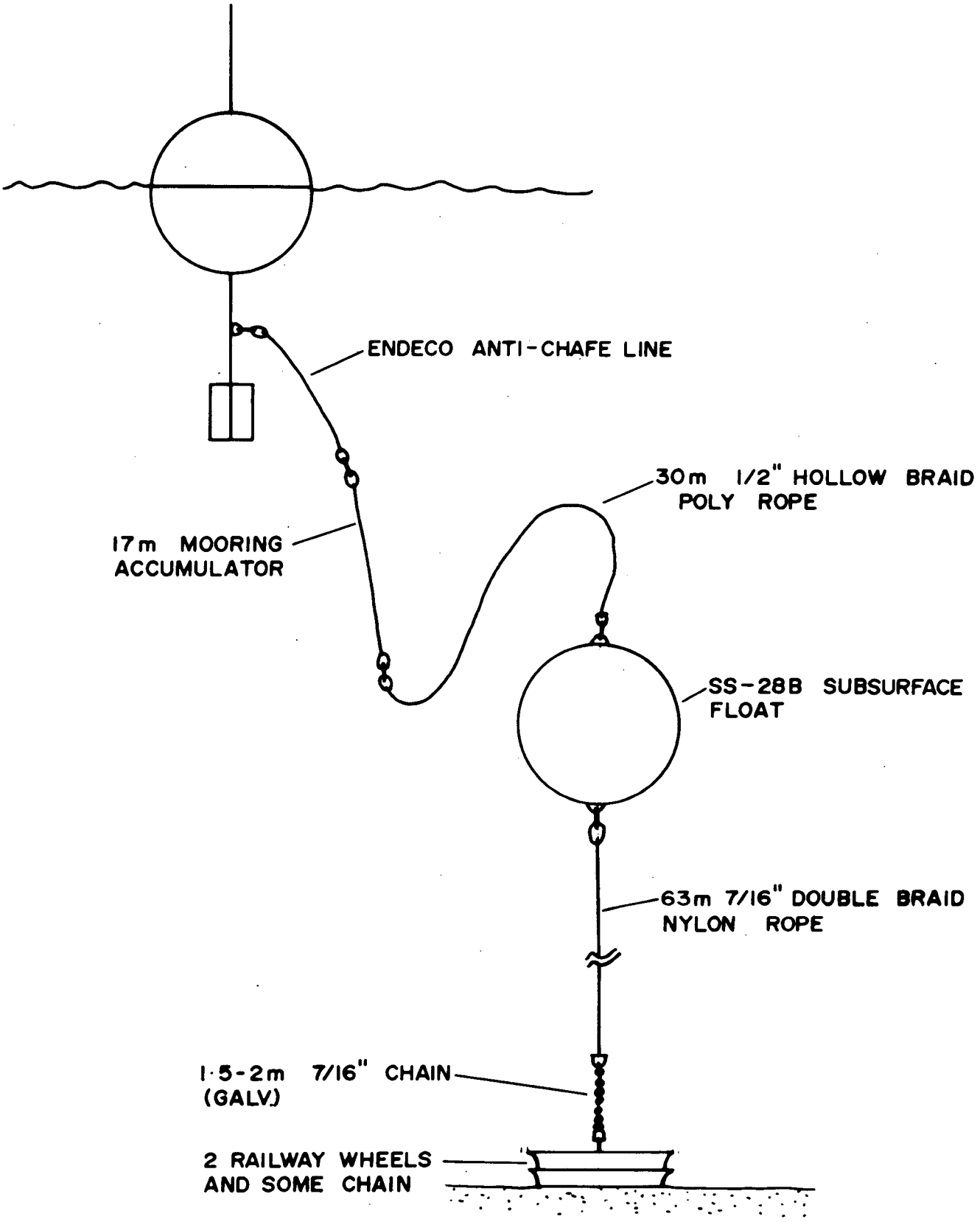

Figure 5. Schematic of WAVE-TRACK mooring.

MINIMET

The MINIMET buoy was a prototype system which measured both wave heave and local meteorological conditions. A schematic of the buoy and mooring are provided in Figure 6. It was present in the area as part of a separate study in order to determine its heave amplitude and phase transfer functions by comparing it with WRIPS and MANMAR data. An analysis of this buoy's performance is contained in Thompson and Buckley (1984).

Visual Observations

Meteorological observers, who report every three hours on the local meteorological and sea state conditions, are stationed on board every offshore drilling unit. The observations of specific interest to this study were the wind conditions and the estimated sea and swell parameters (height, period and direction).

Wind speed and direction are obtained from anemometer dial readings that have been visually averaged over one minute. The procedure for measuring wave parameters is somewhat subjective. Wave periods are calculated by timing the passage of well formed wave crests and dividing by the number of waves observed. An average of at least 15 waves is generally obtained. Wave height is calculated to the nearest 0.5 meters by averaging the estimated crest to trough displacement for 15 waves. Swell wave direction measurement involves sighting along the wave crests then turning 90° to face the on-coming direction and comparing the sighted direction with the rig orientation. The directions (reported as "from") are recorded to the nearest 10°. The direction of the sea waves is assumed to be within 10° of the measured wind direction.

As the wave measurements reported tend to be averaged in frequency, some consideration must be made when deciding on which parameters will be compared to instrument values and on the resolution expected for the parameters.

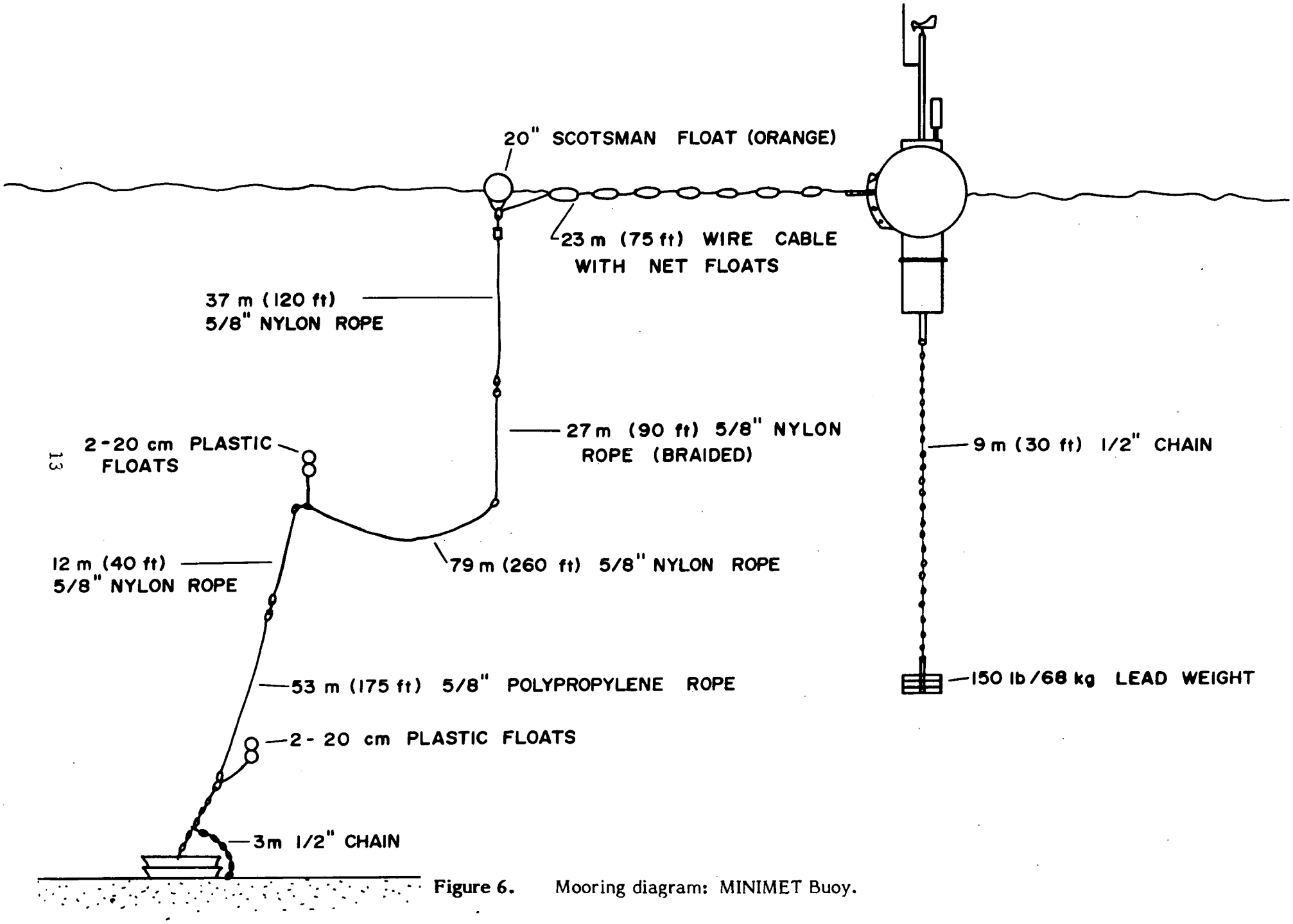

Figure 6. Mooring diagram: MINIMET Buoy.

Synthetic Aperture Radar Imagery

Synthetic aperture radar imagery was performed by Intera Environmental Consultants Ltd. using the STAR-1 system. Details of the experiment are included in Intera Technologies Ltd. (1984) Report R84-070.

The system used an X-band radar with a ground swath width of 23.8 km, with a range resolution of 6 m, an azimuth resolution of 0.14 degrees and a line spacing of 4.2 meters. Two flight lines, orthoginal to each other and crossing over the buoy locations, were necessary in order to resolve an inherent 180° ambiguity in the analysis procedure. The first line was taken parallel to the wave crests and the second flying towards the oncoming waves. On the April 5 flight only a single line pass using a wide swath width of 50 km was conducted.

The data were recorded in two modes. The first consisted of a real-time display of the image on dry silver paper and the second a digital recording on high density digital tape. Selected portions of the latter were then transferred to computer-compatible storage.

FIELD WORK

Mooring Design

Seakem designed and built the moorings for the Endeco WAVE-TRACK and the Petro-Canada Exploration (PEX) WAVEC. MEDS provided the mooring for their WAVEC and Coastal Climate supplied the MINIMET mooring. The Seakem mooring designs were based upon similar moorings used successfully on the British Columbia Coast. The designs for the Hibernia site were checked using a Seakem computer mooring model based on the model of Bell (1977).

Site Selection

The selection of the Hibernia area for the study was made by ESRF, with the semi-submersible rig West Venture as the site of the receiving equipment. Within the study area, buoy locations were based on the physical location of the Environmental Office on the rig (to minimize the length of antenna cables), the location of other moorings in the area, vessel traffic in the area of the rig and the recommendations of the rig's captain and Mobil personnel.

Mooring Deployment

The deployment vessel was the MV Polaris V. All positions were determined primarily by radar using the West Venture mobile drilling unit as a reference. Some of the buoy locations were later checked using satnav.

The MINIMET buoy was deployed with the main buoy first followed by the surface line and float and finally the main mooring line and anchor. Both WAVEC's were deployed by placing the buoy in the water, then streaming out the mooring line and finally dropping the anchor when on location. Similarly the Endeco buoy was deployed buoy first, followed by the thether line and the subsurface float and finally the mooring line and anchor. The RALPH package was deployed marker buoy first, followed by the ground line and instrument package.

Time Schedule

The times of buoy deployment and receiving station installation are summarized in Table 2. Logistical problems caused the delay in the installation of receiving equipment. Recovery procedures were initiated on April 11, 1984 using ships of opportunity to remove wave buoys and moorings. The dismantling of the receiving stations was performed on April 16 with demobilization on shore finished by April 18, 1984.

Table 2. Time of Buoy Deployment and First Recording.

Instrument Type	Buoy Deployment Date	Buoy Deployment Time (NST)	First Recording Date	First Recording Time (NST)
MINIMET	8-2-84	1000	N/A	
WAVEC (PEX)	8-2-84	1140	14-2-84	2032
WAVEC (MEDS)	8-2-84	1414	14-2-84	2032
WAVE-TRACK	8-2-84	1504	14-2-84	2030

OPERATIONAL CONSIDERATIONS

Deployment and Recovery

The Endeco WAVE-TRACK buoy was the easiest to deploy due to its small size, light weight and sensor immunity to rotation. Deployment over the stern roller of a supply vessel should be possible with this buoy and its mooring system although a vessel with a crane or a boom would be preferred. Recovery is also relatively easy and could be done over the stern roller of a supply vessel. Again the size, weight and sensor type contribute to the ease of recovery. One factor that increases the complexity of the moorings is the requirement for keeping the vertical mooring tension down to about 445 Newtons (100 lbs). This requires the use of a subsurface float if there is any significant current or the water is of a depth greater than 50 m. Endeco has indicated that they now make a larger version of this buoy that would reduce this restriction.

The Datawell WAVEC buoy is more difficult to deploy than either a Datawell Waverider or an Endeco WAVE-TRACK due to its size and weight and to a lesser degree its sensitivity to accelerometer damage from spinning. However, the foam flotation sections of the buoy hull do provide some cushioning ability and sensor protection during deployment and recovery. The deployment and recovery vessel does require lifting capability either with an "A" frame, a crane or a boom. Although the manufacturer claims towing of the buoys is possible, we did not find the buoy to tow well the one time we tried it. Some experimentation may help to improve the towing ability, which might ease the deployment. A drilling platform crane could be used to place the buoy in the water or lift it back on board a supply vessel. Once the buoy is in the water, deploying the rest of the mooring is quite simple. In deep water with strong currents, one would have to consider using subsurface flotation. In places like the Grand Banks or the Scotian Shelf, subsurface flotation is not required.

The MINIMET buoy was the most difficult to deploy due to the mast with its fragile sensors, its weight and shape and the somewhat complex mooring design (Figure 6). Corrosion and mechanical wear may be a problem for long term use. Deployment from a supply vessel would be extremely difficult unless sea conditions were good and a crane was available.

Icing

All buoys were observed to collect ice under freezing spray conditions. Our observations and the data recovery indicate that the WAVE-TRACK buoy was affected much more by icing than the WAVEC. Missing data and large mean tilts ($>10^{o}$) were noted in the Endeco data though the latter may also be a result of wind friction and large currents. It appears the low freeboard and protuberances on the buoy hatch contribute to the icing problem. The low reserve buoyancy and asymmetric icing appear to result in degraded buoy response. Figure 7 contains the time series of observed mean tilts and air temperature from MANMAR measurements. There was a good correspondence of large tilts with freezing temperatures.

The range of the tilt sensor is $\pm$ 45^{o}. As a result of the large mean tilts, this range was exceeded on numerous occasions, however, to what extent is unknown as the voltage record is cut off at 45^{o}. The mean tilt calculated was therefore smaller than actually experienced and it cannot be subtracted out directly as this often resulted in a corrected value extending past the operational range in the other direction. The response of the accelerometer may be questionable at these large angles, hence both the directional and heave spectral values are of limited usefulness.

A mass of ice on the surface of a heave or directional measuring wave buoy will act to change the instrument response in a given wave field. The change may be frequency dependent. At low frequencies, the waves have greater energy than at high frequencies, and can overcome the extra inertial resistance supplied by the ice. Once the buoy is set in motion, the increased weight would tend to increase the buoy's response compared with an unweighted buoy. At high frequencies the energy of the waves may not be sufficient to overcome the increased inertia.

If the ice distribution is uniform over the buoy's exposed surface, errors introduced in the slope measurements may cancel each other to some extent when calculating mean wave directions, though the directional spectrum will still be affected. However, an asymmetric weight distribution would affect one direction channel more than the other and create a frequency dependent bias in the direction calculations.

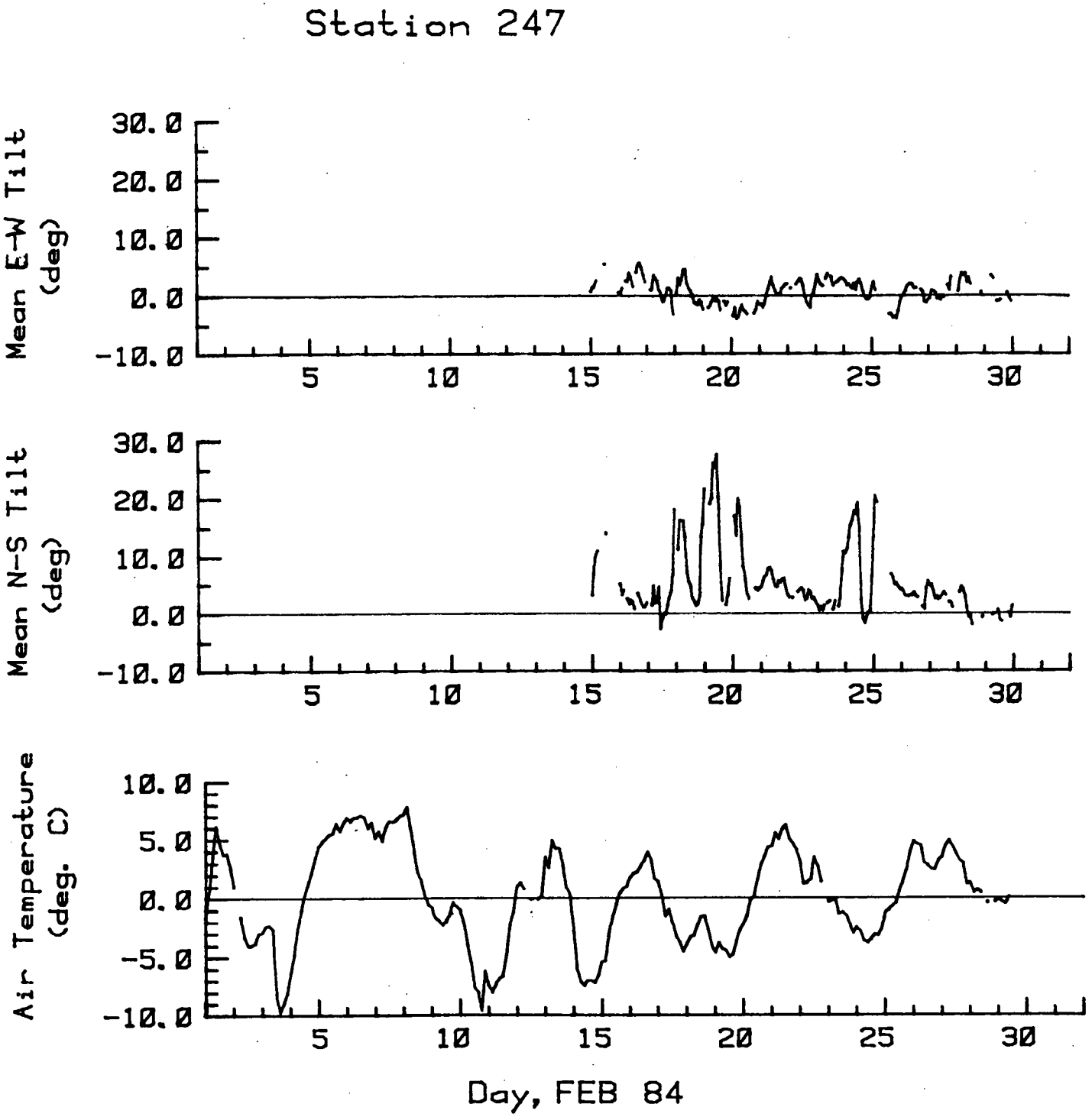

Figure 7. Observed mean tilts in WAVE-TRACK data and corresponding air temperature.

This ice effect is the same for both the WAVEC and WAVE-TRACK buoys. However, the shaft design of the Endeco buoy creates further problems. The "inverted pendulum" concept of measuring orbital velocities requires proper response to the horizontal forces in the orbits. If the shaft experiences a mean tilt, it will also be responding to perceived horizontal velocities induced by the vertical velocity components of the wave orbits. At the least, this will be inducing a phase shift to the tilt signal and may result in phase dependent response changes.

To estimate the effect on the data due to various amounts of icing, or otherwise induced mean tilts, would require modelling of the buoy response for different frequencies.

The WAVEC buoys collected ice mainly on the windward side of the top float and the top leaward side of the main hull.

Reliability

In this study, the WAVEC systems performed much better than the WAVE-TRACK. With the WAVE-TRACK system the receiver failed first. Buoy transmissions then stopped, which may have been due to the buoy coming adrift or battery failure. By the time the buoy was recovered, it was not possible to determine if the transmission problem was due to battery failure.

Both WAVEC systems did not have any failures after deployment although the MEDS buoy was found to have a faulty transmitter which was replaced prior to deployment. The main loss of data with the Petro-Canada WAVEC was after the Endeco receiver was removed which lasted until a new antenna was installed. We suspect that the antenna cable connection was damaged when the Endeco receiver was removed.

Our experience with these systems on the Pacific Coast is similar. After some "prototype" problems with the WAVEC transmitter and receiver systems, we found the WAVEC to work more reliably than the WAVE-TRACK.

Durability

We have noted only one type of problem with the WAVEC in this regard but it is a serious one. On three occasions on the Pacific Coast, the hull flotation

sections have either separated from the buoy or twisted in their retaining wings. The buoy was recovered in all three cases as the top flotation piece provides enough buoyancy to prevent sinking but the potential was there for the buoy to be lost. The onset of the problem seemed to be associated with storm conditions (significant wave heights of 7.0 meters) and could be identified in the recovered data by the presence of large calculated mean slopes (these are normally close to zero in value). Some design modifications may be necessary.

The WAVE-TRACK buoy also has a few problems. We have noted significant corrosion of the aluminum top hatch on two occasions after long deployments. In one case we found that the pendulum staff mounting had pulled out of the fibreglass buoy hull after the buoy mooring had been cut. The PVC sensor housing is quite fragile and can be broken, particularly if exposed to low temperatures.

DATA RETURN

Figure 8 details the operation record of the various buoys, the hindcast period and times of SAR overflights.

Station 169 - Datawell Waverider

This station was in operation prior to the start of this study. The buoy went adrift on March 10 with subsequent data loss. It was recovered and remoored on April 6, however the mooring location was changed. The buoy was damaged on April 9.

Station 247 - Endeco WAVE-TRACK

The station was in operation from 0000 GMT 15 February, 1984 to 0000 GMT 1 March, 1984 when receiver failure occurred. Repairs of the receiver were initiated, however the buoy soon went adrift and was not recovered until the end of the study.

By the end of the operating period, ten data cassettes had been written. As a result of data processing problems discussed in the following section, as well as missing records possibly due to tape runoff, there was only a 56.7% data return while the buoy was in operation. The processing problems can be related to poor signal transfer either due to buoy icing or malfunctioning of the receiver. The data return may be even poorer as all the records before 0600 February 20 are of questionable quality as this was a period when large mean tilts were encountered which would seriously affect the analysis of the tilt signals and, if the cause is a result of buoy icing, could also be influencing the heave signal.

Station 248 - Datawell WAVEC (Petro-Canada)

This station was in operation for the entire experimental period (15 February -11 April, 1984). The recorded data were written onto 14 data cartridges, approximately twice as many as initially expected, due to continuous recording

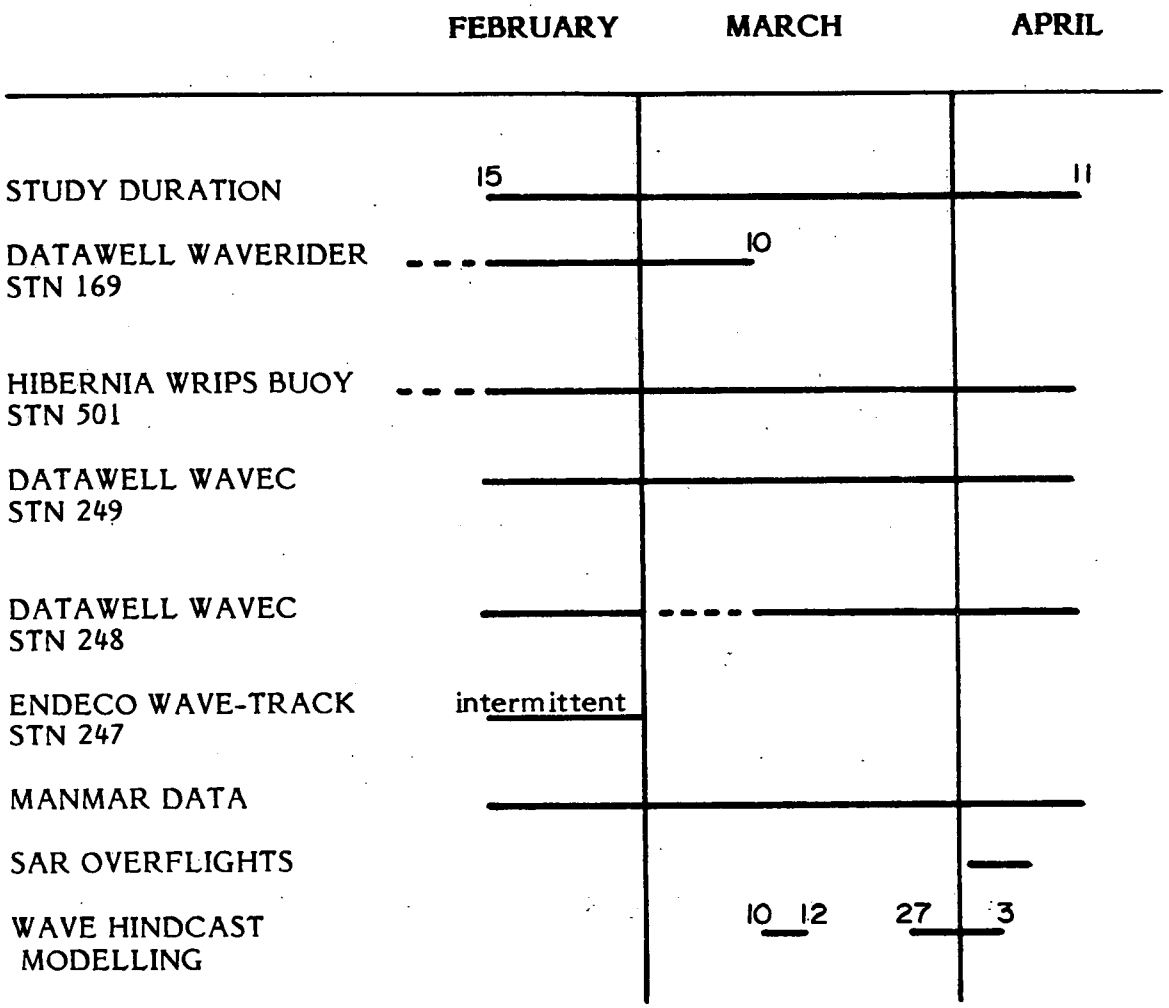

Figure 8. Operation Record.

during storms. The extra data resulted in a significant increase in time spent in data processing and tape handling and in the length of program runs.

During February, there was some data loss and short records (loss of blocks) possibly due to reception interference between its signal and that of the Endeco buoy or a combination of buoy icing and low antenna efficiency. During the first half of March, there was very poor data return. It was suspected that when the Endeco receiver failed and was disconnected to be shipped for repairs, the continuity of the WAVEC receiving set up was disrupted. On March 16, a new antenna was installed upon request, and data recovery after this time improved. Any missing data from March 16 to the end of the study, generally resulted from tape runoff.

The data return was 75% over the entire project with 94% recovery after installation of a new antenna on March 16.

Station 249 - Datawell WAVEC (MEDS)

This station was in operation for the entire study period and the data return throughout was good with any missing records due to tape runoff. By the end of the study, 14 data cartridges were used, again approximately twice as many as initially expected. Total recovery of scheduled data (i.e., every three hours) was 97%.

Station 501 - Hibernia WRIPS Waverider (MEDS)

This buoy provided data throughout the study period.

MANMAR Data

These data were available for the entire study period. The meteorological and sea wave (height and period) records were complete. The direction of wave propagation (from) was only measured directly for observed primary and secondary swell waves. The direction for sea waves is assumed to be within 10^{o} of wind direction.

SAR Overflights

The SAR overflights occurred in conjunction with another study on ice movement and as such do not correspond to a time when all the buoys were functioning nor during high energy sea states. Flights directly over the study area occurred on April 2 and 7. However, only on April 2 were the waves of sufficient energy for a preliminary analysis to be performed and no detailed processing was attempted. The results from this flight were disappointing in that the direction angles are questionable. The problem was believed to be a reflection of the large scanning range used (initially chosen for imaging of icebergs) which allowed the wave crests to move five to ten meters between images. This resulted in weakened images of the crests as well as stretching of the wave image in the azimuth direction which in turn forces the wave peaks to appear as range travelling regardless of their direction of travel. For further details see Intera (1984).

Hindcast Modelling

The periods chosen for the wave hindcast modelling corresponded to the two larger storms observed during the study and the SAR overflight of April 2.

DATA PROCESSING

Table 3 contains a summary of data processing information.

Datawell Waverider

Waverider data were processed by MEDS and required reformatting for use in this study. Satellite transmitted data from the WRIPS buoy were processed internally by the buoy electronics (to spectral estimates) prior to transmission. The spectral statistics were then calculated using the same program code as for the WAVEC and WAVE-TRACK data.

Datawell WAVEC

The following are the processing steps each WAVEC tape has to undergo before any of the data displays will be produced. The processing scheme is detailed in Figure 9.

Tape translation. During tape translation, the recorded information on the data cartridge is transferred, without any modification, to a disc file for handling. The raw data file is backed up on nine-track tape for archiving. This allows for the re-use of the cartridges, which are relatively expensive, and provides an archived file of the lowest order in the processing scheme.

Reading of the raw data. The raw data file is read to convert it into one consisting of individual records, each with a record header indicating the start time of the record and the number of scans it contains. The sample length for this study was set to a nominal 34 minutes resulting in approximately 2688 scans per record.

The start of a new record in the data is indicated by the presence of a time scan line supplied by the receiver which explicitly provides the year, month, day, hour and minute of the first scan. This generally allows for an unambiguous assignment for the time of the transmission. A minor complication arose in this study when the DIREC receivers of both WAVECs "forgot" that 1984 was a leap year. The resulting shift in the dates was easily remedied by a change in program software. The sampling interval was set for once every three hours. However, an

TABLE 3

SUMMARY OF DATA PROCESSING INFORMATION

INSTRUMENT	SAMPLING INTERVAL	BURST DURATION	BURST SAMPLING INTERVAL	BLOCK SIZE	FREQUENCY RESOLUTION	NO. OF FREQUENCIES IN SPECTRUM	NO. OF BLOCKS AVERAGED (Maximum)
DATAWELL WAVERIDER	3.0 hours	20 minutes	0.1333 seconds	1024 samples (136.5 s)	.007324 Hz	64	8
DATAWELL WAVERIDER (WRIPS)	3.0 hours	34 minutes	1.0 seconds	256 samples (256 s)	.00390625 Hz for frequencies <. 11 Hz	35	8
DATAWELL WAVEC	3.0 hours (on continuous recording if RMS waveheight > 1 m)	34 minutes	0.78125 seconds	256 samples (200 s)	.005 Hz for frequencies < .2 Hz .01 Hz for frequencies .2 -.5 Hz	64	10
ENDECO WAVE-TRACK	1.5 hours	34 minutes	1.0 second	128 samples (128 s)	.0078125 Hz .01 Hz (Band-Pass)	60 27	16 -
MANMAR DATA	3.0 hours	NA	NA	NA	NA	NA	NA
SYNTHETIC APERTURE RADAR IMAGERY	NA	NA	NA	128 x 128 meters	NA	NA	4
WAVE HINDCAST MODELLING	3.0 hours	NA	NA	NA	.01 Hz	16	NA

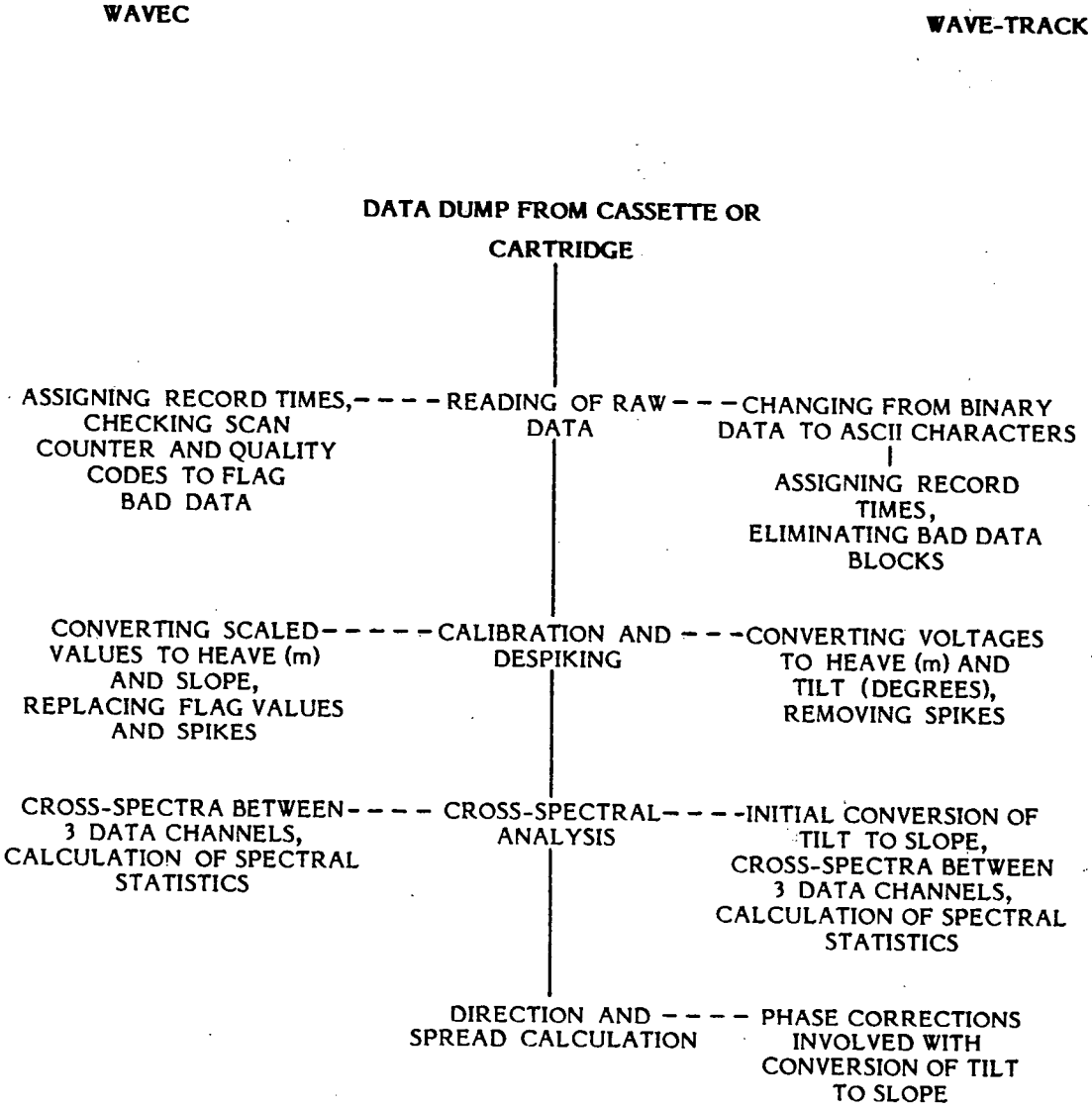

Figure 9. WAVEC and WAVE-TRACK data processing scheme.

option exists to switch to continuous recording when the RMS waveheight exceeds a threshold level. In this study, the threshold was set to one meter to provide better data coverage during high energy sea states. This created a second complication as time headers are only written onto tape at the start of a transmission while days would go by without transmission breaks during storms. In this situation, the time at the start of a new record would have to be calculated using the operator's logs of when the cartridge was inserted into the logger and counting the scans to obtain 34 minutes of data. This may result in some time assignment errors or overlapping of records, although it usually works well if the data quality is good.

During the reading, the receiver supplied counter is examined for any missing scans. These are then padded with flag values. The receiver supplied quality code, a number between 0 and 9 increasing with error severity, was also examined and any scans with a code greater than 2 were replaced with flag values. This provides for a very efficient preliminary error check and quality control of the data. Generally, WAVEC data are good with a quality code of 0. The most frequently encountered problems are an improper orientation check (quality code of 4), which occurs only at powering up of the receiver for the first 100 scans (approximately) and transmission errors (quality codes of 8 and 9).

Calibration and despiking. During calibration, the three raw data channels, stored as scaled integers, are converted to heave in meters and non-dimensional north-south and east-west slope. The despiking procedure consists of reading a record of data (i.e., one 34 minute sample), 256 scans at a time. This number is chosen to coincide with the block size used during the spectral analysis and can be varied. The spike criteria is set as the instrument measurement limit or four times the calculated standard deviation, whichever is smaller. As a cross-spectral analysis must be performed, each channel must conform to the acceptance limits set or the entire block has to be rejected. If more than seven points in a row are bad (flagged or spikes), the block is rejected and a new one started at the next good scan. If less than seven points in a row are bad, they are replaced by interpolated values. If more than 10% of the data in any channel in a block had to be replaced, the entire block is rejected. This method is designed to maximize the number of good data blocks upon which the spectral analysis is later performed. The calibrated, despiked files are archived on nine-track tape.

Spectral analysis. The data were processed according to MEDS standards. Each block of 256 scans, with a maximum of 10 blocks per record, is handled separately with the spectral values ensemble averaged after the last block has been processed. For each block, data from the three channels were handled in pairs with each channel demeaned, passed through a Fast Fourier Transform, the instrument specific phase and amplitude transfer function applied to the Fourier coefficients, the cross-spectral co- and quadrature estimates formed and then truncated to lie between 2 and 30 second periods. Two band averaging for periods less than 5 seconds was also performed to reduce the number of frequencies to be handled. The transfer functions are supplied by the manufacturer and consist of two corrections:

Correction 1. $T_1 = 1/(u + iv)$ (amplitude and phase)

where

$u = 1-a^2 - ab\sqrt{2}$

$v = a\sqrt{2} + b - a^2b$

$a = 1 / (30.8*f)$

$b = 1 / (170*f)$

f = frequency

$i = \sqrt{-1}$

Correction 2. $T_2 = 1/\sqrt{1 + (f/0.6)^{14}}$ (amplitude only)

Both corrections must be applied to the heave signal with only the second one applied to the slope signals.

Ensemble averages are then performed on the spectral values for all the blocks. This results in a maximum of 20 degrees of freedom for frequencies below .2 Hz and 40 degrees of freedom above it. Spectral statistics are then calculated on the heave energy density spectrum. These statistics consist of the following:

1. Moments of the spectrum:

$$M_n = \sum_{i=a}^{b} f_i^n P(f_i) \Delta f$$

$$n = 0, 1, 2, 4$$

where M_n has units of m^2/s^n

where $P(f_i)$ is the spectral density at frequency f_i and the sum is performed over the range a = lowest frequency to b = highest frequency slot.

2. Significant wave height (meters)

$$H_{sig} = 4 * (M_0)^{1/2}$$

3. Spectral peakedness

$$Q_p = 2 \sum_{i=a}^{b} f_i P^2(f_i) \Delta f / M_0^2$$

4. Spectral Width parameters

$$\epsilon = (1 - M_2^2/(M_0 * M_4))^{1/2}$$

5. Spectral Narrowness parameter

$$\nu = ((M_2 * M_0 - M_1^2) / M_1^2)^{1/2}$$

6. Peak period - period of maximum spectral density

7. Average period

$$TM_{01} = M_0/M_1$$

8. Average apparent period

$$TM_{02} = (M_0/M_2)^{1/2}$$

9. Apparent crest period

$$TM_{24} = (M_2/M_4)^{1/2}$$

Direction calculation. The mean direction, angular spread and cosine spread factor are calculated for each frequency band according to the method of Longuet-Higgins et al., (1963) and Hasselman et al. (1980) using selected co- and quadrature spectral estimates in the following manner:

The directional spectrum can be written as:

$$E_n(f,\theta) = E(f)\, D(f,\theta)$$

where

$E(f)$ is the uni-directional heave spectrum

and $D(f,\theta)$ is a spreading function such that

$$\int_0^{2\pi} D(f,\theta)\, d\theta = 1$$

$D(f,\theta)$ can be expressed by the expansion:

$$D(f,\theta) = 1/2\pi + \sum_{n=1}^{\infty} (a_n \cos(n\theta) + b_n \sin(n\theta))$$

where the expression is taken to the order n = 2

The values for the coefficients a_n and b_n are obtained from the cross-spectral estimates:

$$a_1 = \frac{QD_{12}(f)}{k\, E(f)\pi} \qquad a_2 = \frac{Co_{22}(f) - Co_{33}(f)}{k^2\, E(f)\pi}$$

$$b_1 = \frac{QD_{13}(f)}{k\,E(f)\pi} \qquad b_2 = \frac{2Co_{23}(f)}{k^2\,E(f)\pi}$$

where k is the wavenumber, 1 = heave, 2 and 3 = slope

Co_{xy} = co-spectral estimate and QD_{xy} = quadrature spectral estimate

The various directional properties of interest can be obtained as:

mean direction:

$$\theta_m(f) = \text{Arctan}\left(\frac{-QD_{13}(f)}{QD_{12}(f)}\right)$$

angular spread:

$$S_1(f) = \sqrt{\frac{Co_{11}(f) - \text{fact } 1}{Co_{11}(f) + \text{fact } 1}}$$

where

$$\text{fact } 1 = 1/k^2\sqrt{(Co_{22}(f) - Co_{33}(f))^2 + (2\,Co_{23}(f))^2}$$

Cosine spread

$$S_2(f) = \frac{2 * \text{fact } 2}{Co_{11}(f) - \text{fact } 2}$$

where

$$\text{fact } 2 = 1/k\,\sqrt{QD_{12}(f)^2 + QD_{13}(f)^2}$$

The mean direction (taken as "from") is corrected for magnetic declination. The angular spread, $S_1(f)$, also known as the long-crestedness parameter, can be scaled by 90^o and is then almost equal to the RMS angular deviation of energy

when the spectrum is narrow. The cosine spread is the power to which a cosine function, used to model the directional spread, is raised. i.e., when $D(f,\theta)$ has the form:

$$D(f,\theta) = G(f)\cos^{S_2(f)}\left[\frac{\theta - \theta_m(f)}{2}\right]$$

The cosine spread value has been one of the accepted methods of describing directonal spectral shape. The shape can also be described by calculating, directly, the moments of the Longuet-Higgins expansion or by assuming various other distributions such as a Poisson kernel or wrapped normal.

Sorting and checking. The spectral records are sorted into monthly files and each one checked visually, by plotting, for data quality. "Bad" records are flagged and are not used in any of the data displays. A "bad" record generally consists of one with too few blocks used in the ensemble averaging (i.e., < 7 blocks) which would lower the confidence in the estimates. The monthly checked spectral files are archived.

Endeco WAVE-TRACK

The processing of WAVE-TRACK data underwent similar steps as that for the WAVEC in order to reduce any discrepancies in the results due to the processing scheme, although the following differences were unavoidable.

Reading of the raw data. An initial conversion of binary to ASCII characters was required prior to further processing. Unlike the DIREC receiver, the WAVE-TRACK receiver does not supply distinct time and counter values. The time indicator consists of a series of zeros followed by 12-15 hour marks (an incrementing hour counter between 0 and 255). If data transmission is interrupted, this sequence should be written onto tape. The Endeco receiver cannot be adjusted for continuous recording. To process each cassette of data, the expected hour mark at the beginning of the tape had to be calculated from that of a previous tape, the operator's logged start time and the expected time of the first record. This method for record start indication would be sufficient if there are absolutely no problems with the data logging. The processing had to be extremely interactive

so that when any "possible" hour mark was encountered (determined by the number of leading zeros), it was flashed onto the terminal screen and the operator queried whether or not to accept it. This was necessary due to serious signal transmission and/or reception problems at the beginning of the study, which resulted in numerous zeros, few hour marks and short blocks of data. Through the latter part of February, these signal handling problems were reduced and complete records were encountered. However, due to some fault in the receiver, no hour marks were written onto tape. In this case, the starting position of each new record had to be determined by counting the number of scans and initializing a new record when the count equalled that expected according to the set transmission length. The time in the output file was then incremented by 1.5 hours and a new hour mark calculated. The only time known directly was that for the first record of the tape, assuming correct notation in the operator's log. If an hour mark was encountered part way through a tape, it was compared to the one calculated to check for proper time sequencing. They were always found to agree. This allowed for record time assignments generally, but does not ensure against a shift of one or more blocks into adjacent records. On all the tapes when time assignments were in question, there appeared to be missing records at the end when compared with the logged time of tape removal. This may be a result of data writing off the end of the tape or improper time assignments, although, as mentioned earlier, the calculated hour marks always agreed with the few encountered on tape. Because of the data format, there is no independent way of improving confidence in these time assignments.

Again, unlike the DIREC receiver, the WAVE-TRACK receiver does not supply individual scan counters or quality codes. The only indirect counter supplied is a scan of zeros after every 127 scans of data. By counting the number of points between each indicator scan, one can find out if there were any missing data. If so, the entire block of data has to be rejected as there is no way of knowing from which channel or scan the point or points were lost.

Calibration and Despiking. The despiking for WAVE-TRACK data was performed, in a similar manner as that for the WAVEC, on a fixed block size of 128 scans. As adjacent blocks are not necessarily continuous in time, it was not

possible to reject part of a block and start a new block at the next good scan. Each block had to stand on its own.

During the despiking, it became apparent that very large mean tilts were present in some records. The operating limit of the buoy is $\pm 45^{o}$. Any tilt angles greater than 45^{o} are recorded as $\pm 45^{o}$. Therefore the data cannot be corrected properly by removing the calculated mean (which in itself was probably too small). Generally, the despiking is performed with the mean removed, however, this often resulted in tilts exceeding the operating limit in the other direction. These records contain numerous spikes, and the tilt values, thus calculated directions, are questionable.

Spectral Analysis. The calibrated data were passed through the same spectral progam as for the WAVEC. The tilt values were initially corrected to an "equivalent" slope estimate using the relationship

$$\text{Slope} = \text{Tan}(\text{Tilt}/1.41)$$

This relationship was derived by Endeco Inc. from the results of various computer simulation runs of the buoy and mooring under different wave conditions (Brainard and Wang, 1981; and Brainard pers. comm.). The instrument specific transfer function values were obtained from look-up tables supplied by the manufacturer.

A maximum of 16 blocks of data were obtained for use in the ensemble averaging resulting in 32 degrees of freedom. No band-averaging was performed.

Direction Calculation. A phase correction was initially applied to the 'slope' co- and quadrature spectral values to account for the 90^{o} phase shift expected when converting tilts to slopes. The direction and spread estimates were then calculated.

Selected records were also passed through the Endeco 28-frequency Band - Pass directional analysis. The nature of this analysis requires continuous data throughout a record and thus could only be performed, with any confidence, on complete records. The procedure involves sending the entire heave and tilt record, individually, through an FFT, correcting with the instrument transfer functions, applying a band-pass filter for each of the 28 frequency bands required, and then performing an inverse FFT to reconstruct the three signals at a single frequency.

A zero-crossing analysis on the heave signal locates the wave crests and the direction at each wave crest is then calculated from the corresponding tilt values. The wave crest directions are summed, averaged and their standard deviation found.

MANMAR Data

The MANMAR data required no additional processing.

RESULTS

Figures 10 to 20 contain the time series plots of chosen wave and meteorological parameters obtained from the three directional buoys, the Datawell Waverider at Station 169 and the MANMAR observations. These provide a good illustration of the various sea states encountered over the study period and the data return from each instrument. All wave directions are "from" to be consistent with wind convention. Table 4 lists the various data products (i.e., displays) that were produced for this study. Due to their large number, they have not been included in this report. Copies of these displays are available upon request from Seakem Oceanography Ltd. Individuals desiring copies of the data should contact the following sources:

Waverider data (Station 169 and 501):

Marine Environmental Data Service (MEDS), Ottawa, Ontario.

WAVEC and WAVE-TRACK data (Stations 247, 248 and 249):

Marine Environmental Data Service, Ottawa, Ontario

or Seakem Oceanography Ltd., Sidney, B.C.

MANMAR data:

Mobil Oil Canada Ltd., St. John's, Nfld.

Synthetic Aperture Radar (SAR) data:

Intera Technologies Ltd., Calgary, Alberta

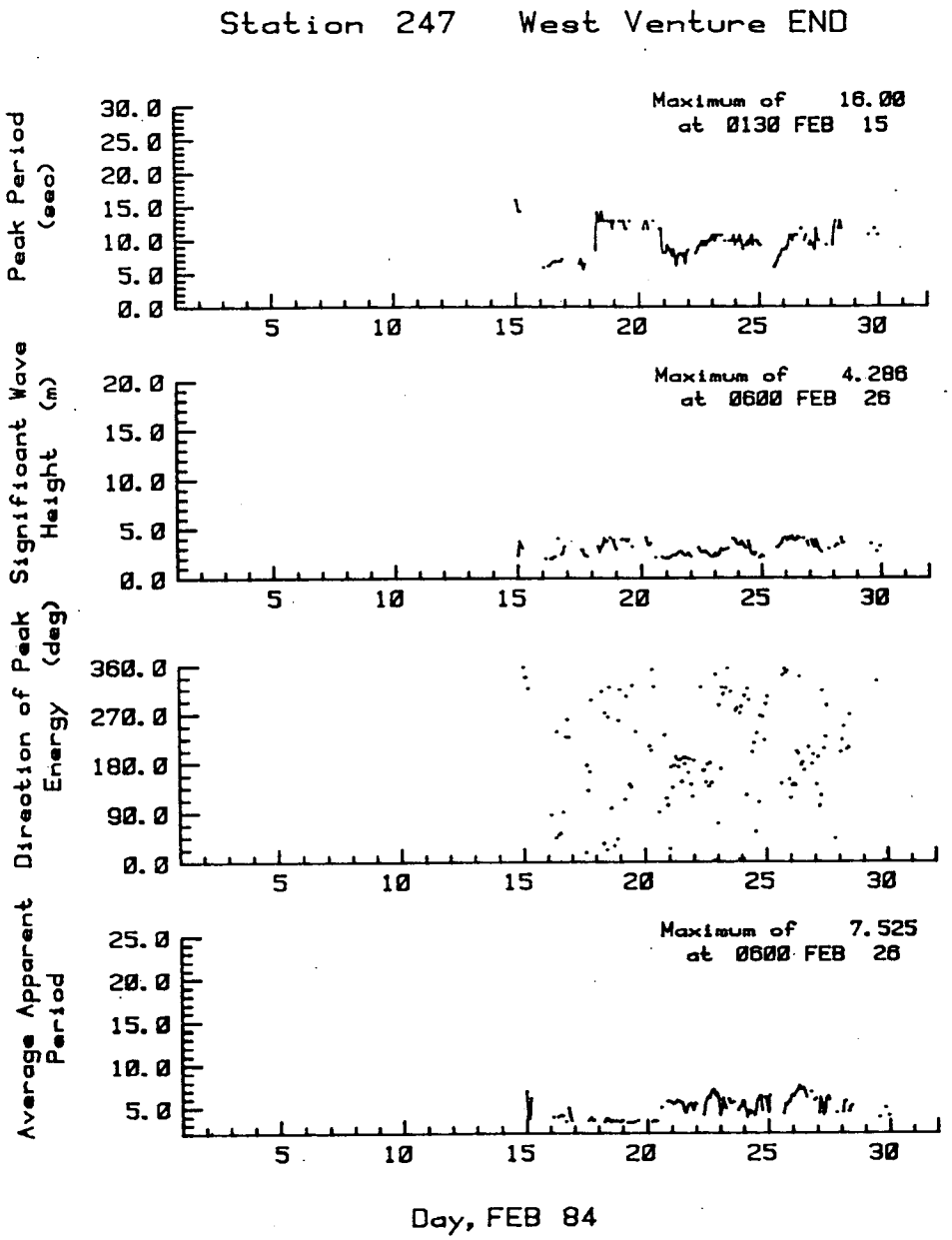

Figure 10. Time series plot of peak period, significant wave height, peak direction and average apparent period for Station 247, February 1984.

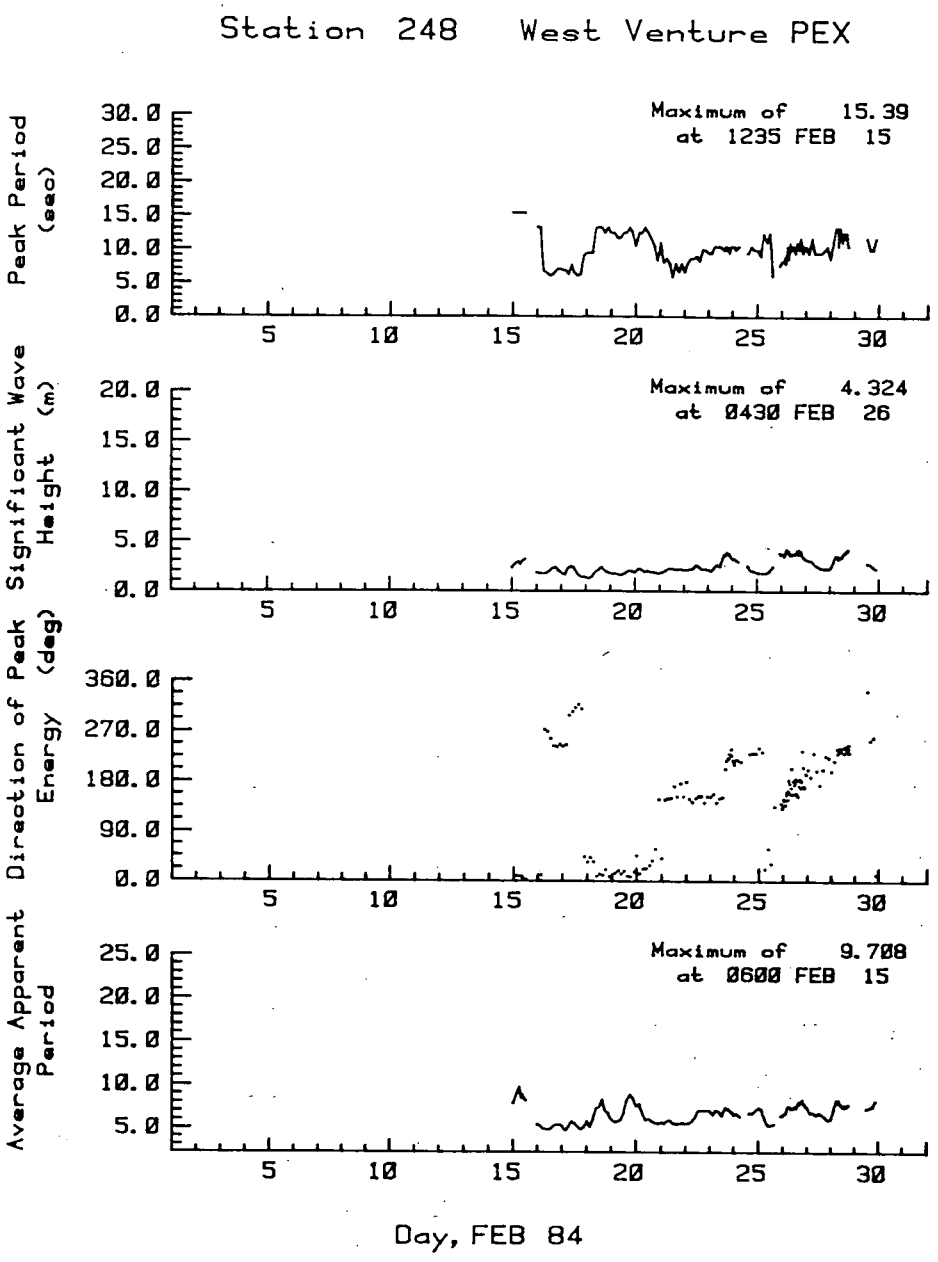

Figure 11. Time series plot of peak period, significant wave height, peak direction and average apparent period for Station 248, February 1984.

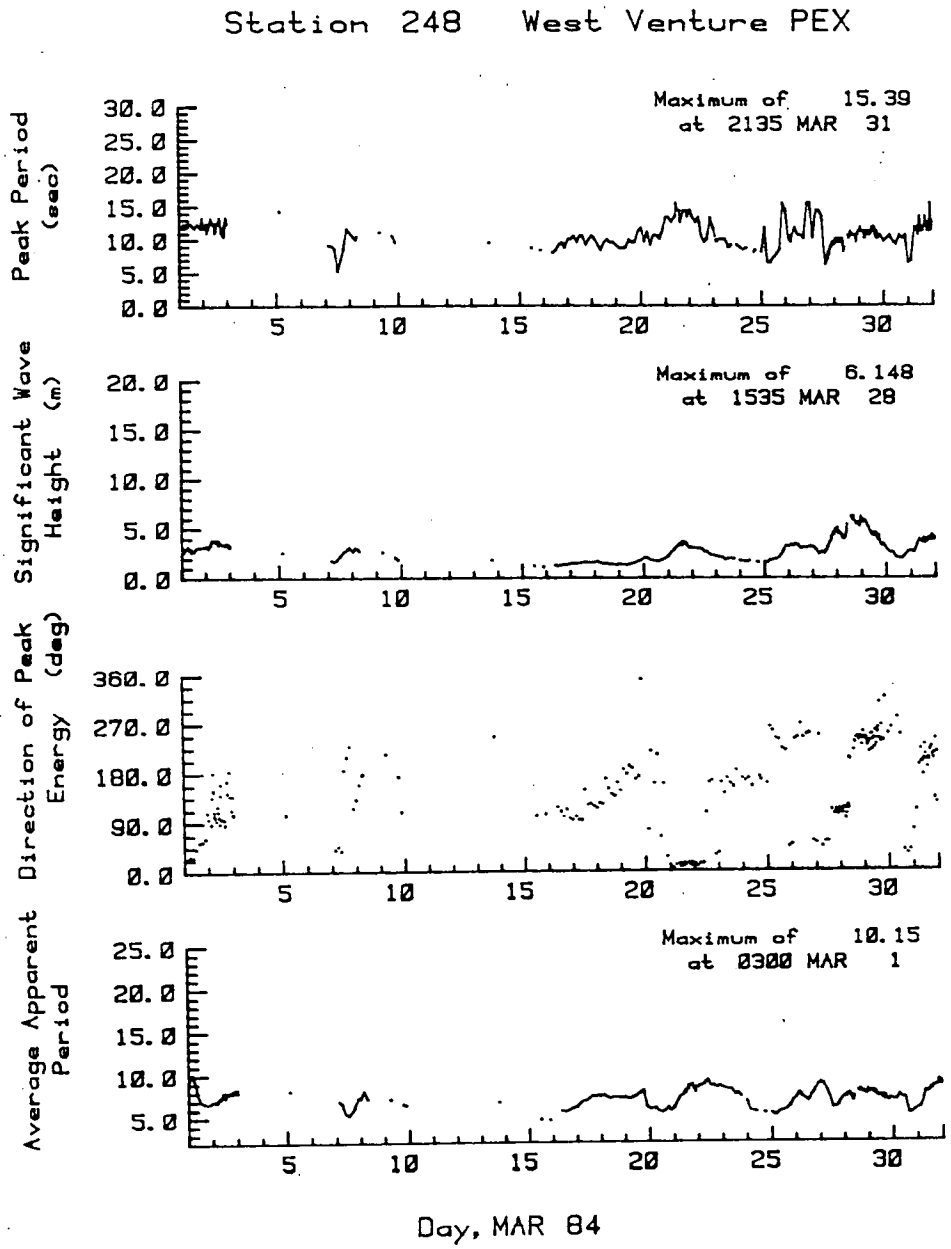

Figure 12. Time series plot of peak period, significant wave height, peak direction and average apparent period for Station 248, March 1984.

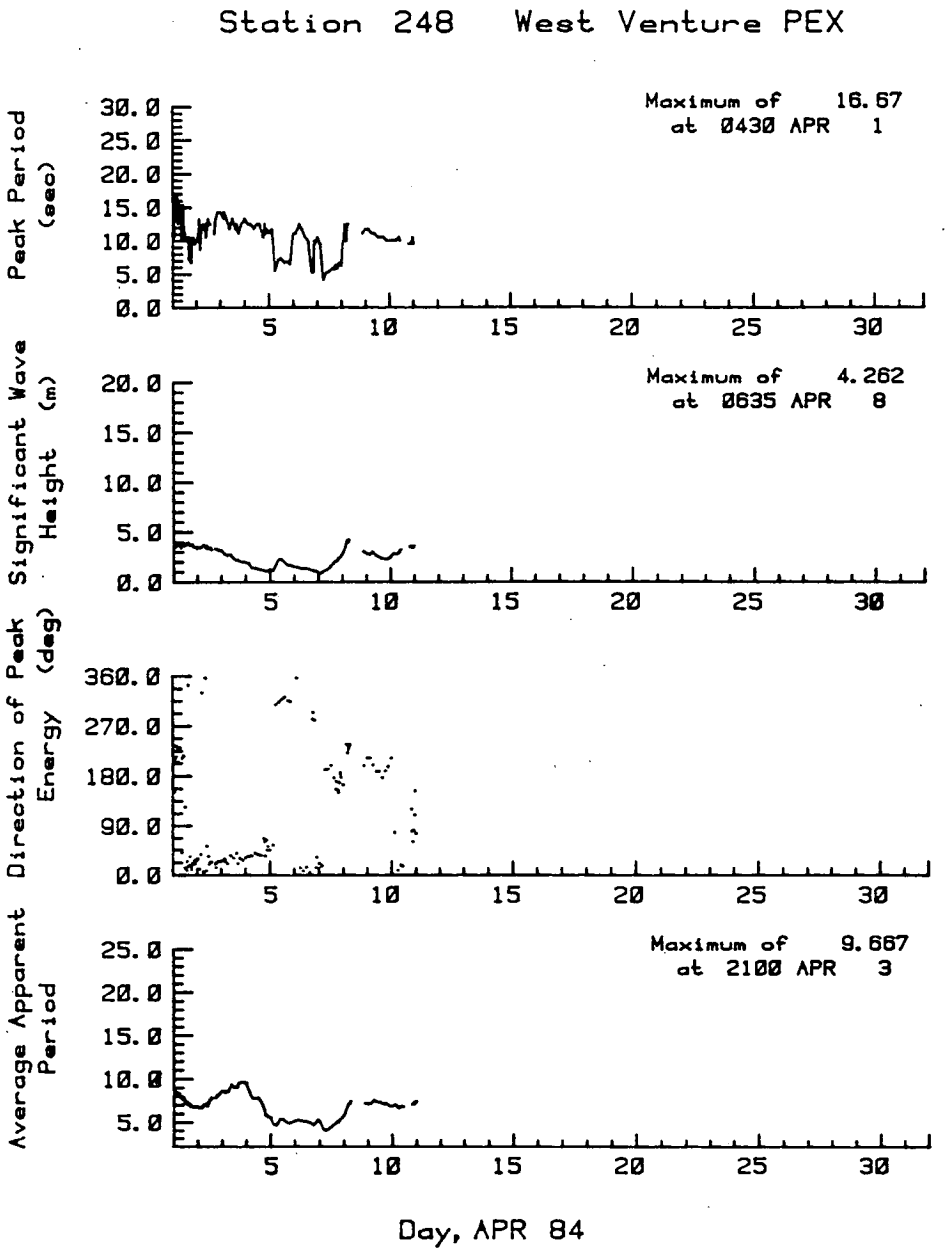

Figure 13. Time series plot of peak period, significant wave height, peak direction and average apparent period for Station 248, April 1984.

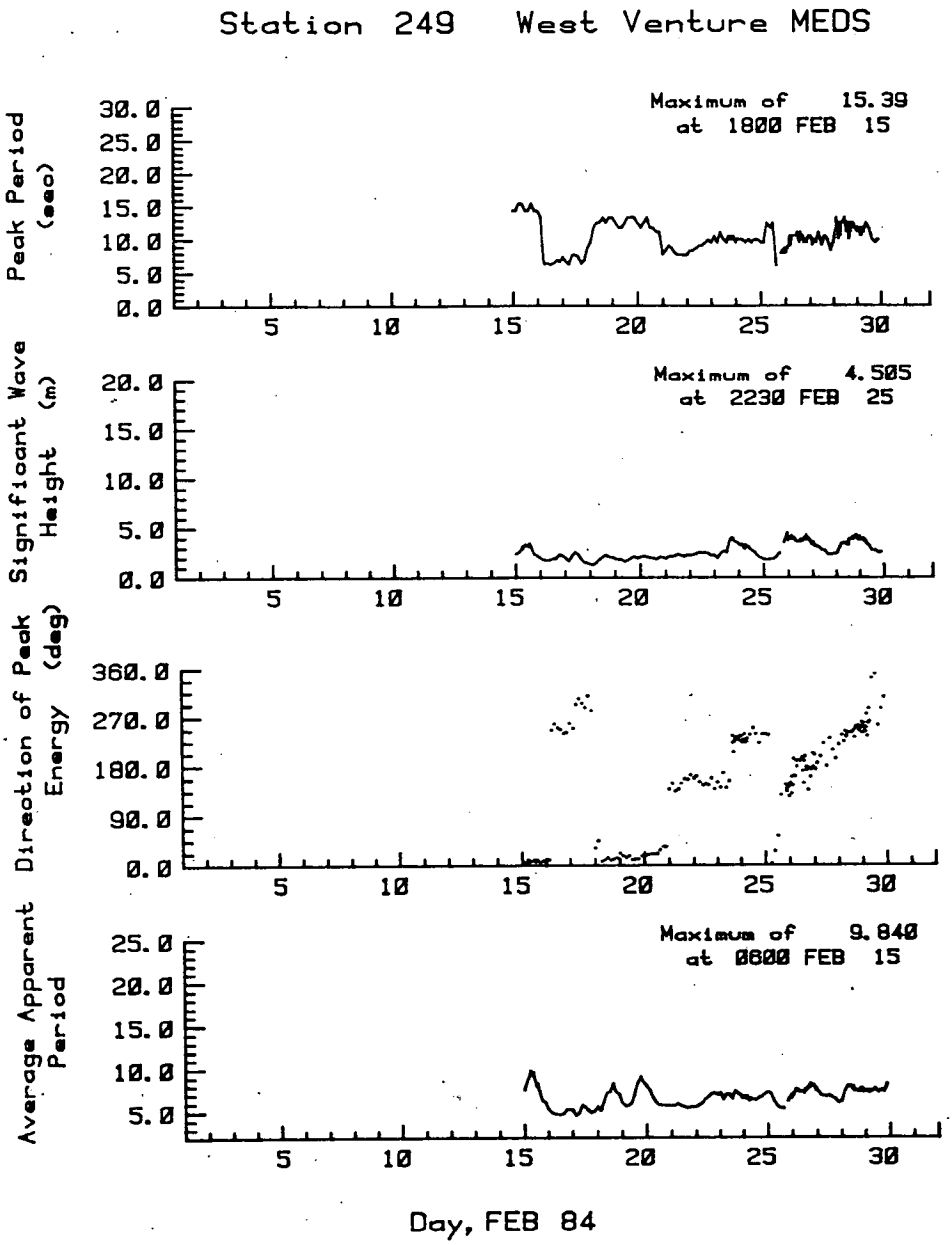

Figure 14. Time series plot of peak period, significant wave height, peak direction and average apparent period for Station 249, February 1984.

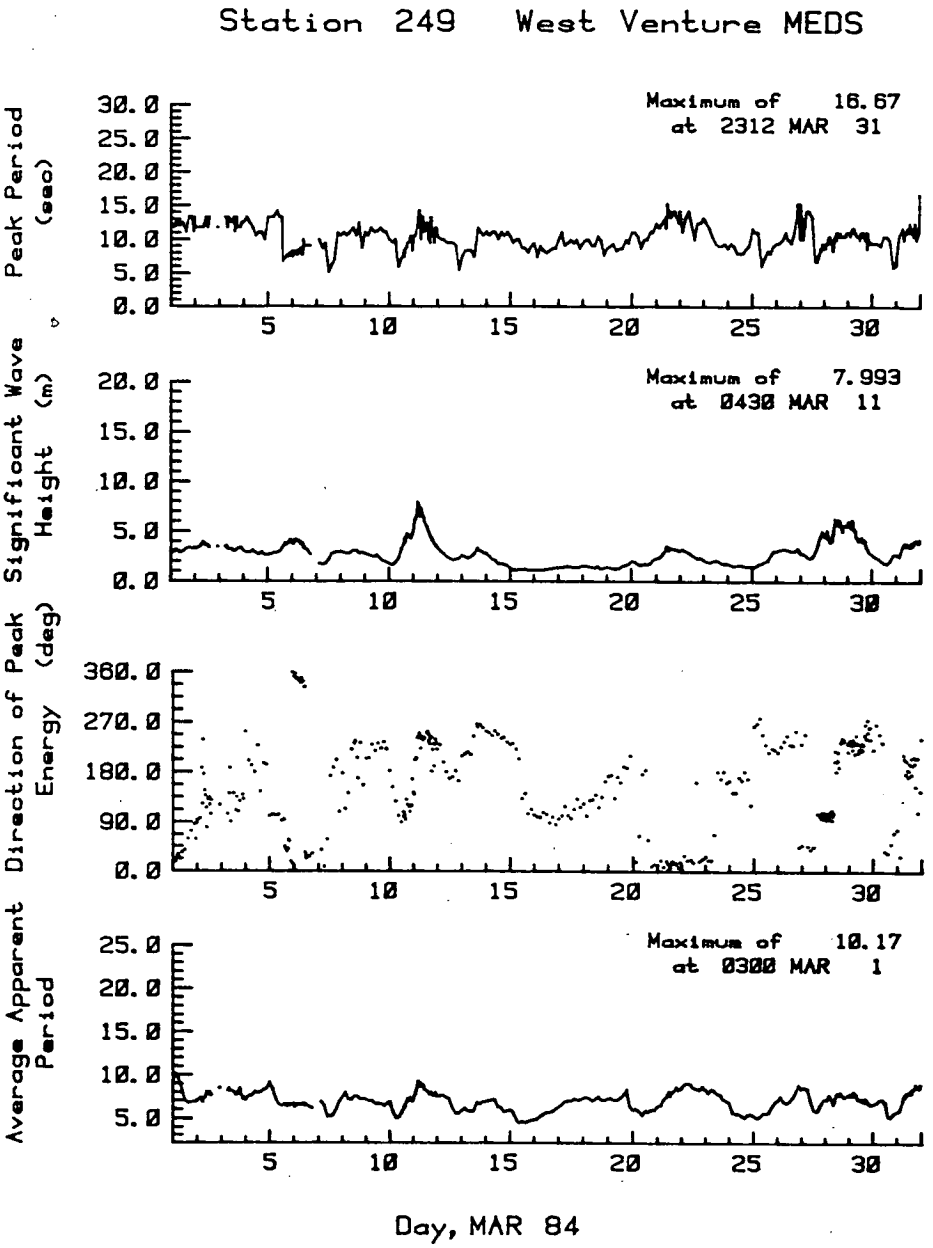

Figure 15. Time series plot of peak period, significant wave height, peak direction and average apparent period for Station 249, March 1984.

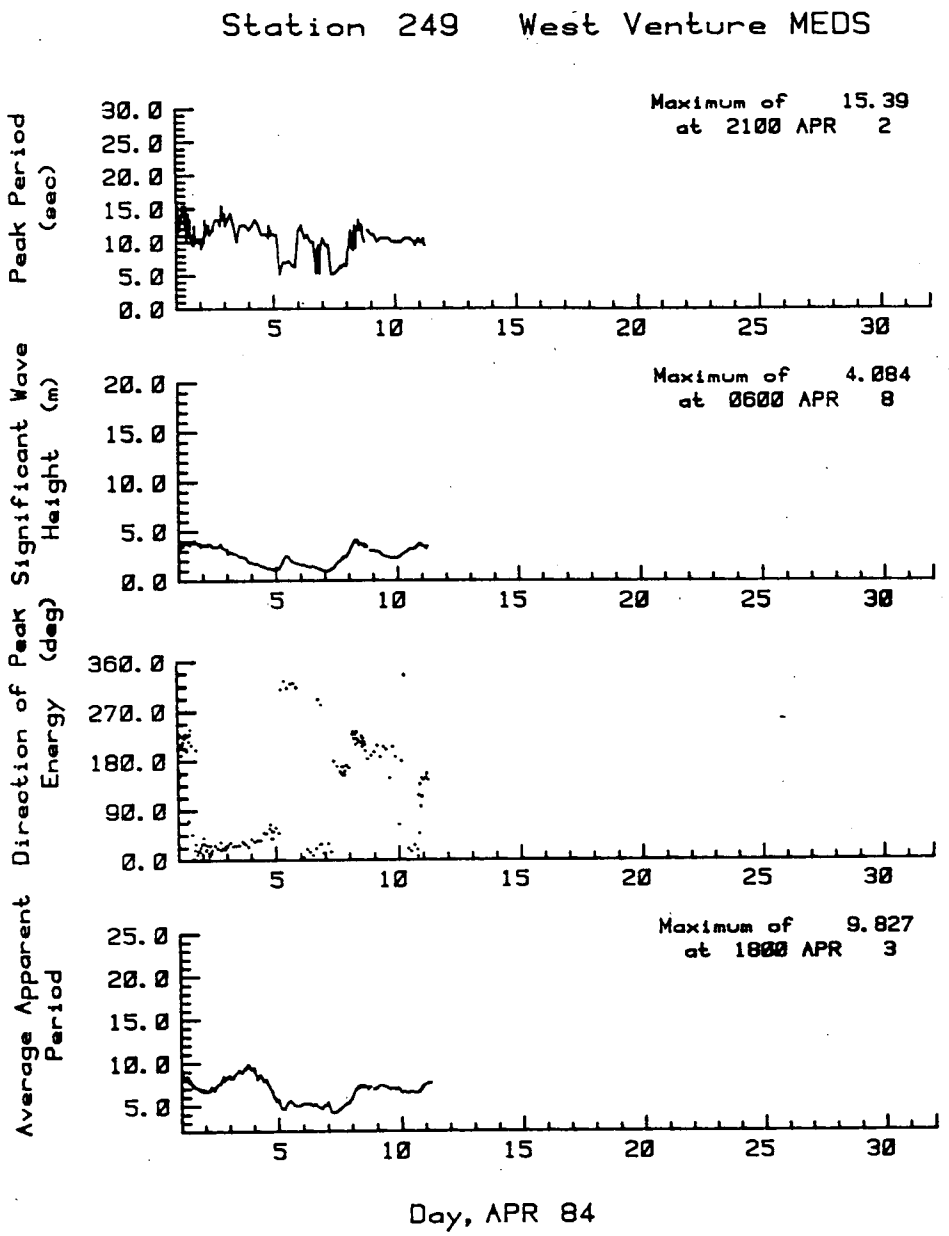

Figure 16. Time series plot of peak period, significant wave height, peak direction and average apparent period for Station 249, April 1984.

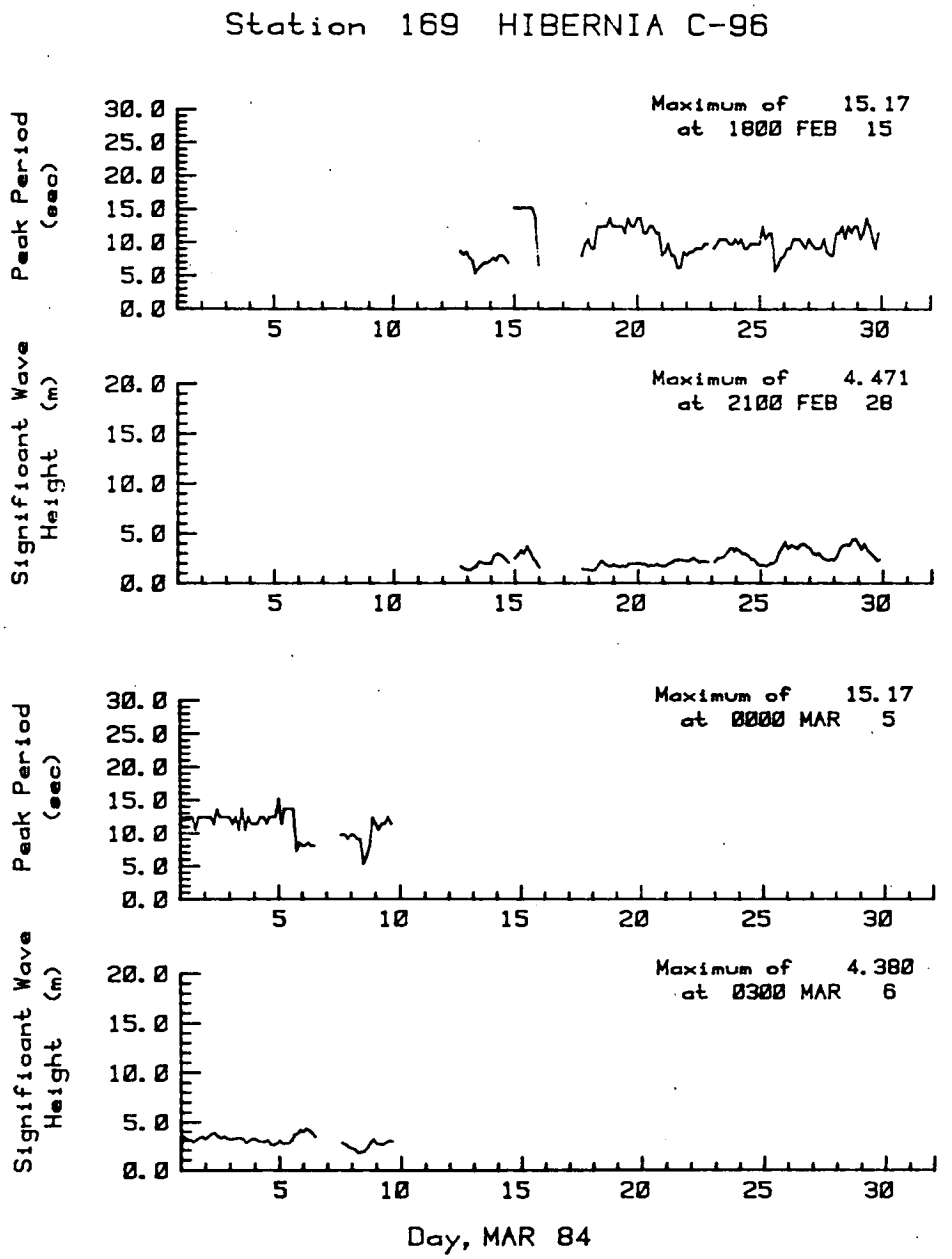

Figure 17. Time series plot of peak period and significant wave height for Station 169, February and March 1984.

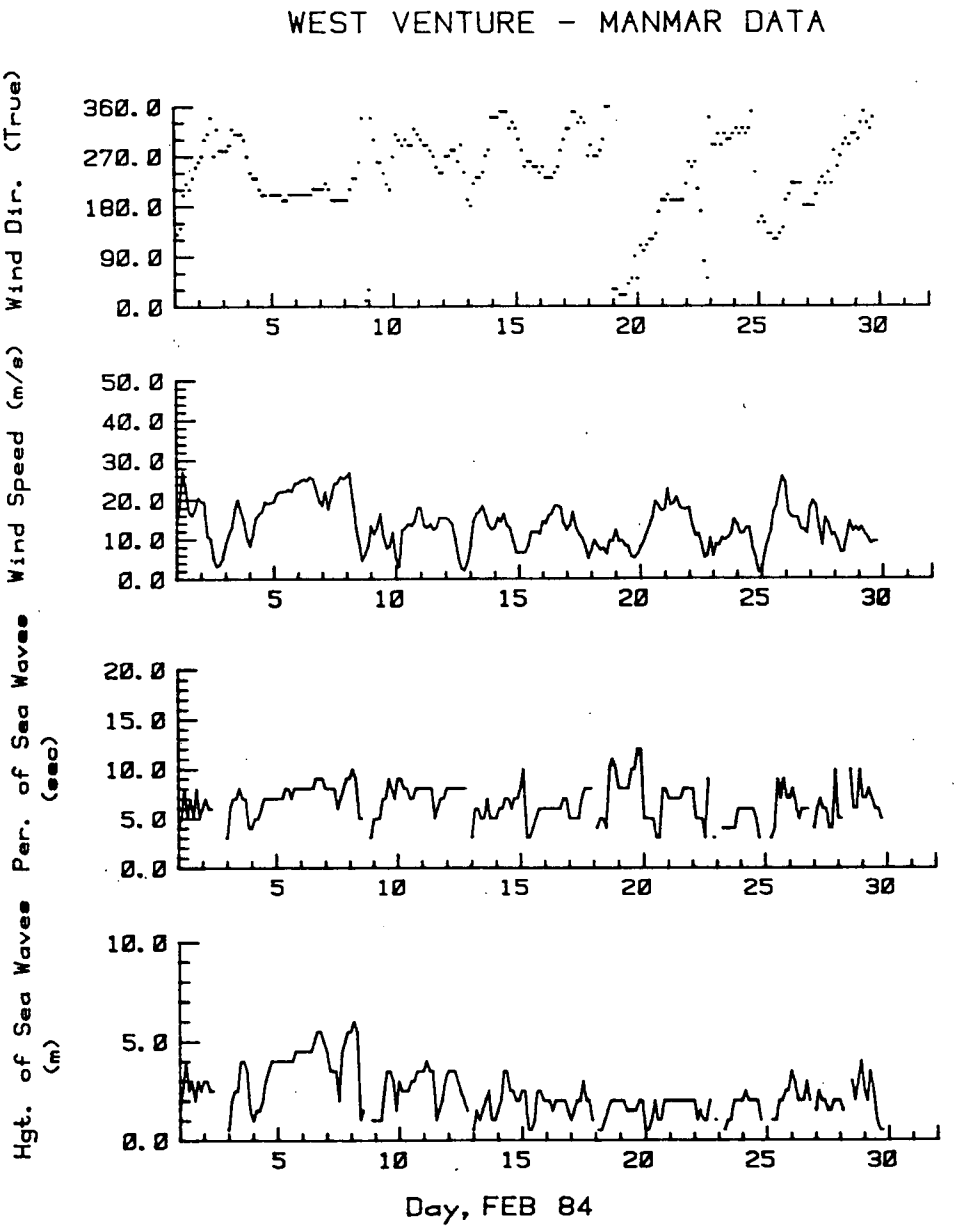

Figure 18. Time series plot of wind direction, wind speed, period of sea waves and height of sea waves, MANMAR data, February 1984.

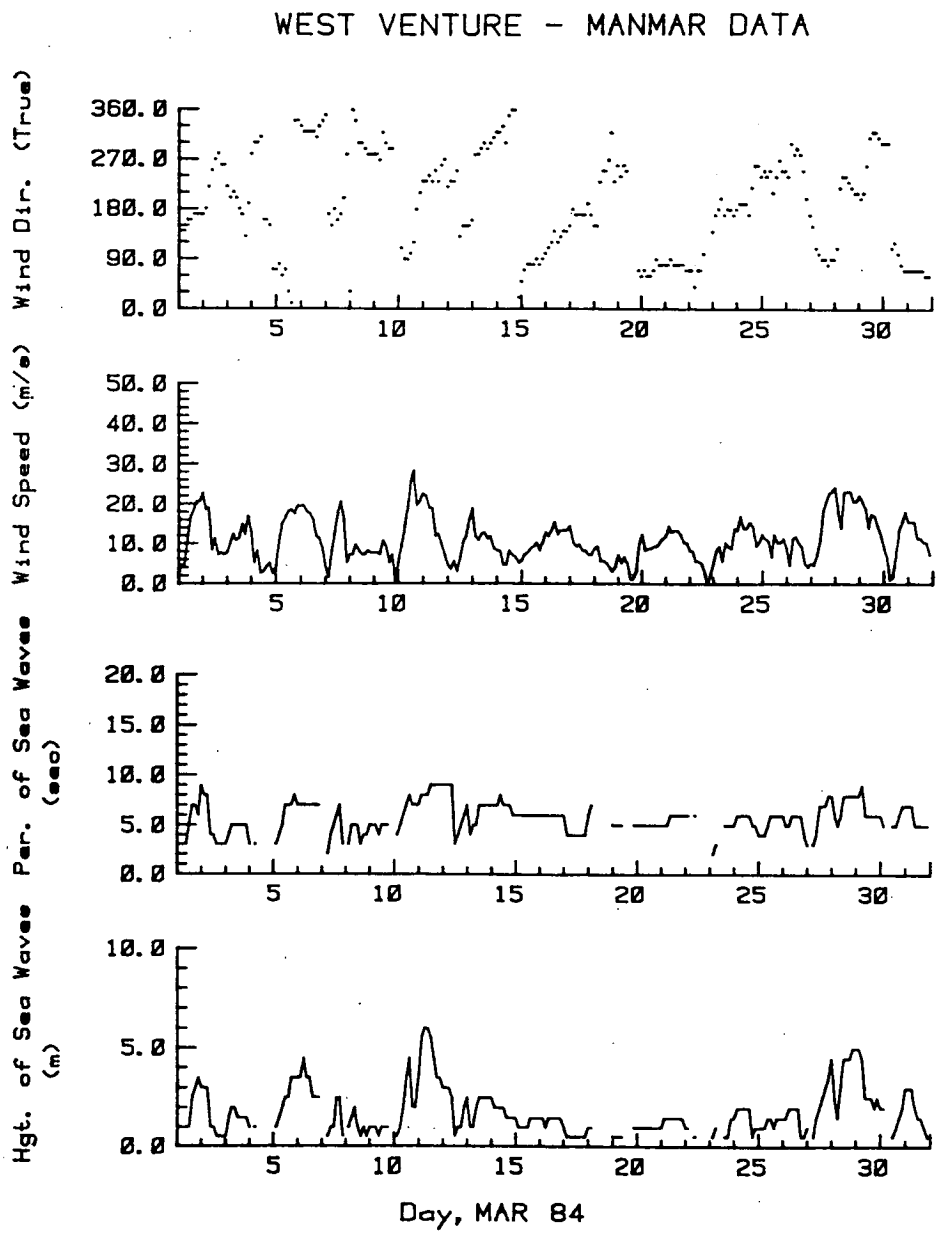

Figure 19. Time series plot of wind direction, wind speed, period of sea waves and height of sea waves, MANMAR data, March 1984.

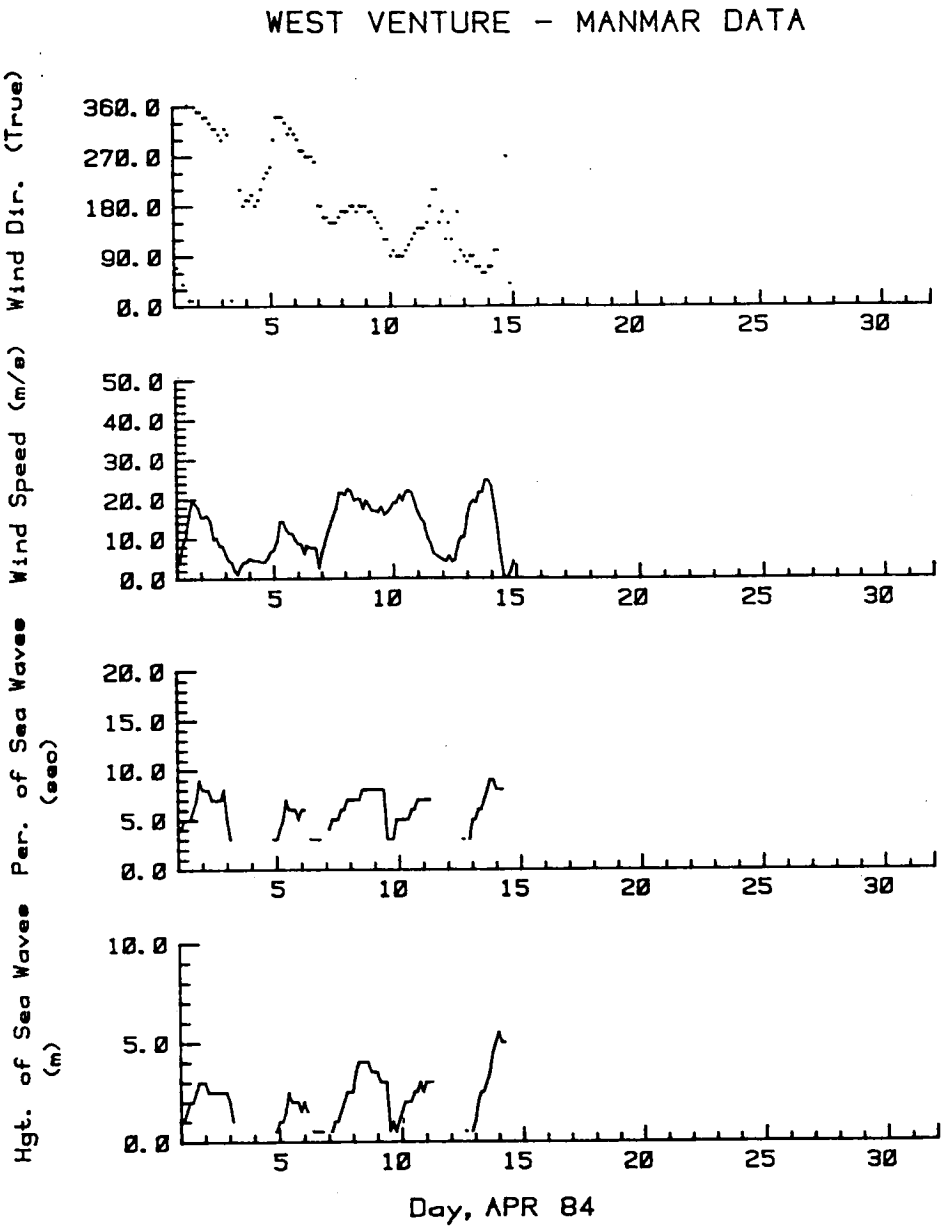

Figure 20. Time series plot of wind direction, wind speed, period of sea waves and height of sea waves, MANMAR data, April 1984.

Table 4. Available Data Displays

Display	STN 169 Feb	STN 169 Mar	STN 169 Apr	STN 247 Feb	STN 247 Mar	STN 247 Apr	STN 248 Feb	STN 248 Mar	STN 248 Apr	STN 249 Feb	STN 249 Mar	STN 249 Apr	MANMAR Data Feb	MANMAR Data Mar	MANMAR Data Apr
Time Series of:															
Significant Wave Height	x	x		x			x	x	x	x	x	x			
Peak Period	x	x		x			x	x	x	x	x	x			
Peakedness Parameter				x			x	x	x	x	x	x			
Spectral Narrowness Parameter				x			x	x	x	x	x	x			
Average Apparent Period				x			x	x	x	x	x	x			
Direction at Peak Energy (LH)				x			x	x	x	x	x	x			
Direction at Peak Energy (BP)				x											
Standard Deviation of Direction (BP)				x											
Average Period				x			x	x	x	x	x	x			
Apparent Crest Period				x			x	x	x	x	x	x			
Wind Speed and Direction													x	x	x
Height and Period of Sea Waves													x	x	x
Air Temperature													x	x	x
Sea Level Pressure													x	x	x
Height and Period of Primary Swell Waves													x	x	x
Height and Period of Secondary Swell Waves													x	x	x
Direction of Primary and Secondary Swell Waves													x	x	x
Scatter Plots of:															
Significant Wave Height vs. Peak Period				x			x	x	x	x	x	x			
Significant Wave Height vs. Average Apparent Period				x			x	x	x	x	x	x			
Significant Wave Height vs. Peak Direction				x			x	x	x	x	x	x			
Peak Period vs Peak Direction				x			x	x	x	x	x	x			
Listings of:															
Root Mean Square Wave Height by Wave Period	x	x		x			x	x	x	x	x	x			
Contour Plots of:															
Energy Density by Frequency and Time										x	x	x			

HINDCAST MODEL OF SEA STATE

As part of the experiment, hindcast modelling of selected time periods was performed in order to compare predicted heave and directional spectra against buoy observations. This work was undertaken by F.G. Bercha and Associates (Nfld.) and reported in Penicka et al. (1985). Most of the following discussion was extracted from this report.

SELECTION OF HINDCAST EVENTS

Selection of Events

The original requirements of the hindcast study were to simulate wave conditions during a high energy period and to coincide with the SAR overflights. There were only two storms during the experiment and as the SAR overflights lasted only about 30 minutes each while the model requires up to 24 hours of spin-up time to bring the simulation energy into balance with the input wind fields, it was decided to hindcast the two storms and to extend the second one to include the SAR overflights.

Event 1: March 10 to March 12. The track of the March 10-12 storm and the surface pressure distribution at the height of the storm are shown in Figure 21. The storm developed off the east coast of the United States at approximately 40°N. On March 10, 0000 GMT, when waves at the hindcast site started to increase, the centre of the low pressure system was located approximately 200 nautical miles south-east of Halifax moving in a northeasterly direction. The mean wind speeds at the hindcast site at that time were about 8 knots (4 m/s) from the east-south-east. The centre of the storm crossed the Island of Newfoundland between 1800 GMT and 2400 GMT on March 10, after that the storm track changed its direction towards the north. The disturbance reached its peak on March 11 between 0300 GMT and 0600 GMT when pressures at the centre of the storm dropped to 975-976 mBar. The maximum winds at the hindcast site, 39 knots (20 m/s) from the SSW occurred when the centre of the storm was just north of

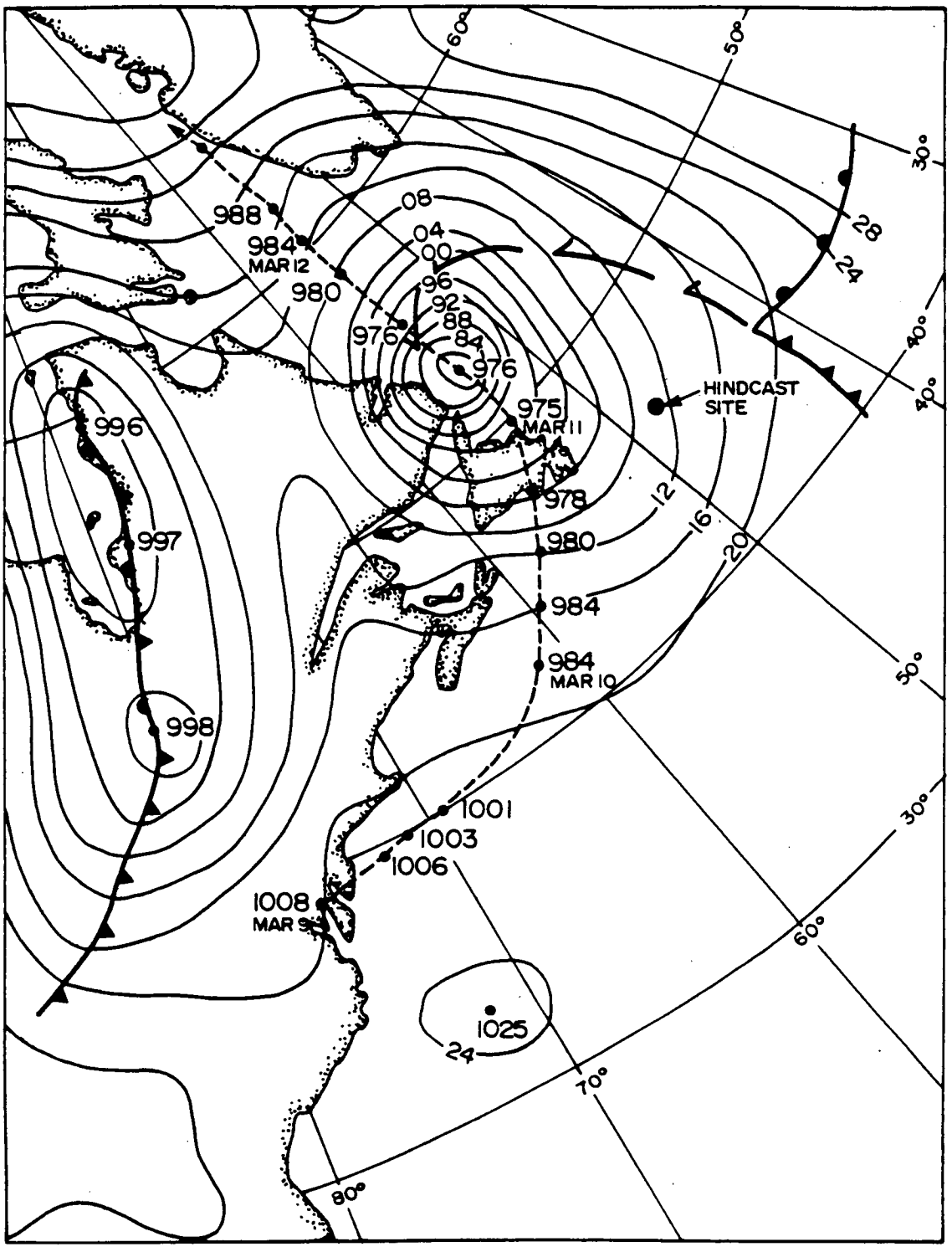

Figure 21. Track of storm, March 10-12, 1984, with surface analysis for March 11, 0600Z (from Newfoundland Weather Office Surface Analysis Charts).

Newfoundland. After 0600 GMT on March 11 the storm started to abate moving north into Davis Strait.

An examination of the wave record showed a concurrent rise in significant wave height from 1.8 m at 0000 GMT March 10 to a peak of 8.0 m at 0430 GMT March 11. The significant wave height stayed above 5.0 m for 15 hours (0000/11 to 1500/11) when winds had already abated. This, as well as the timing of the initial rise in wave height, indicates a lag behind the winds by approximately nine hours.

The time series of mean winds at the hindcast site derived from wind observations at nearby drilling rigs, is shown in Figure 22. A noteable feature of this plot is a rapid and relatively smooth increase in wind speed in the growth stage, and an equally smooth decrease in the decay stage, of the storm. The wind direction changed rapidly from E to ESE in the initial stages of the storm to approximately SSW and W at the peak after which it remained relatively steady between south and south-west during the decay stages of the storm.

Event 2: March 27 to April 2. The track of the storm of March 27-29 together with the isobars at the time of maximum observed wave heights (on March 28, 1200 GMT) are shown in Figure 23. This low pressure weather system also developed off the Atlantic seaboard of the United States. After an initial easterly movement, the centre of the system assumed a north-north-easterly course which took it directly over the experimental area. The storm appears to have stalled over the Grand Banks for over 30 hours (March 28, 0600 GMT to March 29, 1200 GMT) before resuming its northeasterly course out into the North Atlantic. The direct pass of the low pressure centre over the measurement site is reflected in the time series of wind speeds and directions, derived from the rig observations (Figure 24), as a drop in the wind speed and a rapid change in the wind direction between 0000 GMT and 0600 GMT on March 28. It can also be seen in the wave record which showed an initial build up of significant wave height from 2.4 m (0900/22) to 5.0 m (2100/27) and then a drop to 4.0 m (0600/28). For the following 24 hours, while the centre of the storm stayed over the Grand Banks, the directions, and to a lesser degree the wind speeds, remained relatively steady, around 32 knots (16 m/s), from the south-west. The observed wind speeds reached a flat maximum, 38

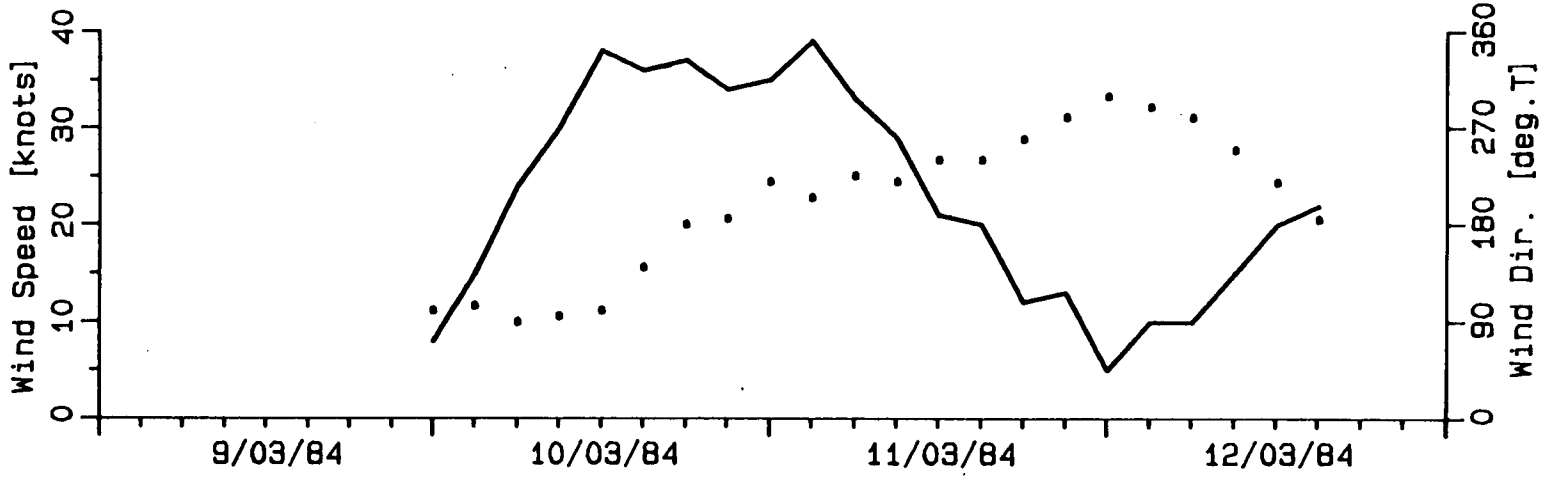

Figure 22. Wind speed and wind direction at hindcast site during first event.

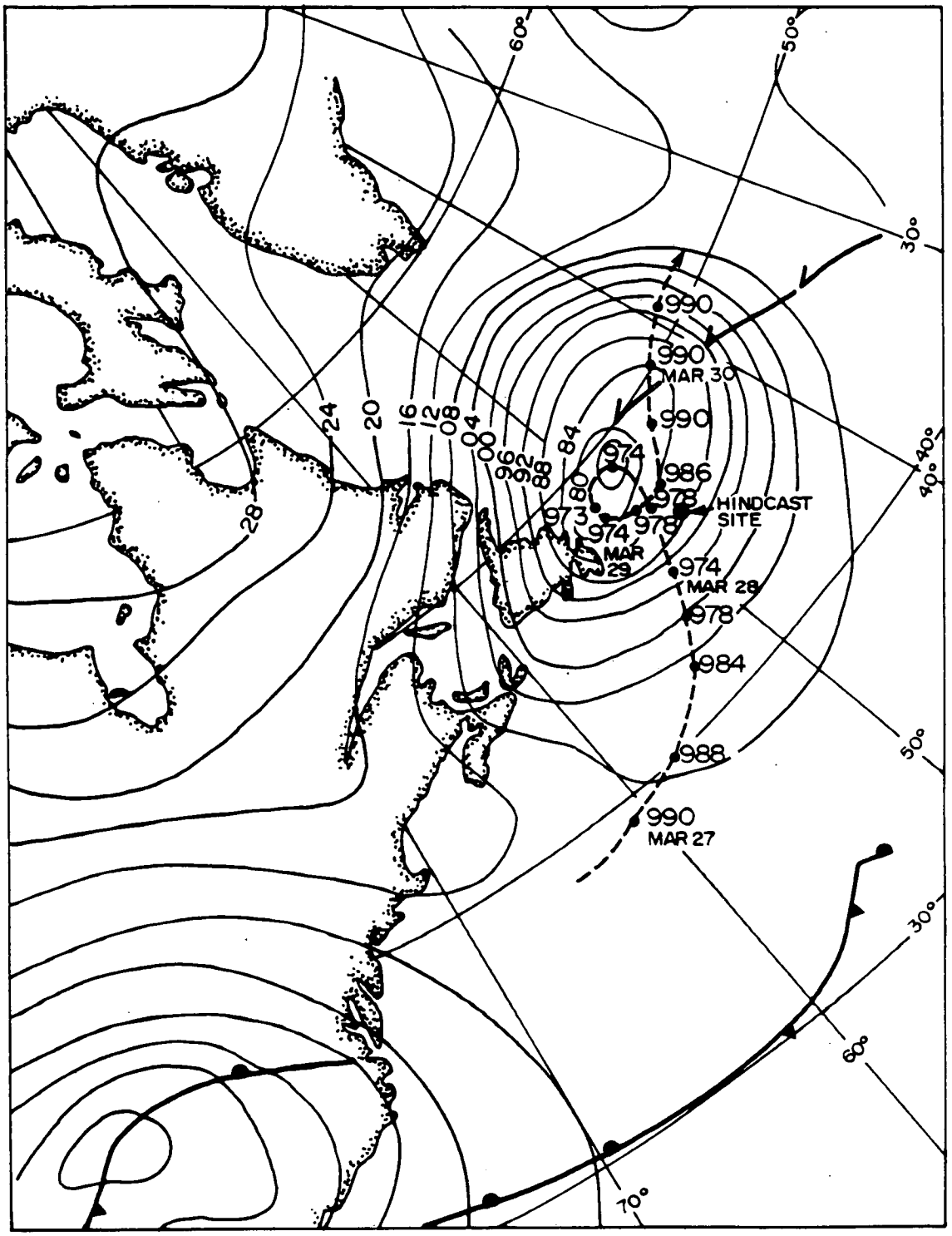

Figure 23. Track of storm, March 27-30, 1984, with surface analysis for March 28, 1200Z (from Newfoundland Weather Office Surface Analysis Charts).

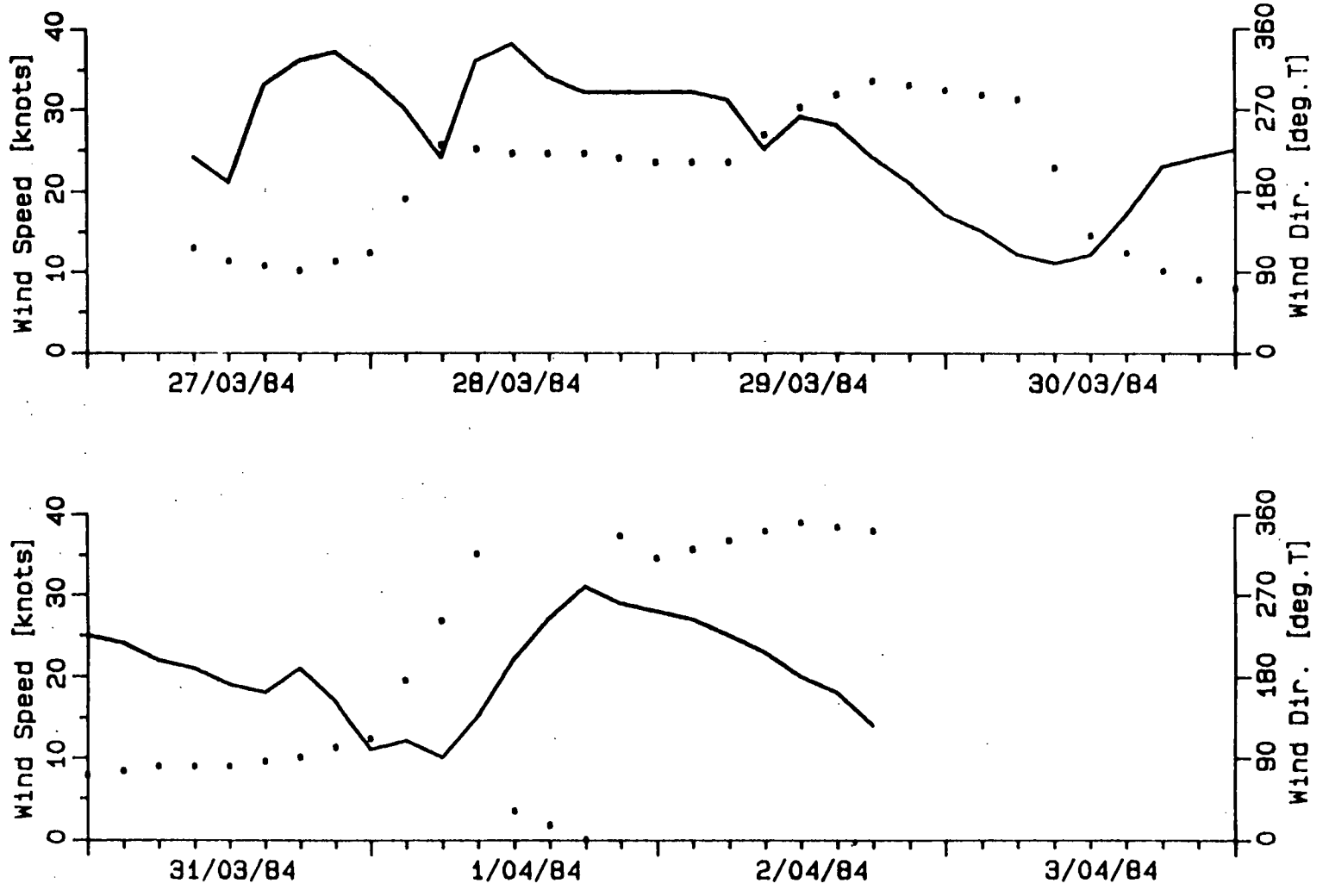

Figure 24. Wind speed and wind direction at hindcast site during second event.

knots (19 m/s), on March 28, 1200 GMT at which time the measured wave heights reached 6 m. The maximum significant wave height, 6.3 m, was recorded about two hours earlier at 1030 GMT.

After the low pressure system left the Grand Banks the winds and the resulting seas in the experimental area began to abate. At the same time a new low pressure disturbance started to develop over the southeastern United States tracking in an east-south-easterly direction. On March 31, a low pressure trough was overlying the Grand Banks over the experiment area. The winds were light and the wave activity (H_{sig} about 4 m) may be attributed to swell originating south to south-west of the hindcast site. The trough tracked north-east while at the same time gradually developing into two, more distinct, depressions. On April 2, 1800 GMT, at the time of the SAR overflight, the low pressure system (now again a rather broad arched trough) was east to north-north-east of the Grand Banks. The winds observed at West Venture were from the northwest at about 16 knots (8 m/s). Waves recorded at the hindcast site reached H_{sig} between 3.0 and 4.0 m and weather observation logs from West Venture indicate swell of about 1.5 m arriving from the north-east.

Implications For wave hindcasting. From the wave generation point of view the two storms represent different types of conditions.

During the first storm the winds increased very rapidly to near maximum value. The winds then leveled off for about five hours before starting to abate. This is not long enough for the seas to reach the saturation condition of fully developed seas. The corresponding spectra are peaky and they continue growing until the winds start to abate.

The second storm, on the other hand, exhibited a less regular development. The winds remained relatively steady, both in speed and direction, for a long period of time (up to 24 hours). For a wind of 16 m/s (32 knots) this is sufficiently long for the seas to approach full development in which the energy input from the atmosphere is balanced by dissipative processes, and the wave spectra, now rather broad, stop growing.

During both storms there were periods of rapid change in wind direction. The wave field requires a certain relaxation time to adjust to the new wind

direction and this may result in the wave direction deviating initially from the new direction of the wind.

Thus the two events provide a limited verification of the model under three important types of conditions: duration limited wave growth, fully developed sea state and rapidly changing wind direction. The wave growth does not appear to have been limited by fetch in either of the storms.

In addition, during both events there were periods when a large part of the total energy was due to swell. A comparison of these segments of the hindcast with directional wave measurements will provide an indication of the ability of the model to simulate transition between sea and swell and swell propagation.

It should be noted that during both events the winds and the wave conditions in the area were relatively moderate. The wind force reached Beaufort number 9 only briefly which, in standard terminology, would be classified as "gale" to "strong gale" (for comparison during a "storm" winds reach 48-55 knots). During a large part of the second event the winds were light and the waves did not exceed 4 m. Models used for hindcasting design wave conditions are typically calibrated for the highest observed sea states and they may not necessarily be equally accurate when used to hindcast less severe conditions.

Hindcast Site

For practical reasons, the computational grid employed in the study has gridpoints located at integer multiples of degrees of longitude and latitude (with 2^{o} spacing). The gridpoint chosen to represent the measurement site is located at 46^{o}N and 48^{o}W. Since the distance between the measurement site and the hindcast site is small, compared to the scale of the weather systems which produced the storms, the sea states would not have noticeably differed at the two sites.

Presence of Sea Ice

Sea ice was present during both hindcast periods N to NE of the hindcast site. The time series plot of the measured wave data (for example: Figure 15), indicates that during the March 10-12 event the wave direction ranged from

approximately 90° to 247°T. The range of wind directions with respect to the ice edge is shown schematically in Figure 25. It seems safe to assume that at no time during this period did the presence of pack ice interfere with wave generation at the measurement site.

The situation was more complex during the second event (Figure 26). The wave direction on March 27 0900 GMT, was about 45°T, and for a brief period intersected a tongue of pack ice projecting ENE of the hindcast site. A few hours later the wave direction shifted to the east while the ice edge somewhat retreated in the northwesterly direction. For the rest of the storm until about March 30, 1200 GMT the wave direction remained between 90° and 270°T, clear of the ice edge. As indicated in Figure 26, the range of wind directions during this time was between 90° and 300°T and the fetch was not restricted by the ice presence. During the remainder of the second event the wind directions at various times intersected the area covered with ice. However, from the observed wave directions (Figures 15 and 16) it appears that the pack ice is unlikely to have had a noticeable effect on the wave conditions at the measured site. On April 2 the wave direction ranged between 0° and 30°T. At that time the ice edge projected approximately to the longitude of the measurement site and it may have affected the wave conditions there.

No allowance has been made in the model grid for the presence of the pack ice. While the ice presence at various times during the March 27 - April 2 hindcast event may have somewhat affected wave conditions at the hindcast site, this effect would have been small and less than the expected accuracy of the hindcasts.

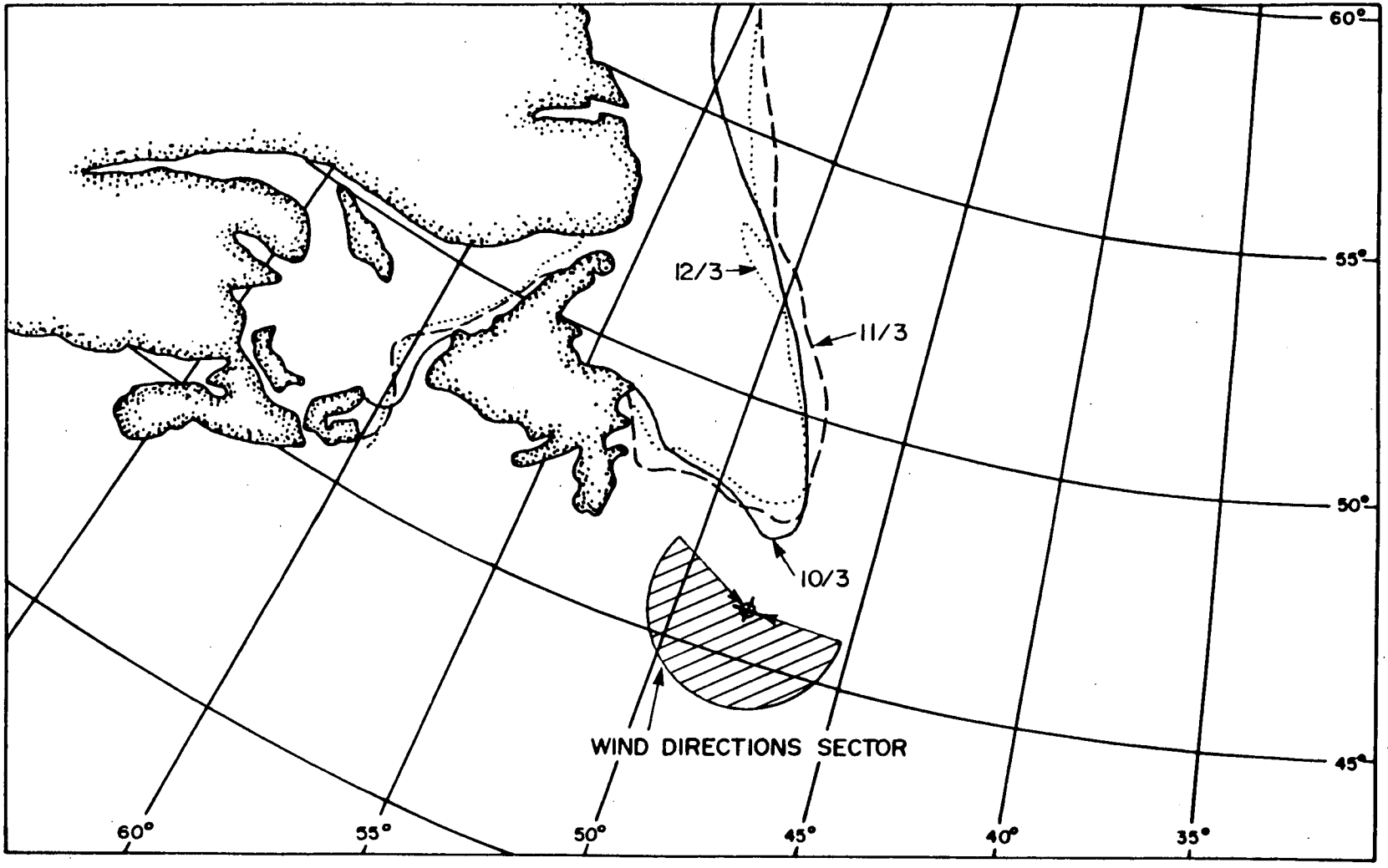

Figure 25. Ice edge extent during first event (from METOC Significant Wave Height Analysis Charts).

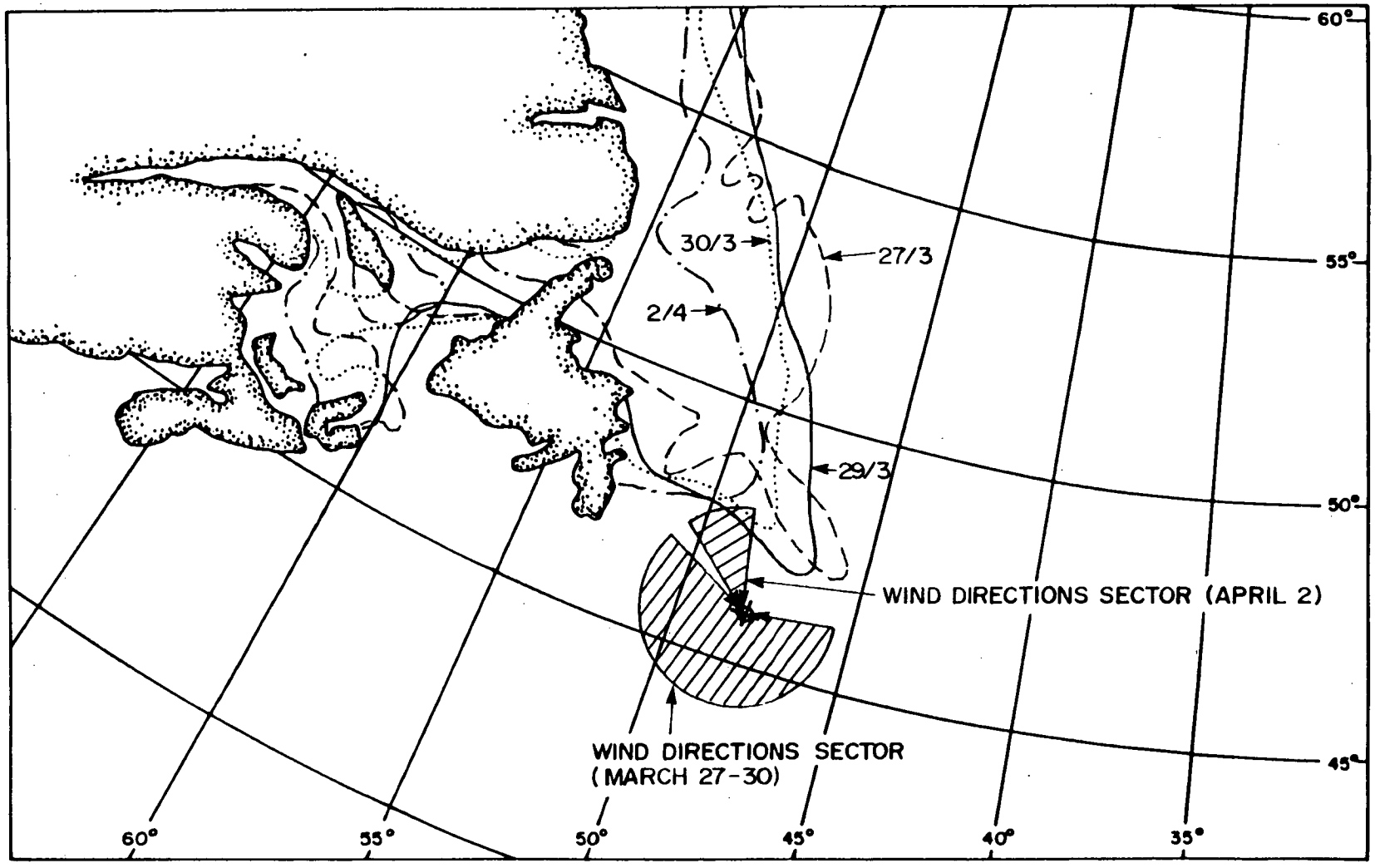

Figure 26. Ice edge extent during second event (from METOC Significant Wave Height Analysis Charts).

SELECTION OF HINDCAST MODEL

Hindcast Model Selection

The wave model employed in this study is a most recent version of a deep water discrete spectrum model originated by D.T. Resio at the U.S. Army Waterways Experiment Station. It was developed after an extensive evaluation of various existing wave prediction techniques (Resio et al. 1978; Resio and Vincent, 1979) for application in coastal regions where fetch may be limited by the presence of the coast or in regions under the influence of rapidly varying weather systems. Under these conditions the wind-wave spectrum exhibits properties different from saturated spectra of fully developed seas: the growing wind-wave spectra are sharply peaked and the higher frequencies often show energy levels exceeding the eventual equilibrium level (the "overshoot affect"). These properties are believed to be the result of a nonlinear energy transfer between various frequency components of the spectrum (Hasselmann et al. 1973). Since duration and fetch limited wave-growth conditions frequently occur at the experimental site it was concluded that a wave model which includes nonlinear wave-wave interaction is more appropriate for the present hindcast than a model in which the nonlinear interaction was omitted.

During its development, the model performance was tested both against empirical relationships between various nondimensional wave growth parameters (Resio and Vincent, 1979; Resio, 1981) and against actual wave observations (Corson and Resio, 1981; Resio, 1982). In these tests, the model lead to fetch and duration growth rates (nondimensional wave height vs. nondimensional fetch; nondimensional wave height vs. nondimensional time) consistent with the rates observed during the Joint North Sea Wave Program (JONSWAP) and those observed by Mitsuyasu (1968). Providing that input wind fields could be adequately specified, the model predictions exhibited negligible bias and RMS error in significant wave height and in peak period of the order of 1. - 1.5 m and 1.0 s respectively. No allowance is made in this model for shallow water effects.

Hindcast Model

Most numerical wave spectrum models in existence today can be classified as belonging to one of two types: parametric models in which the wave spectrum is represented by one or more parameters and discrete spectrum models in which the spectrum is resolved into a finite number of frequency and direction bands. The model employed in this study is of the latter type (however, as explained later, a simple nonpropagating parametric model is used to initiate wave growth until a peak frequency reaches a certain cutoff value). The directional wave spectrum is represented by 16 direction and 16 frequency bands over a 0^{o} to 360^{o} direction range and 0.04 Hz to 0.19 Hz frequency range. A spatial grid is overlaid over the wave generation area (Figure 27) and at each grid point and each time step the discrete spectrum is computed from input wind fields by numerically solving the energy balance equation

$$\frac{\partial E}{\partial t} = G + \vec{C}_g \cdot \nabla E \qquad (1)$$

Here $E=E(f, \theta, \vec{x}, t)$ is the energy density of the wave field as a function of frequency, f, direction of propagation, θ, position $\vec{x}$, and time, t; G is the source function which represents the physical processes that add energy to, or subtract energy from, the spectrum; and $\vec{C}g = \vec{C}g(f, \theta)$ is the wave group velocity. The last term in Equation 1 represents the propagation of wave energy across the model grid.

The source function

$$G = G_{in}+G_{nl}+G_{ds}$$

in general is a sum of three terms: the energy input from the atmosphere, G_{in}, the transfer of energy across the spectrum due to conservative nonlinear wave-wave interaction, G_{nl}, and wave energy dissipation term G_{ds}.

In numerical wave models the source function is generally simplified and it is the processes which are retained in the source function, and the analytical expressions that approximate these processes, which mainly distinguish existing wave models from each other. The model used in this study was designed to be consistent with the results of the JONSWAP experiment in which wave growth under fetch-limited conditions was measured. The conclusion of that project was

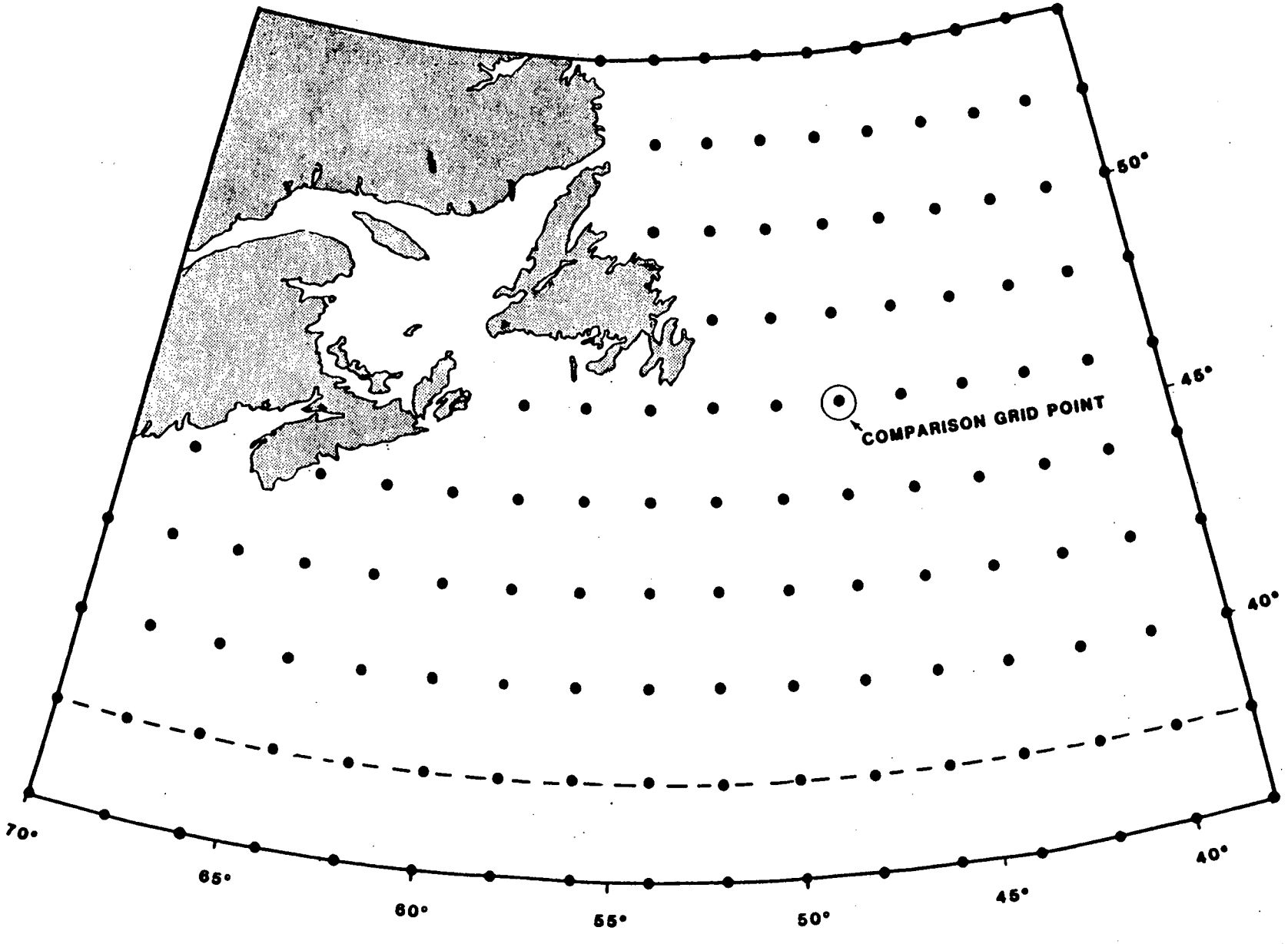

Figure 27. Computational grid used for event 1 - Dashed line indicates grid boundary for event 2.

that the shape of the wave spectrum in growing seas is governed primarily by nonlinear wave-wave interaction which distributes energy, input from the atmosphere into the central and high frequency part of the spectrum, to lower and higher frequencies. This nonlinear energy transfer is believed to be responsible for a number of characteristics observed in developing spectra: the tendency of growing spectra to overshoot their eventual equilibrium position, the sharp peaks observed in growing spectra, the invariance of spectrum shape with fetch, etc.

A rigorous numerical solution of the nonlinear wave-wave interaction component requires evaluation of quadruple Boltzman integrals at each grid point and it is impractical in the context of wave modelling. Instead, in the present model, the G_{nl} term is parameterized in terms of the peak frequency, f_p, and the Phillips' equilibrium coefficient, , as

$$G_{nl} = D_1 \alpha^3 g^2 f_p^{-4} \exp\left[1 - (f_p/f)^4\right] (f/f_p)^3 \qquad (2)$$

where D_1 is a constant and g is the gravitational acceleration (for reasoning behind this parameterization see Resio, 1981). Using empirical relationships between , f_p and the wind speed, u, equation (2) can be recast into

$$G_{nl} = D_2 g^6 (u/f_p)^2 \exp\left[1 - (f_p/f)^4\right] (f/f_p)^3 \qquad (2a)$$

which is the expression actually used in the model.

The energy from the atmosphere enters the wave field through an exponential growth term

$$G_{in} = BE$$

The expression for the coefficient B, used in the original version of the model (Resio, 1981), which was similar to that proposed by Snyder and Cox (1966), was found to result in excessive wave energy growth under certain conditions. A modified G_{in} source term is used in the present version of the model. It is based on the observation that a constant proportion (approximately 20%) of the total momentum flux from the atmosphere enters the wave field. Presumably, the remainder of the momentum is directly input into currents.

A linear growth term which is common to other wave models is not present in this model. The linear term transfers more energy into the forward face of the

spectrum than into the midrange which is contrary to recent wave growth observations. The exponential and the nonlinear terms alone cannot initiate wave growth from zero energy. Some energy must be present in the wave field before these terms become non zero. In order to initiate wave growth a local (non-propagating) high-frequency parametric model is incorporated into the discrete spectrum model. The boundary between the parametric and discrete spectrum domains of this model is maintained at a fixed frequency. Once the peak frequency of the parametric spectrum passes this cutoff value the discrete domain takes over spectrum growth at frequencies below the cutoff and the parametric domain assumes an f^{-5} equilibrium form.

The calculation of a new peak frequency, f_p, at the end of a time step in the parametric domain follows from the solution to the equations of Hasselmann et al. (1973)

$$f_p^{n+1} = (f_p^n)^{-7/3} + \frac{7}{3} N \left(\frac{u}{g}\right)^{4/3} t^{-3/7} \qquad (3)$$

where the superscript, n, denotes the time step, t is the time increment and N is a constant.

There is no explicit dissipation term in the present model. Wave energy dissipation takes place primarily in the high frequency equilibrium range of the spectrum and it is responsible for the f^{-5} dependence of the tail of the spectrum. In this model wave dissipation is included implicitly by forcing the tail of the spectrum to conform to the f^{-5} dependence in the high frequency parametric domain.

No limiting shape is imposed, in this model, on the spectrum at the final stages of wave growth. As discussed by Resio (1981), a property of the combined source term results in an asymptotic approach of the computed spectrum to a saturated shape as wave growth approaches fully developed seas for a given wind speed. The wind energy enters the central frequencies and is redistributed within the spectrum by the nonlinear wave-wave interactions. As the spectrum approaches saturated conditions, a negative lobe of the wave-wave interaction term (i.e. the range of frequencies which lose energy due to the nonlinear interaction) moves progressively into lower frequencies until it approaches the so-

called wind frequency ($f = g/2\pi u$). At this point the exponential term, G_{in}, goes to zero and the growth of the spectrum is stopped.

The last term in Equation 1 represents the propagation of wave energy across the model grid. Propagation is achieved for all spectral components lower than the parametric high frequency domain by using an explicit finite difference formula

$$E_{ij}^{n+1} = \sum_{k=1}^{2} \lambda_k E_{ijk}^{n} \qquad (4)$$

where the superscript, n, denotes the time step and the subscripts i, j, and k refer to frequency, direction and space counters respectively. This scheme has superseded the modified Lax-Wendroff scheme used in the previous version of the model after a study of the dispersion effects and angular spreading effects in long distance swell propagation.

The model equations are solved on a regular 2^{o} geographical coordinate grid (Figure 27). The grid boundaries for the first storm are formed by the coast and the 70th meridian in the west, by the 38th meridian in the east and by the 36th and 54th parallel in the south and north respectively. For the second storm a somewhat smaller extent in the south, to 38^{o}N was found to be adequate. The grid spacing therefore varies between 70.5 nautical miles at the northern boundary and about 97.1 nautical miles (94.5 nautical miles for the second storm) at the southern boundary. At the hindcast site the spacing is approximately 83.3 nautical miles. The computational grid consists of 130 and 113 active grid points for the first and second storm respectively.

The wave spectrum at each grid point is resolved into 16 frequencies and 16 direction bands. At each three hour time step, the wave energy from the previous time step is propagated across the grid according to the finite difference scheme (Eq. 4). After the spectral peaks of the locally generated waves and of the swell are determined, the wave-wave interaction source for the local sea and for the swell spectrum is computed using Equation 2a and the total source integration (Eq. 1) is performed. Each hindcast starts from zero energy (calm seas everywhere). A certain amount of simulation time ("spin-up") is required to bring the wave field in balance with the input wind field. In the case of the two events hindcast for this study a spin-up time of 24 hours was found to be sufficient.

MODEL INPUT

The accuracy of input wind fields is the most important factor determining the accuracy of wave hindcasts. The fully developed wave energy is approximately proportional to the fourth power, and the corresponding wave height to the square, of the wind speed. Thus a small fractional error in the input winds leads to approximately four times the fractional error in the corresponding wave energy and twice the fractional error in the corresponding wave height.

Specification of accurate input winds is especially important in a study involving intercomparison with other wave data acquisition methods. Here it is important to isolate errors due to the physics or numerics of the wave model from errors caused by deficiencies in the input. Cardone et al. (1979) discuss the error characteristics of three methods used to hindcast surface marine wind fields in historical storms: (a) manual scaling of winds from surface weather charts, using a planetary boundary layer model to relate the wind to the distributions of surface pressure and air and sea temperatures; (b) computer-based objective analysis of gridded pressure data and wind observations; (c) construction of streamlines/isotachs through manual kinematic analysis. Their conclusion is that the most accurate method is the direct manual synthesis of ships' wind observations into a continuous field through the kinematic analysis. Fields derived from sea-level pressure gradients were found by Cardone et al. (1979) to have generally negative bias in wind speed, most likely due to smoothing of sharp pressure gradients. Where wind observations are sparse the most stable estimates are obtained from a mix (a weighted average) of independently derived wind fields: one based on surface pressure, the other based on kinematic analysis (Resio, 1982). Typical weighting factors are 0.8 on the kinematic analysis and 0.2 on the pressure-based winds. Such a mix was used in the present study.

A planetary boundary layer (PBL) model described by Resio et al. (1982) was employed to relate surface wind velocity to the local pressure gradient and to the air-sea temperature difference. The pressure gradients were extracted from surface analysis charts which also provided information on the air temperatures. Sea temperature was determined from METOC Sea Surface Temperature Charts.

Three sets of surface analysis charts were acquired for the study: those prepared by the Canadian Meteorological Centre (CMC) in Montreal, charts

prepared by the Newfoundland Weather Office in Gander and charts prepared by the Atlantic Weather Centre in Bedford, Nova Scotia. The pressure analysis is, to some extent, affected by a subjective judgement on the part of the analyst. It was considered desirable to first compare the three sets for possible inconsistencies before selecting one of them as the source of the surface pressures. The three sets did not show any significant discrepancies. In the end, Atlantic Weather Centre Surface Analyses were selected for reading off the pressure fields at model grid points mainly because of their legibility and because they covered the whole model grid. CMC gridded surface pressure data for the Northern Hemisphere were also obtained. However, the magnetic tape with these data arrived after the wind analysis had been completed and thus could not form part of the input.

For the kinematic analysis, wind speeds in the area of the experiment (Figure .. were obtained from weather observation logs from drilling vessels West Venture, John Shaw, Sedco 706 and Sedco 710. The PBL model was employed to relate wind velocities at the drilling vessel's anemometer height (60 - 90 m) to the surface wind velocities at a 10-metre reference level required by the kinematic analysis. Outside this area, the wind information was limited to ship reports listed on the weather charts. These are the weather reports transmitted to shore in real-time by radio. The non-real-time reports become available only with several months' delay and they could not be obtained at the time of the study. During the experiment a MINIMET meteorological buoy, equipped with an anemometer, was located about 0.5 nautical miles east of the MEDS directional wave buoy. The winds recorded by the MINIMET buoy were found to be inconsistent with those observed from the drilling rigs. This may be due to the fact that the buoy anemometer was only three meters above the sea surface and thus within the turbulent boundary layer strongly influenced by the wave field. Since the four, independently obtained, rig observations were mutually consistent they, rather than the buoy data, were used for the kinematic analysis.

The wind data coverage and quality in the immediate vicinity of the hindcast site were excellent and therefore observed wind speeds and directions were used directly as input at the hindcast site grid point (i.e. 1.0 weighting factor on the kinematic analysis). For wind estimates at the remaining grid points the 0.8 and 0.2 weighting factors, on the kinematic analysis and pressure-based winds respectively, were maintained.

MODEL OUTPUT

Derived Quantities

The output from the hindcast model is a time series of discrete directional spectra, each consisting of 16 directions and 16 frequency bands

$$E(f_i, \theta_j);\ i = 1,16;\ j = 1,16$$

where f_i and θ_j are, respectively, frequency and direction in the middle of the band;

$$f_1 = 0.04 \text{ Hz},\ f_{16} = 0.19 \text{ Hz},\ \Delta f = 0.01 \text{ Hz}$$
$$\theta_1 = 0^\circ,\ \theta_{16} = 360^\circ,\ \Delta\theta = 22.5^\circ$$

For the purpose of comparison with observed wave spectra, the following wave products and parameters have been computed from the hindcast directional spectra:

One-dimensional spectrum

$$S(f_i) = \sum_{j=1}^{16} E(f_i, \theta_j)\Delta\theta$$

Directional distribution function

$$D(f_i, \theta_j) = E(f_i, \theta_j)/S(f_i)$$

First five moments of the one-dimensional spectrum

$$M_n = \sum_{i=1}^{16} f_i^{\,n} S(f_i)\ \Delta f \quad n = 0, \ldots 4$$

Characteristic wave height (approximately equal to the significant wave height)

$$H_{sig} = 4\,(M_0 + \Delta M_0)^{1/2}$$

where ΔM_0 is the contribution to the total variance from the high frequency tail of the spectrum above the cutoff frequency (i.e. $f > f_{16}$).
Peak period (frequency), T_p (f_p), as the period (frequency) at the middle of a frequency band where the spectral density, $S(f_i)$ reaches its maximum.

Average period

$$TM_{01} = \frac{M_0}{M_1}$$

Average apparent period

$$TM_{02} = \left[\frac{M_0}{M_2}\right]^{1/2}$$

Apparent crest period

$$TM_{24} = \left[\frac{M_2}{M_4}\right]^{1/2}$$

Spectral peakedness

$$Q_p = \frac{2}{M_0^2} \sum_{i=1}^{16} f_i \left[P(f_i)\right]^2 \Delta f$$

Spectral narrowness

$$\nu = \left[\frac{M_2 M_0 - M_1^2}{M_1^2}\right]^{1/2}$$

Mean direction

$$\overline{\theta}_i = \overline{\theta}(f_i) = \text{Arctan } (y/x)$$

where $$y = \sum_{j=1}^{16} \sin \theta_j \, D(f_i, \theta_j) \Delta\theta$$

where $x = \sum_{j=1}^{16} \cos\theta_j \, D(f_i, \theta_j) \Delta\theta$

Direction spread (standard deviation)

$$\sigma(f_i) = \left[\sum_{j=1}^{16} (\theta_j - \bar{\theta}_i)^2 \, D(f_i, \theta_j) \Delta\theta \right]^{1/2}$$

where $\theta_j - \bar{\theta}_i$ is taken as $2\pi - (\theta_j - \bar{\theta}_i)$ if $\theta_j - \bar{\theta}_i > \pi$.

All variables defined above, with the exception of the directional distribution function, $D(f, \theta)$ and the spectral moments, M_n, are provided on magnetic tape together with the input wind fields and with the hindcast directional spectra. The values of H_{M0}, recorded on tape, may be somewhat greater than those computed from the spectra by summing over the 16 frequency bands. The difference is due to the contribution to M_0 from the tail of the spectrum above the high frequency cutoff of 0.19 Hz. Unlike the remaining parameters, H_{M0} is computed as part of the model simulation at each time step. In the model the tail of the spectrum is represented by an analytical function (with f^{-5} dependence) and it is integrated also analytically. The difference is greatest for small H_{M0} and high f_p in growing seas when a significant part of the total energy is present in the high frequency range. The high frequency cutoff also affects other parameters, particularly those which are a function of higher order moments. This should be taken into account when comparing the hindcast parameters with those computed from observed spectra having a different high frequency cutoff.

It should be noted that the hindcast model computes only the energy density or variance spectrum but not a phase spectrum. Thus wave variables which depend on the relative phase of the constituent spectral components, such as the actual time series of the individual wave heights or of the surface slopes cannot be reconstructed from the hindcast information. Similarly, in order to obtain maximum wave heights corresponding to the computed wave spectra, a statistical distribution of individual wave heights must be assumed. Such a maximum wave

height is a statistical parameter and it is not directly comparable to the maximum wave height actually observed in a wave record.

Swell

For computing efficiency reasons, the total source integration in the present model is performed on the combined sea and swell energies. Thus at the end of each time step the distinction between locally generated sea and swell is lost. In order to separate the swell part from the combined spectrum, a forward face of a parametric sea spectrum, defined as a function of peak frequency of the locally generated waves, f_p,

$$E_{sea}\ (f < f_p, \theta) = E\ (f_p, \theta)\ \exp\left[\lambda - \lambda\left(\frac{f}{f_p}\right)^{-4}\right] \tag{5}$$

is subtracted from the combined energy density

$E\ (f<f_p, \theta)$:

$$E_{swell} = E - E_{sea} \tag{6}$$

In the above expression for E_{sea}, λ is a parameter which depends on the peakedness of the spectrum. This functional form permits a representation of a wide range of empirical sea spectra, including those observed during JONSWAP.

The swell height is defined analogously to the characteristic wave height as

$$H_{swell} = 4\left[M_{0,\,swell}\right]^{1/2}$$

where $M_{0,swell}$ is the total variance (the zeroth moment) of the swell spectrum. The swell period is defined as the mean period of the swell spectrum

$$T_{swell} = \frac{M_{0,\,swell}}{M_{1,\,swell}}$$

where $M_{0,swell}$ and $M_{1,swell}$ are the zeroth and first moment of the swell spectrum.

The swell direction is determined as

$$\theta_{swell} = \text{Arctan } (y/x)$$

where $$y = \sum_{i=1}^{16} \sum_{j=1}^{16} E_{swell} \sin\theta \, \Delta f \Delta\theta$$

$$x = \sum_{i=1}^{16} \sum_{j=1}^{16} E_{swell} \cos\theta \, \Delta f \Delta\theta$$

and E_{swell} is given by Equations 5 and 6.

RESULTS

The primary discussion of the hindcast model results in light of buoy observations is included in the "Comparison of Data Sets" section of this report. Here can be found further illustrations of the hindcast energy spectra, mean direction by frequency and directional spectra for selected records A brief summary of model behaviour follows.

Event 1: March 10 to March 12.

Energy first appears in the spectrum at 0300/10, at high frequencies, (>.15Hz) as part of the model spin-up. As winds build up to a maximum between 0300 and 0600/11, the model peak moves to lower frequencies and the energy in the spectra increases reaching a maximum H_{sig} of 7.5 m and peak period of 12.5 s (Fig. 28). As winds abate, the spectrum broadens, overall energy drops, while the peak period, in some spectra, moves to very low frequencies (16.7 s). This energy may be representing forerunner swell from the storm centre that had moved off or continued wave development. Wave directions at the peak frequency agree exactly with wind direction during model spin-up and lie generally within 20 degrees at the storm peak. As the storm abated, the peak frequency, associated with a 16-17 second swell , showed a mean direction as much as 60 degrees rotated (counter-clockwise) from the wind direction.

Event 2: March 29 to April 2.

During storm build-up, the spectra behaved similarly to the first event. As the storm centre passed over the study area, spectral development stopped temporarily (0600/28 Fig. 29), then resumed to reach a peak at 1200/28. There was very little change until 0900/29 (Figure 30) when the storm began to abate. At this time, the spectra broadened, total energy was reduced, and energy at very low frequencies appeared (Fig. 30).

From March 30 to April 2, small "blows" occurred in the area and the significant wave height stayed between 3.0 and 5.0 m. The behaviour of the

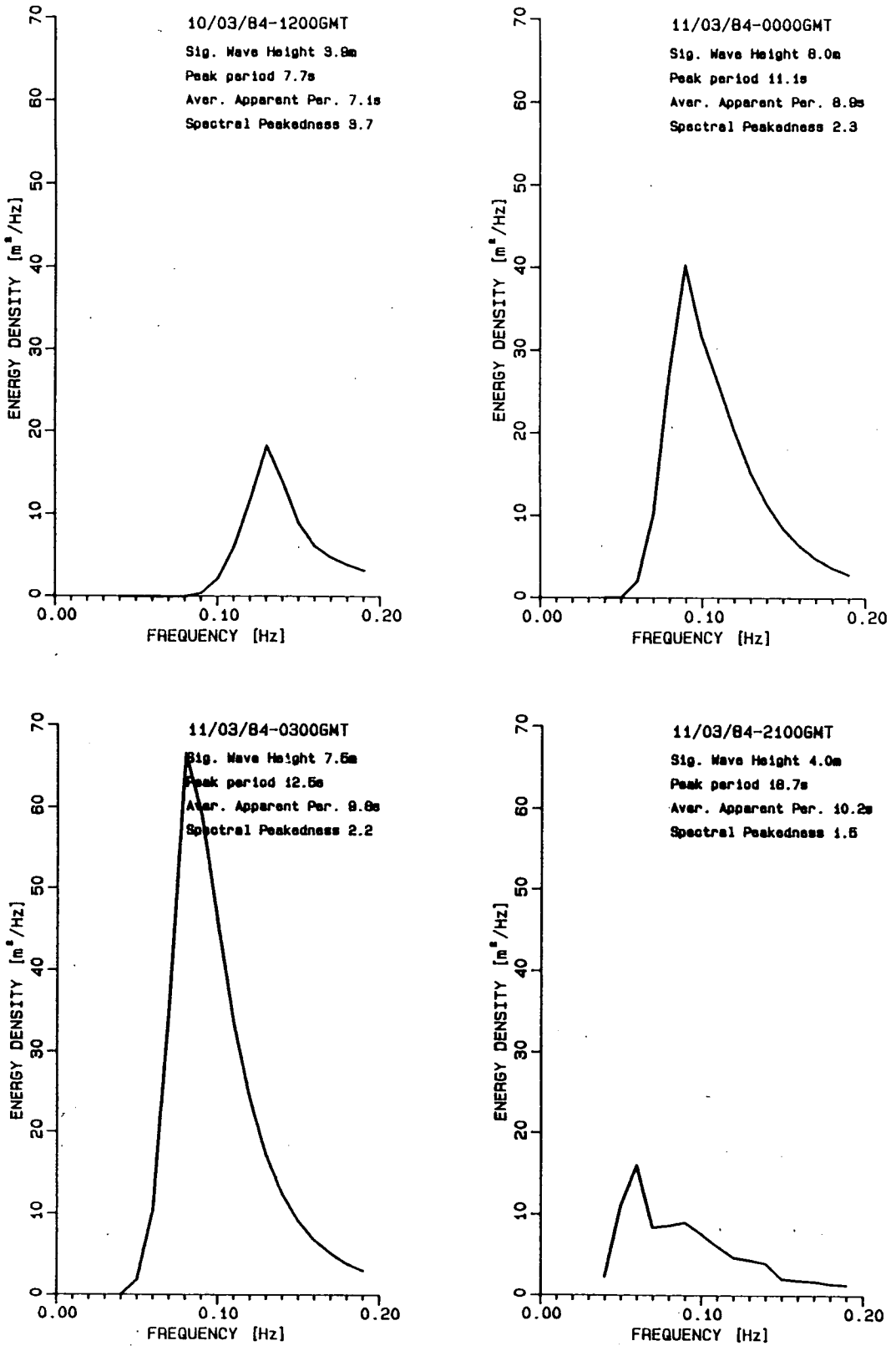

Figure 28. Hindcast spectra for 1200/10, 0000/11, 0300/11, and 2100/11.

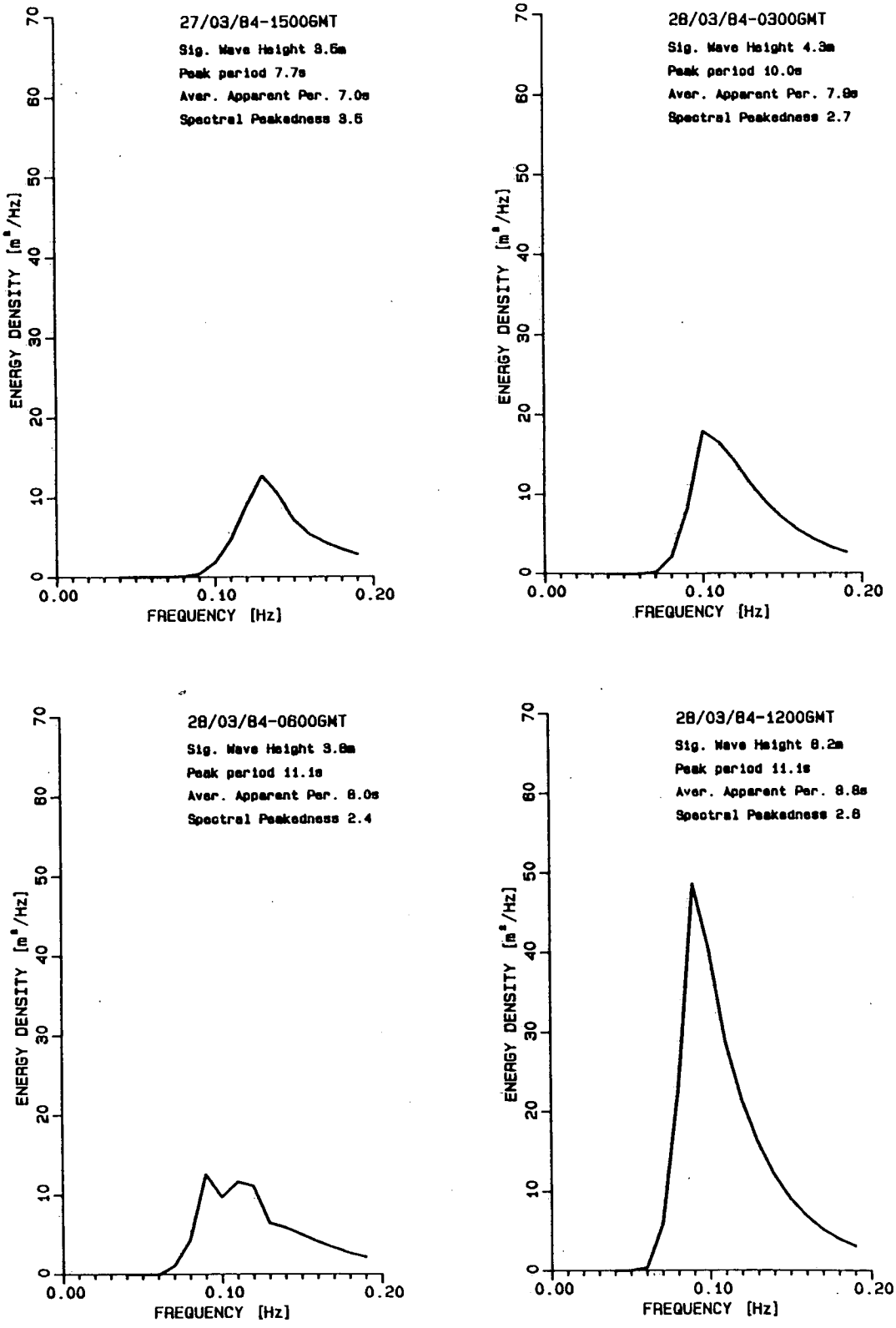

Figure 29. Hindcast spectra for 1500/27, 0300/28, 0600/28, and 1200/28.

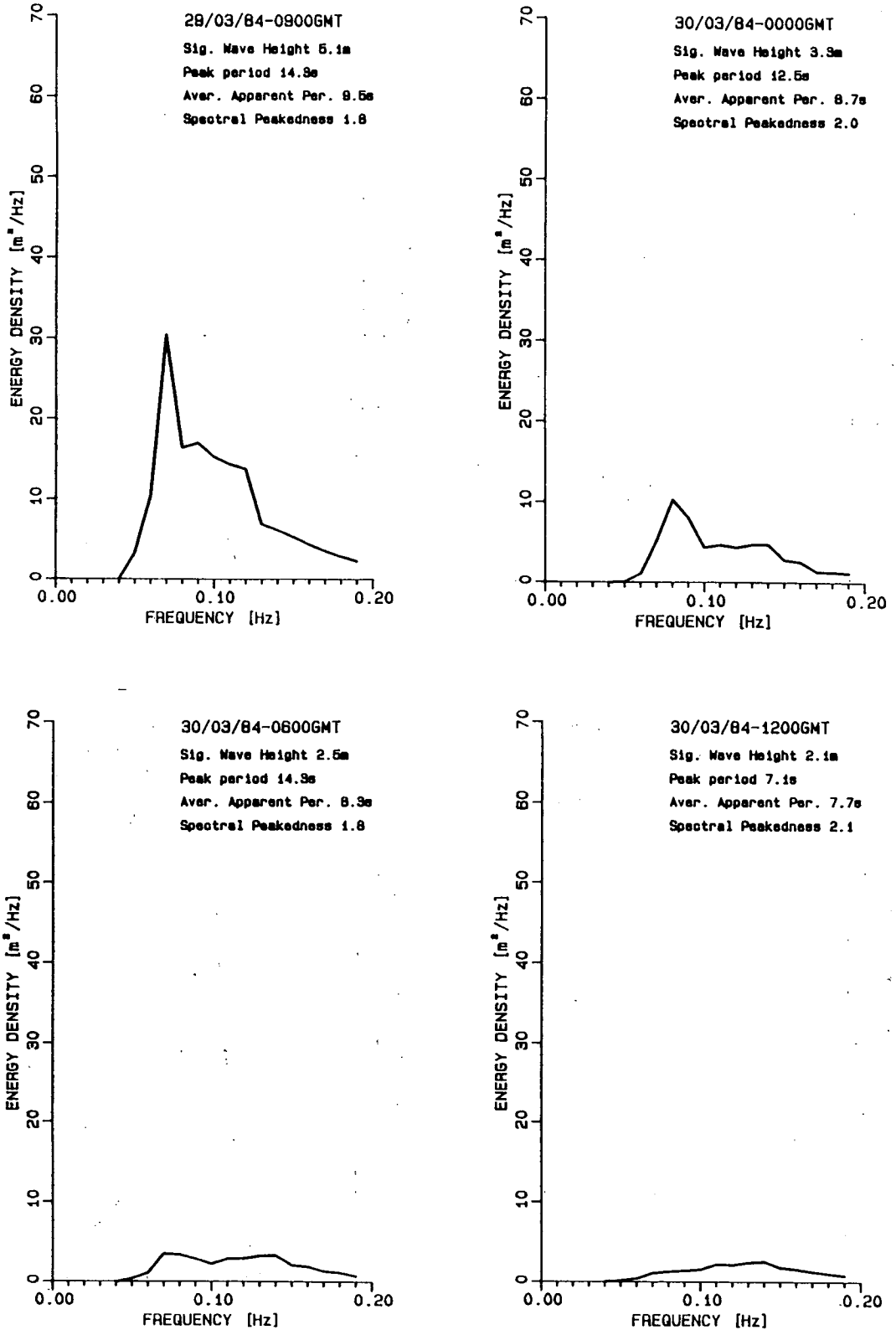

Figure 30. Hindcast spectra for 0900/29, 0000/30, 0600/30, and 1200/30.

spectra during the first sub-event, was similar to the build-ups seen earlier (Fig. 31, 2100/30). Energy is again being dumped into very low frequencies as winds drop slightly (March 31). During the second sub-event (April 1, Fig. 31), winds appeared to put energy directly into the mid-frequencies. A maximum H_{sig} of 4.7 m was reached at 1800 on April 1. Following this peak, winds dropped and the spectra followed similar decay behaviour as during the major storms.

During storm build-up, wave mean directions agreed well with the measured wind directions. The hindcast directional spectra often showed bimodal distributions in which case one peak would be associated with the wind direction and the other a remnant peak. These generally occurred during veering winds (e.g. when the storm centre passed over the study) and the calculated mean directions are misleading. With the appearance of low frequency energy on March 29, wave directions showed two distinct regimes with the high frequencies aligned with the wind and the low frequencies having a 30^{o} to 40^{o} clockwise rotation, initially, then counter-clockwise by the end of the day as local winds shifted from approximately 210^{o} to 300^{o}. Responses to veering winds in the following days showed similar high frequency initial response with little change in the very low frequencies. The behaviour at the mid frequencies (.08 to 1.2 Hz) is quite variable. Further discussion on the directional spectra can be found in the comparison against buoy data in the following section.

The input wind fields and the hindcast directional spectra are available on magnetic tape. The following data displays were also produced.

1. Time series plots of:
   a) Wind Speed;
   b) Wind Direction;
   c) Significant Wave Height, H_{sig};
   d) Peak Period, T_p;
   e) Average Apparent Period, $T_{M,2}$;
   f) Spectral Peakedness, Q_p;
   g) Spectral Narrowness, ν;
   h) Mean Direction at Peak Frequency, $\bar{\theta}(f_p)$;
   i) Direction Spread at Peak Frequency, $\sigma(f_p)$;

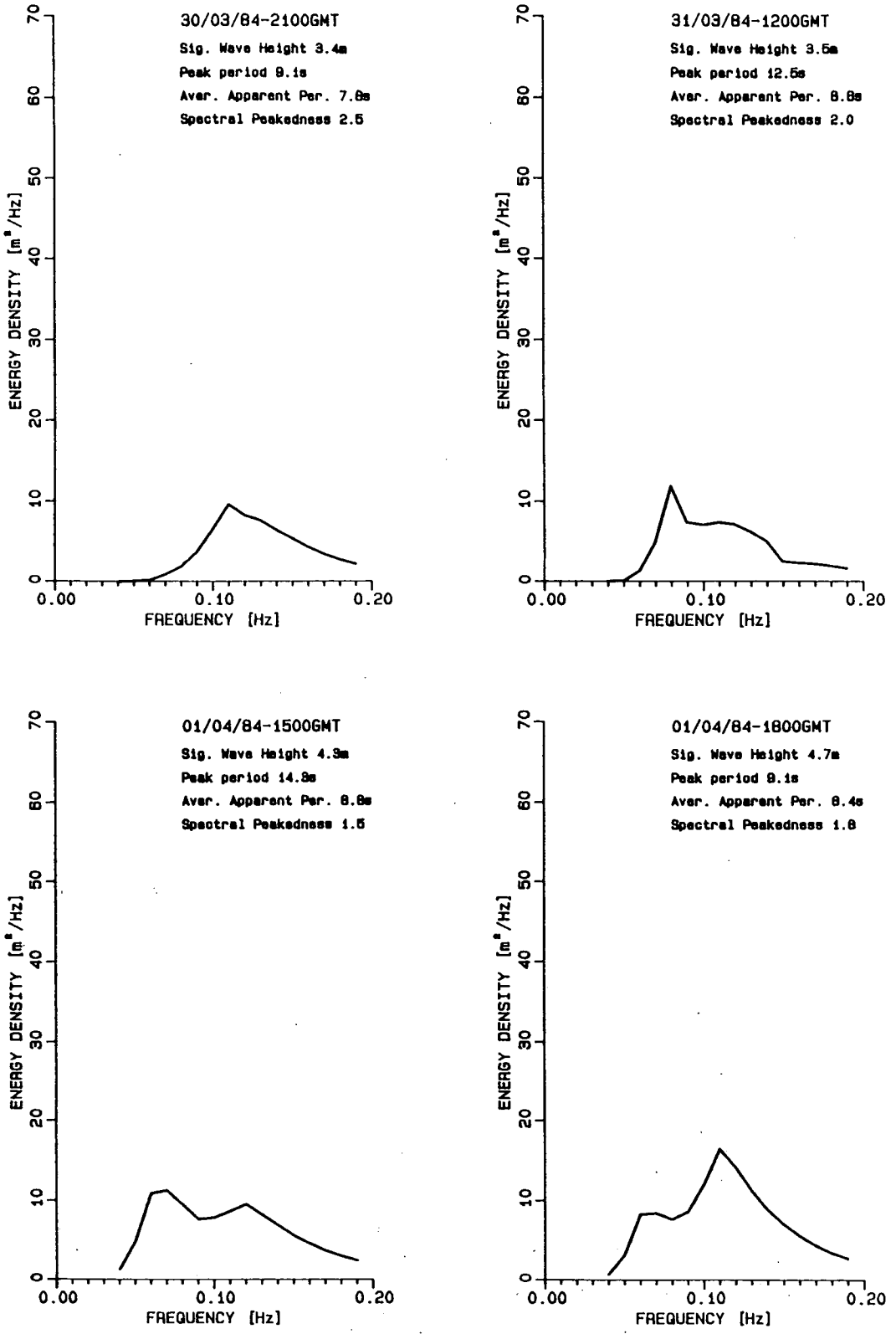

Figure 31. Hindcast spectra for 2100/30, 1200/31, 1500/1, and 1800/1.

2. One-dimensional spectra, S(f).
3. Summary listings of wave parameters at each time step.
4. Tables of two-dimensional spectra, $E(f,\theta)$, at each time step (partially contoured).

Questions about access to the above information should be addressed to F.G. Bercha and Associates Ltd. (Nfld) St. John's, Nfld.

COMPARISON OF DATA SETS

DATA QUALITY

Prior to performing any kind of comparison between data sets obtained from different instruments or techniques, one requires an understanding of their inherent limitations. With experimental results, one also needs to assess the data return and any operational problems that may have been encountered. In the first section of this report, the buoy data were initially examined and their data return discussed in light of instrument operation, data processing complications (e.g. assignment of time headers) and environmental effects (e.g. icing). The amount of data return has obvious importance in a statistical sense. The following sections continue the discussion of sources of error from a mathematical viewpoint and suggest some quality control measures that may be taken.

Sources of Error

In any experimental situation, there always exists a minimum probability that, when comparing two sets of measurements of the same parameter, they will disagree with statistical significance. This arises from various sources of error or uncertainty, which introduce variability into the parameter set. For this study, three possible sources of error will be discussed: Instrument measurement error, sampling error and environmental error.

Instrument measurement error. Instrument measurement errors are inherent to the equipment used in the experiment and are generally minimized, for the proposed usages, during design. The errors can arise from three sources: systematic errors, instrument resolution and measurement accuracy. Systematic errors, such as a non-zero offset, can generally be reduced or eliminated during the data processing. The instrument resolution is the smallest change in the parameter that can be measured or recorded. This would be controlled by the physical limits of the sensor or by data storage requirements (for example, 8-bit vs. 12-bit digitization). Generally, instrument resolution is, to an order of magnitude or more, better than measurement accuracy. The accuracy is how well the measured

value agrees with the true value and can be considered as the confidence limit about the measured value within which the true value should fall. The accuracy for the three wave buoys is on the order of ±2% for all channels. It is assumed that this error is random. When performing a spectral analysis, this error will propagate through the calculations in the following manner:

- For energy terms Co_{11}, Co_{22}, Co_{33}

  let $x_i = \hat{X}_i + \epsilon_i \hat{X}_i$

  where $\hat{X}_i$ is the mean value of x_i and ϵ_i is the percent error (+ or -)

  $$< x_i^2 > = <(\hat{X}_i + \epsilon_i \hat{X}_i)^2 > = <\hat{X}_i^2 > + 2 < \epsilon_i \hat{X}_i^2 > + < \epsilon_i^2 \hat{X}_i^2 >$$

  As the error is random, the central term equals zero and the error, for each frequency, in the energy density is ±.04%.

- For cross-spectral terms, the error in the original signals will result in both a random amplitude and random phase error. The error is assumed to be isotropic so that each co- and quad-spectral term will have the same amplitude error of ±.04%.

  The phase error is given by:

  $$\arcsin \frac{(\text{magnitude error})}{\text{magnitude}} = \arcsin (.0004) = 0.023^{\circ}$$

A second possible source of error (variable) is the presence of non-linearities in the accelerometer which can cause a rectification of the periodic motions into an average signal. To some extent, this can be handled in the data processing. These errors are quite small when compared against sampling and environmental errors.

Another source of error is related to the accuracy of the transfer functions that need to be applied during the data processing to correct amplitude and phase errors resulting from the electronics and signal handling procedures. There was not enough information available from the manufacturer to assess these. However, properties of the measured parameters can be used to determine the applicability of these transfer functions and will be discussed with the linearity analysis in a later section.

Sampling error. This is the error introduced due to the sampling and data processing methods. There are two approaches that can be used to obtain confidence limits on the estimate of interest. The first involves fitting a known statistical distribution to the population. This requires pre-knowledge of the system as well as various assumptions of independence between samples and a stationary population. When these conditions cannot be met, a direct calculation of the mean and standard deviation from repeated sampling may be performed.

When performing a spectral analysis, it is first assumed that the initial population of heave and slopes (or tilt) are independent, stationary, and follow a Gaussian distribution. The Fourier transforms are composed of real and imaginary components that are uncorrelated random variables with zero means and equal variances. They also follow a Gaussian distribution as this is not changed during Fourier transformation. The magnitude of the transform is given by the sum of the squares of the two components which will thus result in a new population having a chi-squared (χ_n^2) distribution with 2 degrees of freedom. The cross-spectral terms have a circular normal distribution which is equivalent to a non-central χ_2^2 distribution. For this analysis, it was assumed that a normal χ^2 distribution could be used to represent the cross spectral terms.

If the spectral analysis is performed on the entire record of N values, N/2 independent frequency estimates would be produced. To increase the number of degrees of freedom, thereby improving confidence, Band averaging and/or ensemble averaging is performed. The number of degrees of freedom will then be increased to 2* number of ensembles or 2* number of ensembles * number of Bands averaged. This is actually the maximum number of degrees of freedom available as any auto-correlation between samples would effectively reduce this number (e.g. see Bayley and Hammersley, 1946). Table 5 contains the minimum values needed to multiply each energy density estimate to obtain 95% confidence limits.

TABLE 5
CONFIDENCE LIMITS ON SPECTRAL ESTIMATES

Instrument	No. of Degrees of freedom	Lower Bound Multipliers	Upper Bound Multipliers
WAVERIDER	16	.43	1.80
WAVE-TRACK	32	.57	1.55
WAVEC	20 (frequency < .2 Hz) 40 (frequency > .2 Hz)	.48 .61	1.71 1.48

These values are large compared with instrument error. The assumptions of independence and stationarity are generally violated for a real wave field, as it is continuously evolving and has a non-Gaussian distribution due to groupiness.

Similar confidence limits can be calculated for various spectral statistics.

As the frequencies are taken to be exact and known, one does not explicitly calculate confidence limits on, for example, peak period. The error in period assignment would be variable, as the frequency resolution is constant, and can be taken to equal the bandwidth. In this study, wave periods of greater than 16 seconds would not be expected due to the shallow water depth, and for periods less than this, the bandwidth is always less than 2 seconds.

Significant wave height is defined as $4*\sqrt{(M_0)}$, based on a Gaussian assumption, where M_0 is the zeroth moment of the spectral density distribution. The significant wave height can also be considered as 4* the standard deviation of the original time series. When calculating the confidence limits on the standard deviation, a χ^2 distribution is assumed with the number of degrees of freedom equal to the number of samples. Similarly, a χ^2 distribution is assumed for the spectral densities and the number of degrees of freedom equal to:

DF = 2 * No. of ensembles * No. of frequencies summed over

or = 2 * No. of frequencies * No. of Bands averaged

The number of degrees of freedom would equal the original number of samples in a record if no truncation of frequencies occurs. Table 6 contains the minimum values needed for determining the confidence limits. These are approximations using

$$\chi^2_{n;\alpha} = (1 - 2/9n + Z_\alpha\sqrt{2/9n})^3$$

where Z_α is the percentage of a standardized normal distribution and n is the number of degrees of freedom.

Szabados (1982) and Long (1980) estimated the total number of degrees of freedom for a χ^2 distribution of significant wave height as

$$\gamma = 2(\sum_n En)^2 \Big/ \sum_n En^2$$

where En is wave variance at the nth Fourier frequency and it is summed over all frequencies. This would imply a variable number of degrees of freedom between records even though the processing was similar.

TABLE 6

CONFIDENCE LIMITS ON SIGNIFICANT WAVE HEIGHT

Instrument	No. of Degrees of freedom	Lower Bound	Upper Bound
WAVERIDER	960	0.9702	1.0298
WAVE-TRACK	1920	0.9790	1.0210
WAVEC	1900	0.9789	1.0211

Note: These values are approaching the instruments' accuracy limits for a direct heave measurement.

Confidence limits in calculations of average period, average apparent period, and average crest period can be estimated using an F-distribution (i.e. a ratio of two χ^2 distributions). The approximated bounds are given in Table 7 for average period. Those for average apparent period and apparent crest period would approach the square root of these values.

TABLE 7

CONFIDENCE LIMITS ON AVERAGE PERIOD

Instrument	No. of Degrees of freedom	Lower Bound	Upper Bound
WAVERIDER	960/960	.871	1.129
WAVE-TRACK	1920/1920	.909	1.091
WAVEC	1900/1900	.909	1.091

A variable error will also be introduced into any estimates involving a summation over frequency due to the assumption of equal value over the band width. The magnitude of this error will be directly related to the kurtosis of the spectrum. Significant differences can occur in spectral parameters measured by different instruments when the range for the summation of terms is different. The chosen high frequency cutoffs for parameters calculated from the second and fourth spectral moments are particularly important as they are unstable (e.g. average apparent period, spectral width parameter used in spectral modelling) due to their respective f^2 and f^4 dependence. A discussion on the stability of spectral parameters can be found in Rye (1980) and on zero up-crossing parameters in Goda (1979).

Confidence limits can also be calculated for the dispersion ratio at each frequency found using the linear analysis described in the Linearity of Buoy Response section of this report. Again, an F-distribution was assumed. The results are given in Table 8.

TABLE 8

CONFIDENCE LIMITS ON THE CALCULATED DISPERSION RATIO

Instrument	No. of Degrees of freedom	Lower Bound	Upper Bound
WAVE-TRACK	32/64	.7420	1.393
WAVEC	20/40	.6612	1.439

The approach used to this point is not appropriate when examining the direction parameters as no standard distribution fits, for example, a population of cosine spread estimates. An error propagation analysis has to be performed and this was done by Long (1980).

The analysis performed by Long serves two purposes. Firstly, he explicitly provides calculations for the variance of the directional spectral statistics. (i.e. mean direction, cosine power, root mean square spread angle and the dispersion ratio R). Secondly, he has set up a method to test the applicability of a given model parameterization of the directional spectrum for specific records. The mathematics to calculate the expected variance are quite involved and the reader is referred to Long (1980).

Briefly the expected variance can be related to the cross-spectral terms in the following manner:

A) $\text{Var}(\theta \text{ mean}) = K_1^{-4}\left[K_1^2 - d_3(d_1^2 - d_2^2) - 2d_1d_2d_4\right]\left(\frac{1}{2\gamma}\right)$

B) $\text{Var (Cosine Power)} = \frac{1}{1-K_1}\left\{K_1^4 + \frac{1}{4}K_1^2(K_2^2 - 1) + (\frac{1}{2}K_1^{-2} - 1) * \left[K_1^2 + d_3(d_1^2 - d_2^2) + 2d_1d_2d_4\right]\right\}\frac{1}{\gamma}$

C) $\text{Var}(\theta \text{ spread}) = 1/2\,(1 - K_1)^3 * \text{var(Cosine Power)}$

D) $\text{Var (R)} = \frac{(2\pi f)^4}{g^2k^2} * (3 - 4K_1^2 + K_2^2) * \frac{1}{4\gamma}$

where $k = \text{wavenumber} \equiv \left[\frac{Co_{22} + Co_{33}}{Co_{11}}\right]^{1/2}$

f = frequency
γ = no. of degrees of freedom
R = dispersion ratio

$K_1 = \left(\frac{Qd_{12}^2 + Qd_{13}^2}{Co_{11}(Co_{22} + Co_{33})}\right)^{1/2}$

$$K_2 = \left[\frac{(Co_{22} - Co_{33})^2 + (2Co_{23})^2}{(Co_{22} + Co_{33})^2} \right]^{1/2}$$

$$d_1 = Qd12 \Big/ \left[Co11 \, (Co22 + Co33) \right]^{1/2}$$

$$d_2 = Qd13 \Big/ \left[Co11 \, (Co22 + Co33) \right]^{1/2}$$

$$d_3 = (Co22 - Co33) \, / \, (Co22 + Co33)$$

$$d_4 = 2 \, Co23 \, / \, (Co22 + Co33)$$

Qd = quadrature spectral values
Co = Co-spectral values
1 = heave
2,3 = slopes

As expected, the variance is inversely proportional to the number of degrees of freedom. The variance is generally assumed to be distributed in a Gaussian manner, therefore the confidence limits could be written as $\pm 2 \sqrt{\text{var.}}$ The wavenumber is not calculated explicitly for estimates (A) to (C) above and hence the dispersion characteristics of the waves are not assumed. However care must be taken in this approach as discussed in reference to the linearity analysis results.

Similar error analyses can be performed on any model parameters given a different model approach (from a cosine power function) such as a Poisson Kernel or wrapped normal distribution as well as a goodness of fit test (Long, 1980; Barstow and Krogstad, 1983). The important point of the study by Long is that, unlike confidence limits on spectral density which are only dependent on the number of degrees of freedom, confidence limits on directional parameters are dependent on the model chosen and the hypothesis that the model spectrum is the true spectrum.

Long's test of the applicability of a given model parameterization has recently been questioned, however, by Hodgins et al. (1985). They found that

Long's approach, as well as a new optimization method they had developed, tended to lead to model rejection at the spectral peaks where one would expect a narrow angular spread, as given, for example by the larger cosine spread estimate at the peak. They concluded that there was an inherent problem with this goodness of fit test when applied to a cosine power model, resulting from the poor angular resolution provided by the first four terms of the Fourier series, which are all that are available. A narrow directional spectrum, indicated by a large cosine power, will thus differ from the Fourier series over the directions considered and lead to rejection of a model which may actually be appropriate.

As part of the instrument specifications, Endeco Inc. indicates that the Band-Pass Spectral method provides a $\pm 10^{o}$ accuracy in mean direction.

Assessment of the results from the wave hindcast modelling has to take into account two potential sources of error: the model design and the input wind field. If the latter can be properly determined, tests have shown that the model predictions provide significant wave heights and peak periods with an RMS error of 1-1.5 m and 1 s respectively. The poorer frequency and direction resolution of the model directional spectra (.01 Hz and 16-pt compass) must also be kept in mind when comparing model results with buoy results and the frequency cutoff at .19 Hz will affect calculations of spectral statistics using the higher moments.

When calculating statistics on numerous records, or when comparing two data sets, the data are not independent. Error bars, in this case, can be calculated directly as ±2* standard deviation as a first estimate.

Environmental errors. The purpose of this study is to compare the performance of various buoys in their measurement of a given wave field. However, it is impossible to control the input signal such that each buoy is observing exactly the same environment. Site variability was reduced in this study by ensuring a uniform water depth in the area. As the buoys are separated by some distance, directionality in the wave field and the time needed for waves to travel between buoys, lead to discrepancies between data samples recorded at the same time. A numerical value cannot be put onto these differences. Noise would be a misnomer as the variations are usually signals not wanted in the given study and are neither random, white or stationary. In general, one would expect better agreement between two buoys at low frequencies than at high. The presence of

two WAVEC buoys and two Waveriders aids in assessing natural site variability under various conditions and one should not expect better agreement with a different buoy when put in a similar location.

Imposed Quality Control

For the WAVEC and Endeco WAVE-TRACK buoys, the initial quality controls were performed during tape reading and despiking. When comparing processed spectral information, records which had fewer than 7 blocks averaged during the spectral analysis were excluded due to the reduced confidence in the estimates. The spectrum for each WAVEC, WAVE-TRACK and Waverider record was plotted and examined for noise and other obvious problems. Time series of the spectral statistics from the various buoys were compared to check time assignments, when in question, and general data quality. As a result, it was observed that there were serious problems with the Endeco data for the period February 16 to 21 (period of large mean tilts) and that the time assignments for the Waverider data supplied by MEDS were probably in error from March 6 to 10. These data were not used during the intercomparison.

The linearity of the directional buoys' response in a given wave field was also examined for frequency dependent problems. This procedure is discussed in detail in the following section.

Linearity of Buoy Response

The techniques developed by Longuet-Higgins et al. (1963) to obtain a wave directional spectrum is based on the product of an uni-directional heave spectrum E(f) and a spreading function D (f,θ) such that

$$En(f,\theta) = E(f)D(f,\theta)$$

$$\text{where} \quad \int_0^{2\pi} D(f,\theta)\, d\theta = 1$$

and

$D(f,\theta)$ is given by the expansion

$$D(f,\theta) = 1/2\pi + \sum_{n=1}^{\infty}(a_n\cos(n\theta) + b_n\sin(n\theta))$$

For a heave/pitch/roll buoy the expansion is to n = 2 which can be extended if other parameters, such as curvature of the surface measured by a cloverleaf buoy, are available. The values of the coefficients a_n and b_n can be obtained from the cross-spectral estimates between the heave and two slope (or tilt, or velocity) channels:

$$a_1 = \frac{Qd_{12}(f)}{\pi K\, E(f)} \qquad a_2 = \frac{Co_{22}(f) - Co_{33}(f)}{\pi K^2\, E(f)}$$

$$b_1 = \frac{Qd_{13}(f)}{\pi K\, E(f)} \qquad b_2 = \frac{2Co_{23}(f)}{\pi K^2\, E(f)}$$

where K is the wavenumber, 1 = heave, 2 and 3 = slopes

$$E(f) = Co_{11}(f)$$

$$Co_{22}(f) = K^2E(f)\int_0^{2\pi}\cos^2\theta\, D(f,\theta)d\theta$$

$$Co_{33}(f) = K^2E(f)\int_0^{2\pi}\sin^2\theta\, D(f,\theta)d\theta$$

$$Co_{23}(f) = K^2E(f)\int_0^{2\pi}\sin\theta\cos\theta\, D(f,\theta)d\theta$$

$$Qd_{12}(f) = KE(f)\int_0^{2\pi}\cos\theta\, D(f,\theta)d\theta$$

$$Qd_{13}(f) = KE(f)\int_0^{2\pi}\sin\theta\, D(f,\theta)d\theta$$

There are only five independent equations as

$$K^2Co_{11}(f) = Co_{22}(f) + Co_{33}(f) \qquad (7)$$

The above equation forms the basis of the linearity analysis for signal amplitude.

If R is defined as the experimental dispersion ratio given as

$$R = \left[\frac{K^2 Co_{11}(f)}{Co_{22}(f) + Co_{33}(f)} \right]^{1/2}$$

then it should equal 1 for deep water waves and be reduced in shallow water by a factor proportional to tanh (KH), where H is water depth (if the wave field is behaving according to linear theory).

The check for linearity in terms of signal phase is based on the assumption that the phase angle calculated from the cross-spectral terms should be zero for 2 x 3 and 90° for 1 x 2 or 1 x 3 given surface slope measurements.

The usefulness of this analysis is twofold:

a) For the Assessment of Buoy Response:

The linearity analysis can be used to assess how well a given buoy, mooring design, or processing method measures the surface wave field.

Figure 32 contains plots of the calculated theoretical dispersion ratio and phase deviation for 172 samples measured off Norway in 1980 (Audunson et al., 1982). A schematic of the buoy used is given in Figure 33. The buoy was developed by the Christian Michelsens Institute in Bergen and the Continental Shelf Institute in Trondheim and is currently manufactured by Bergen Ocean Data. It contains a HIPPY sensor which is the same as the one currently used in the Datawell WAVEC buoy to measure surface heave and slope. It can be seen in Figure 32 that the response is generally quite linear though low up to 0.3 Hz. During the study, a damping chain was lost from the mooring and it could be shown from the linearity analysis that the loss actually improved the overall system response, indicating a problem with the original mooring design.

Ezraty and Cavanie (1981) used the linearity analysis to assess much smaller deviations resulting from Doppler shift effects due to tidal currents in

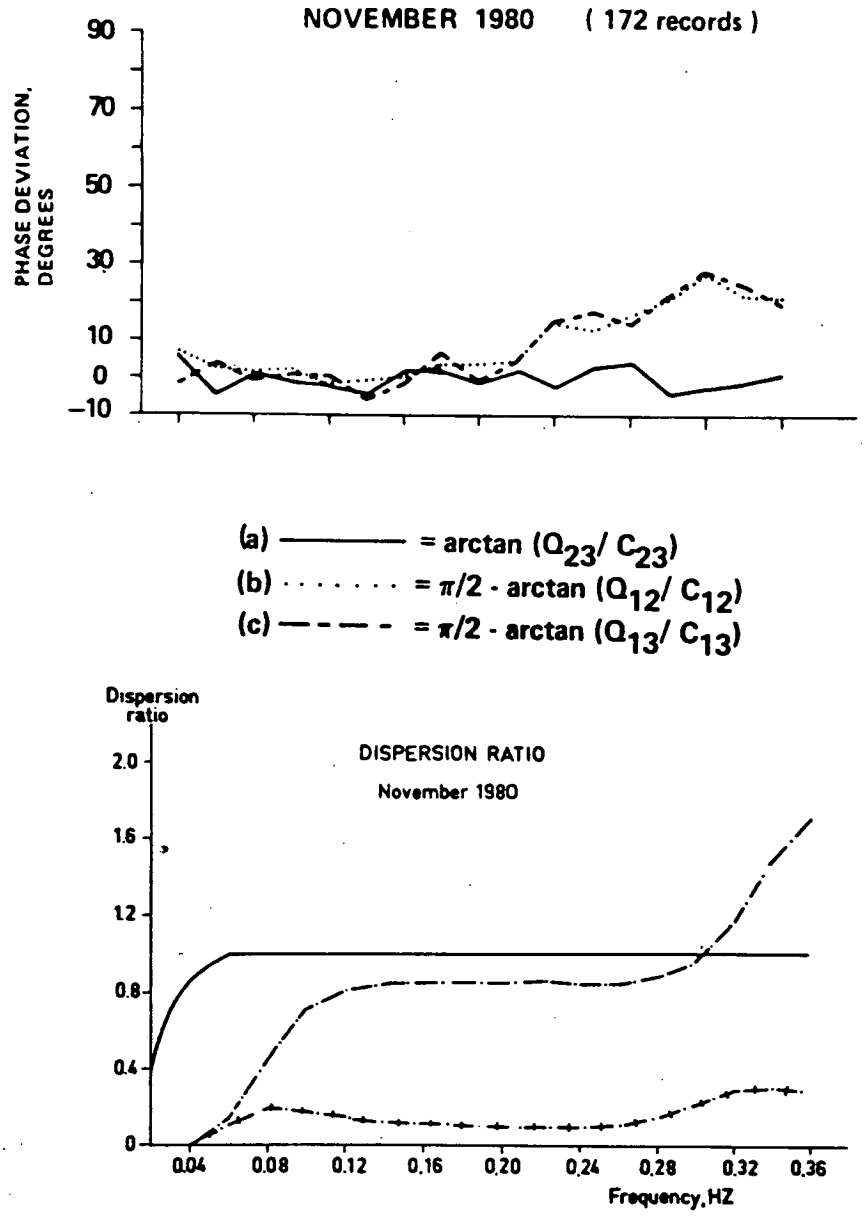

Comparison between linear theory (solid line) and November mean dispersion ratio (4.12) — · — · and its standard deviation + · + · (172 samples).

Figure 32. Calculated theoretical dispersion ratio and phase deviation (from Audunson et al. (1982)).

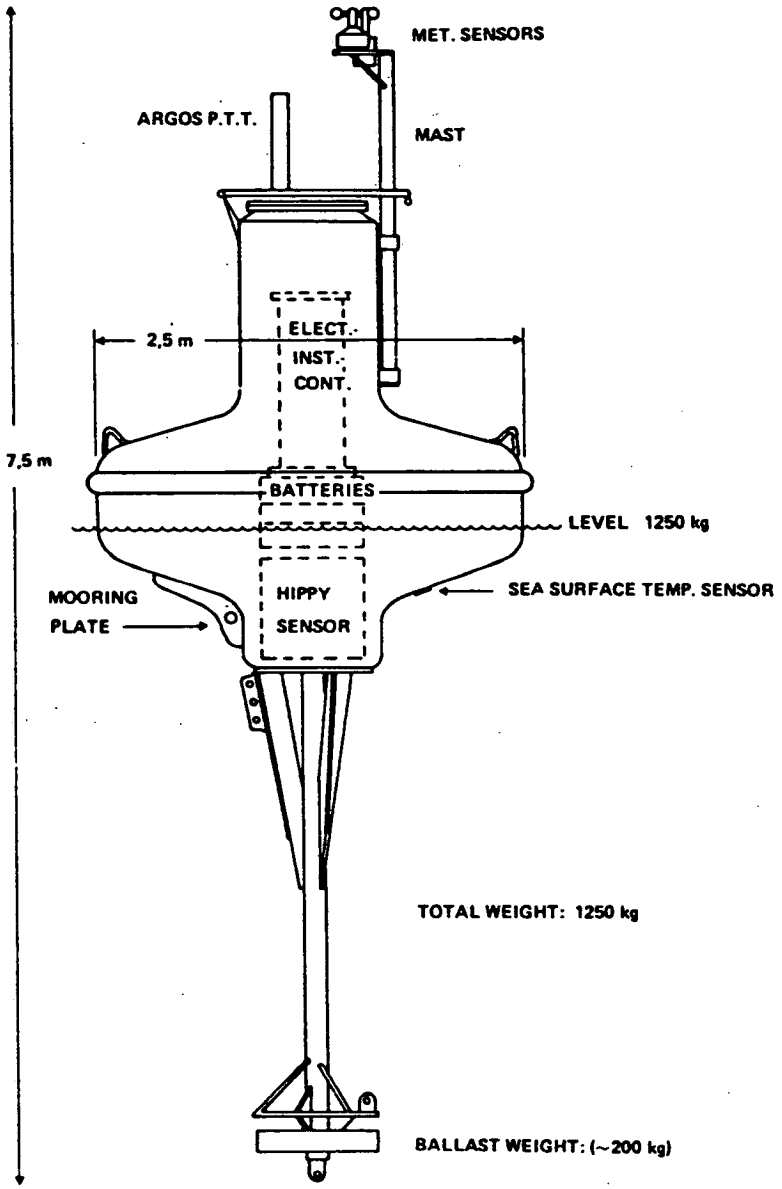

Figure 33. Schematic of the NORWAVE buoy.

their study area. From Figure 34 (their figures 9 and 10), it can be seen that by correcting for the Doppler shift, the typical error in the ratio R was reduced at nearly all frequencies though the mean value of R was not significantly changed as it was averaged over a few tidal cycles. The slope-following buoy used in this experiment was a toroid buoy (WADIBUOY), with a diameter of 2.5 m, a flat bottom and which also uses a HIPPY sensor. It was developed by CNEXO (Centre National Pour L'Exploration des Oceans, Centre Oceanologique de Bretagne) and the NEREIDES company. In general, the response of this buoy was linear. A drop off in linearity at long periods was due to the shallowness of the experimental site ($\sim$40 meters). It does not show the very large high frequency rise in the R-value as seen in Figure 32 for the Norwegian buoy.

Barstow and Krogstad (1983) were also able to show the Doppler shift effects from induced wind drift in the surface layer as well as from measured currents at 2 meters depth.

In a different application, Forristall et al. (1978), used this same linearity approach to compare a dispersion ratio, in this case, calculated using surface wave heave measurements and subsurface current velocities to that predicted by linear theory. They found that linear wave theory was able to predict both the velocity spectrum and the extreme speed distribution while nonlinear regular wave theory overpredicted velocities under high waves.

b) For the Calculation of Transfer Functions:

Equation 7 and the expected phase relationships can be used to calculate frequency dependent amplitude and phase transfer functions to "correct" the co- and quad-spectral estimates in the direction calculation without any pre-knowledge of the dispersion relationship of the wave field, as one no longer has to calculate a wavenumber. The assumption has to be made, however, that the amplitude correction for the two directional channels is applied equally to both. This approach is particularly useful when an equivalent slope measurement must be calculated from an induced tilt, subsurface velocity, or other directional measurement when the correspondence is a complicated relationship or is frequency dependent. A version of this approach is used by Dr. Lester Le Blanc (Univ. of Rhode Island) to process Endeco WAVE-TRACK data (Pers. comm.;

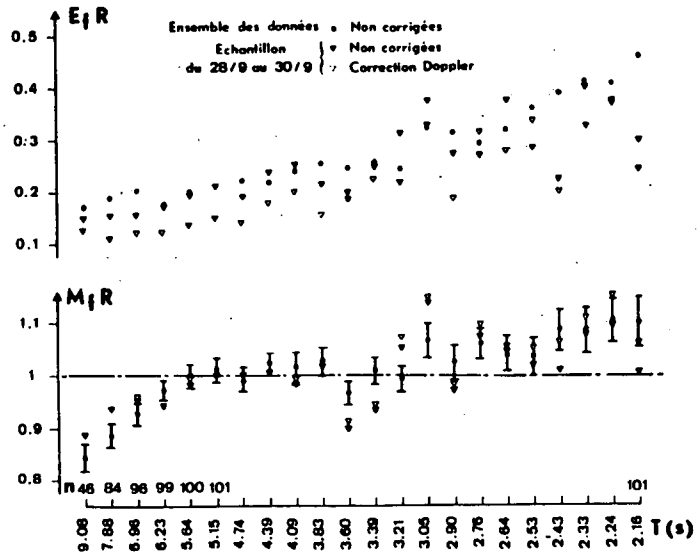

Figure 9
Moyennes (M) et écarts-types (E) du rapport (R) en fonction de la fréquence.
Mean (M) and standard deviation (E) of the ratio R as functions of frequency.

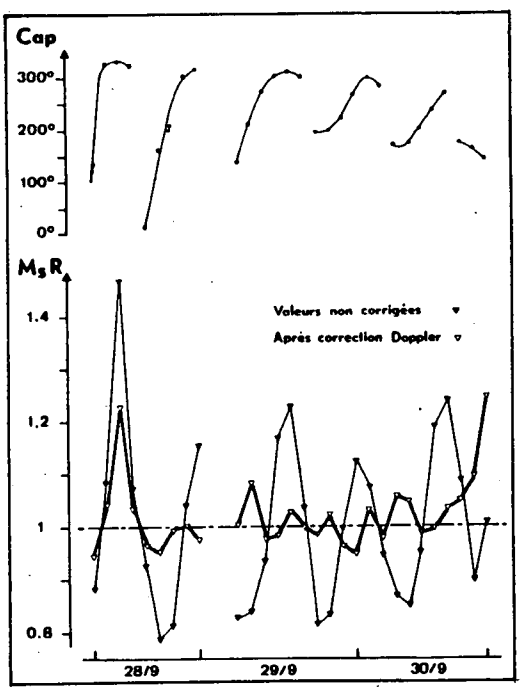

Figure 10
Chronologie des caps moyens et des moyennes par enregistrement du rapport R.
Means of buoy heading and ratio R as a function of time.

Figure 34. Doppler shift effects (from Ezraty and Cavanie (1981), Fig. 9 and 10).

LeBlanc and Middleton, 1982). It has also been used as the standard processing method by Long (1980) and Barstow and Krogstad (1983).

The linearity analysis was performed on both the WAVEC and WAVE-TRACK data collected during this study and during the deployment of similar buoys off the West coast. Figures 35 a, b, and c show the calculated and theoretical dispersion ratios for the three months of WAVEC data at Station 249. In these plots, the dashed lines are the theoretical ratio, solid lines the calculated ones, and the dots correspond to one standard deviation. The response is linear, requiring no amplitude or phase adjustments, for the entire frequency range of buoy operation. The drop at low frequencies reflects the fact that waves at these frequencies were beginning to feel bottom. The rise in R during March may be a reflection of the larger winds that were observed during this month. The upper plots on Figures 36 and 37 show the calculated dispersion ratio for the storm peaks on March 11 and March 27 to 29. Both before and after these periods, the calculated ratio approached one. There are various possible causes for this behaviour. A wind induced surface drift layer, in the same direction as the waves, or increased Stokes drift from wave steepening would Doppler shift the observed frequencies to higher values independent of any nonlinearities of the wave field proper. The lower plots on Figures 36 and 37 show the "corrected" ratio, taking into account a Doppler shift induced by a velocity of 20 cm/s in the direction of wave travel. It can be seen from these figures that part of the deviation in R can be explained purely on the basis of a frequency shift. This is an important point when using R to derive instrument transfer functions, as the change in R resulting from a Doppler shift is not a function of relative heave and slope energy but only a translation of the frame of reference. Correcting the co's and quad's through R would introduce errors. It is also important to note that equivalent Doppler shifts are present in "heave-only" buoy measurements but they cannot be resolved in this case. A Doppler shift in the data would have repercussions ranging from the calculation of spectral statistics to estimation of wavelengths from zero-crossing analysis. In a practical sense, correcting for Doppler shifts in a standard processing scheme would be quite difficult as it would be dependent on both current speed and direction relative to wave propagation, which in turn would be dependent on background circulation, wind speed, direction, fetch and duration. Any non-linearities which affect the relative contribution of heave and slope energies would

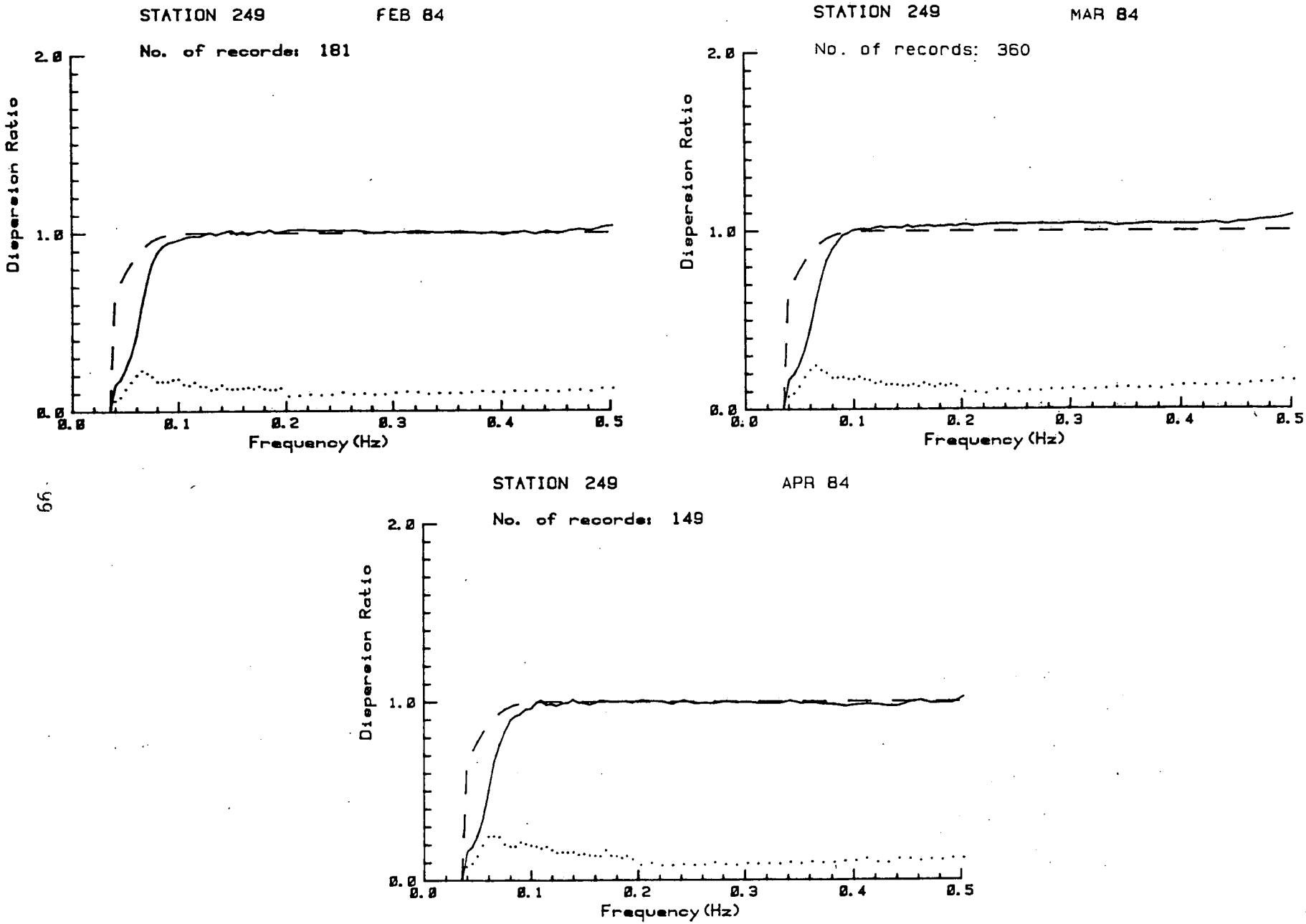

Figure 35. Average calculated dispersion ratio and standard deviation for February (a), March (b) and April (c) (Station 249).

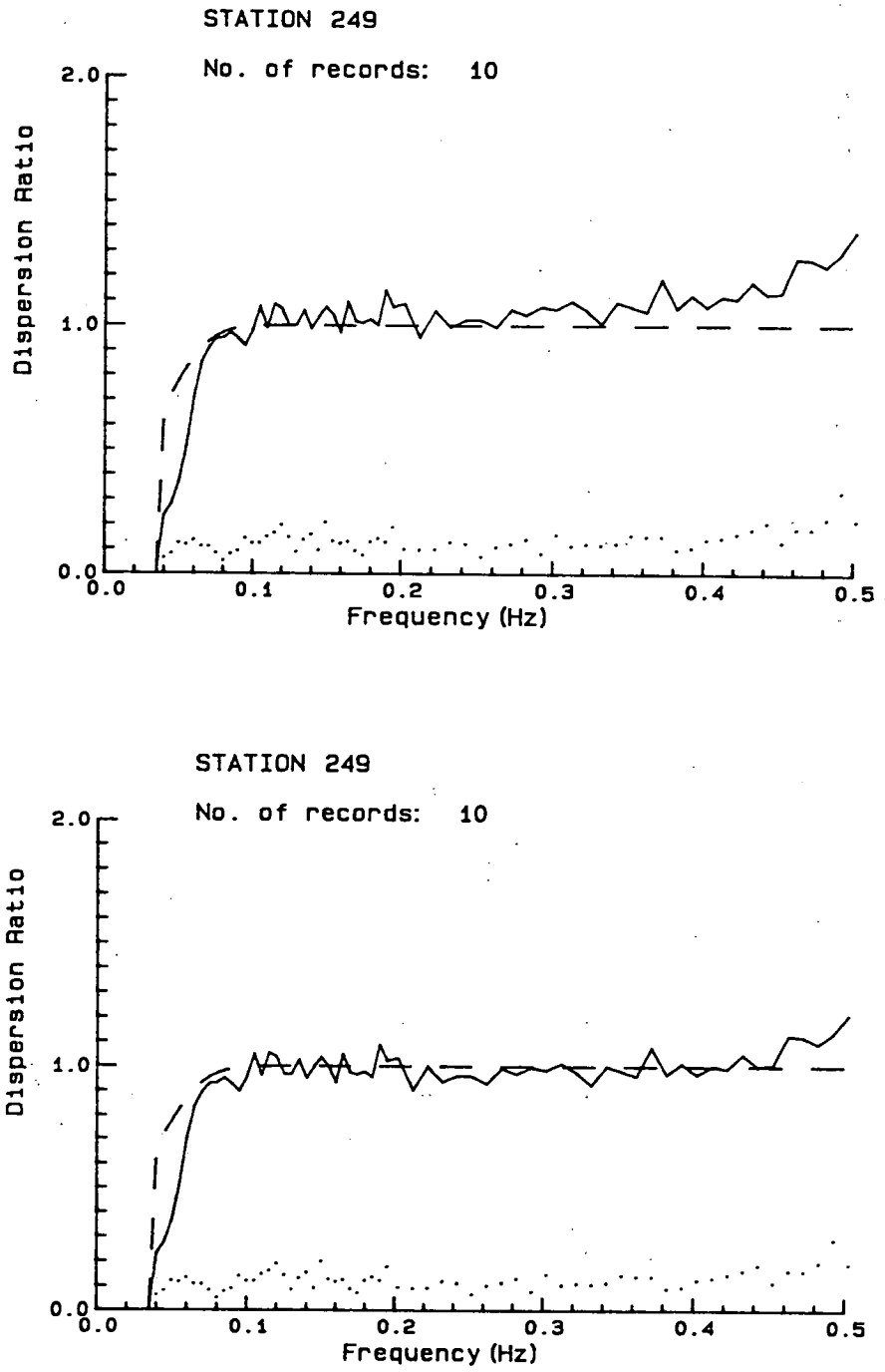

Figure 36. Average calculated dispersion ratio and standard deviation for March 11, 0300 GMT to 0935 GMT (upper) and corrected for a Doppler shift induced by a 20 cm/s current (lower).

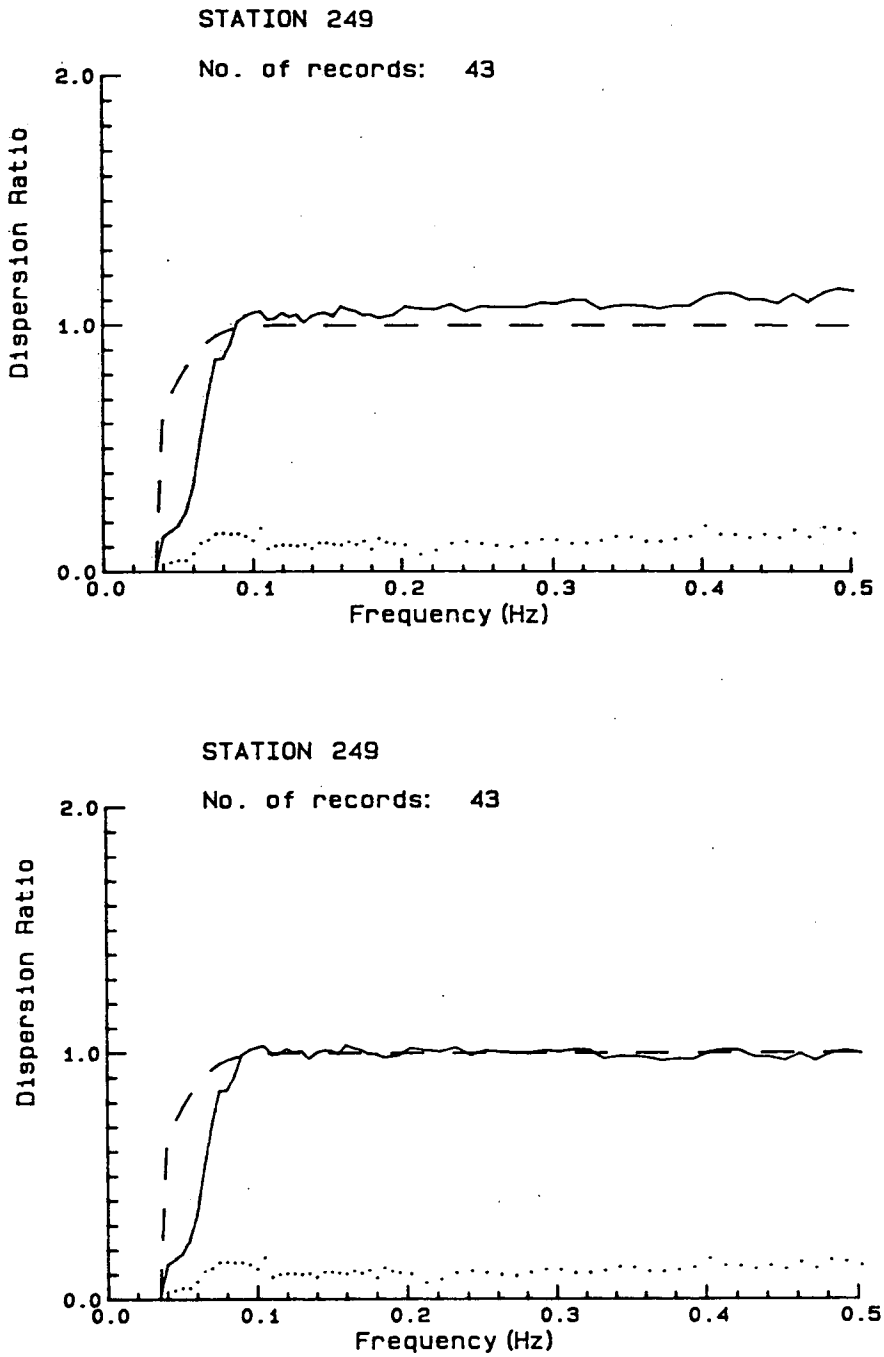

Figure 37. Average calculated dispersion ratio and standard deviation for 2100 March 27 to 0730 March 29 (upper) and corrected for a Doppler shift induced by a 20 cm/s current (lower).

also change R and be Doppler shifted correspondingly in frequency. Surface currents can also contribute to changes in the shape of the wave. Breaking waves during storms and forward face steepening during wind build-up would also be occurring. There are some indications of changes in wave shape in the data which will be discussed later. The nonlinearities are not necessarily isotropic and care must be taken when using R to correct for them. Figure 38 illustrates the results of this analysis on WAVEC data from the West Coast buoy after two of its flotation segments had become dislodged from their retaining straps. The problem shows up clearly in this plot. The buoy was sitting at an angle with an asymmetric mean slope as large as 0.7 seen in the data, although no obvious problems could be seen in the individual spectral plots.

Figure 39 shows the calculated and theoretical dispersion ratio for data from the Endeco WAVE-TRACK buoy not experiencing large mean tilts. The calculated ratio is low to 0.26 Hz after which it rises dramatically. The ratio at low frequencies is reduced more, if data showing large mean tilts are included. The rise at high frequencies could be a result of improper transfer functions supplied by the manufacturer or an inability of the instrument to resolve these high frequency motions. One of the original reasons for the buoy's shaft-like design was to dampen high frequency noise. It is interesting to note that the behaviour of the calculated dispersion ratio is very similar to that for the Norwegian buoy (Figure 32) which also has a subsurface shaft and damping weight to avoid overturning but which measures surface slope. The lower dispersion ratios do not necessarily imply an error in the calculated mean directions if the amplitude change is isotropic and if the proper phase corrections are applied, as any amplitude errors will cancel. During processing of the WAVE-TRACK data, the phases calculated from the cross-spectral analysis were compared with those expected and were corrected when necessary, as this proved to significantly reduce noise in the directional spectrum. However, even if the mean directions are correct, the estimates of directional spread and the directional spectrum itself will be in error unless Equation 7 is used to replace the wave number values in the calculation. The amplitudes at low frequency can be corrected using Equation 7 if the WAVE-TRACK buoy is not being affected by external influences. It is not clear whether or not the estimates at high frequencies can be corrected properly as the large standard deviations indicate serious problems.

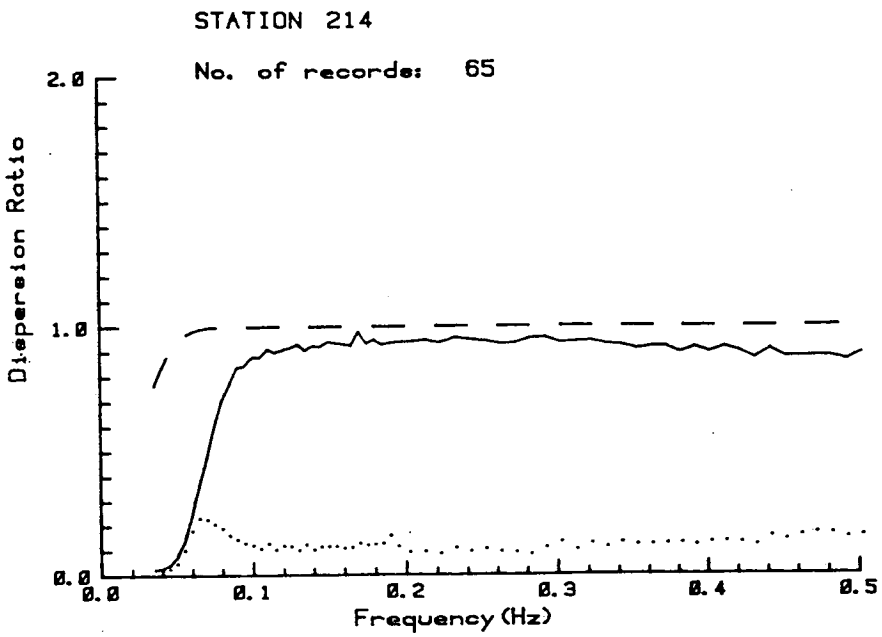

Figure 38. Average calculated dispersion ratio for the Westcoast WAVEC buoy after dislodgement of its flotation segments.

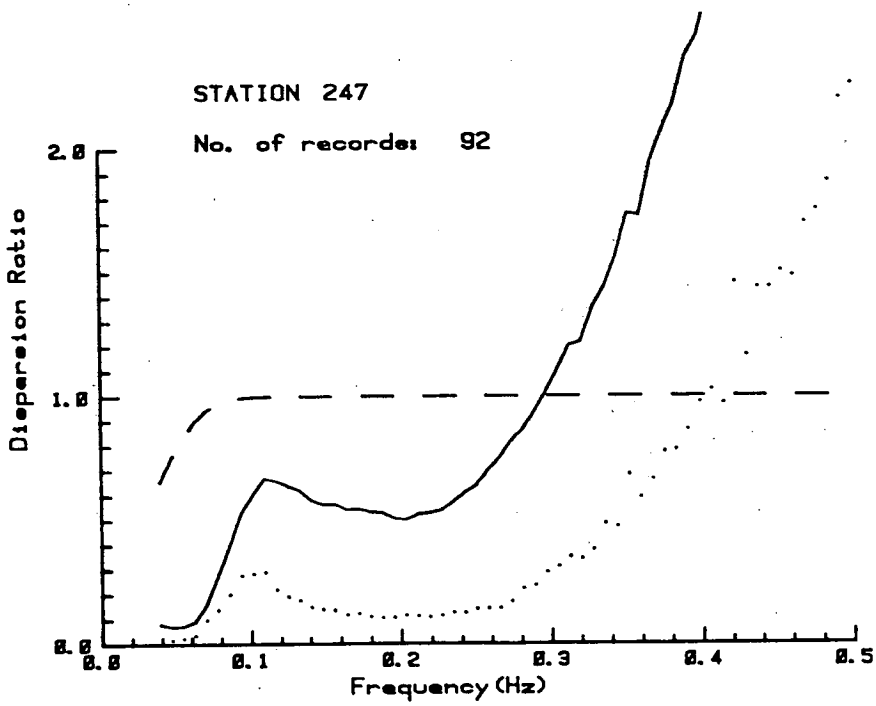

Figure 39. Average calculated dispersion ratio and standard deviation for February (Station 247) (records without large mean tilts).

COMPARISON OF RESULTS

Spectral Statistics

In this section, any confidence limits drawn are to the 95% confidence level.

WAVEC (Station 249) vs. WAVEC (Station 248). Data from the two WAVEC buoys were compared initially to estimate natural site variability and the resultant scatter in regressions. Figures 40 to 42 show regression plots of significant wave height, peak period and average apparent period, respectively. The agreement in all three cases is good with increased scatter observed in peak period. This large scatter for a single period estimate is generally the case and will increase at longer periods due to the poorer resolution. The expected error from a regression line of slope 1.0 would be on the order of 0.2 seconds at 5.0 seconds, 0.7 seconds at 10.0 seconds and 1.4 seconds at 16.0 seconds simply due to bandwidth, and this can explain most of the scatter. Other discrepancies arise from a choice between multiple peaks in a spectrum. The increased scatter at higher significant wave heights and at longer average apparent periods is again expected when considering the confidence limits calculated in the error analysis which are constant multipliers. The confidence limits on a single estimate for significant wave height would result in an error of ±.03 m at 1 meter and ±.14 m at 5 meters. Similarly, the error on an average apparent period estimate varies from 0.2 to 0.5 seconds. The outlying point in Figure 40 at 3 meters may be the result of a bad record, recorded in the middle of the period of reception problems at Station 248, which otherwise had passed all the quality control criteria.

Figures 43 to 45 contain regression plots of the three spectral shape parameters. The large scatter in the peakedness parameter, increasing with increasing value, is to be expected as it contains a spectral density squared term, which in itself, contains larger variability than each of the moments used in the calculation of the other parameters. However, this parameter is more stable than for example, spectral narrowness.

Figure 46 is a regression plot of the mean direction at the spectral peak for each instrument. The axes are extended to 450° to handle the 0° to 360° ambiguity. There is a fair amount of scatter some of which reflects that in the

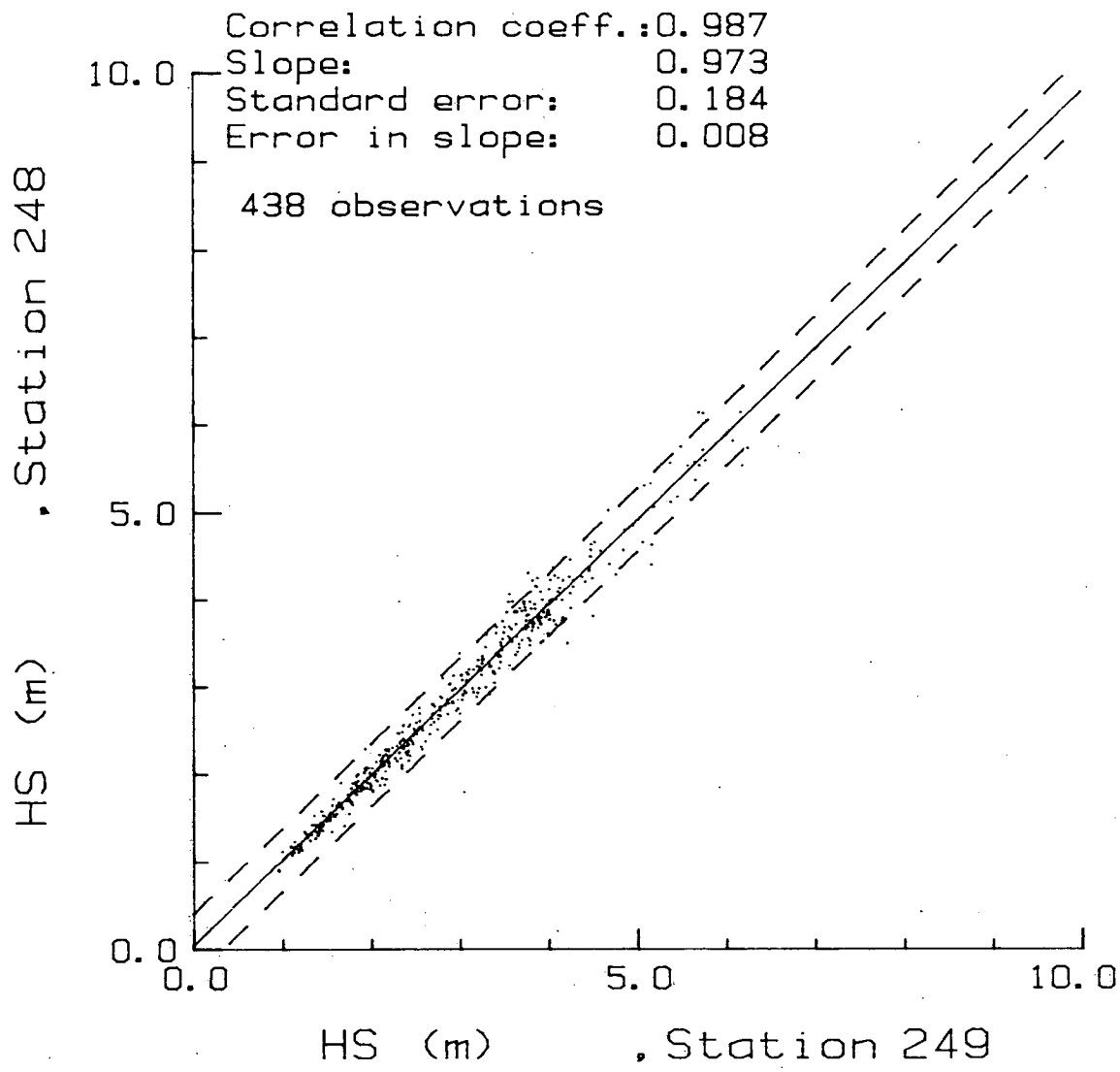

Figure 40. Regression plot of significant wave height (Station 248 vs. Station 249).

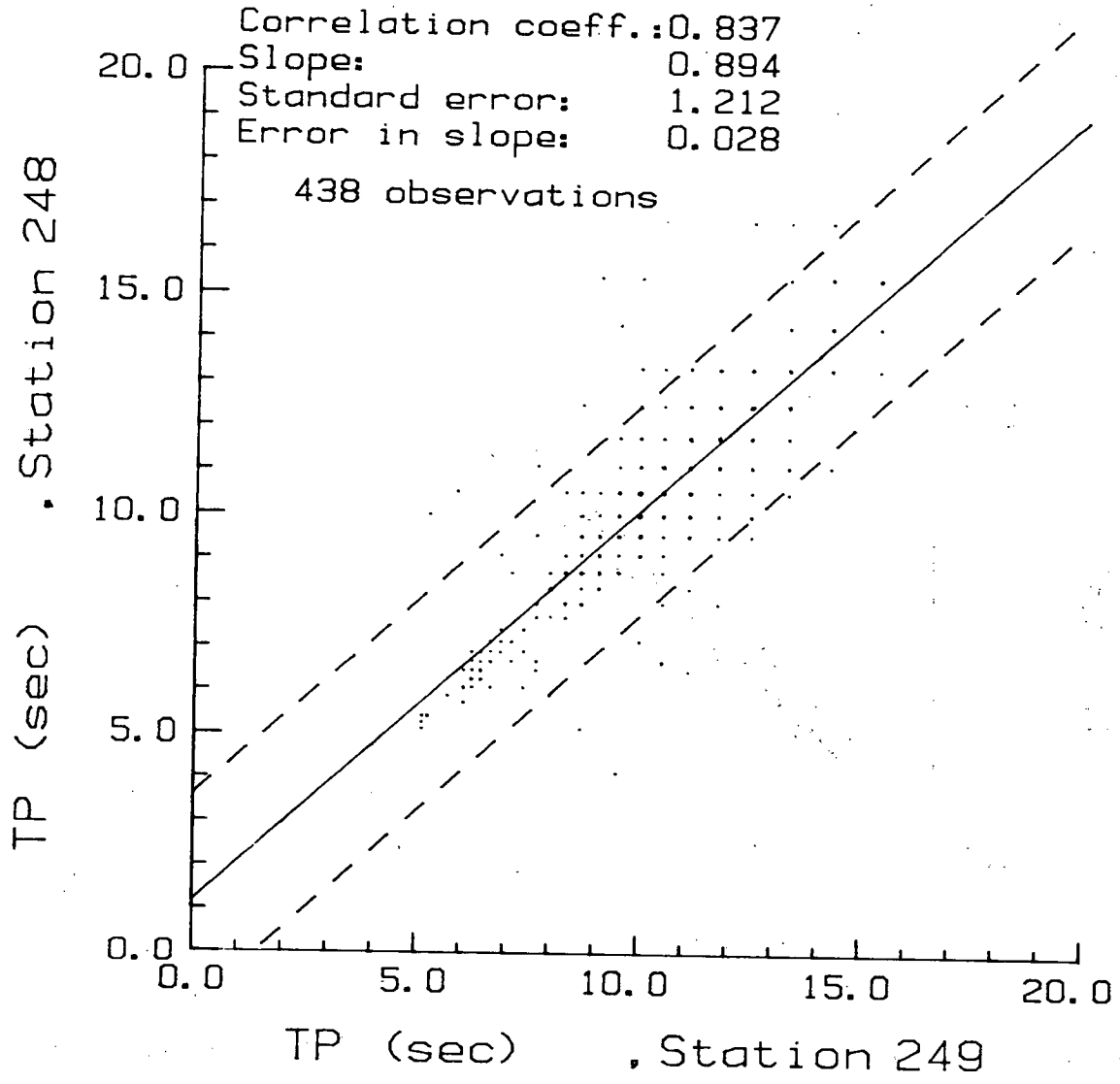

Figure 41. Regression plot of peak period (Station 248 vs. Station 249).

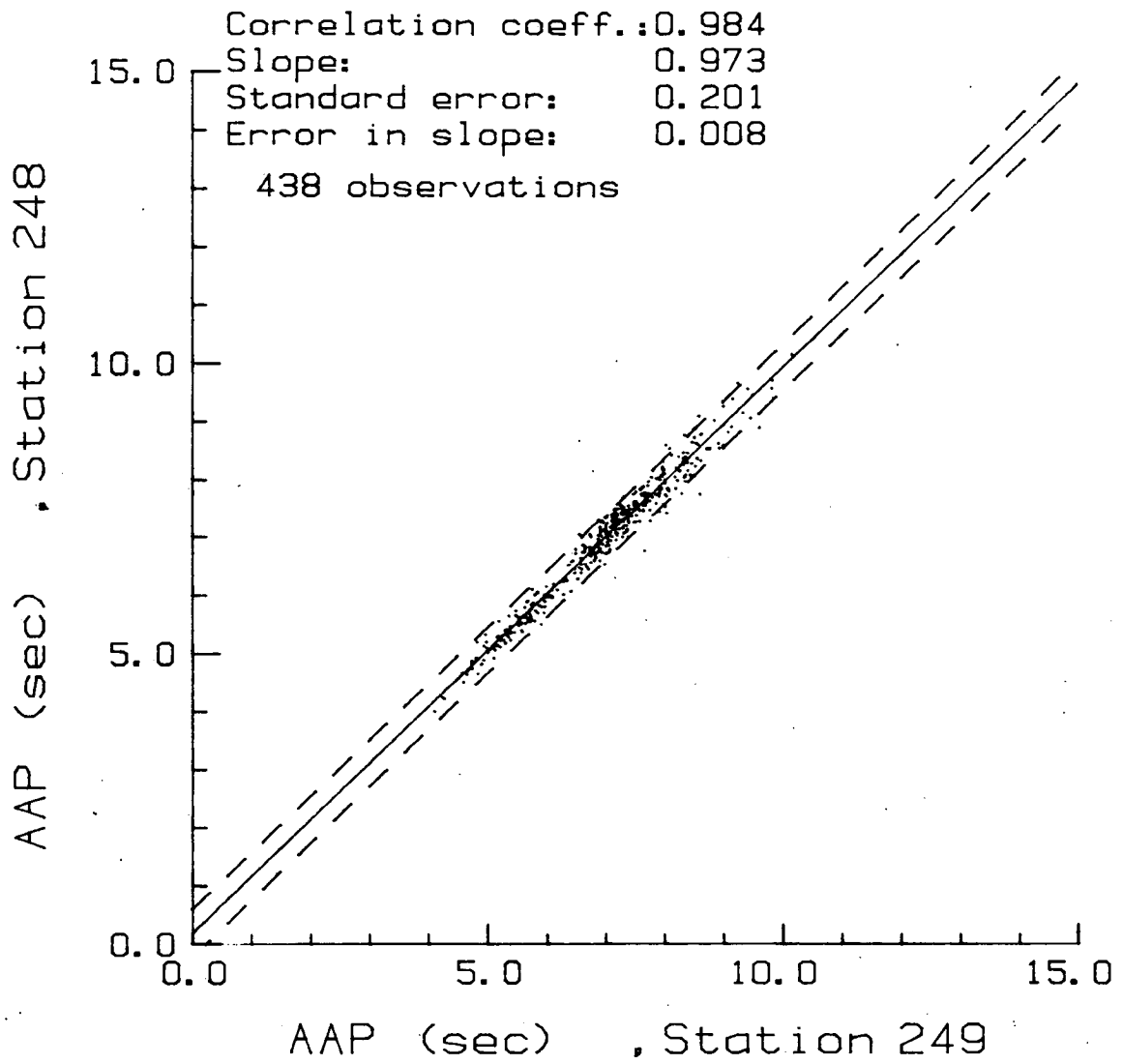

Figure 42. Regression plot of average apparent period (Station 248 vs. Station 249).

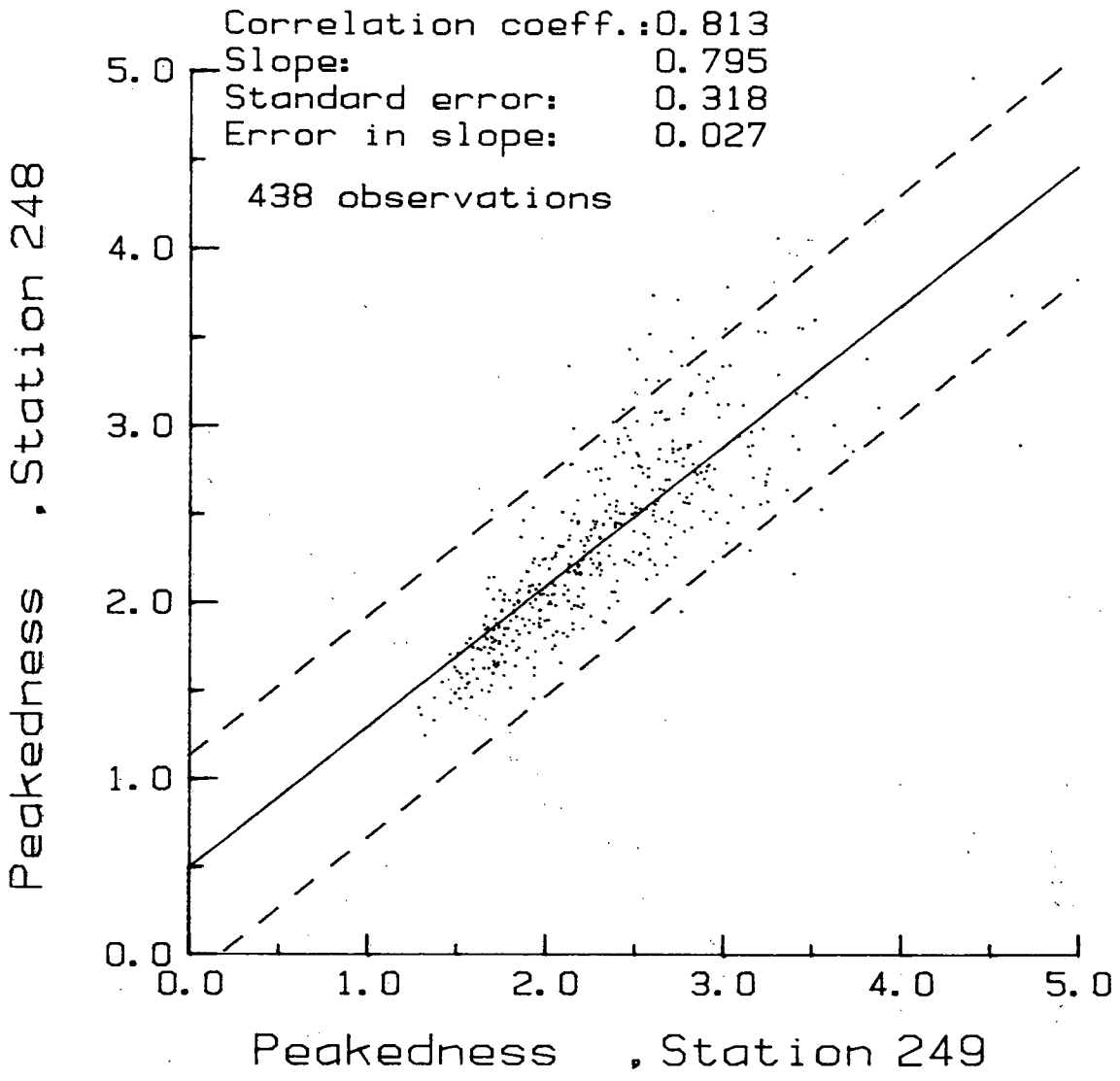

Figure 43. Regression plot of peakedness parameter (Station 248 vs. Station 249).

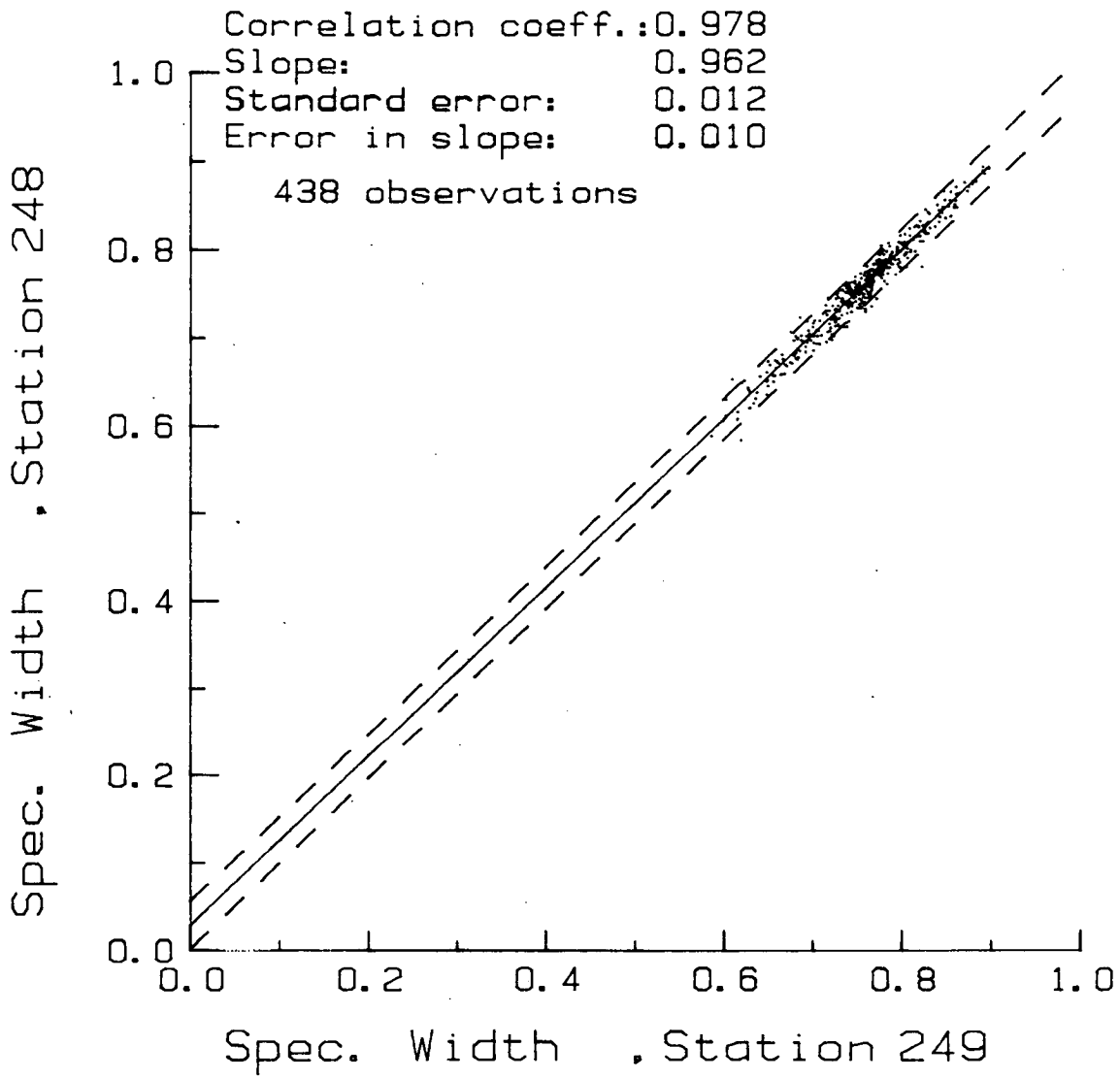

Figure 44. Regression plot of spectral width parameter (Station 248 vs. Station 249).

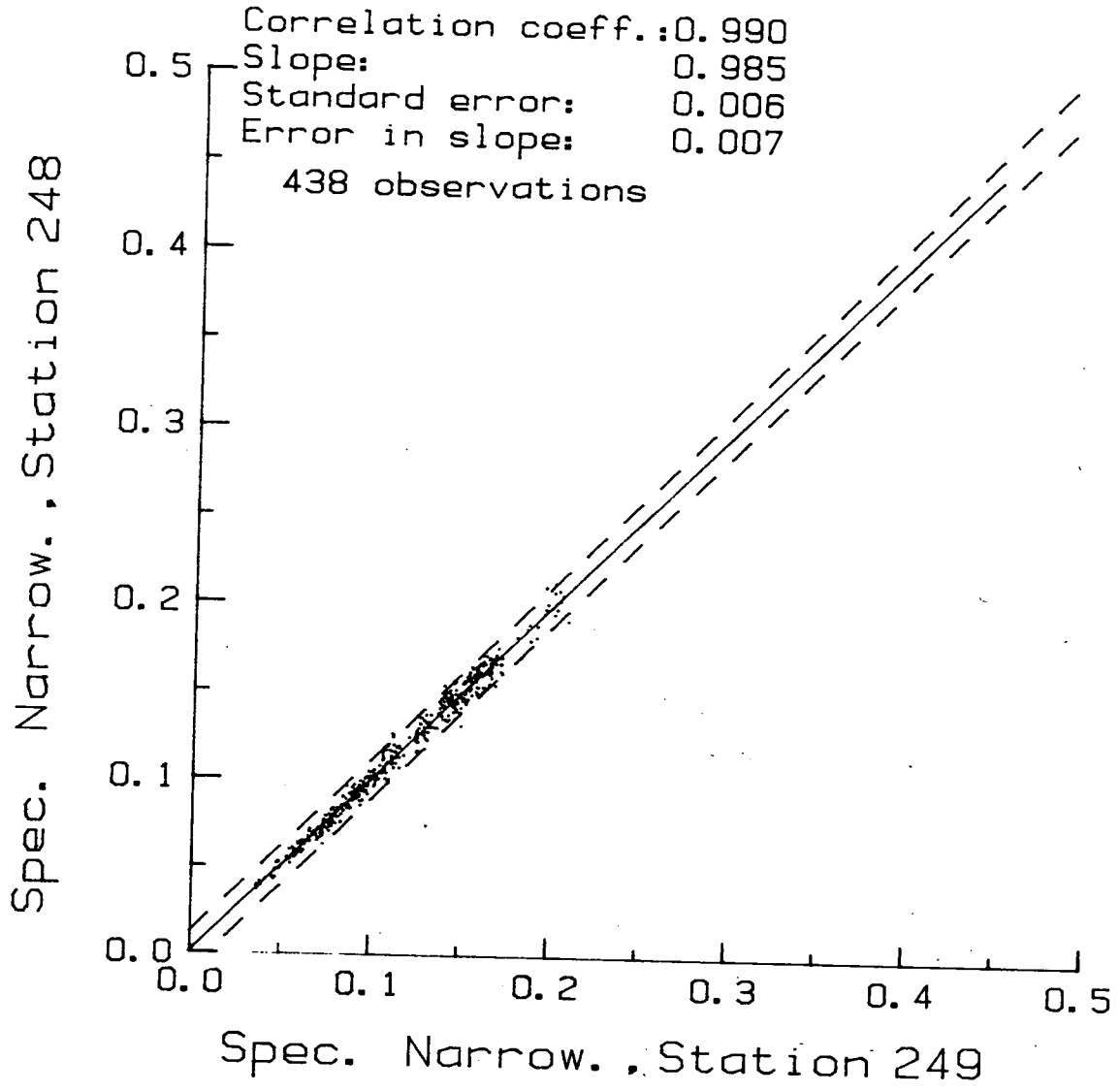

Figure 45. Regression plot of spectral narrowness parameter (Station 248 vs. Station 249).

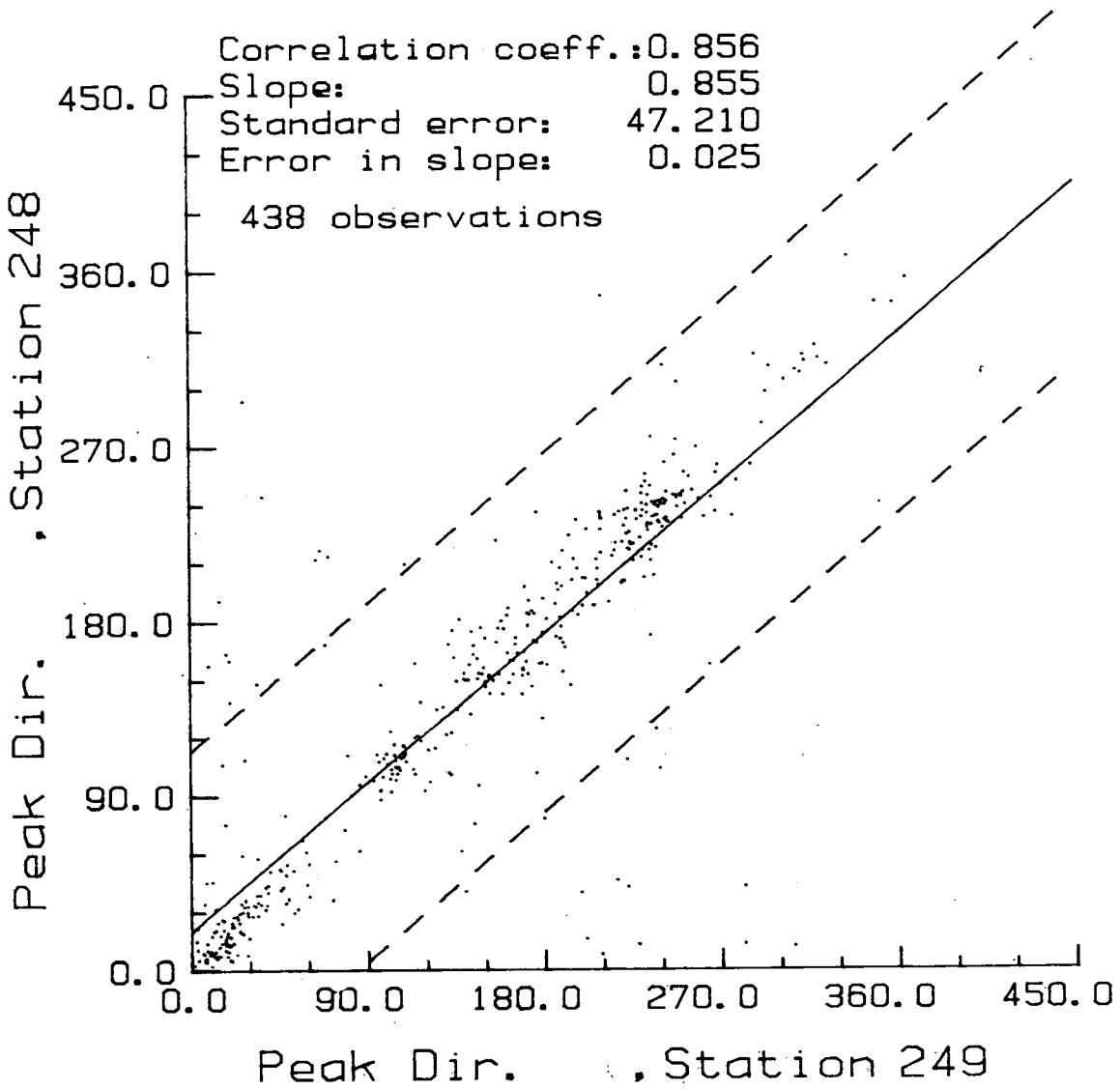

Figure 46. Regression plot of mean direction at spectral peak (Station 248 vs. Station 249).

peak periods. Variations would be expected in confused or turning seas. The standard error is biased high due to the few outlying points and generally appears to be less than 30°, from a line with slope 1.0 forced through zero, when comparing well-established regimes.

In order to obtain a directional estimate which contains some information on signal strength, a statistic was calculated which consists of a weighted average of the mean directions from each frequency. The weighting was performed using either the spectral energy density or one of the directional spread estimates. i.e.:

$$\frac{\sum_{i=a}^{b} \theta m_i * P_i \ \Delta f_i}{\sum_{i=a}^{b} P_i \ \Delta f_i} \quad \text{OR} \quad \frac{\sum_{i=a}^{b} \theta m_i * SPRD_i \Delta f_i}{\sum_{i=a}^{b} SPRD_i \Delta f_i}$$

frequency range a to b

Weighting by spectral density is a common procedure to reflect the relative importance of a frequency band and was also used by Longuet-Higgins to obtain a "Principal Direction" (see Section on Groupiness). Weighting by a directional spread estimate, in itself a function of spectral density, allows for greater contributions to the average by a narrow beamed wave field. Figures 47, 48 and 49 show the results when regressing this weighted statistic. In all cases, the scatter is reduced with the standard error less than 20°. Weighting by the cosine spread (Figure 49) provided the best error reduction. Sample time series of peak direction and average direction for March (Station 249) are given in Figure 50. The reduction in scatter is obvious but what is also of interest is that the turning of the wave field direction can now be seen in the average statistic. Note that the direction of the turning (clockwise or counterclockwise) can be different between the two weighted directions (examples: March 14-15 and 26-27). This possibly reflects the dominating influence of the low frequency spectral peak in the direction weighted by energy. The average direction weighted by energy has an implicit low to high frequency spectral development while that weighted by the cosine spread indicates a turning from high to low frequency. These statistics

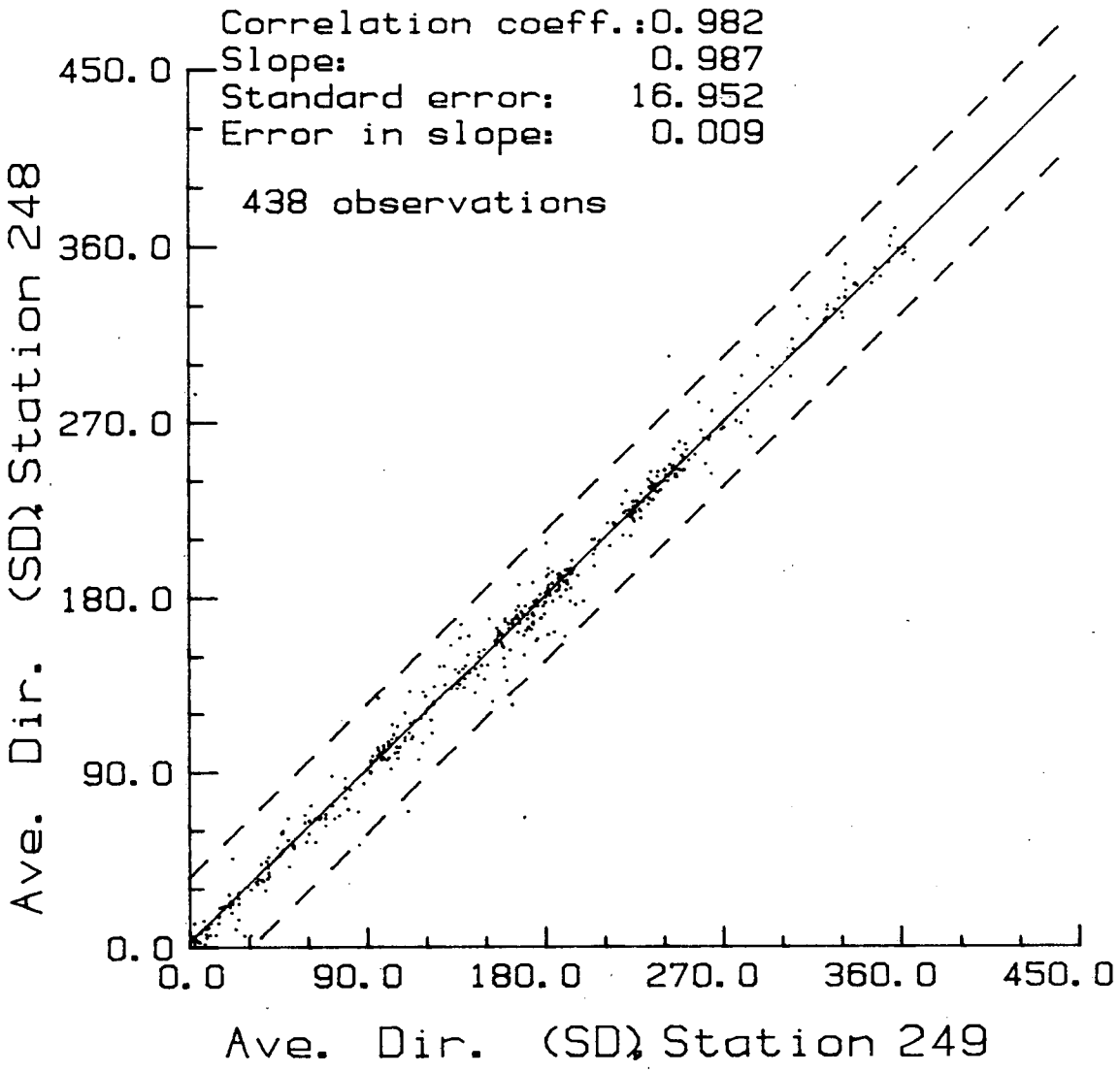

Figure 47. Regression plot of average direction weighted by spectral density (Station 248 vs. Station 249).

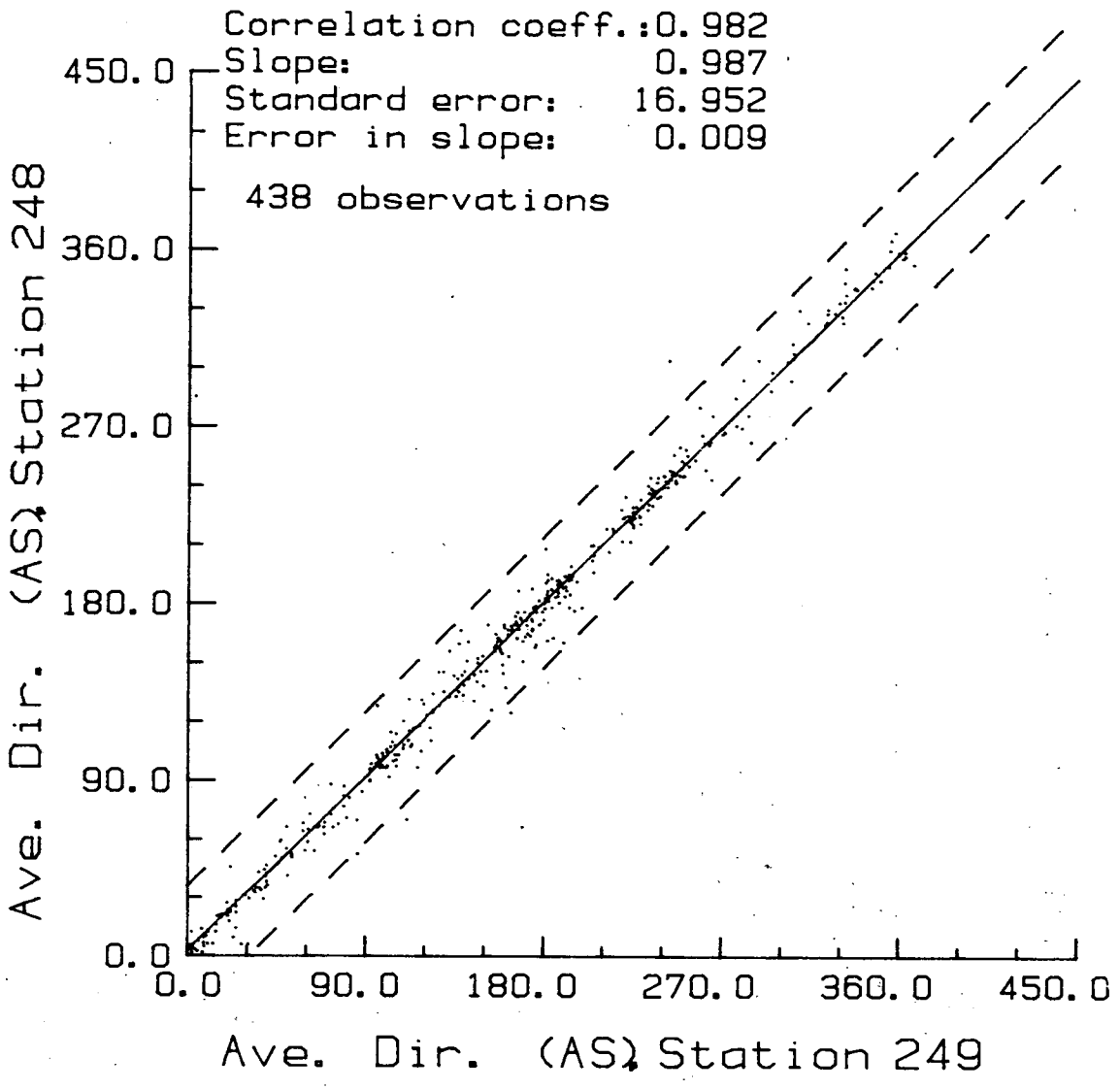

Figure 48. Regression plot of average direction weighted by angular spread (Station 248 vs. Station 249).

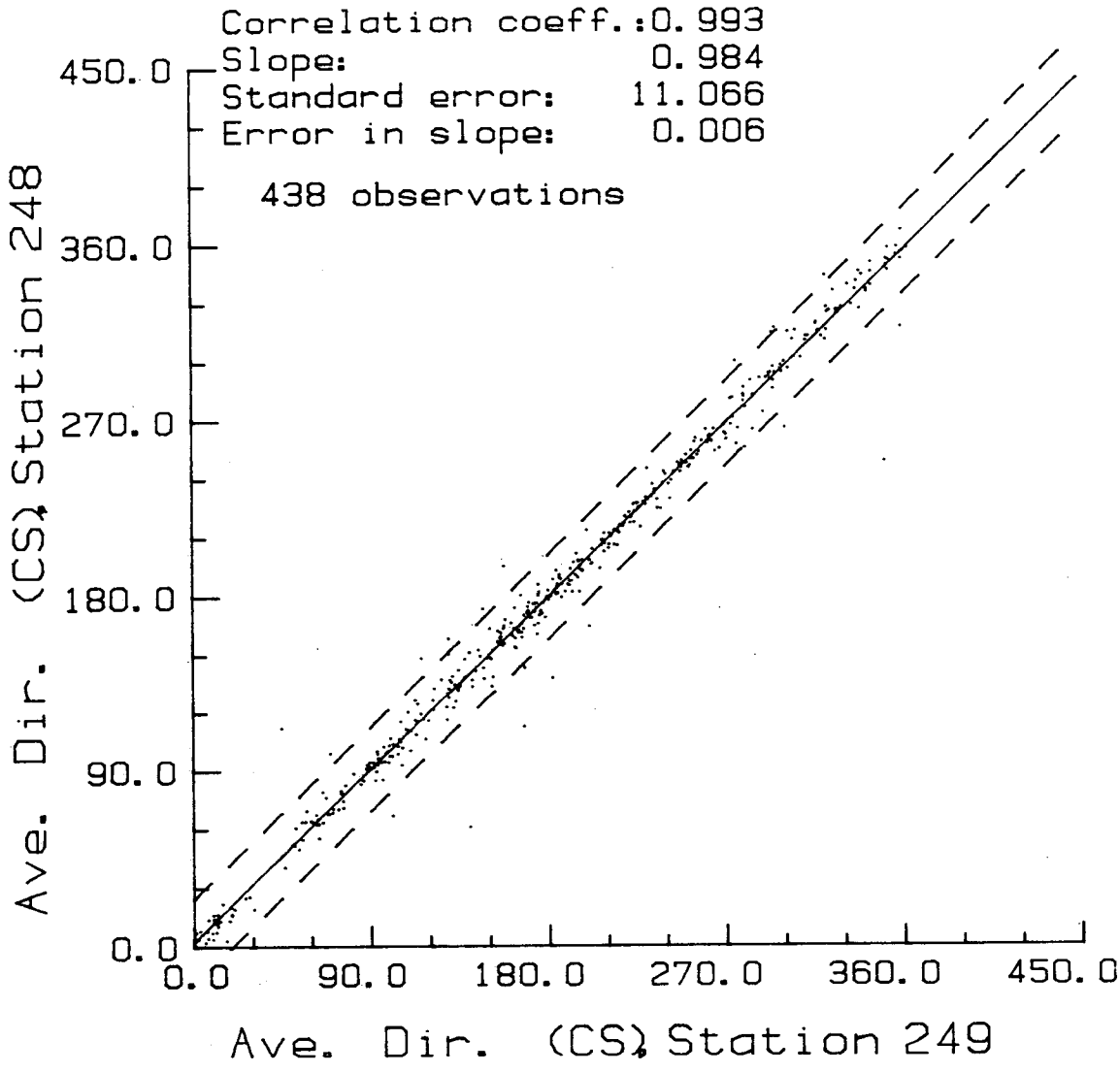

Figure 49. Regression plot of average direction weighted by cosine spread (Station 248 vs. Station 249).

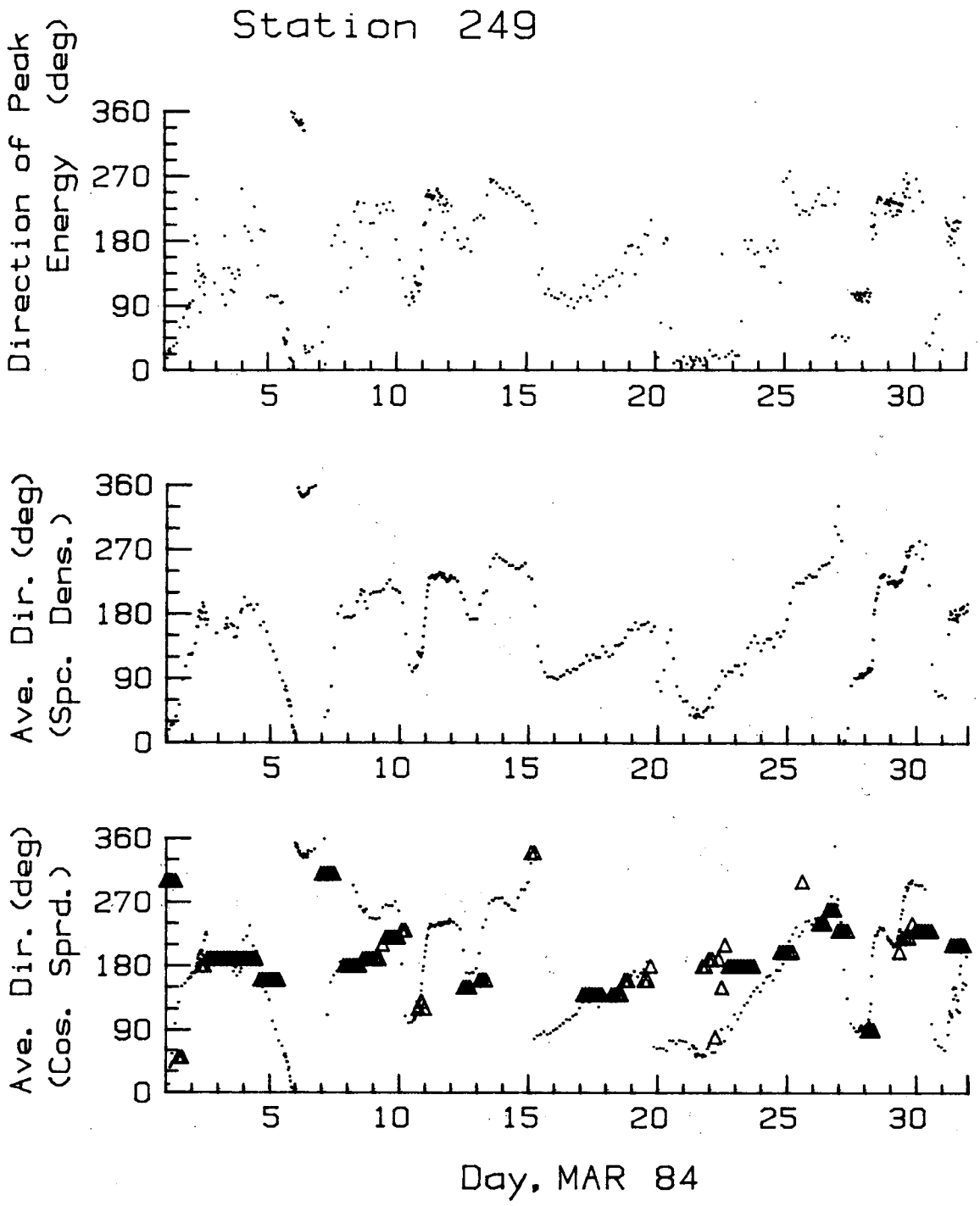

Figure 50. Time series of peak direction, average direction weighted by spectral density and cosine spread (March, Station 249).

appear to be a better indicator of the directional behaviour of the average sea state than the peak direction.

WAVEC vs. MANMAR Data. As an independent check on the WAVEC calculated directions, these were compared with MANMAR observed wind and primary swell directions. The latter agree well with both the peak and average direction (e.g: the MANMAR swell directions are superimposed on Figure 50 as triangles) for swell dominated spectra. However, as visual swell estimates are quite subjective, a comparison with wind directions would be preferred if one could take into account influences of fetch, duration and water depth. As such, a better agreement between winds and waves would be expected for high frequency waves. A weighted average "sea" direction was calculated from the spectral mean directions for periods less than 7.0 seconds. These, as well as the overall spectral average direction, are super-imposed on the wind direction plots given in Figures 51 to 53. These wind values have not been corrected for anemometer height. The wave directions do follow wind directions though with a variable time lag reflecting sea response times. Instances when the overall average direction and wind direction disagree sharply (for example, March 1, 15-20, 31) are also instances of large average apparent wave period and visually observed swells indicating swell dominated spectra. There was very good agreement between all three measurements during the buildup of the two storms in March.

As the WAVEC calculated directions were consistent with those expected from the wind data and the data quality was good both in terms of data return and linearity, they were used as the basis for direction comparison against the Endeco WAVE-TRACK results as well as model and SAR estimates.

WAVEC vs. WAVERIDER. Similar regression comparisons between the heave spectral statistics of the Waverider at Station 169 and the WAVEC at Station 249 were performed. The results are shown in Figures 54 to 59. The agreement between the two buoys is very good considering the larger confidence limits on each Waverider estimate, the poorer frequency resolution, the greater distance separating the two buoys and the fewer estimates compared with the inter-WAVEC plots. As there were no large storms during the operational period of the Waverider, data from the satellite transmitting WRIPS buoy were used for comparison. This buoy was located out of the immediate study area and environmental differences may have been important. Figures 60 to 62 illustrate

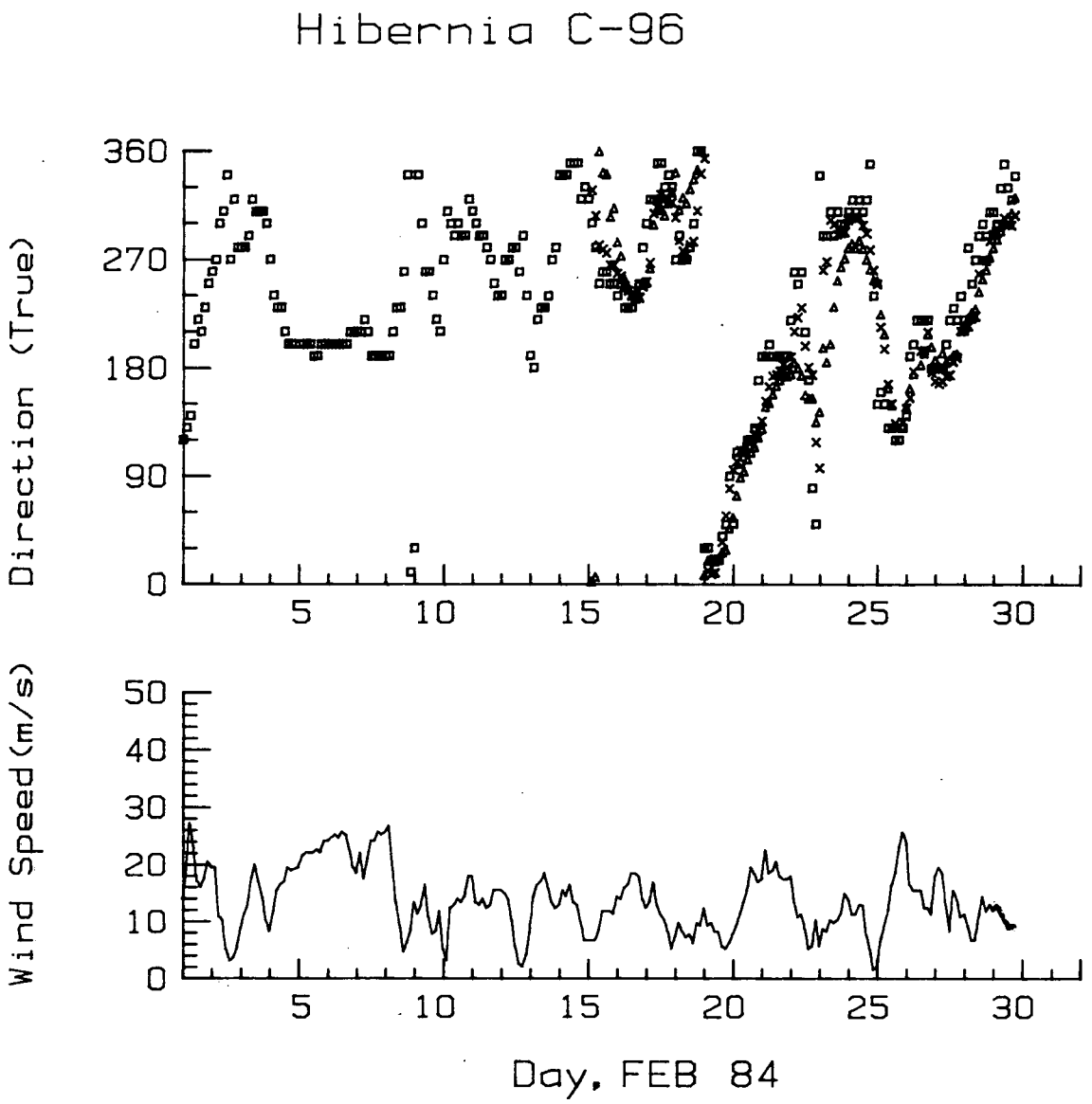

Figure 51. Time series of wind speed and direction with superimposed wave direction (February) (squares: wind, triangles: apparent direction, crosses: apparent direction for periods less than 7 s).

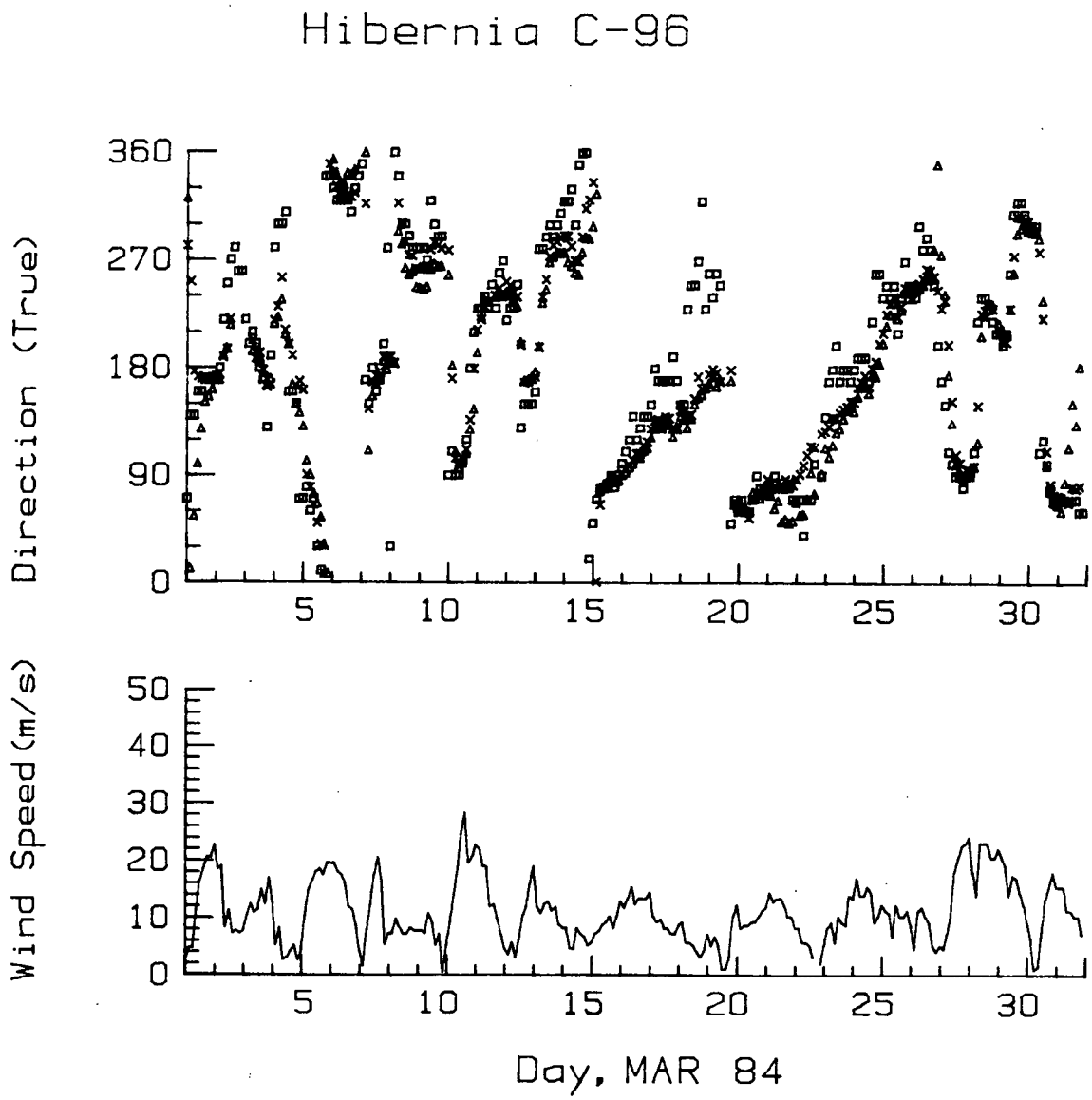

Figure 52. Time series of wind speed and direction with superimposed wave direction (March) (squares: wind, triangles: apparent direction, crosses: apparent direction for periods less than 7 s).

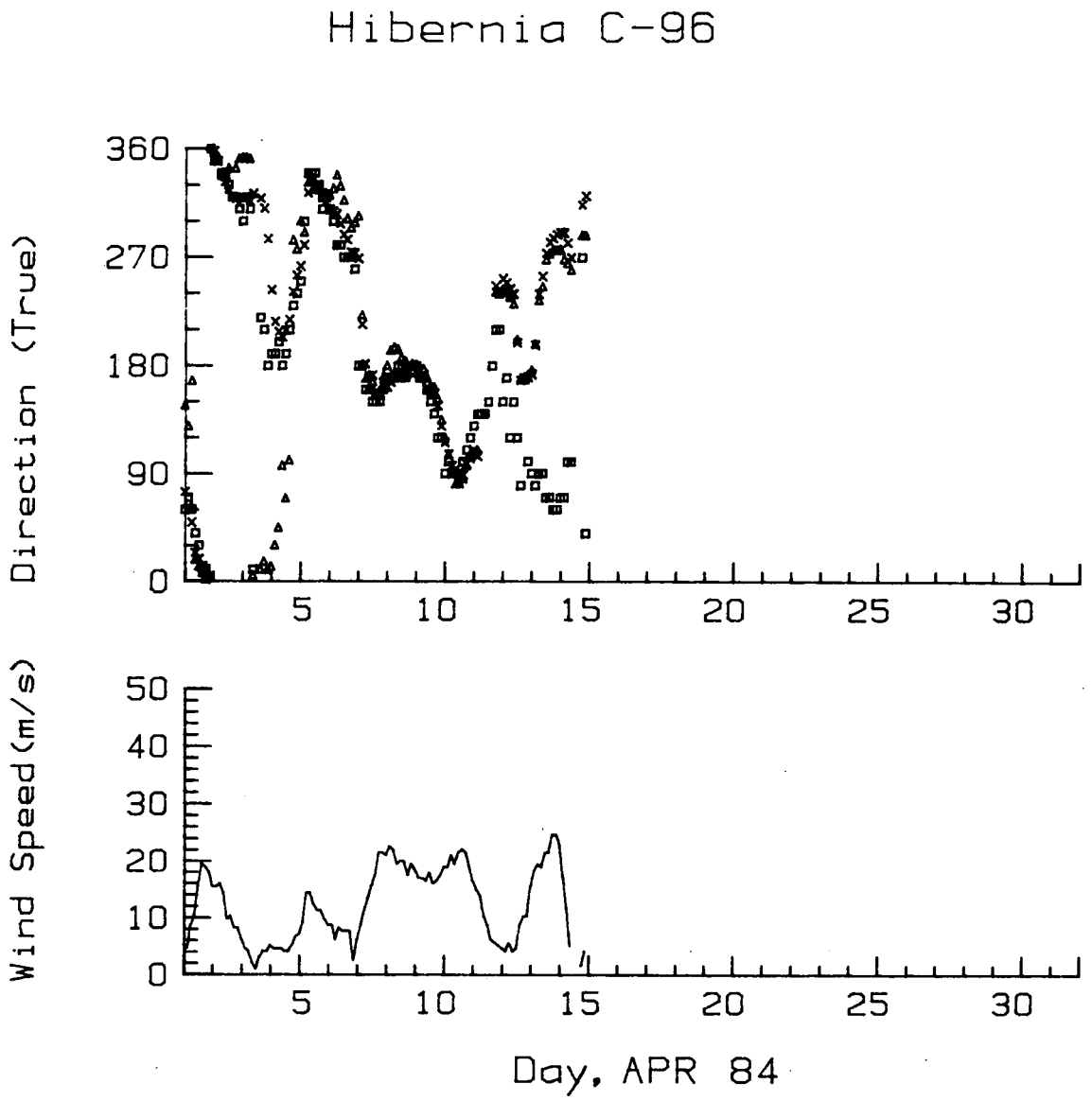

Figure 53. Time series of wind speed and direction with superimposed wave direction (April) (squares: wind, triangles: apparent direction, crosses: apparent direction for periods less than 7 s).

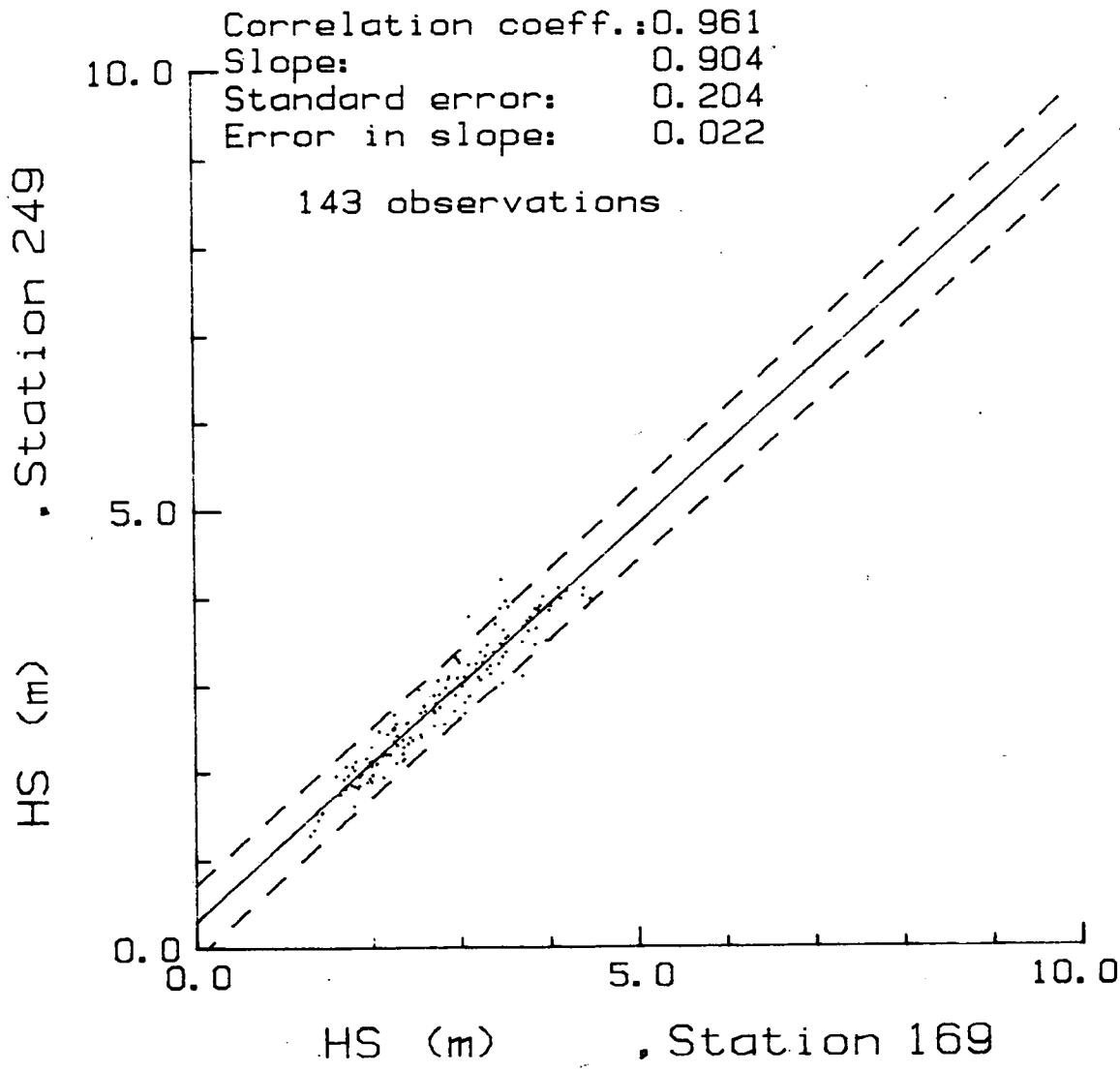

Figure 54. Regression plot of significant wave height (Station 249 vs. Station 169).

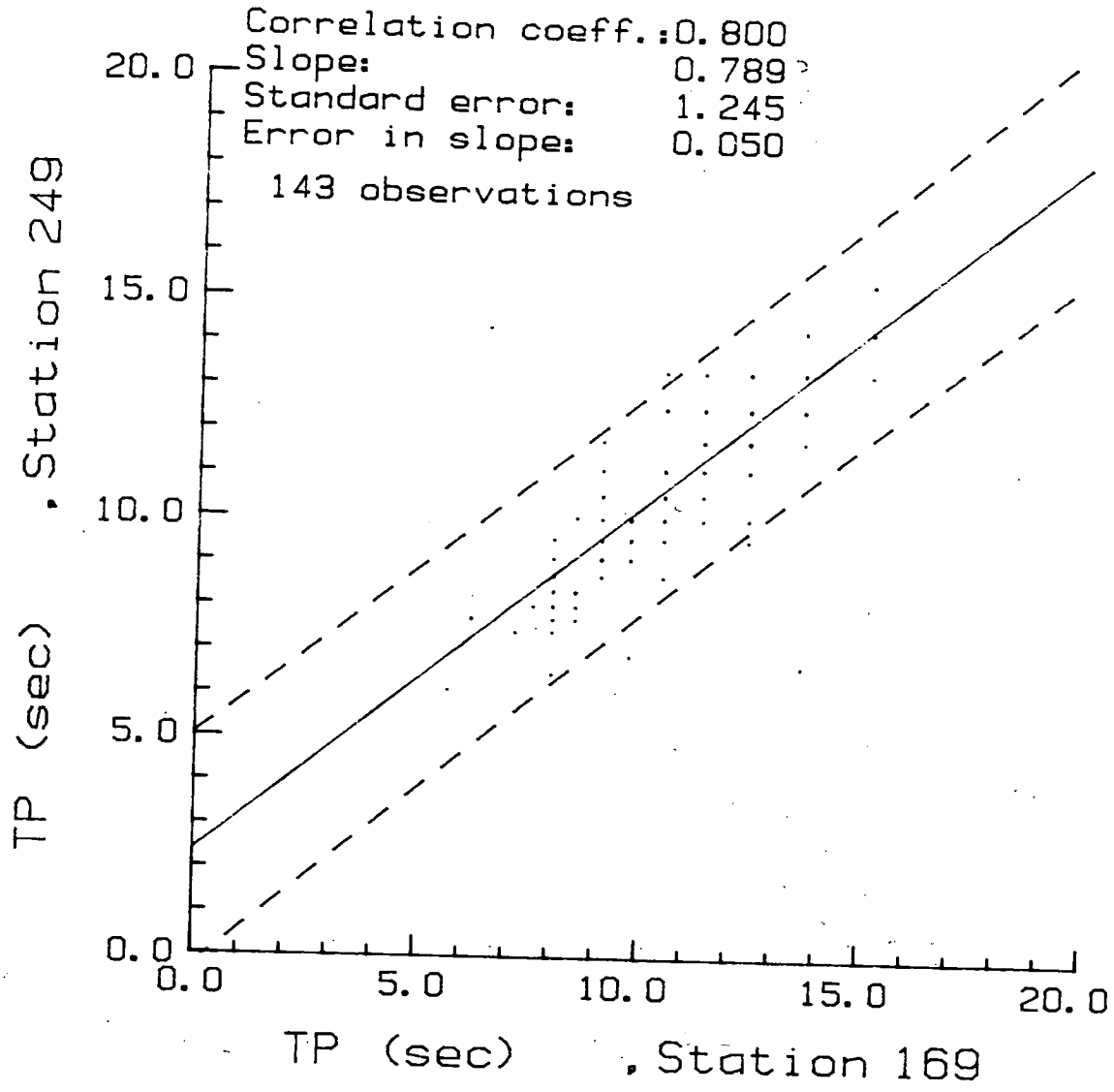

Figure 55. Regression plot of peak period (Station 249 vs. Station 169).

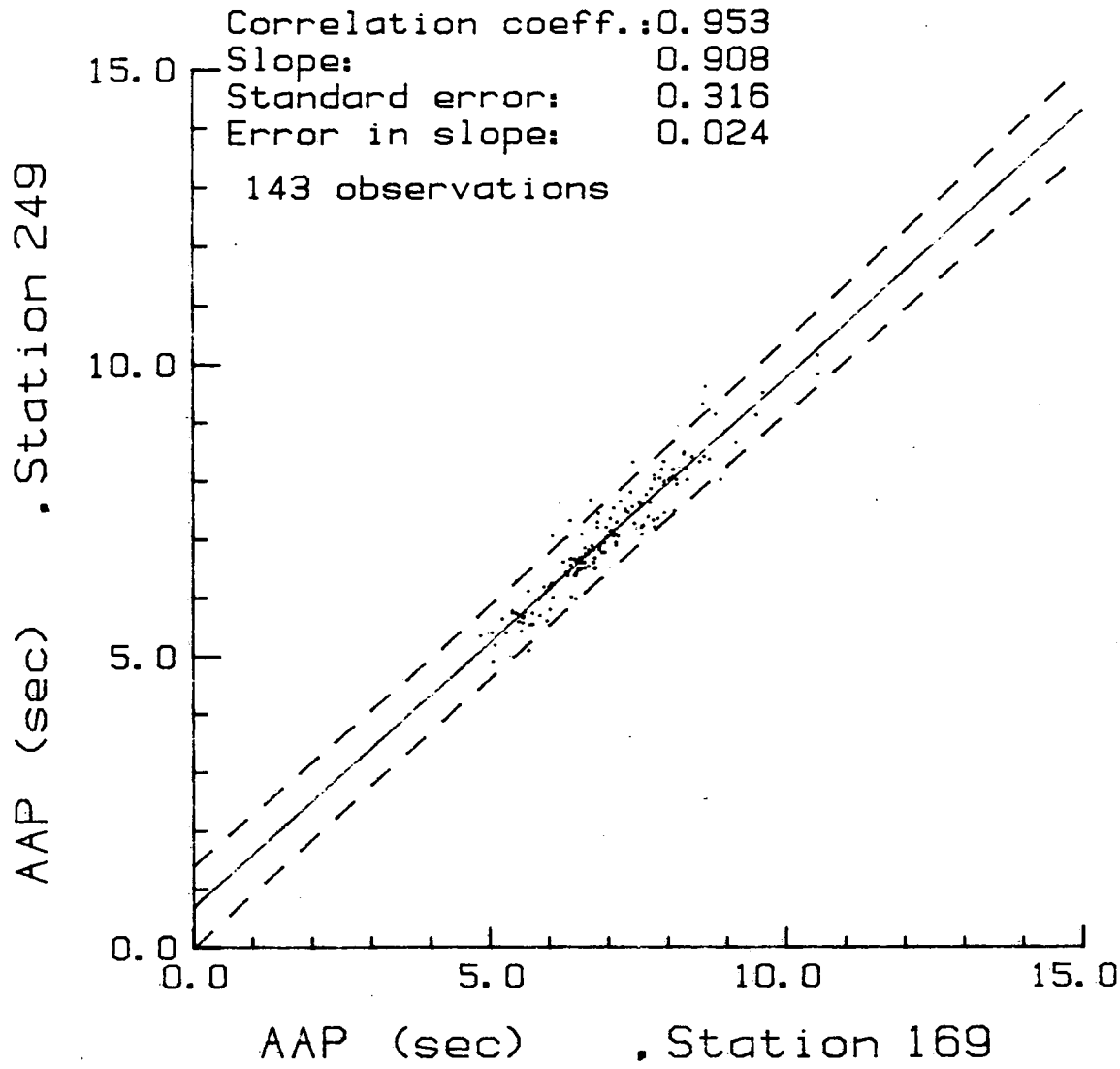

Figure 56. Regression plot of average apparent period (Station 249 vs. Station 169).

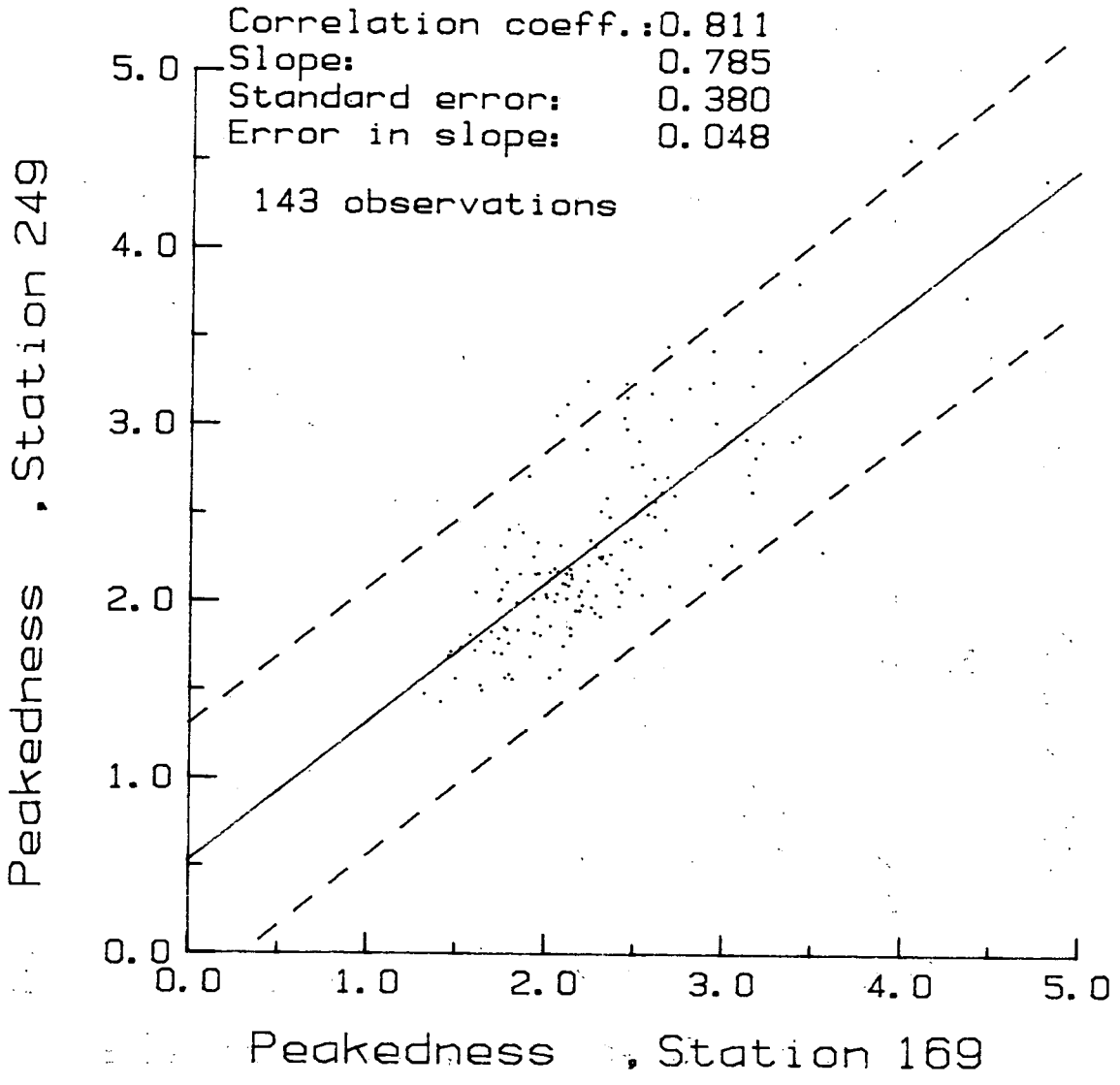

Figure 57. Regression plot of peakedness parameter (Station 249 vs. Station 169).

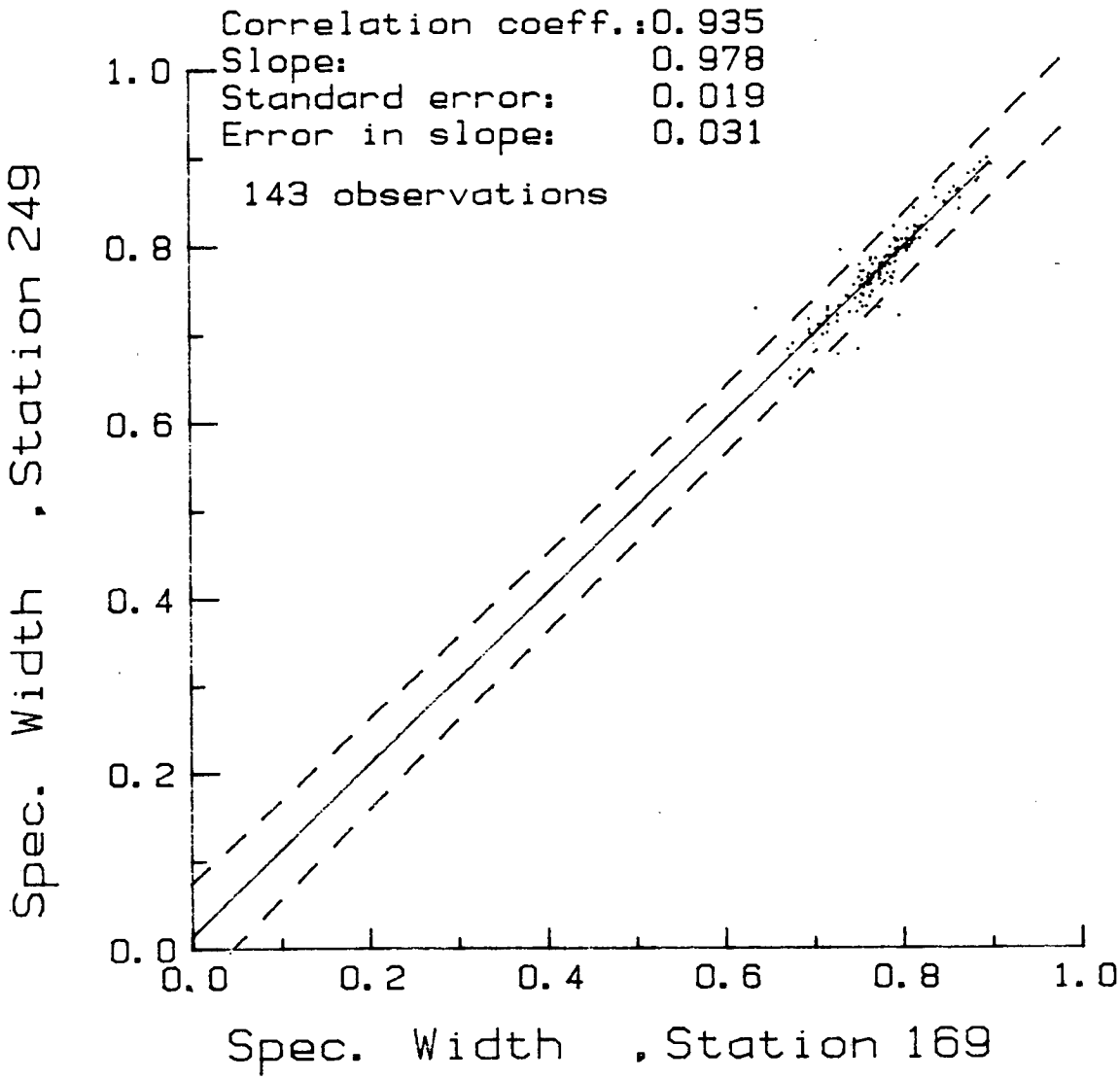

Figure 58. Regression plot of spectral width parameter (Station 249 vs. Station 169).

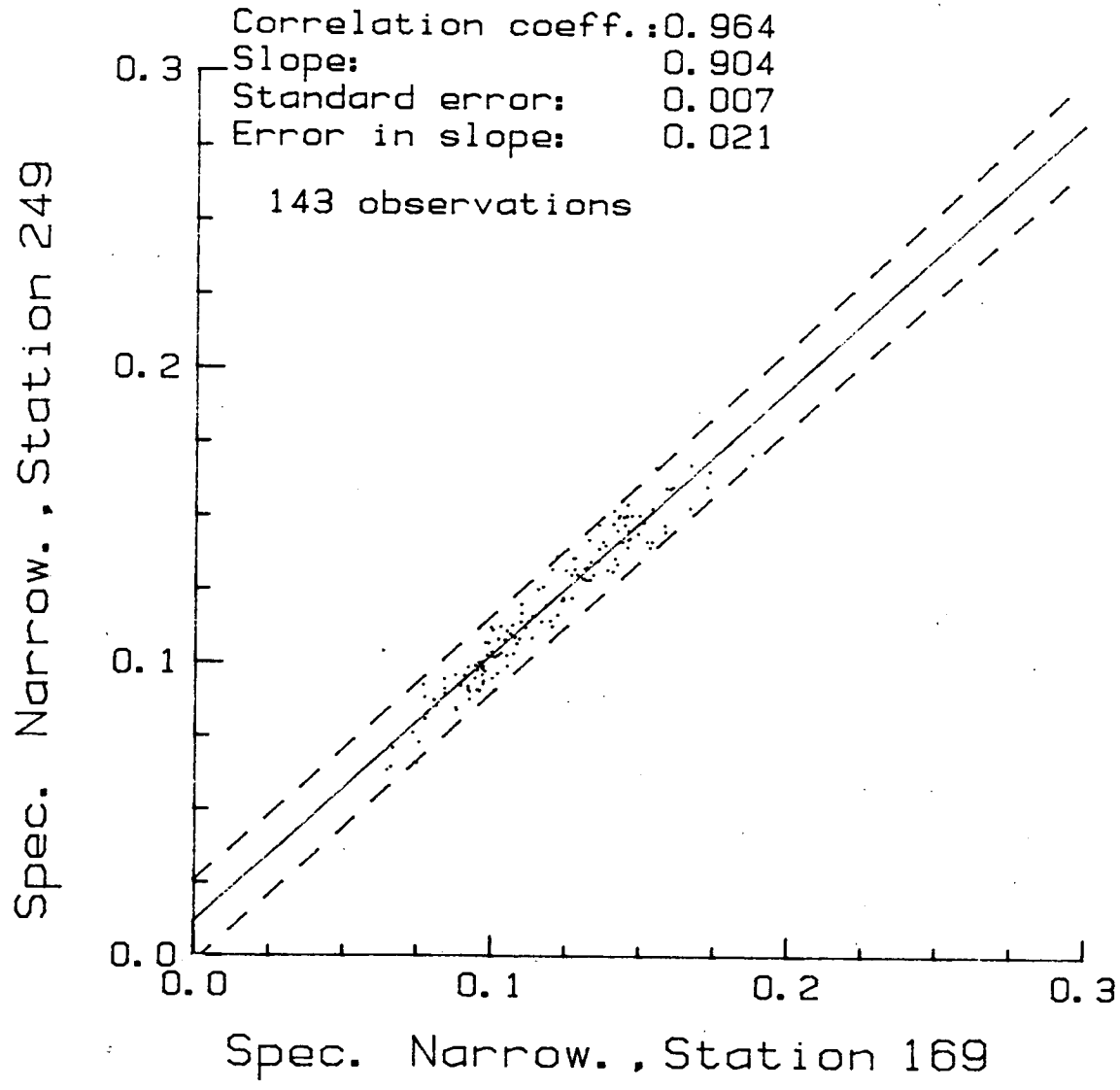

Figure 59. Regression plot of spectral narrowness parameter (Station 249 vs. Station 169).

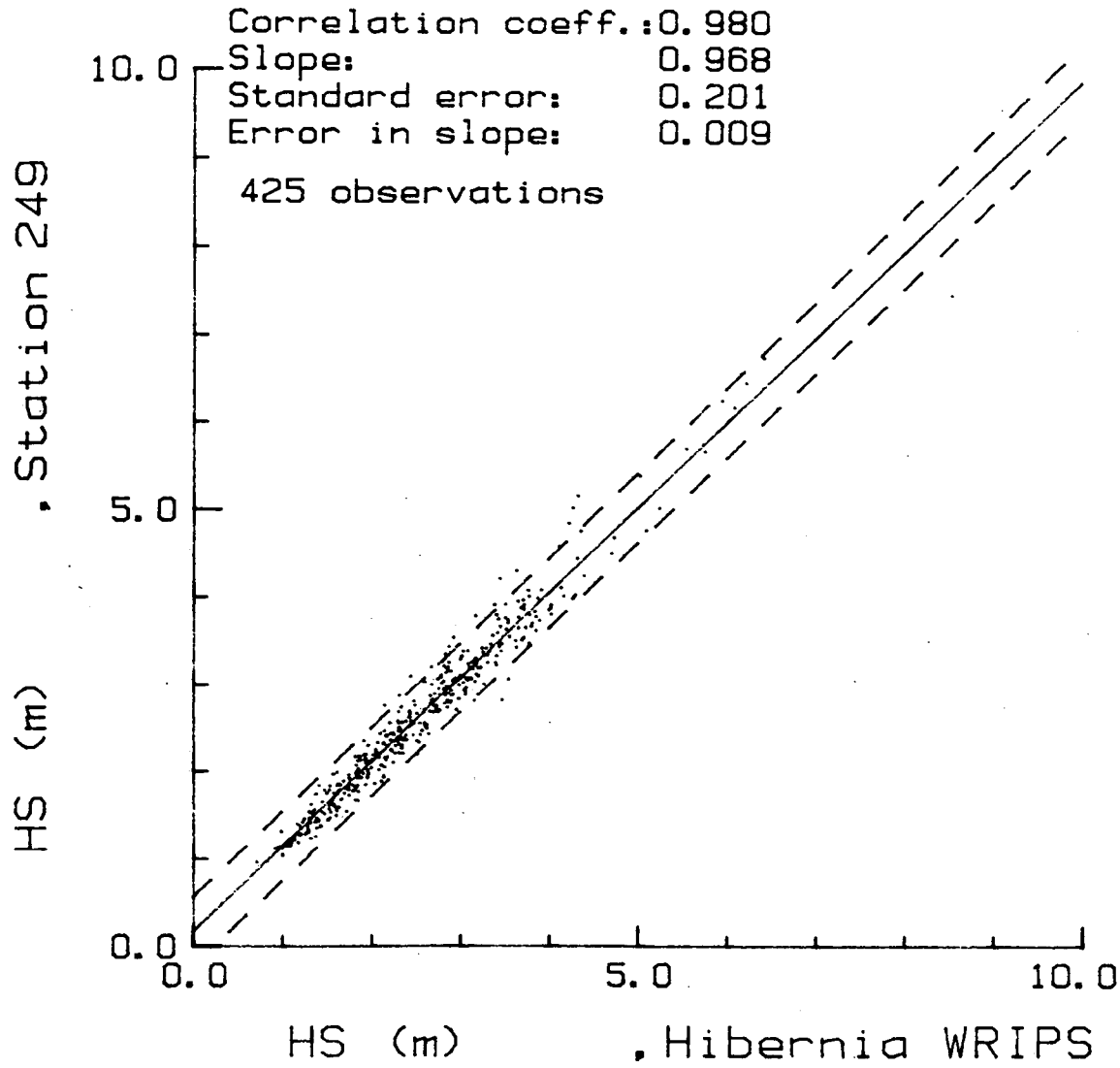

Figure 60. Regression plot of significant wave height (Station 249 vs. WRIPS Buoy).

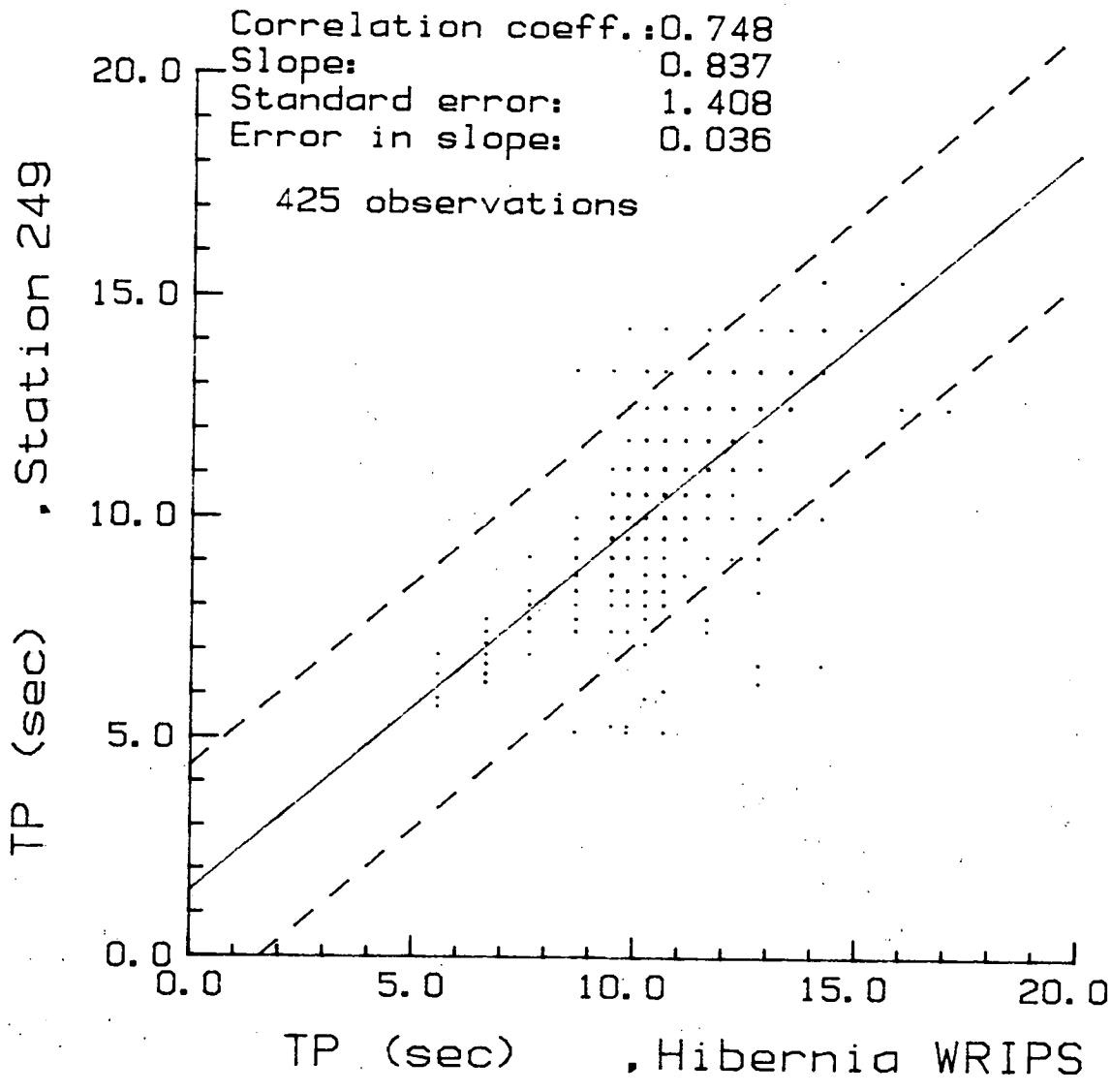

Figure 61. Regression plot of peak period (Station 249 vs. WRIPS buoy).

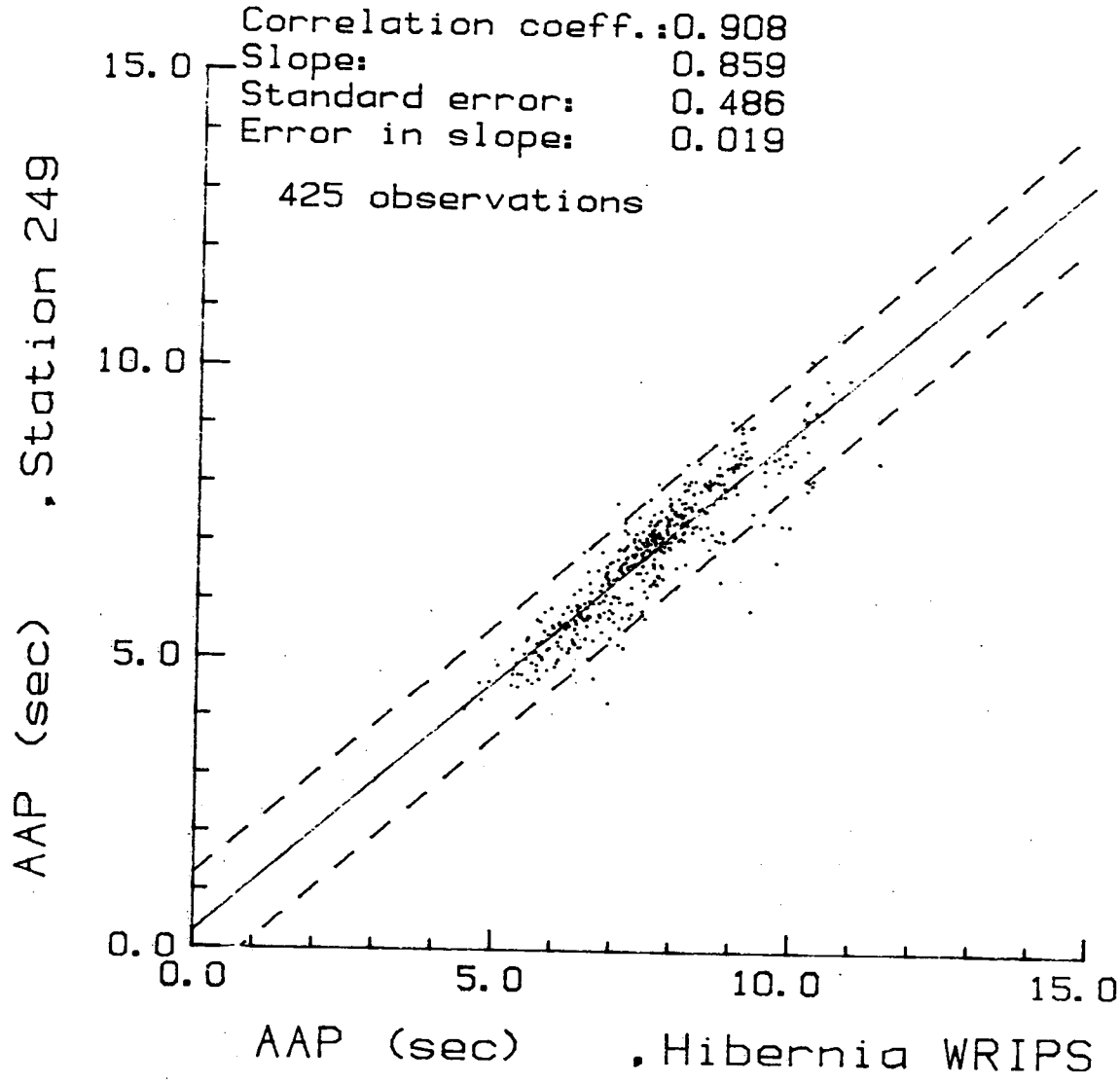

Figure 62. Regression plot of average apparent period (Station 249 vs. WRIPS buoy).

the regression plots for significant wave height, peak period and average apparent period. It is to be noted that the times of the records cannot be made the same, as the satellite data recordings were fixed at 0209, 0509, 0809, etc. (GMT). These were compared with the following "three hour" WAVEC record. The agreement between significant wave heights was good, given the separation, and indicates a conservation of variance in the wave field. The agreement between peak periods was poorer, however, compared with the similar regression for Station 169. Band averaging is performed on satellite data for frequencies greater than 0.11 Hz, which reduces agreement at high frequencies, where for other buoys, agreement is generally better as the bandwidth is much reduced. Outlying points are usually associated with multiple peaks in the WAVEC spectrum, often at higher frequencies, which are not showing up in the averaged satellite data. There is better correlation between values for average apparent period, however the WRIPS estimates are considerably higher. A likely reason for this is a bias being introduced due to the band averaging at high frequency of the WRIPS data in the calculation of average apparent period and the unstable nature of this parameter. Other spectral properties calculated using the higher moments of the energy density distribution should also be affected to various extents.

The behaviour of both instruments through the two storms was very similar, though the WAVEC buoy did not record as high a maximum significant wave height on March 11 (8.54 meters vs. 8.0 meters). This may be a reflection of location differences, however a similar underestimate was observed on the West Coast when a Waverider and WAVEC were moored near each other off Tofino. Unfortunately, in this study there were too few storms to determine the presence of any consistent behaviour of the WAVEC buoy in high energy sea conditions.

WAVEC vs. WAVE-TRACK. The numerous problems encountered, the reduced data return and the poor quality from the Endeco WAVE-TRACK system, created difficulties in drawing any strong conclusions from the intercomparison. Figure 63 contains superimposed time series of Waverider, WAVEC and WAVE-TRACK significant wave height, peak period, average apparent period and spectral width parameter. Obvious problems can be seen in the data prior to February 21 in the average statistics (average apparent period and significant wave height) and spectral shape even though the peak periods agree. There is better agreement in significant wave height after this date, indicating that the total variance was

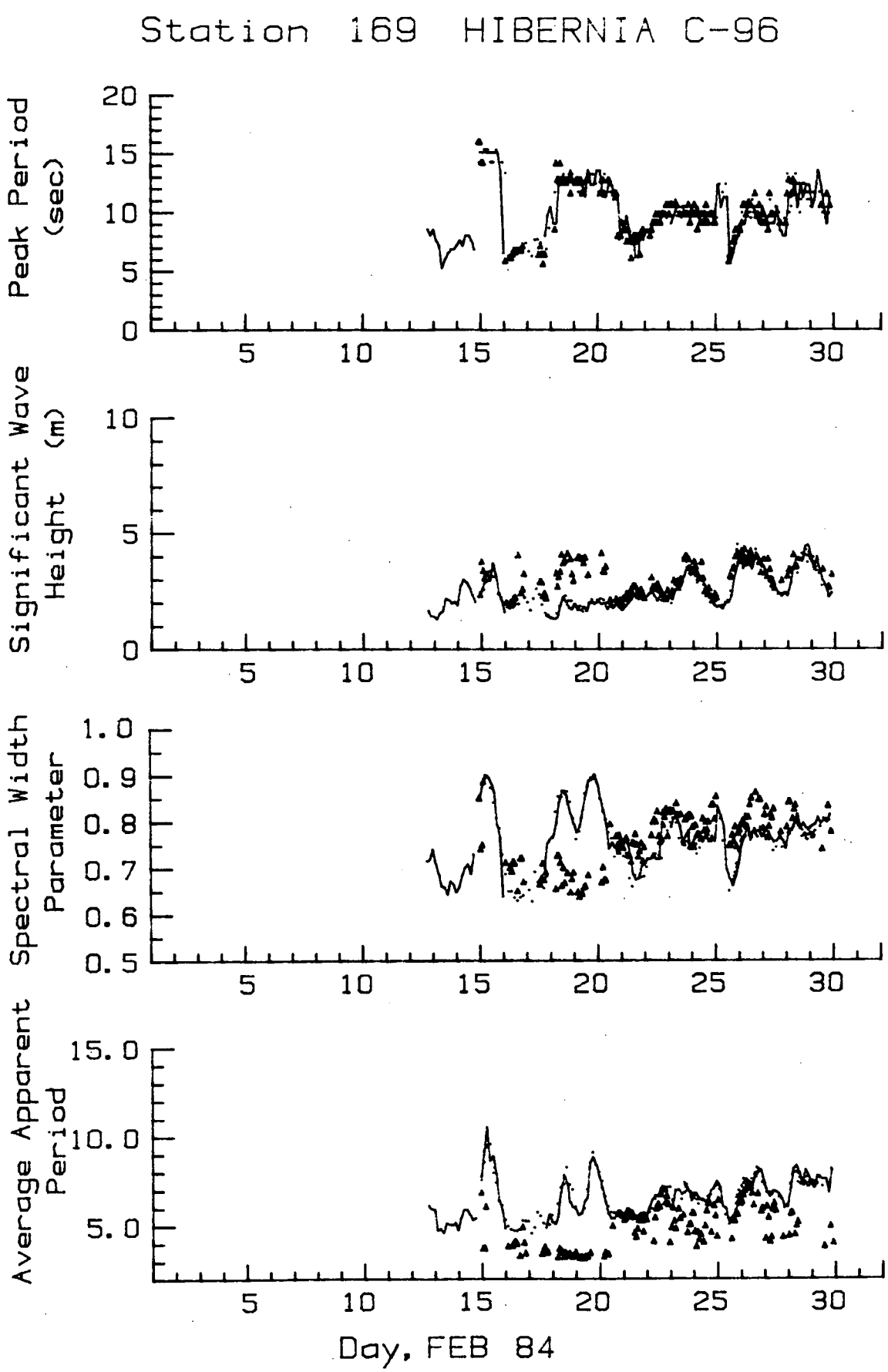

Figure 63. Superimposed time series of Waverider, WAVEC and WAVE-TRACK significant wave height, peak period, average apparent period and spectral width parameter (solid line: Waverider, triangles: WAVE-TRACK, dots: Station 249 WAVEC).

estimated properly, but the shape of the spectrum is still often questionable as seen by the average apparent period and spectral width parameter. Figure 64 and 65 contain the regression plots for significant wave height and peak period for data after February 20. The agreement is good considering all the problems and the short data set.

Before comparing the mean directions against those obtained from the WAVEC buoy, a comparison was made between the corresponding peak direction estimates calculated using the Longuet-Higgins analysis and using the 28 frequency band-pass analysis. The band-pass analysis was performed on 51 records which contained complete data sets. Figures 66, 67 and 68 show the regression plots for significant wave height, peak period and peak direction obtained with the two methods with the x-axis being the Longuet-Higgins (L-H) results. The error in significant wave height is within computational error and that in peak period can often be related to bandwidth differences. The large amount of scatter in the peak direction for the same records but using a different calculation approach, is an indication of a serious problem in one or the other method. There is even poorer agreement when comparing the L-H peak directions with those from the WAVEC records (Figures 69 and 70). A weighted direction was also calculated for the Endeco data but only on frequencies less than 0.2 Hz in light of the linearity analysis results which indicated that the higher frequency estimates were questionable. The results are shown in Figure 71 (weighted by cosine spread). The agreement has improved considerably, lending faith to the Longuet-Higgins approach, especially since the standard error is biased high due to the few outlying points. The scatter in both the peak direction and average direction plots cannot be attributed solely to environmental differences but to a difference in the way the Endeco buoy was viewing the environment. It is not clear, however, if this is a normal operational problem or a reflection of external influences such as icing. Either way, the WAVEC buoy, exposed to the same conditions, showed a more consistent operation.

Energy Density Heave and Directional Spectra

In order to assess frequency dependent behaviour of the various instruments and site considerations, selected energy density heave and directional

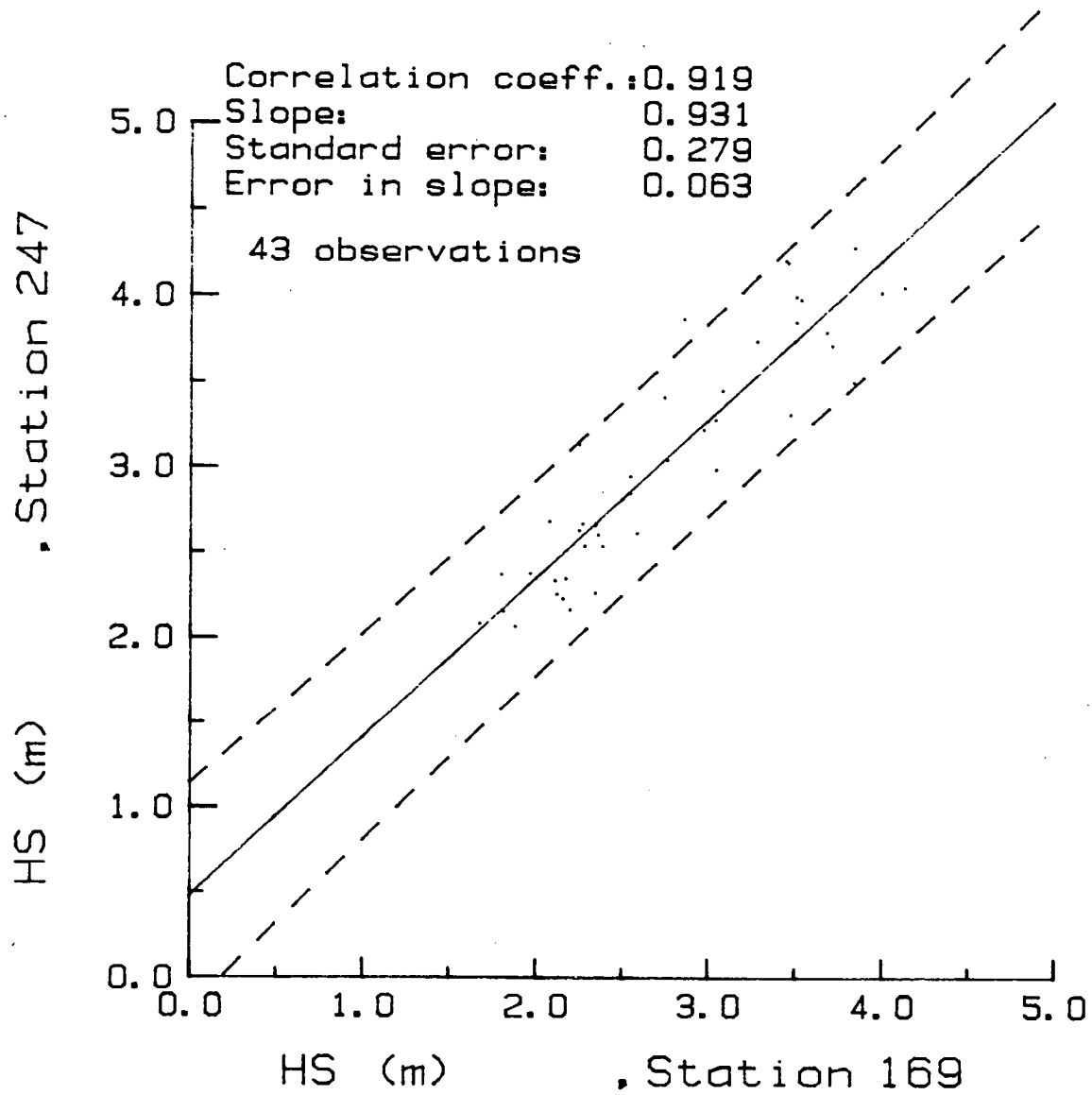

Figure 64. Regression plot of significant wave height (Station 247 vs. Station 169).

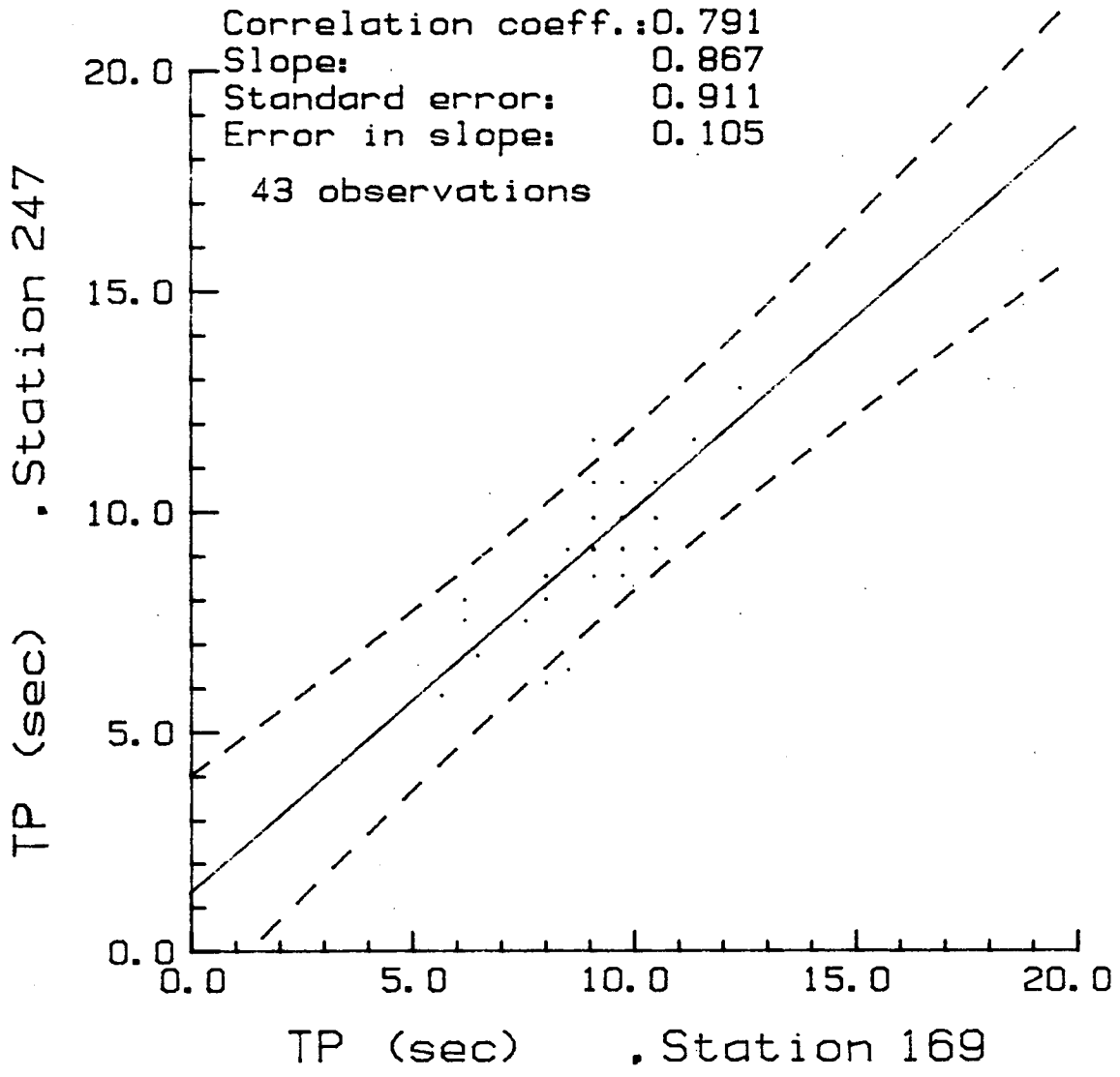

Figure 65. Regression plot of peak period (Station 247 vs. Station 169).

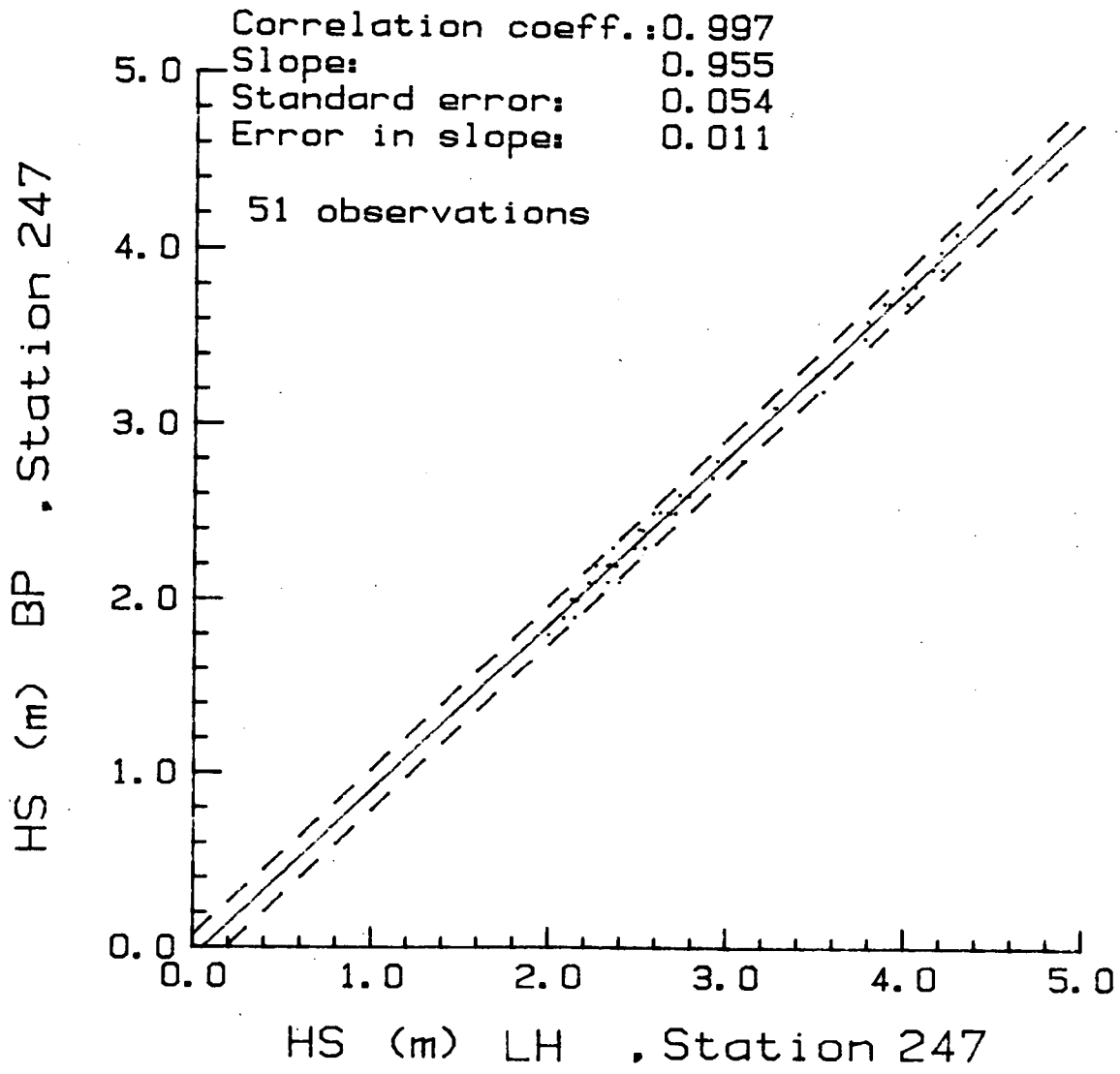

Figure 66. Regression plot of significant wave height (Station 247 -band-pass vs. Longuet-Higgins calculation).

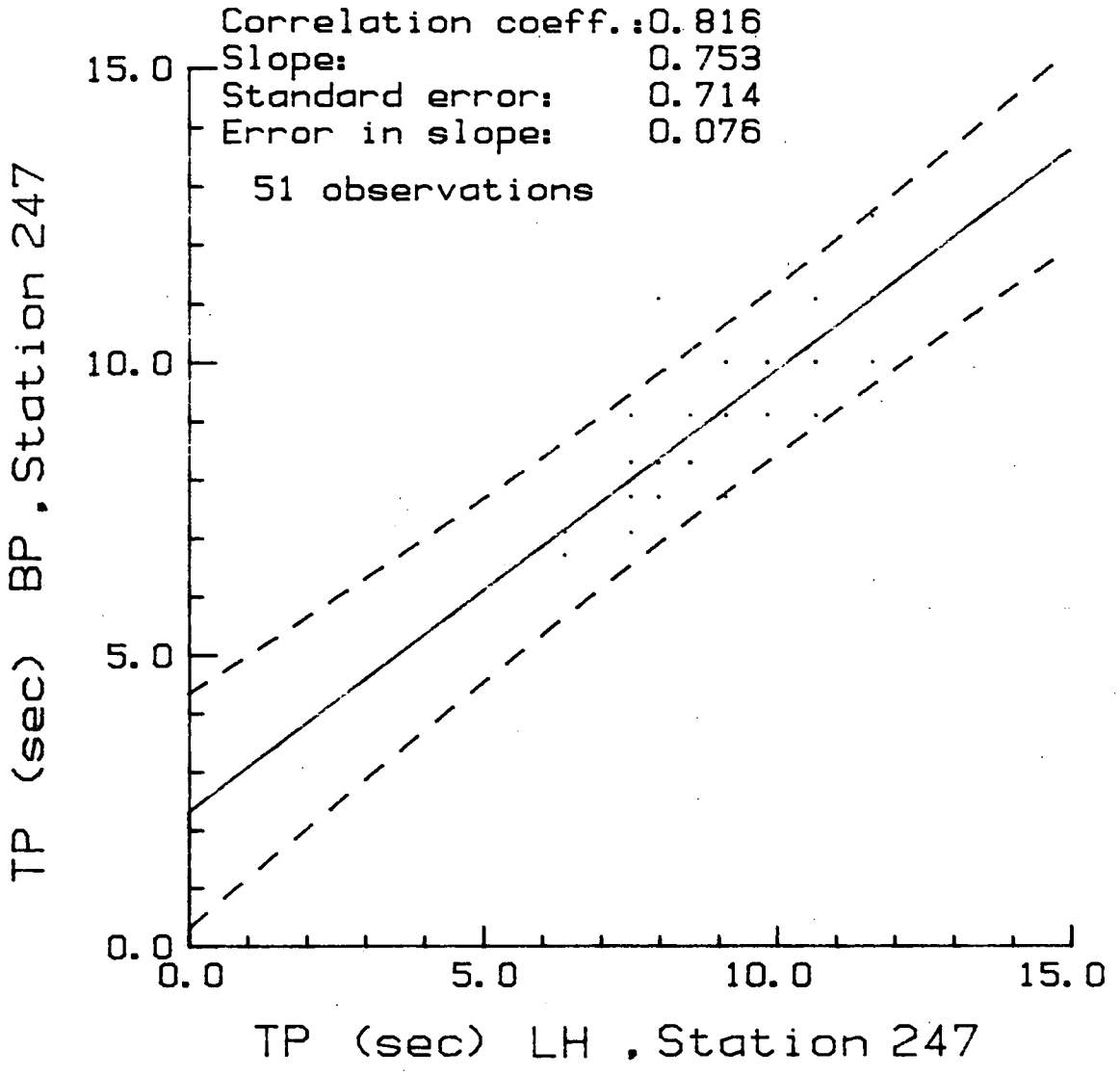

Figure 67. Regression plot of peak period (Station 247 - band-pass vs. Longuet-Higgins calculation).

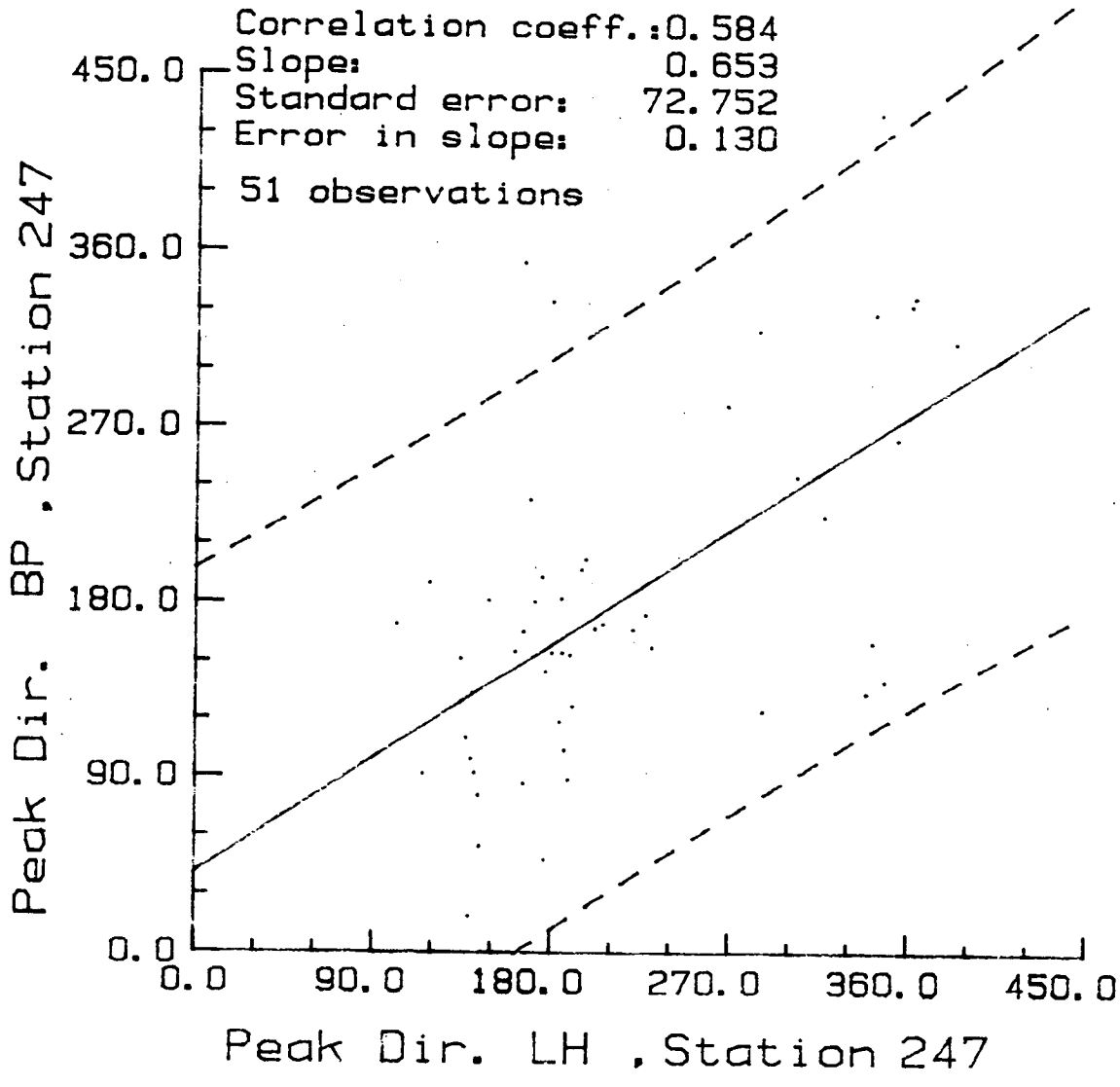

Figure 68. Regression plot of peak direction (Station 247 - band-pass vs. Longuet-Higgins calculation).

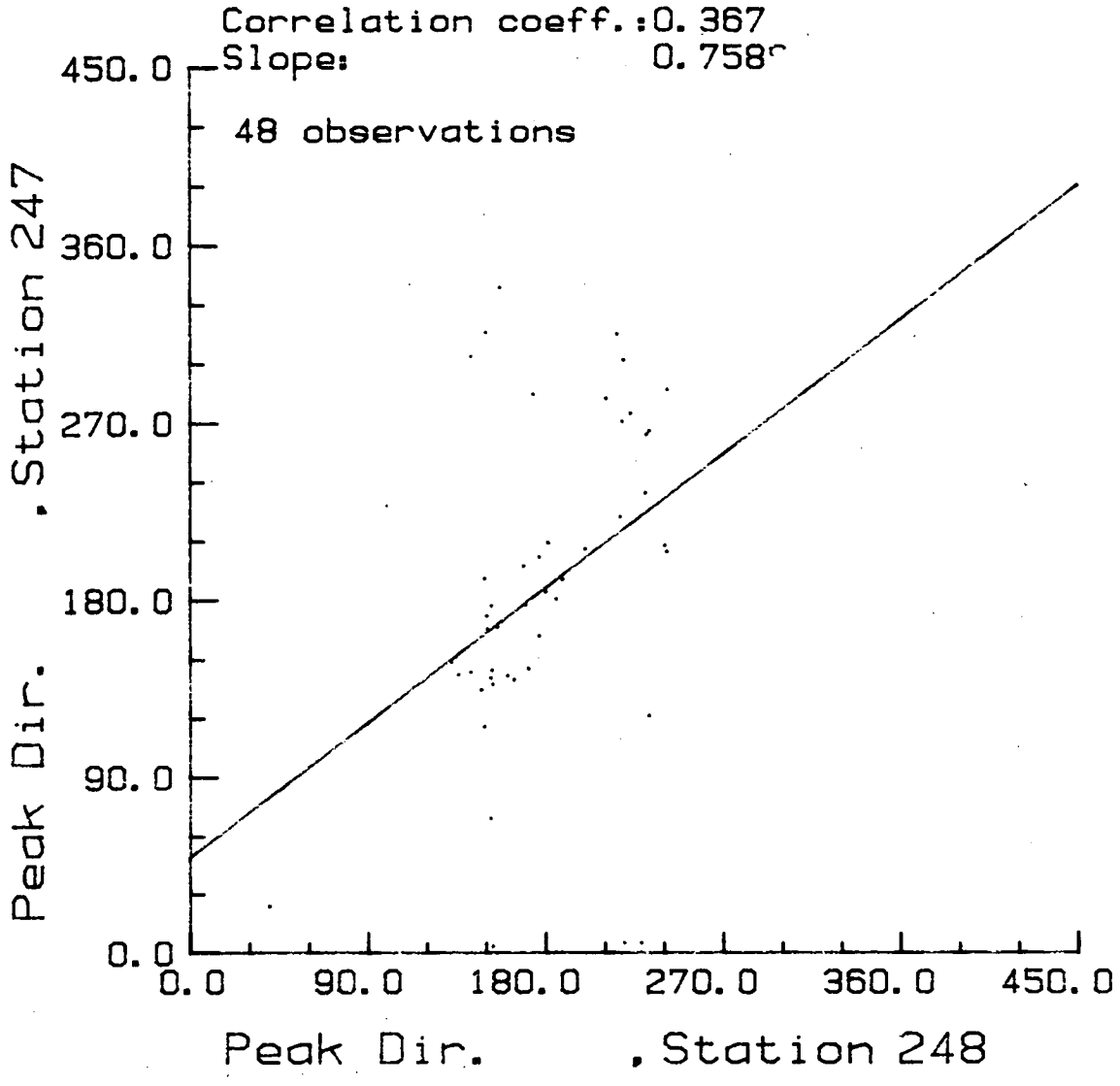

Figure 69. Regression plot of peak direction (Station 247 vs. Station 248).

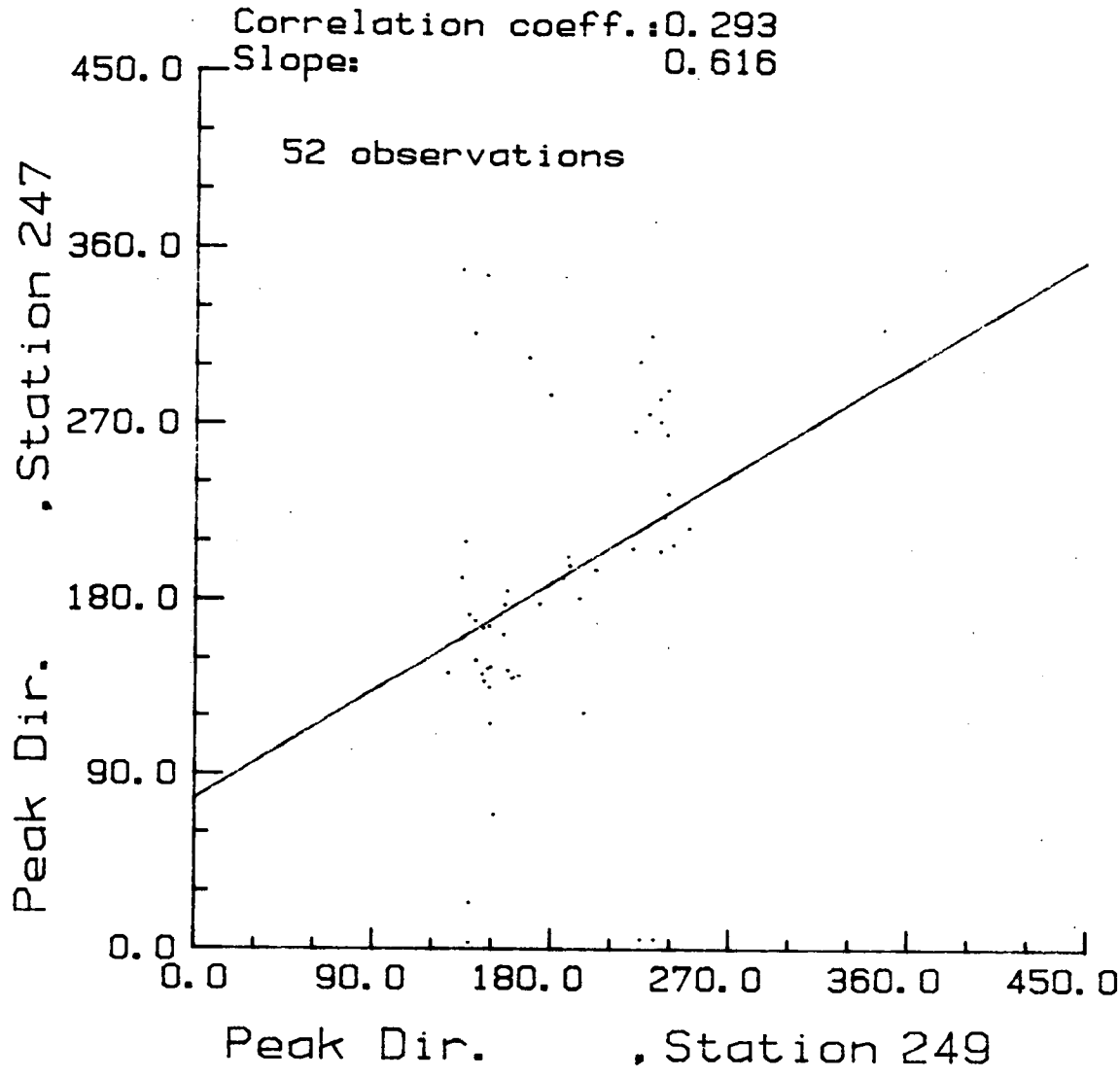

Figure 70. Regression plot of peak direction (Station 247 vs. Station 249).

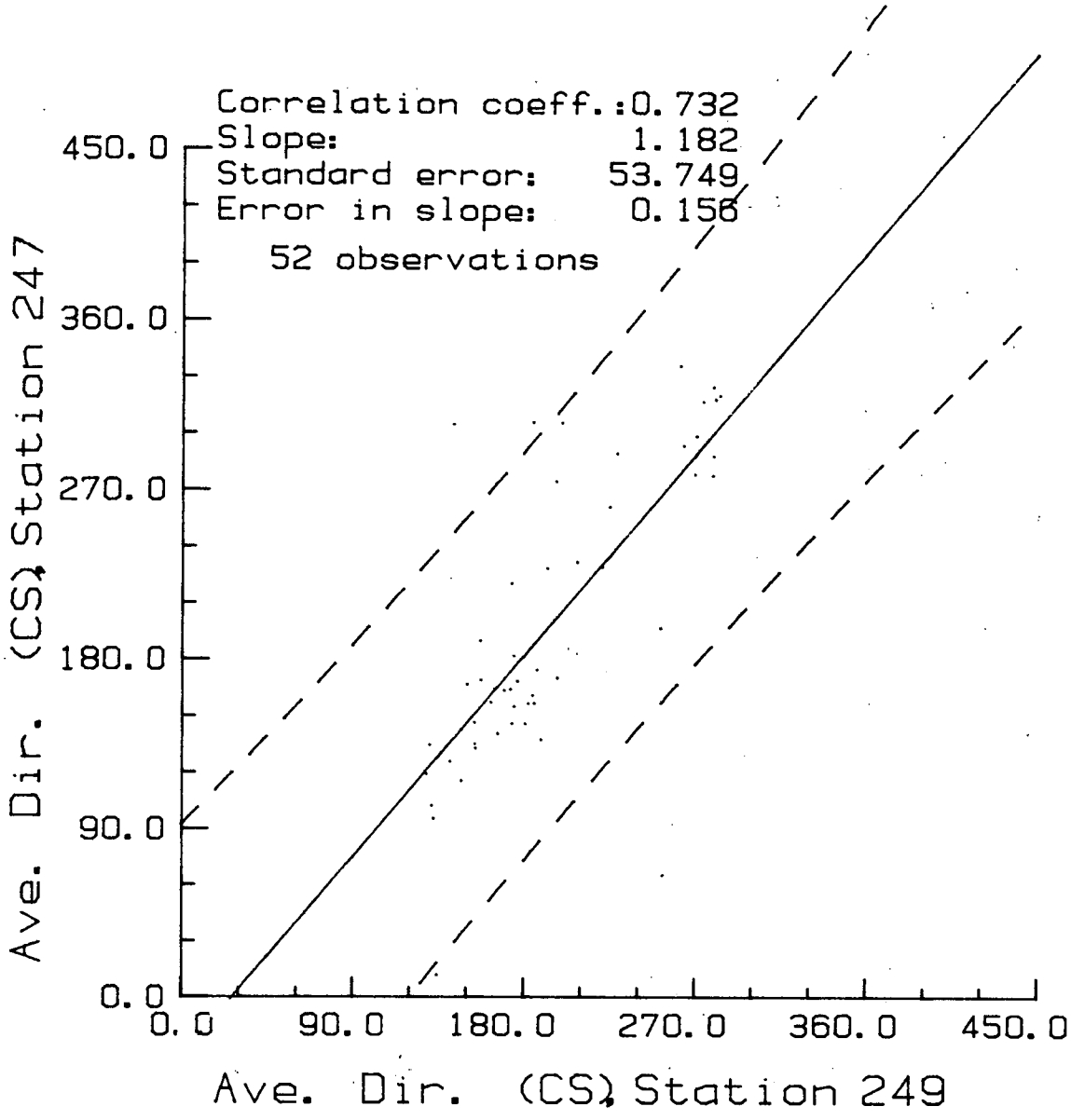

Figure 71. Regression plot of average apparent direction weighted by cosine spread (Station 247 vs. Station 249).

spectra were produced. Energy density spectra for the two WAVEC buoys, for the Station 249 WAVEC and the WAVE-TRACK buoy and for Station 249 and the Waverider at Station 169, were overlayed for examination. This provided a large number of figures which are not reproduced here. Copies of these plots as well as contoured directional spectra, may be requested from Seakem Oceanography Ltd., (Sidney, British Columbia). The following summarizes the observations and selected examples are included.

Generally, the heave spectra for the two WAVEC buoys are similar in shape, however there were often distinct differences in the number of peaks and their location in February. This is probably reflecting site differences as there was often better agreement between the WAVEC at Station 248 and the WAVE-TRACK buoy at Station 247 (for example, on 1800 Feb. 23, 2230 Feb. 25 and 0300 Feb. 26; Fig. 78, 79 and 80, respectively). This is an interesting feature given the proximity of all the buoys (less than 1 nautical mile separation).

The mean directions by frequency for the two WAVEC buoys agree extremely well at all frequencies when wave energy is sufficiently above noise levels. This is true even for separate sea and swell events as can be seen, for example, on March 30 (Fig. 72). The largest differences in mean direction observed throughout the study were seen late February 25 to 26 at high frequencies (See Fig. 79, 81). This corresponded to a period of turning wind directions, from approximately 120^{o} to 225^{o} and the sea response may have been felt at Station 249 before either Station 248 or 247.

Agreement between the directional spread at the peak frequency is variable. Figure 73 shows a regression of the cosine spread exponent for corresponding records between the two WAVEC buoys. The agreement is better at lower values. A relationship between the cosine spread and spectral shape parameters was sought and Figure 74 contains a regression against the peakedness parameter. However, the degree of scatter does not allow for any conclusions. No statistical correlation with the spectral narrowness parameter was observed (Corr. Coeff. = .073). The applicability of both the cosine spread model and Longuet-Higgins model have been questioned (Long, 1980; Barstow and Krogstad, 1983) and it may be found that sea, swell and site will all influence the choice of distribution needed for a given application. In this study, it was assumed that the model would

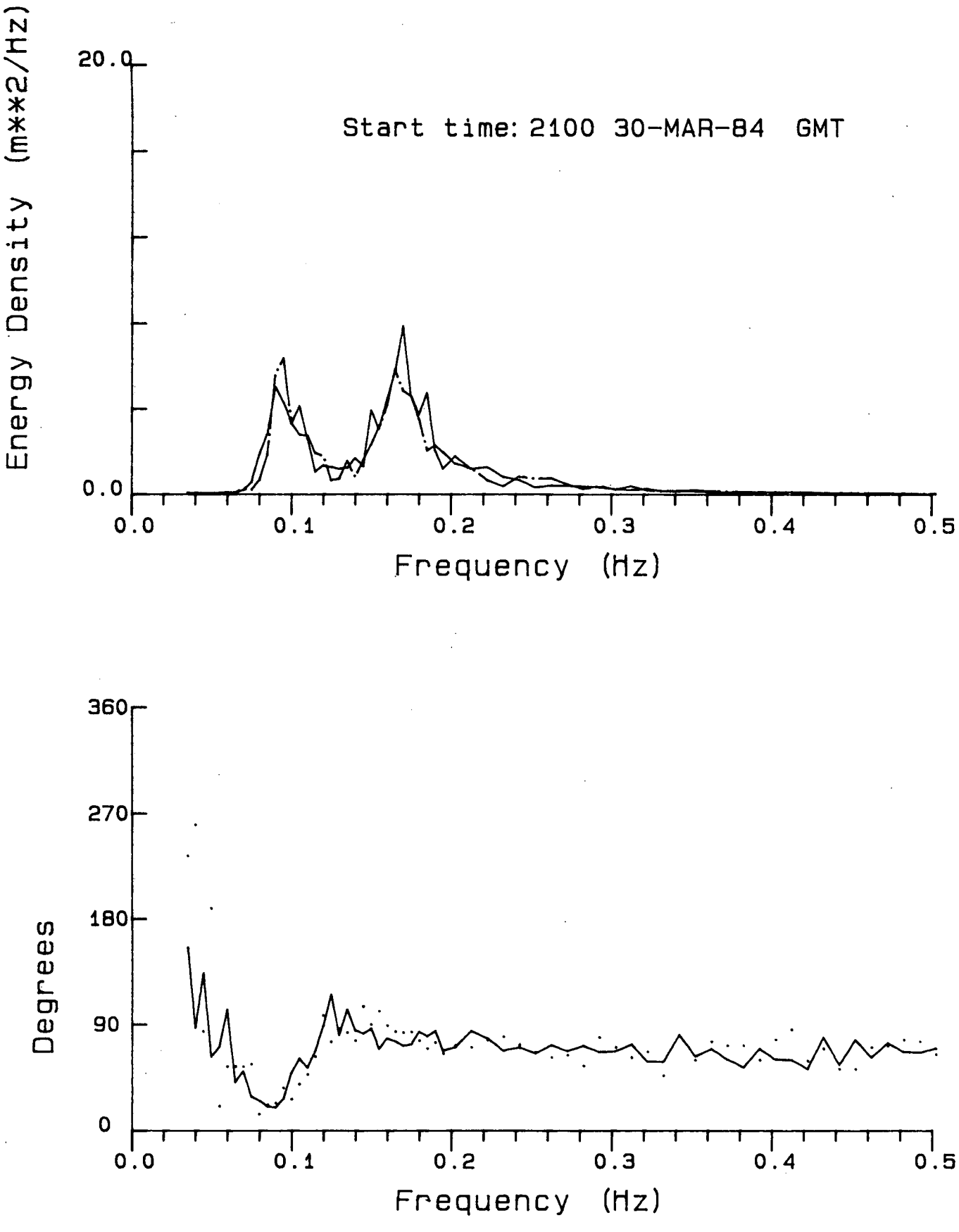

Figure 72. Heave spectra and mean direction for 2100 Mar. 30 (Station 249 solid, Station 248 - dashed and dotted).

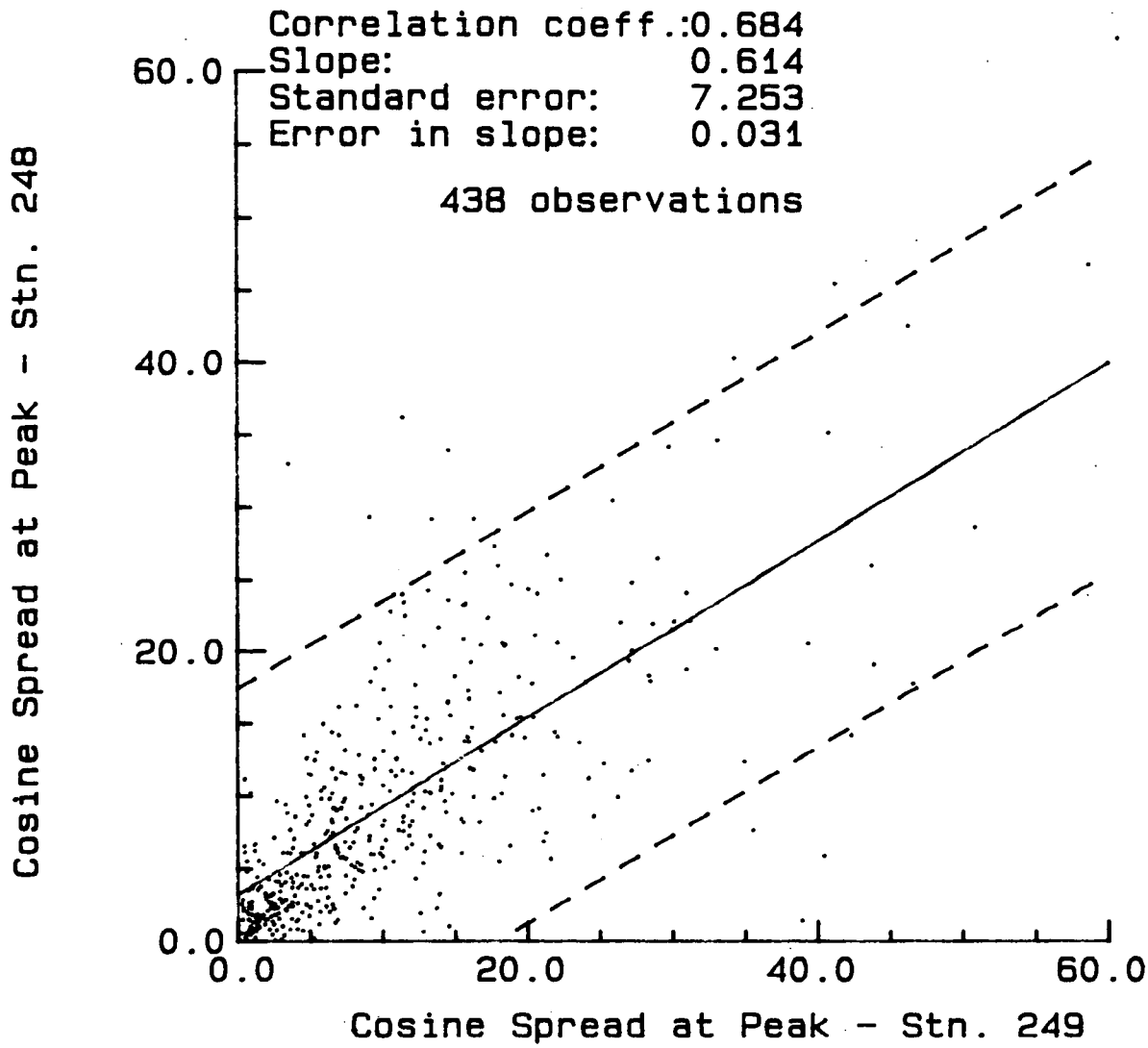

Figure 73. Regression plot of cosine spread at the peak frequency (Station 248 vs. Station 249).

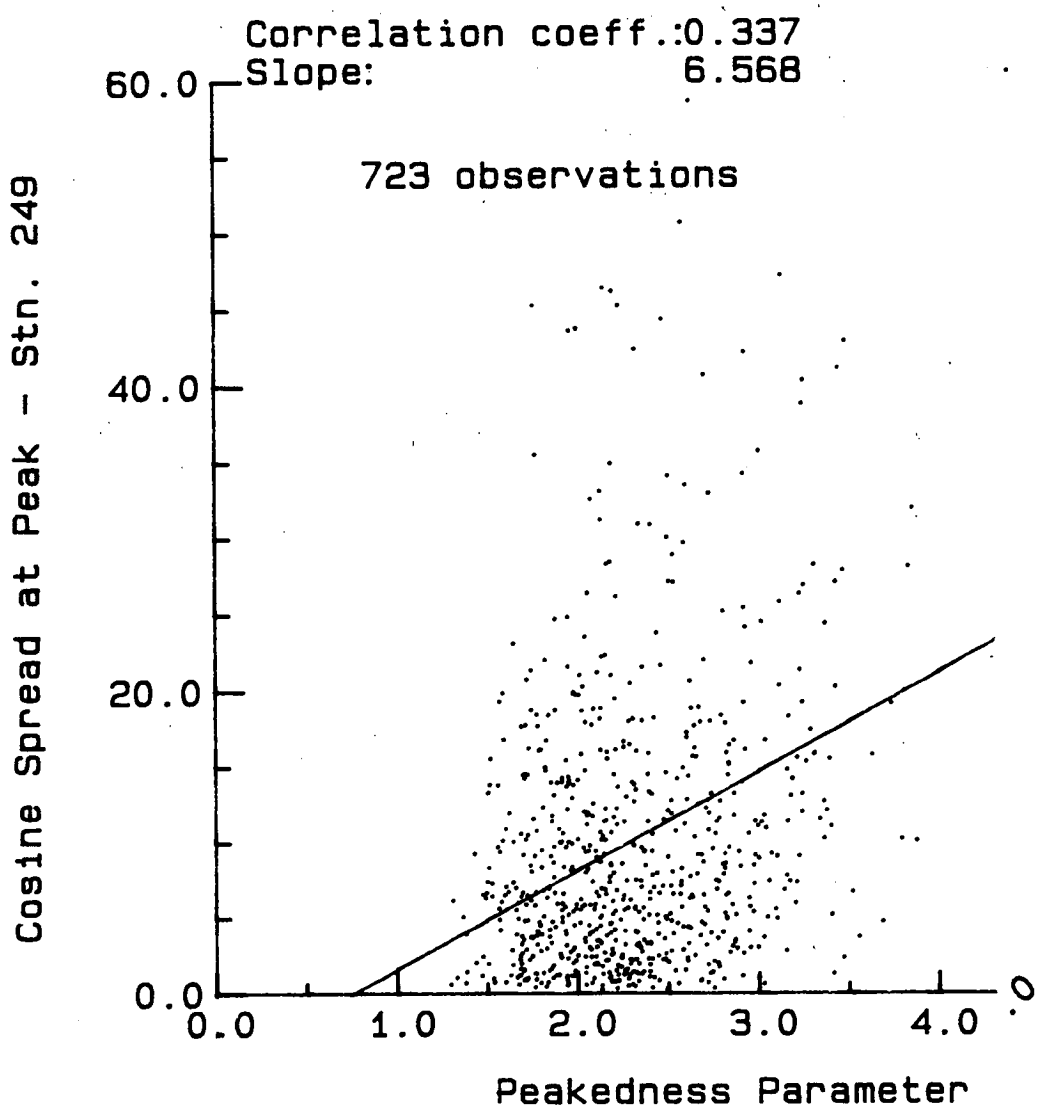

Figure 74. Regression of cosine spread at peak frequency against peakedness parameter.

fit equally well, or equally poorly, the two sets of data and only relative differences assessed.

Selected contoured directional spectra, calculated using Longuet-Higgins expansion, were produced. The contour intervals here and for all other applications (unless otherwise specified) were set to 1, 5, 10, 15, 20, 30, 40, 50,...100, 150 and 200 m^2/Hz. An example of a multiple peaked spectrum is included in Figure 75, a and b. The energy spread with direction is obvious and is considered one of the limitations of this analysis. The Longuet-Higgins analysis uses binomial weighting in order to eliminate side lobe and negative energy values introduced by truncation of the Fourier expansion. This results in a directional resolution or beam width of 131° (i.e., two wave trains must be travelling in a direction separated by more than 131° to be resolved). LeBlanc and Middleton (1982), discussed this point, and have suggested the use of a different weighting in order to reduce the spread. Figure 76 shows the same WAVEC record whose directional spectrum was calculated using both weighting schemes. A reduction in spread does occur, however, the question is raised concerning how much of the spread is real and how much a function of the mathematics, as one could potentially force the spread to zero, or within any previously set bounds, if one is willing to ignore increased levels of negative energy.

Figure 77 contains the energy density spectrum and mean direction by frequency for a record when the Endeco buoy was experiencing icing. Because of the often large variability in the mean direction for the Endeco buoy, only dots are plotted in the lower half of this and following figures. The effect of the icing can be seen by the presence of background white noise added onto the spectrum and by the large amount of scatter in the mean directions. Figures 78, 79, 80 and 81 depict selected spectra including that record containing the maximum significant wave height measured at Station 247 (Fig. 79). The heave spectra are generally similar though with better agreement between Stations 247, 248 and 169. Figure 78 shows slight icing problems but these are only sporadic in nature. What is important is the presence of increased low frequency energy in all of the WAVE-TRACK records. The presence of spurious low frequency energy was also a serious problem in WAVE-TRACK data collected over two years off the Northern British Columbia Coast. In that study, the low frequency band, on numerous occasions, dominated the spectrum. The cause of this energy has not been determined. The

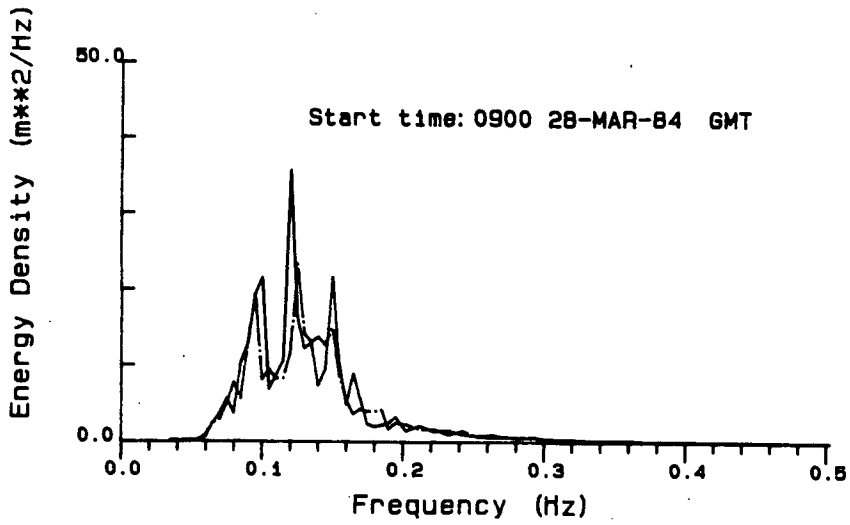

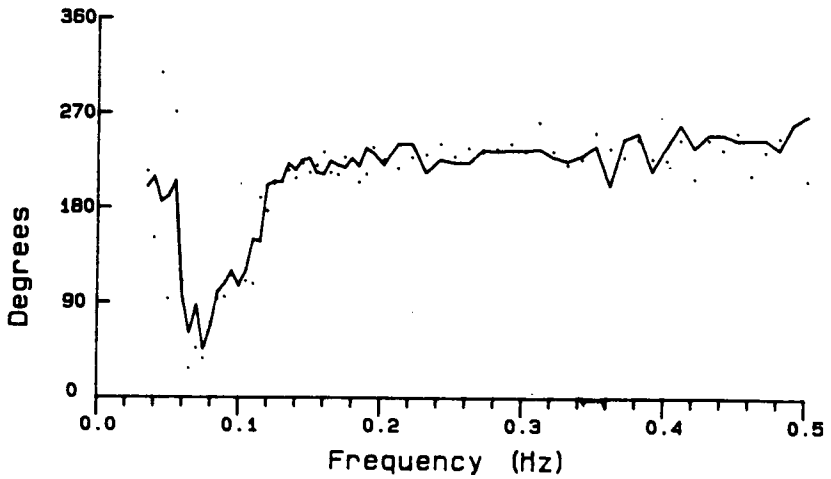

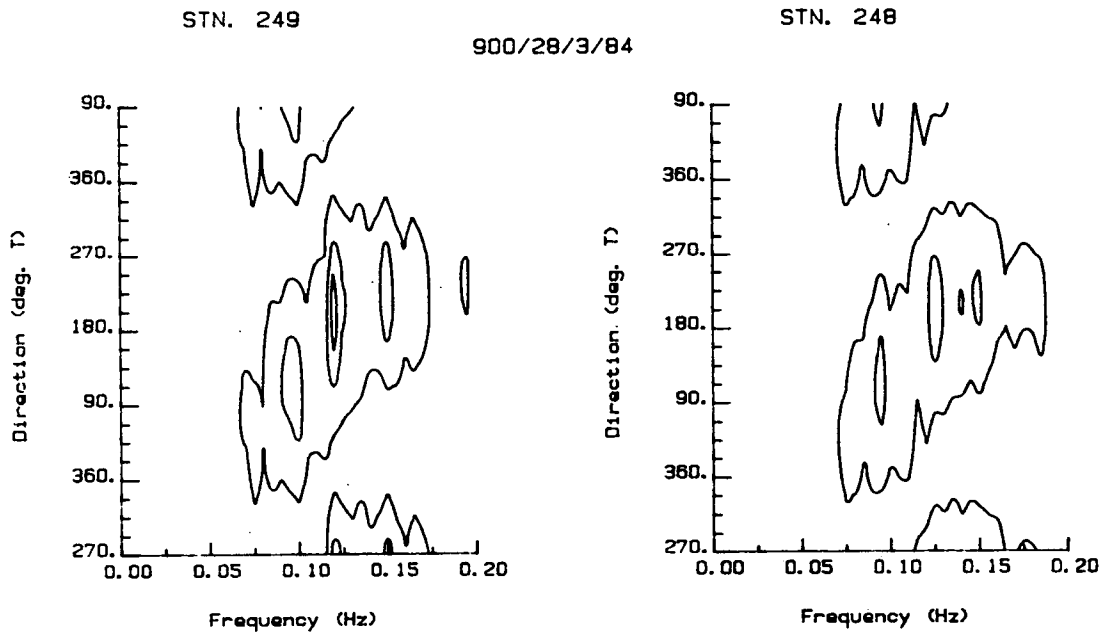

Figure 75. Heave and directional spectra for 0900 March 28.
a) Heave and mean direction Station 249 - solid; Station 248 - dashed and dotted.
b) Contoured directional spectra.

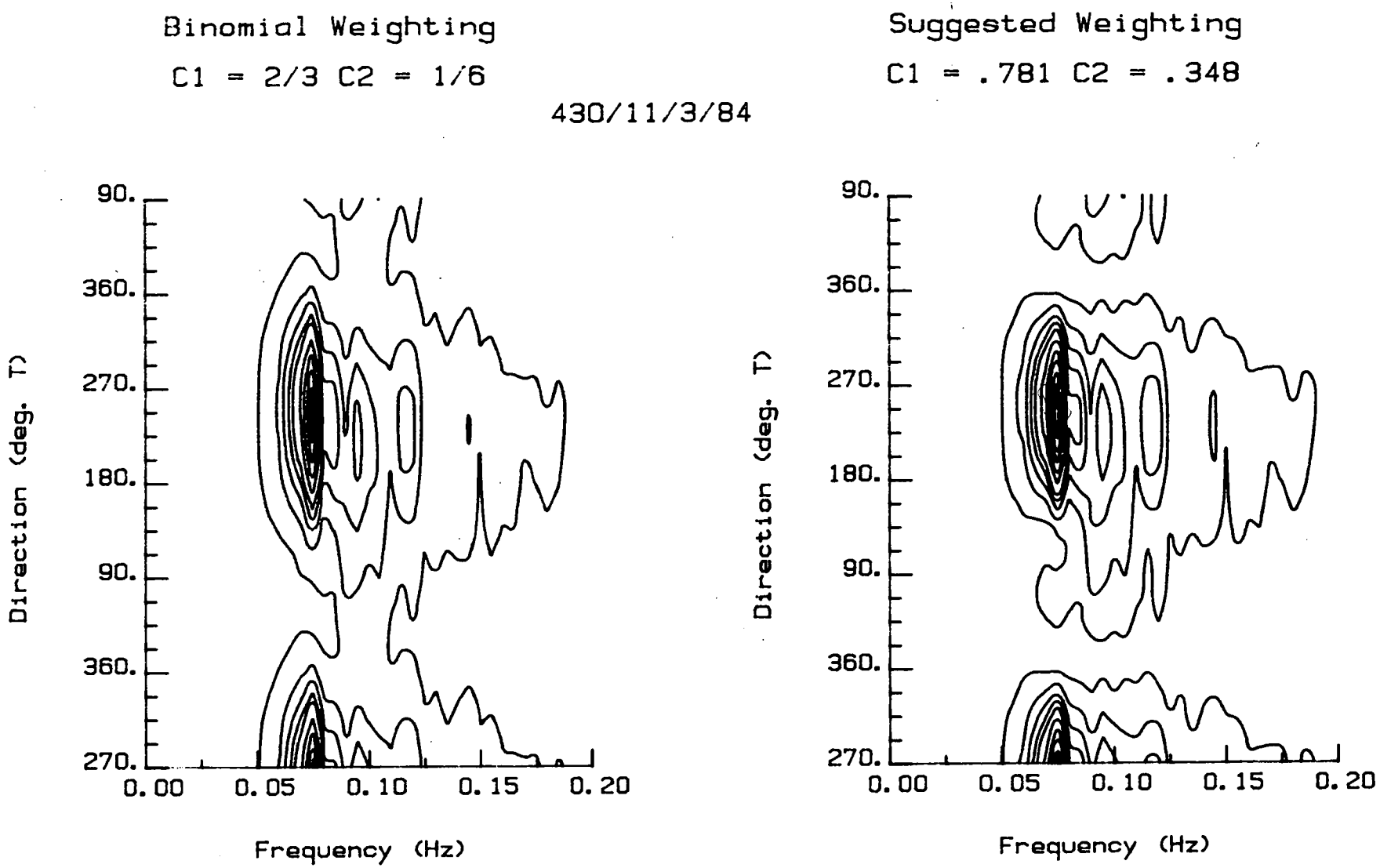

Figure 76. Sample directional spectrum using binomial weighting and weighting suggested by LeBlanc and Middleton (1982).

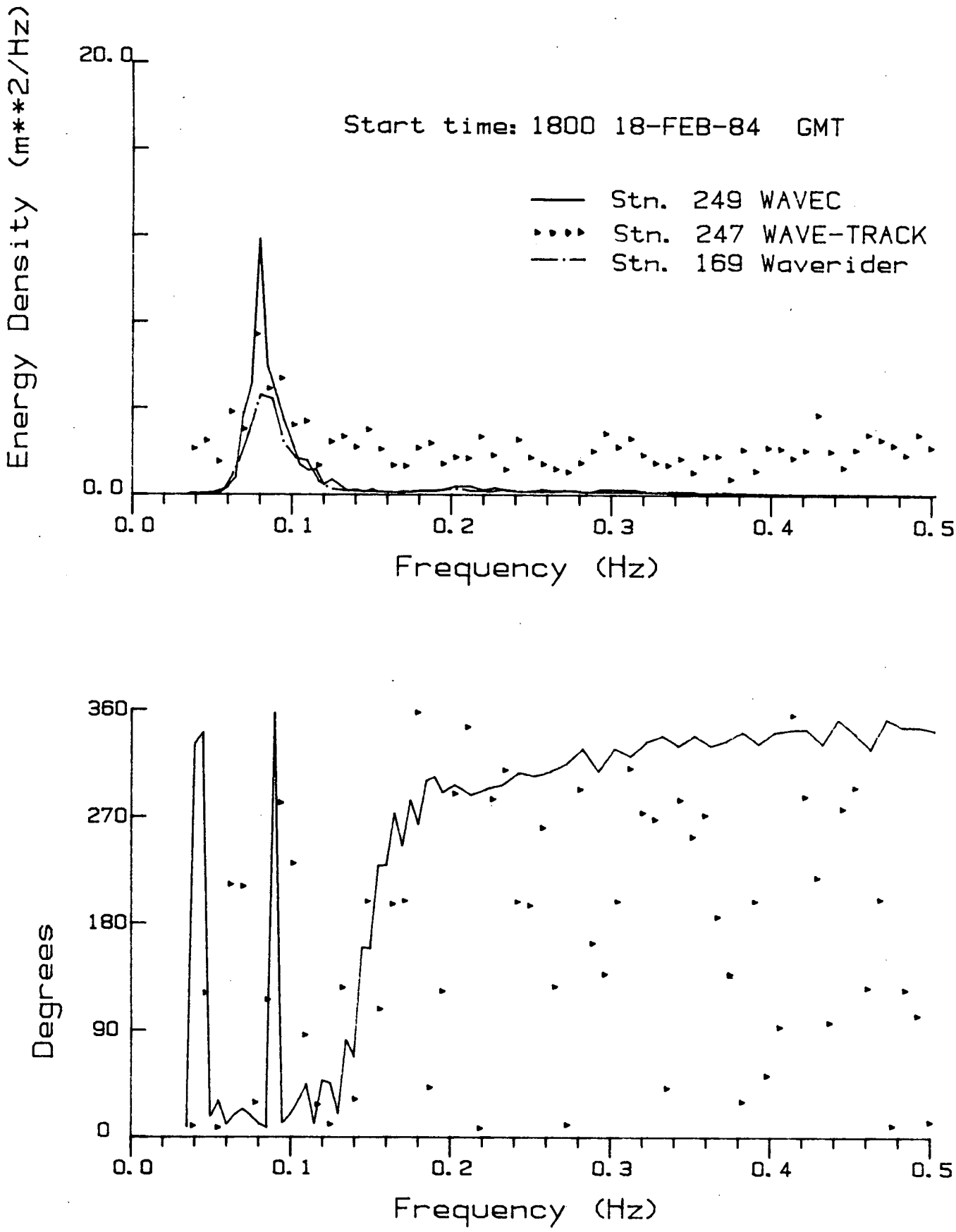

Figure 77. Spectra for 1800, February 18, 1984.

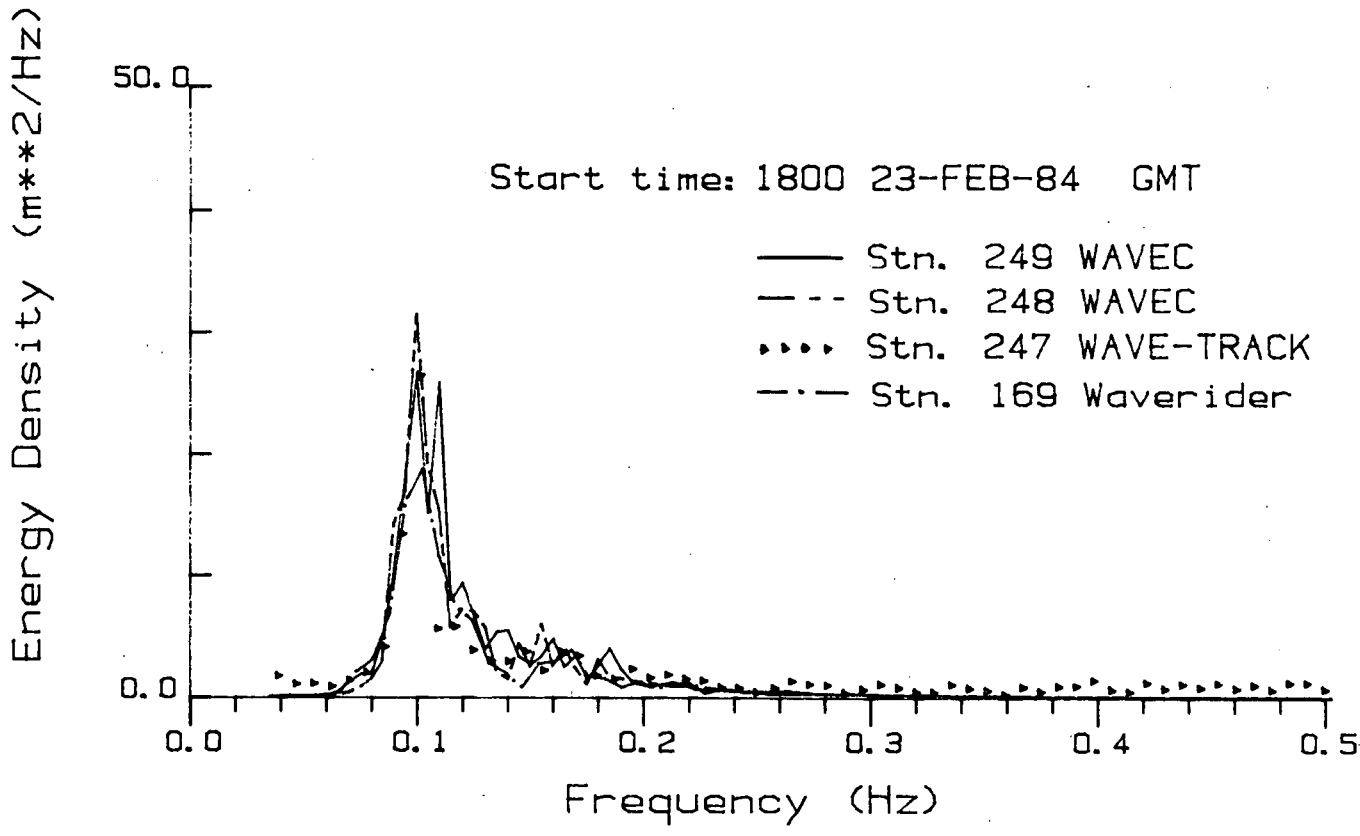

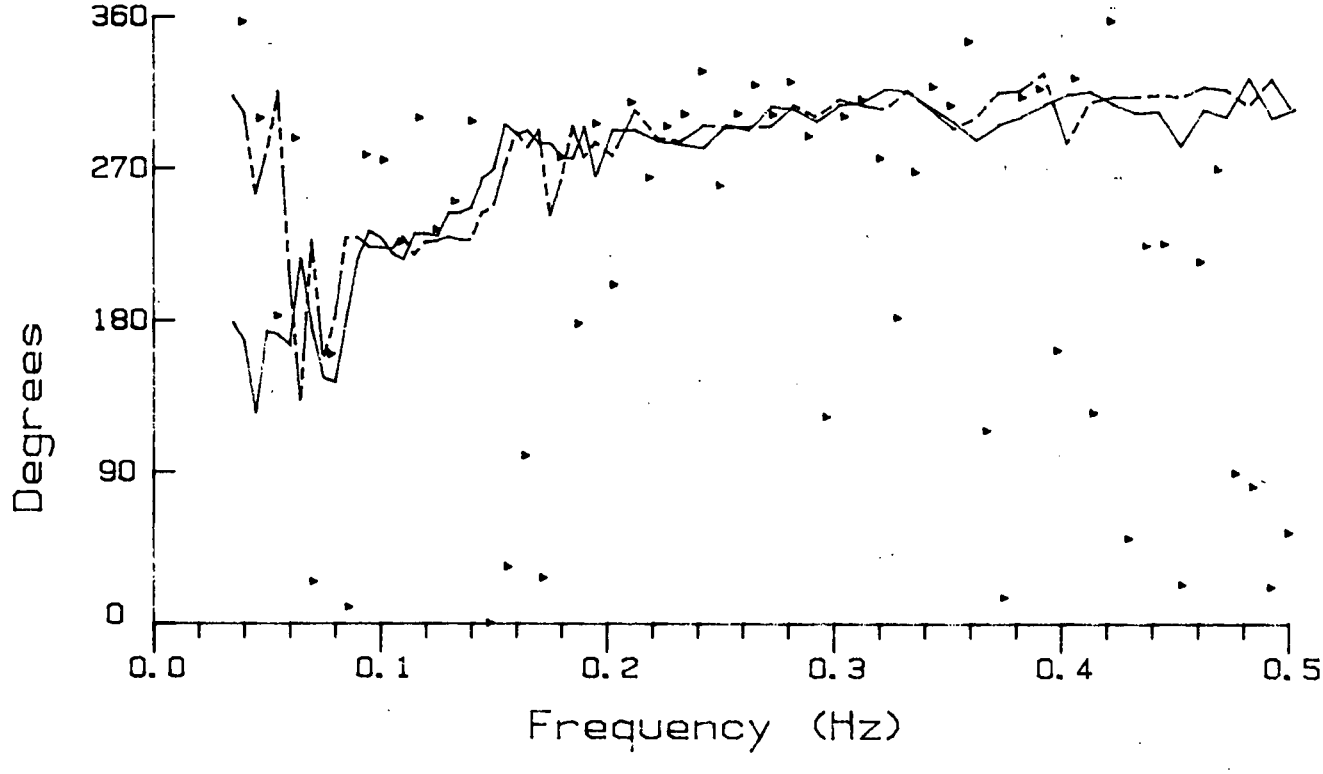

Figure 78. Spectra for 1800, February 23,1984.

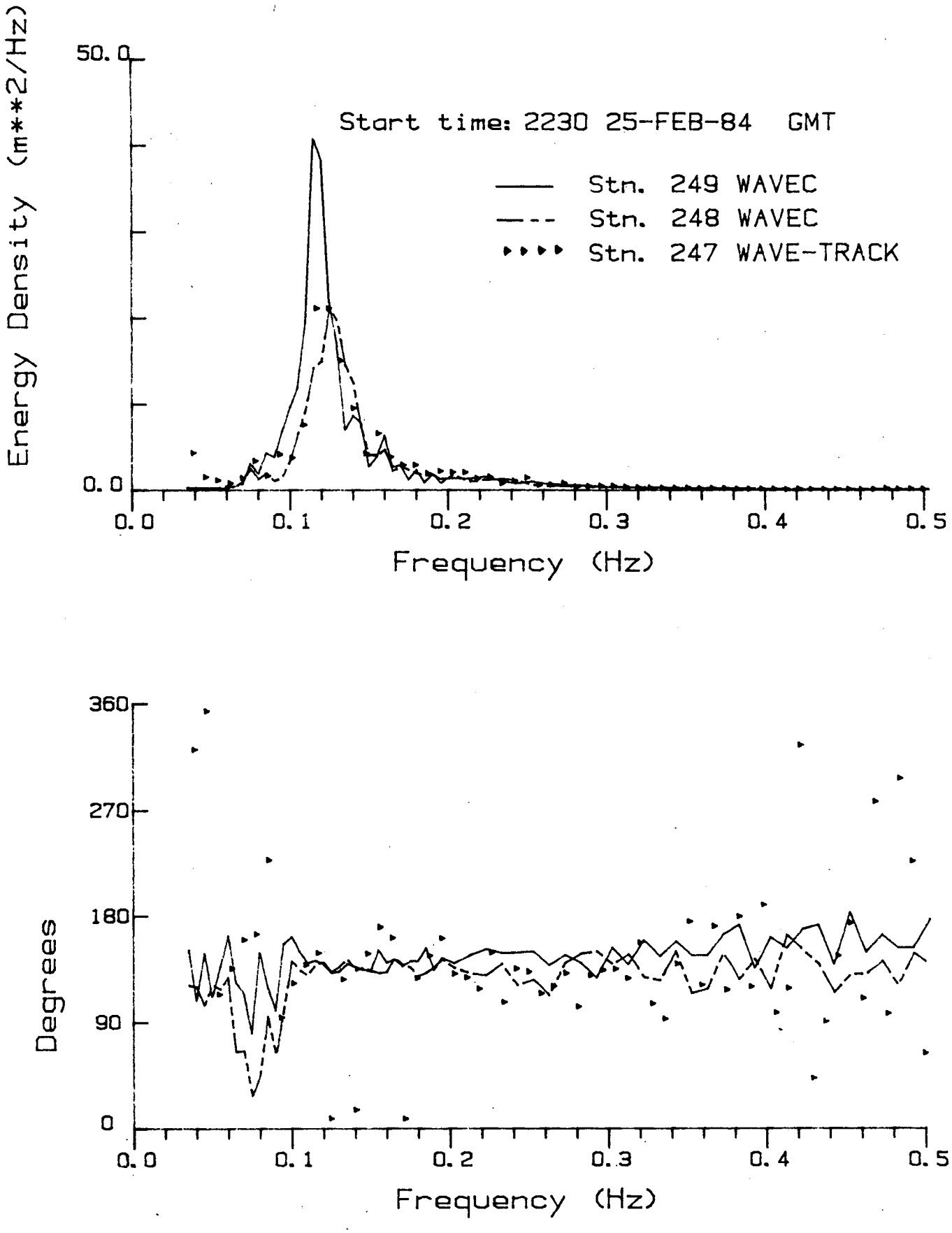

Figure 79. Spectra for 2230, February 25, 1984.

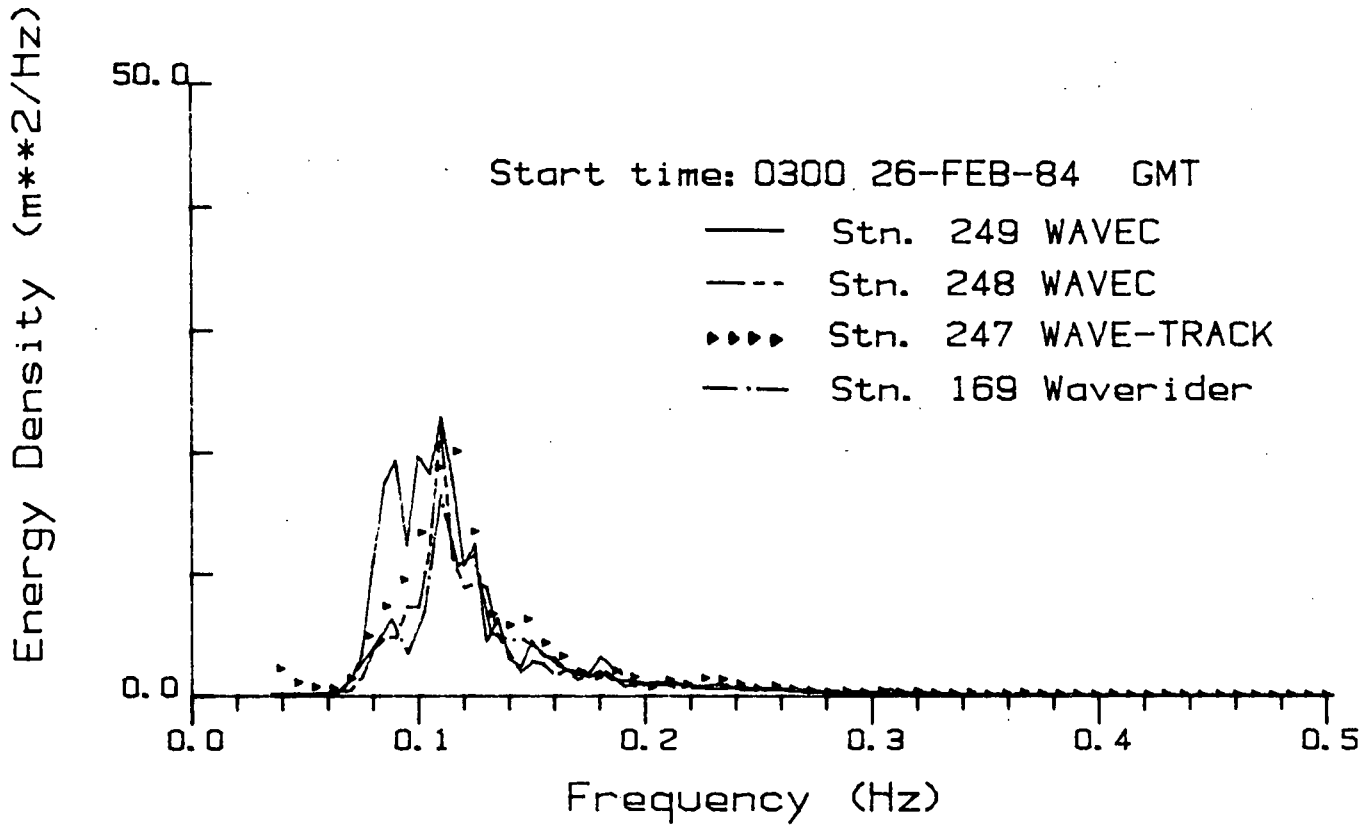

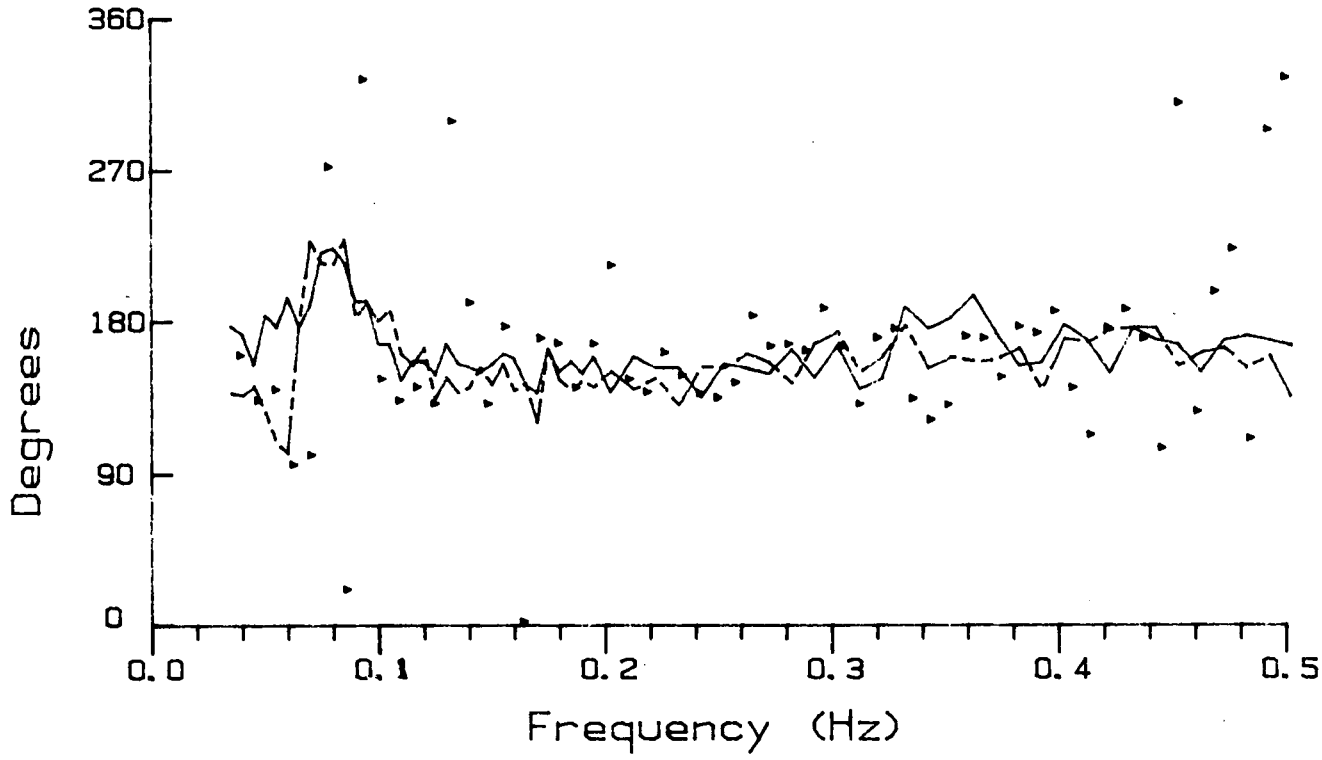

Figure 80. Spectra for 0300, February 26, 1984.

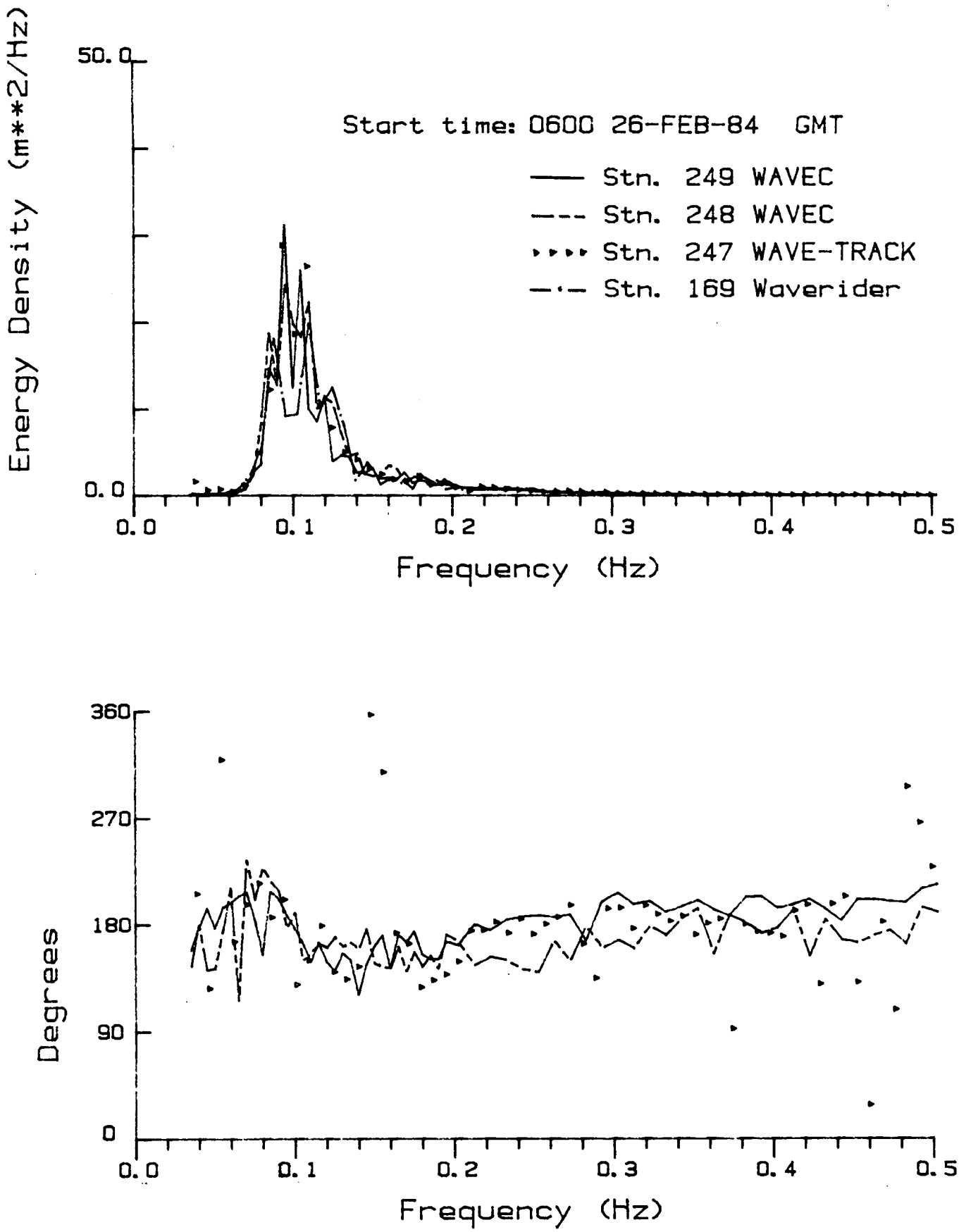

Figure 81. Spectra for 0600, February 26, 1984.

manufacturer suggests either setting the first three or four bands to zero arbitrarily, or by examining the energy in the tilt channels. It is an apparent design problem with the buoy and leads to difficulties, if not accounted for, in the calculation of spectral statistics or of time series corrected with the necessary instrument transfer functions. The mean direction by frequency shows a consistent increase in scatter for frequencies greater than 0.3 Hz which is to be expected given the linearity analysis results shown in Figure 39. The agreement between the buoys is generally better from the spectral peak to 0.3 Hz, however, it does vary from record to record.

Figures 82 and 83 are the corresponding contoured directional energy spectra for the heave spectra in Figures 79 and 81. The upper plots use the Longuet-Higgins expansion in order to calculate $En(f,\theta)$ with a wavenumber obtained from an iterative procedure on the wave dispersion equation. The lower plots show the results when corrected using the linearity relationship. This correction eliminated spurious energy at low frequency for the Endeco data and reduced the directional spread for both buoys. However, the Endeco data still showed greater energy spread with direction than the WAVEC data. Using the calculated wavenumber from the energy in the three channels appears to be one way of reducing directional spread experimentally, if one keeps in mind the limitations of the linearity analysis discussed earlier.

Synthetic Aperture Radar Imagery

As the largest waves were expected during the two overflights of April 2, these data were initially processed. Table 9 gives the results reported by Intera as well as reference observations from the MANMAR, Station 249 WAVEC, and hindcast model data sets.

The poor agreement in direction between passes led Intera to conclude that the STAR-1 imaging parameters were not appropriate for the estimation of wave spectra, though the peak periods agreed fairly well. The Pass 2 wave direction results did agree with wind direction and hindcast model swell directions but did not agree with either the visual or buoy data at equivalent periods. No further

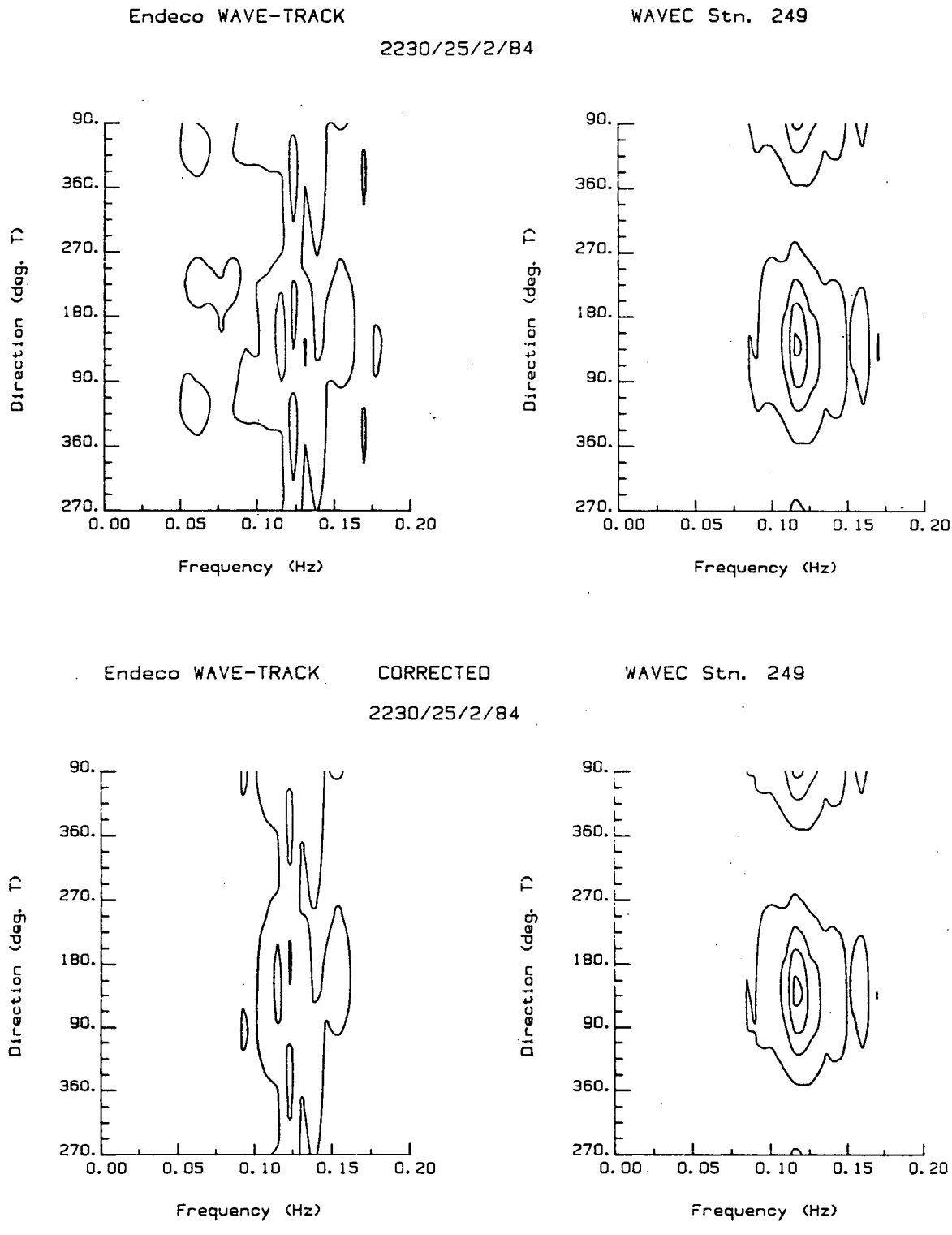

Figure 82. Directional spectra for Stations 247 and 249 for 2230 February 25, 1984 (upper) and corrected using Linearity analysis (lower).

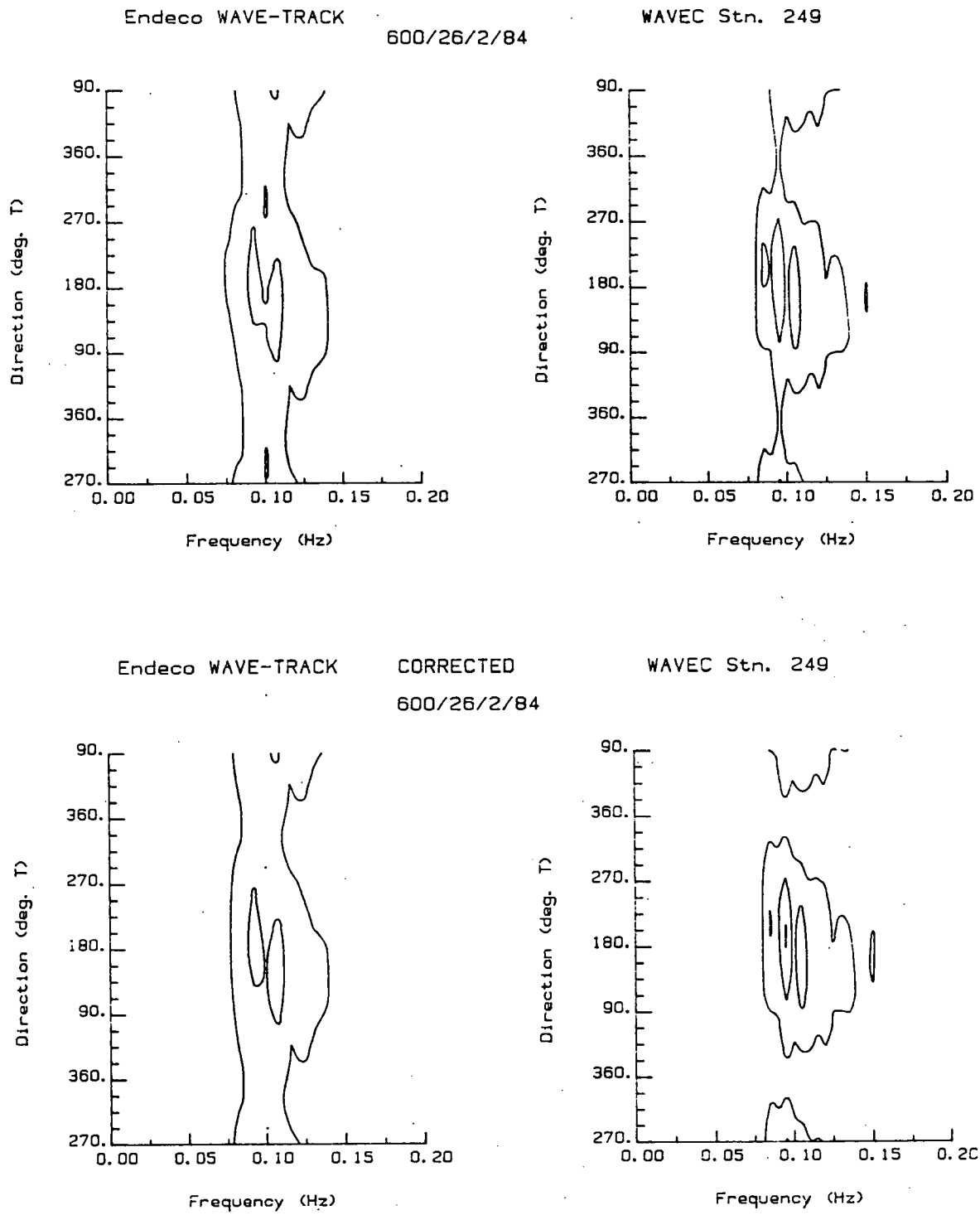

Figure 83. Directional spectra for Stations 247 and 249 for 0600, February 26, 1984 (upper) and corrected using Linearity analysis (lower).

TABLE 9

RESULTS OF THE SAR ANALYSIS OF APRIL 2

REFERENCE	TIME	PEAK PERIOD (s)	PEAK WAVELENGTH (m)	PEAK WAVE DIRECTION (degree)
SAR Pass 1	1733	11.80	260	261°
SAR Pass 2	1749	12.55	245	323°
MANMAR	1500-1800	10.0 (swell only)	-	50° (swell only)
WAVEC Station 249	1727	13.3	-	32.6° (~320° for sea direction)
Hindcast Model	1500	11.1	-	340°
	1800	8.3	-	343°
Wind Direction	1500	-	-	345°
	1800	-	-	340°

analyses were conducted on the collected data. Further intercomparisons will need to be performed to answer the many questions that remain, particularly in regard to the directional spread of the wave field as SAR analysis is one of the only methods available to estimate this value directly.

Hindcast Model Results

Results from the hindcast modelling were supplied by F.G. Bercha Ltd. on magnetic tape. These were replotted to aid in the intercomparison.

Two distinctly different storms were modelled. A discussion on storm selection and characteristics can be found in the previous section on hindcast modelling.

Figures 84 and 85 contain overlayed time series plots of the predicted hindcast model (line) and measured buoy (dots) (Station 249) spectral statistics (significant wave height, peak period, average apparent period and peak direction) for the two storm periods. There are hindcast estimates every three hours with no missing observations. Although the two storms differed, some similarities in the model behaviour can be seen when examining these figures. The model predicts the total variance in the wave field (as represented by the significant wave height) quite well reproducing even small changes such as the drop during the passage of the storm centre on March 28. The peak of Event 1 was missed, probably due to the three-hour time step, resulting in an underestimate of the maximum significant wave height by 0.5 metres. The maximum discrepancy was around 1 metre. Both the predicted peak period and peak direction agree during storm build-up, though there is a tendency for the hindcast results to lead buoy observations (also seen in significant wave height). Once the storms were established or were abating, significant differences occurred in peak period and at times in peak direction. The hindcast model did not reproduce as well the more confused conditions from April 1 to April 3. The difference in average apparent period reflects the different cutoff frequency of the two sets of spectra.

To clarify these observations, corresponding heave and directional spectra were plotted. If one examines figures of storm development from 0900/10 to 0300/11 and 1500/27 to 0000/28 (Figures 86 and 87 respectively), it can be seen that the shift in the model peak precedes the observations even considering the

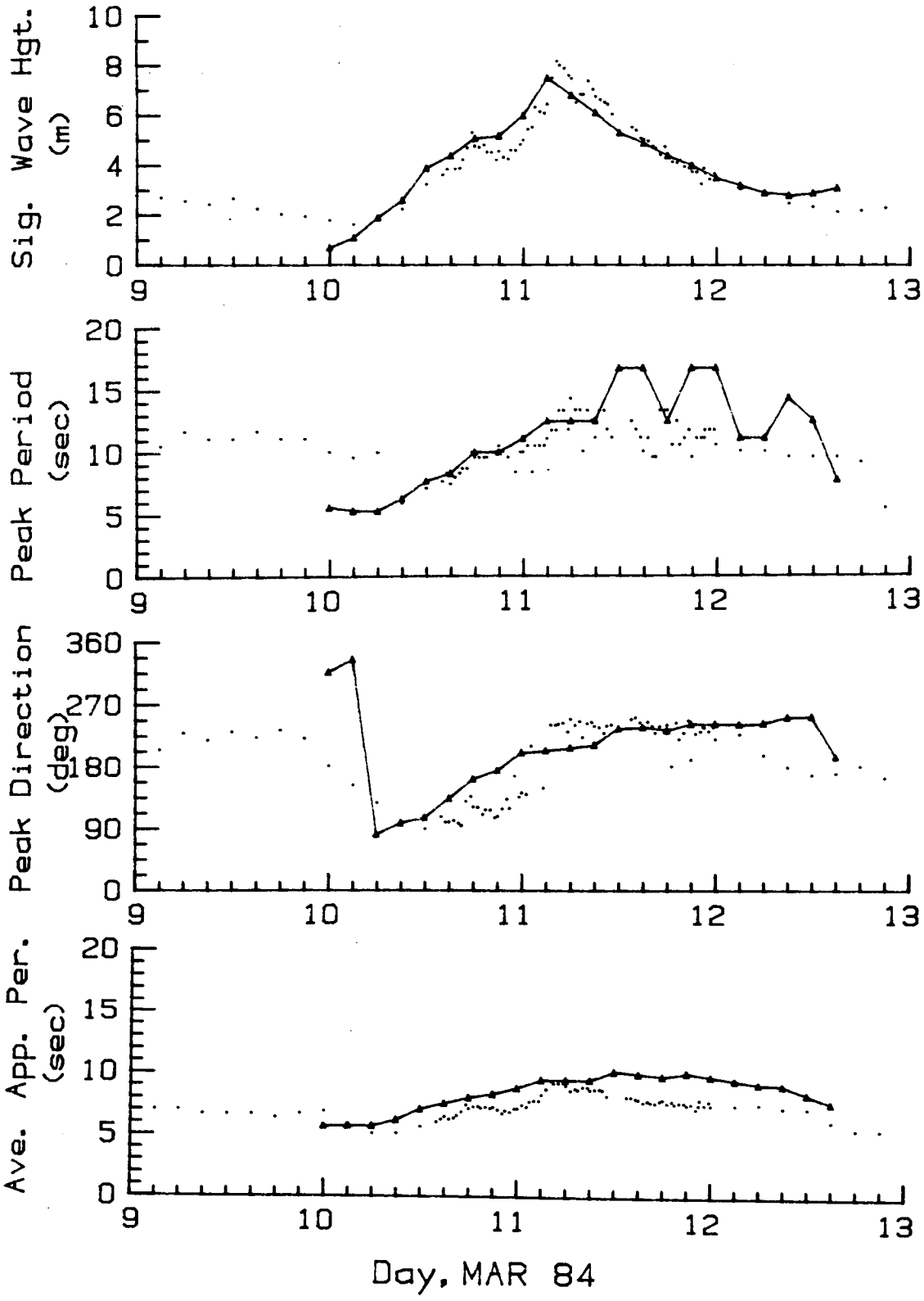

Figure 84. Event 1 significant wave height, peak period, average apparent period and peak direction hindcast results (solid) and buoy Station 249 (dotted).

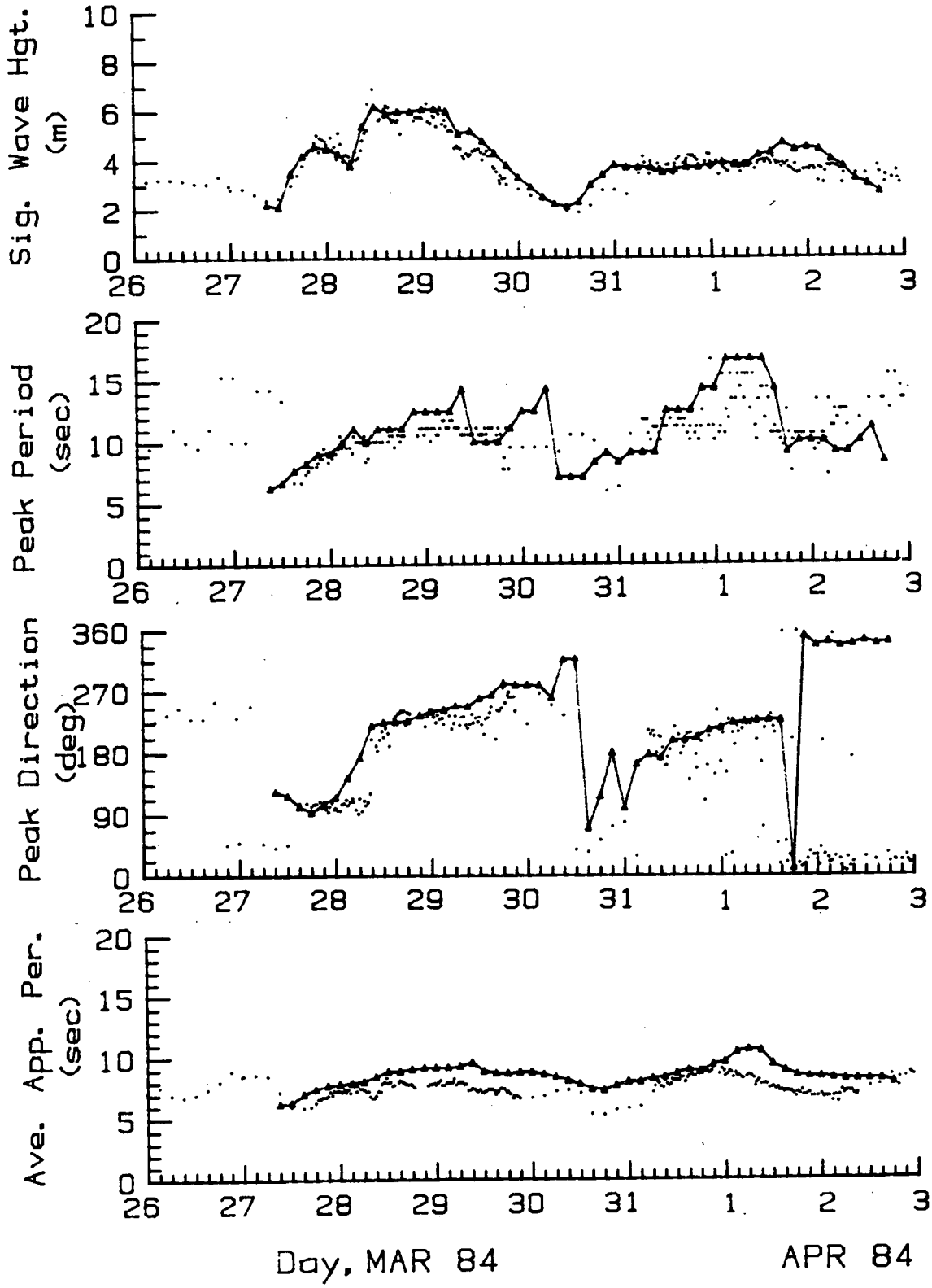

Figure 85. Event 2 significant wave height, peak period, average apparent period and peak direction hindcast results (solid) and buoy Station 249 (dotted).

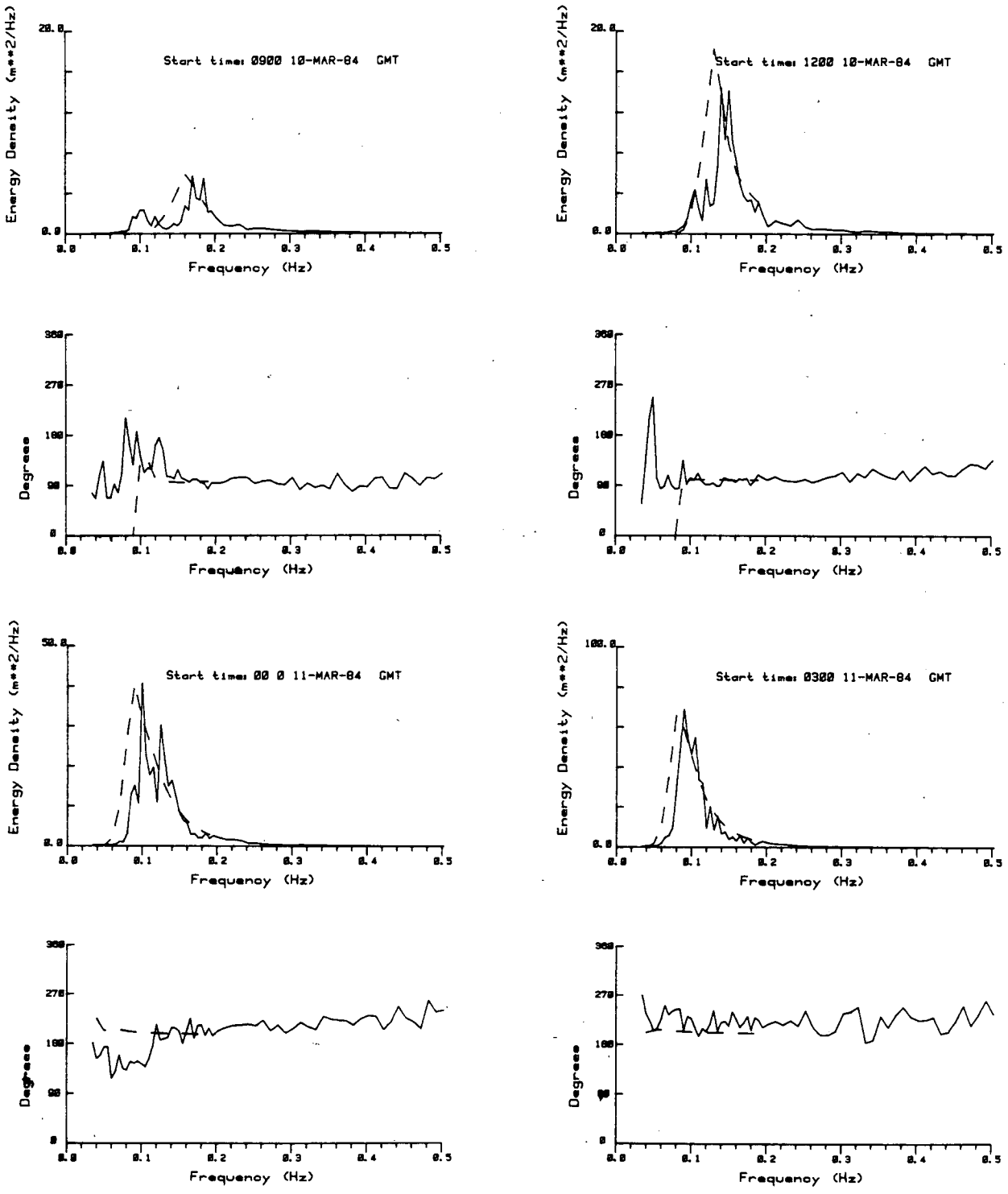

Figure 86. Overlayed heave spectra and mean direction Station 249 (solid) and model results (dashed) for records 0900/10, 1200/10, 0000/11 and 0300/11.

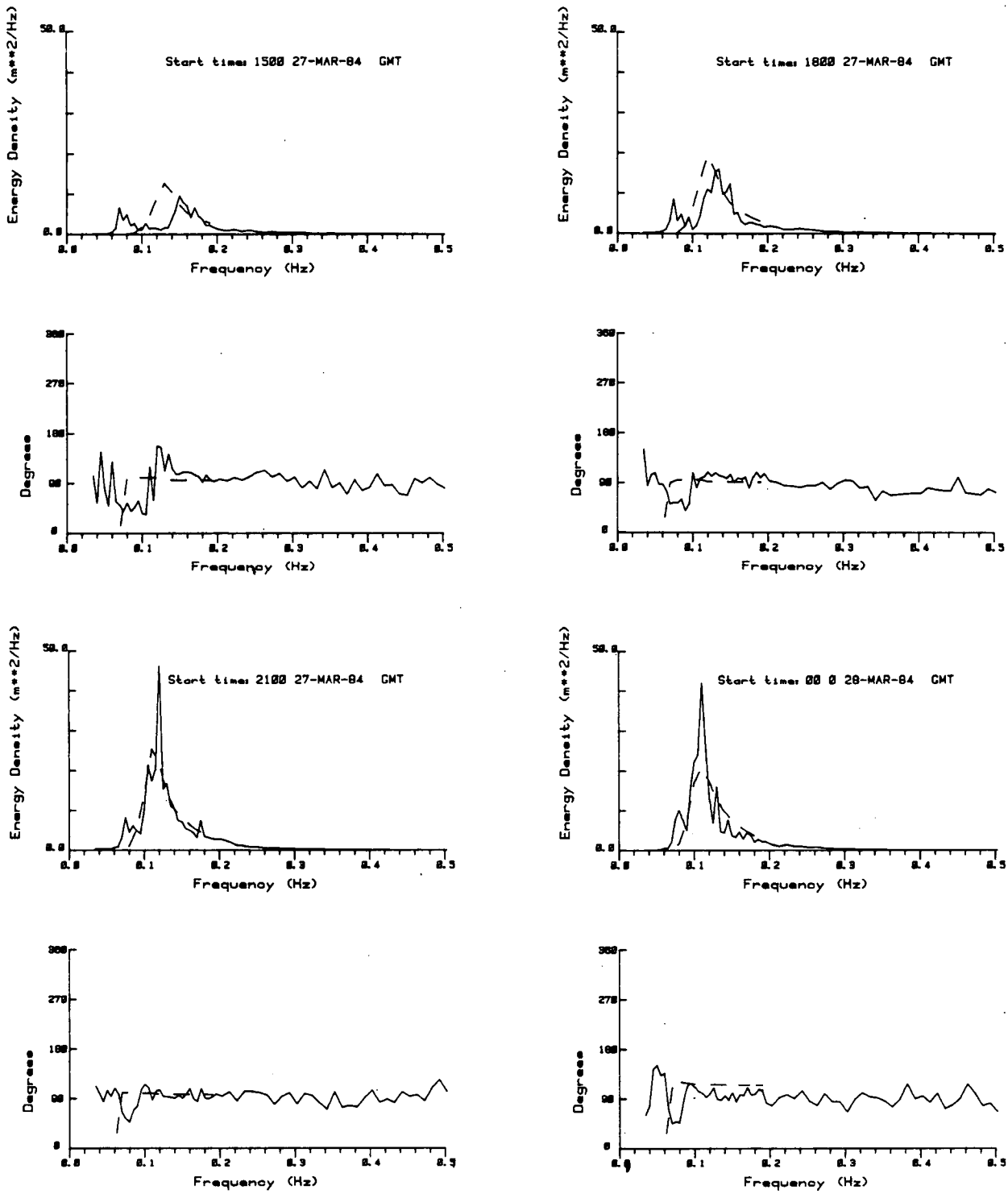

Figure 87. Overlayed heave spectra and mean direction Station 249 (solid) and model results (dashed) for records 1500/27, 1800/27, 2100/27 and 0000/28.

model frequency resolution of 0.01 Hz. This is also true for the mean directions (see 1500/10 to 0000/11). The model directions at all frequencies respond to the turning winds in unison while those for the buoy show a progression in response from high to low frequencies. The low frequency energy, present during both these build-up periods, is remnant energy from a previous event and is not expected to be modelled. Its presence, though, affects buoy estimates of significant wave height and the faster rise in energy of the model results, mentioned earlier when examining the time series (Figures 84 and 85), is more severe than these plots indicate.

During Event 1, the buoy spectra continue to grow through 0600/11 and the mean directions align with the wind. As this storm abates, 0900/11 to 0300/12 (Figure 88), significant energy in the model spectra shifts to low frequencies not observed by the buoy. This is possibly "forerunner" swell from the storm centre which has moved off although the directions would not support this.

As the storm centre passes over the study site during Event 2 (0000/28 - 0600/28) (Figures 87 and 89), the model responds to the shifting directions immediately at all frequencies. Again, the buoy results indicate a slower, progressive shift from high to low frequencies (through to 1200/28). Through the period of constant wind speed and direction (1200/28 - 0300/29), (Figure 90) , the two sets of spectra agree well, though with the buoy results considerably "peakier" and with an indication of less energy at low frequencies than in the model. This energy may be forerunner swell, given its direction preceding local wind shifts. As the winds abate (0600/29 - 0000/30), (Figure 91), the model spectra broaden and appear to have distinct swell. The predicted mean directions agree well until 1200/29, when the model again responds more quickly to the winds turning to the west. Through 0900 March 30, the low frequency energy from the west remains. Forerunner northeasterly swell is appearing in both the buoy (0.08 Hz) and model spectra (see directional spectra 0000/30, 0300/30 Figure 92) however, remnant westerly swell (< 0.08 Hz) is still present in the latter. By 1200/30 (Figure 93), local seas are being developed due to the rise in easterly winds (see mean buoy directions $f > 0.4$ Hz, 1200/30). By 1500/30 (Figure 93), energy is appearing in the mid-frequency bands of the hindcast spectrum though the buoy spectrum still consists of three distinct regimes, long period swell from the northeast (< 0.1 Hz), mid-frequency (0.1 - 0.15 Hz) remnant southwesterly energy from the previous

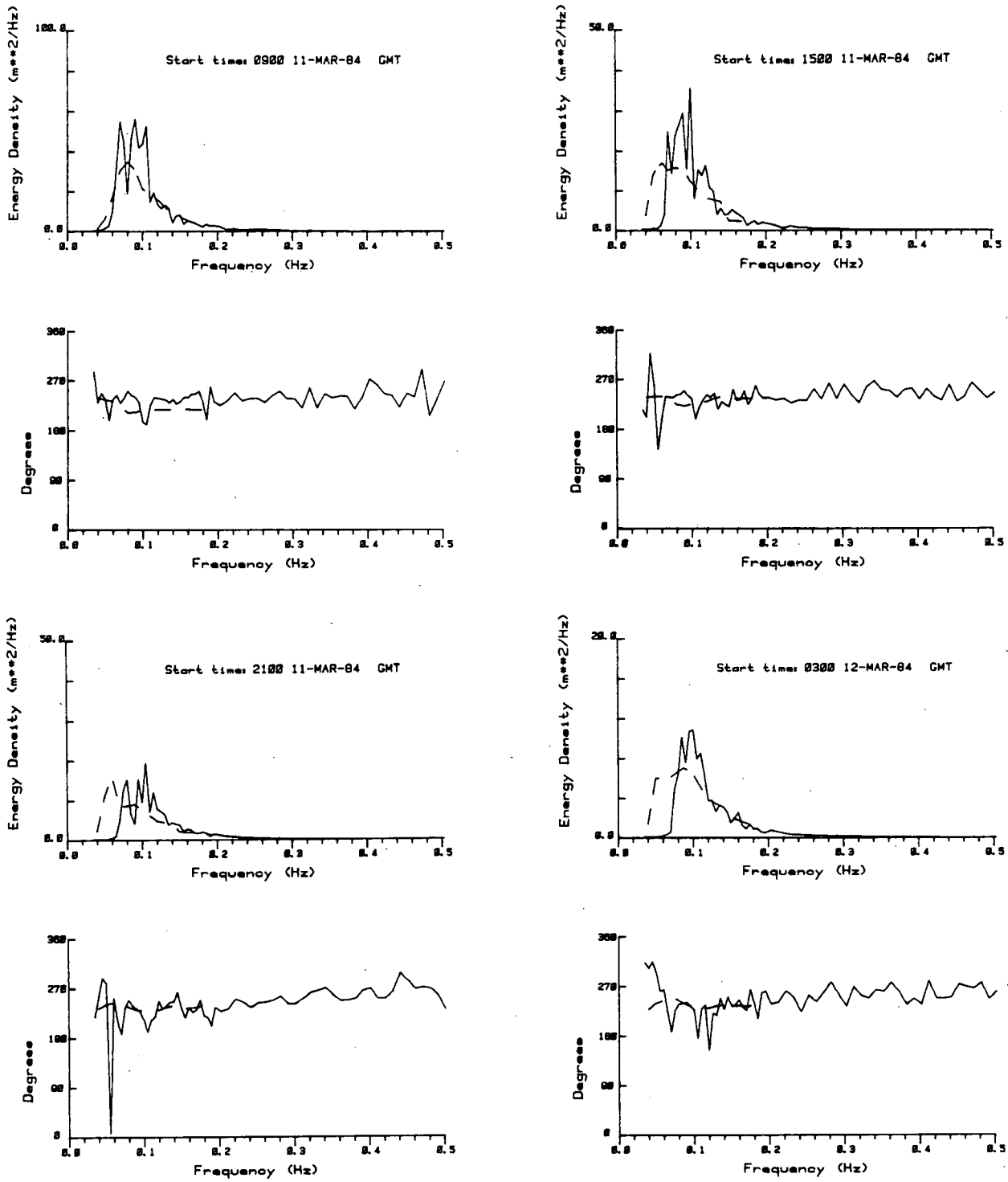

Figure 88. Overlayed heave spectra and mean direction Station 249 (solid) and model results (dashed) for records 0900/11, 1500/11, 2100/11, 0300/12.

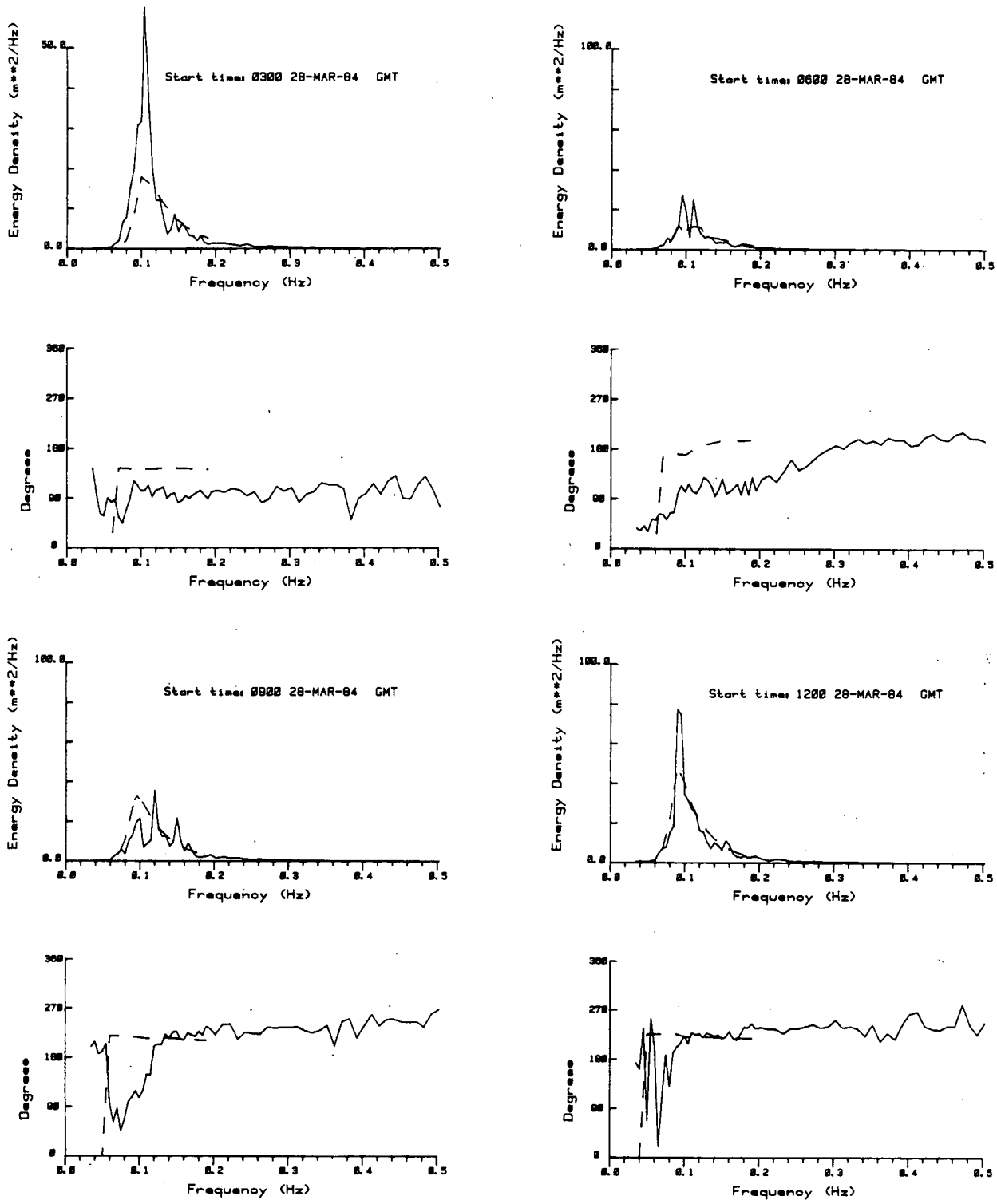

Figure 89. Overlayed heave spectra and mean direction Station 249 (solid) and model results (dashed) for records 0300/28, 0600/28, 0900/28, 1200/28.

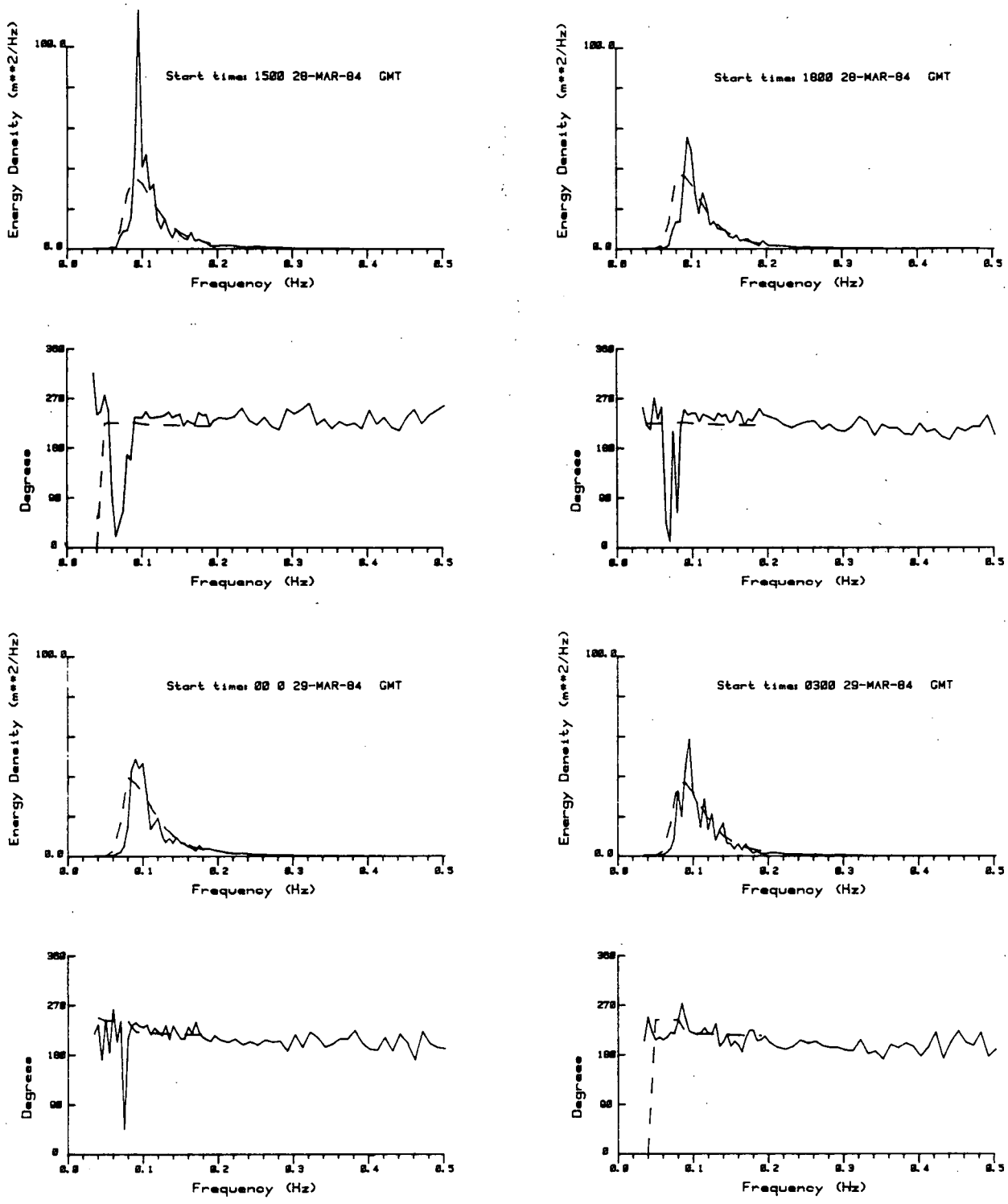

Figure 90. Overlayed heave spectra and mean direction Station 249 (solid) and model results (dashed) for records 1500/28, 1800/28, 0000/29, 0300/29.

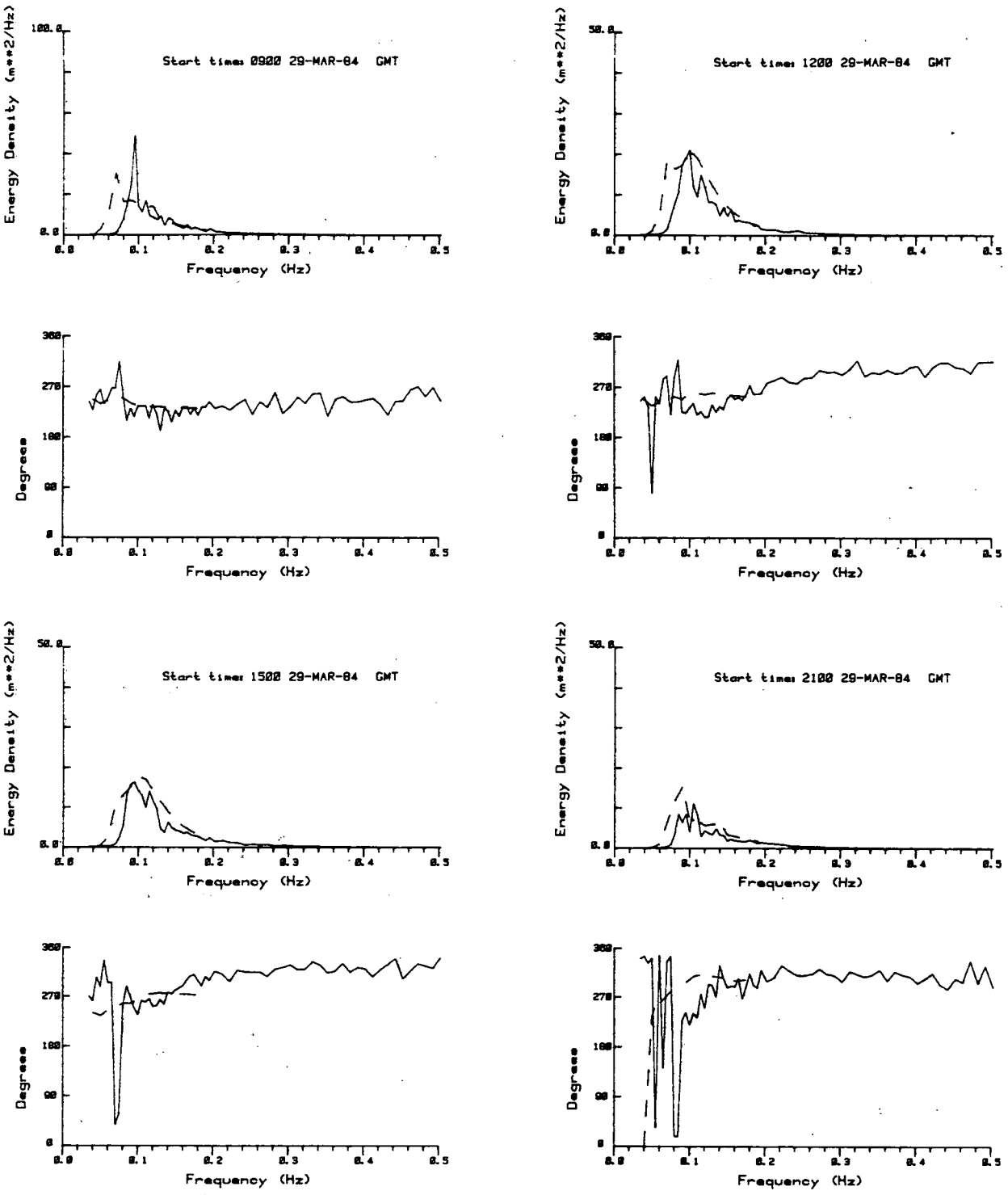

Figure 91. Overlayed heave spectra and mean direction Station 249 (solid) and model results (dashed) for records 0900/29, 1200/29, 1500/29, 2100/29.

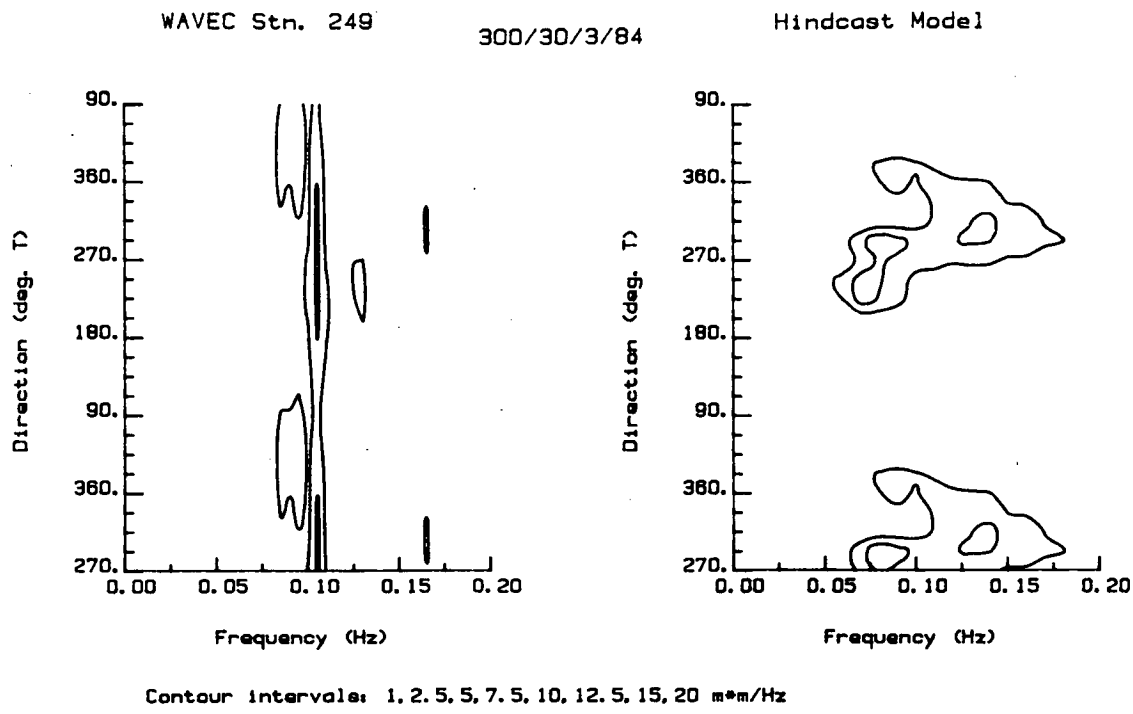

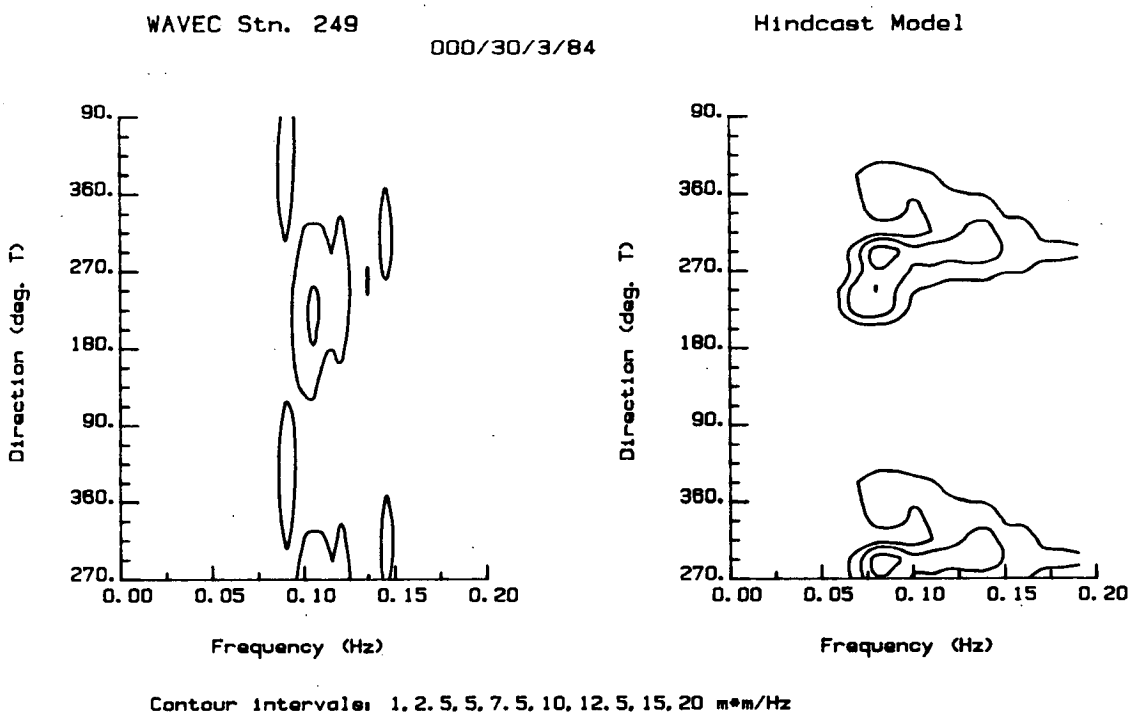

Figure 92. Contoured directional spectra Station 249 and model results for records 0000/30 and 0300/30.

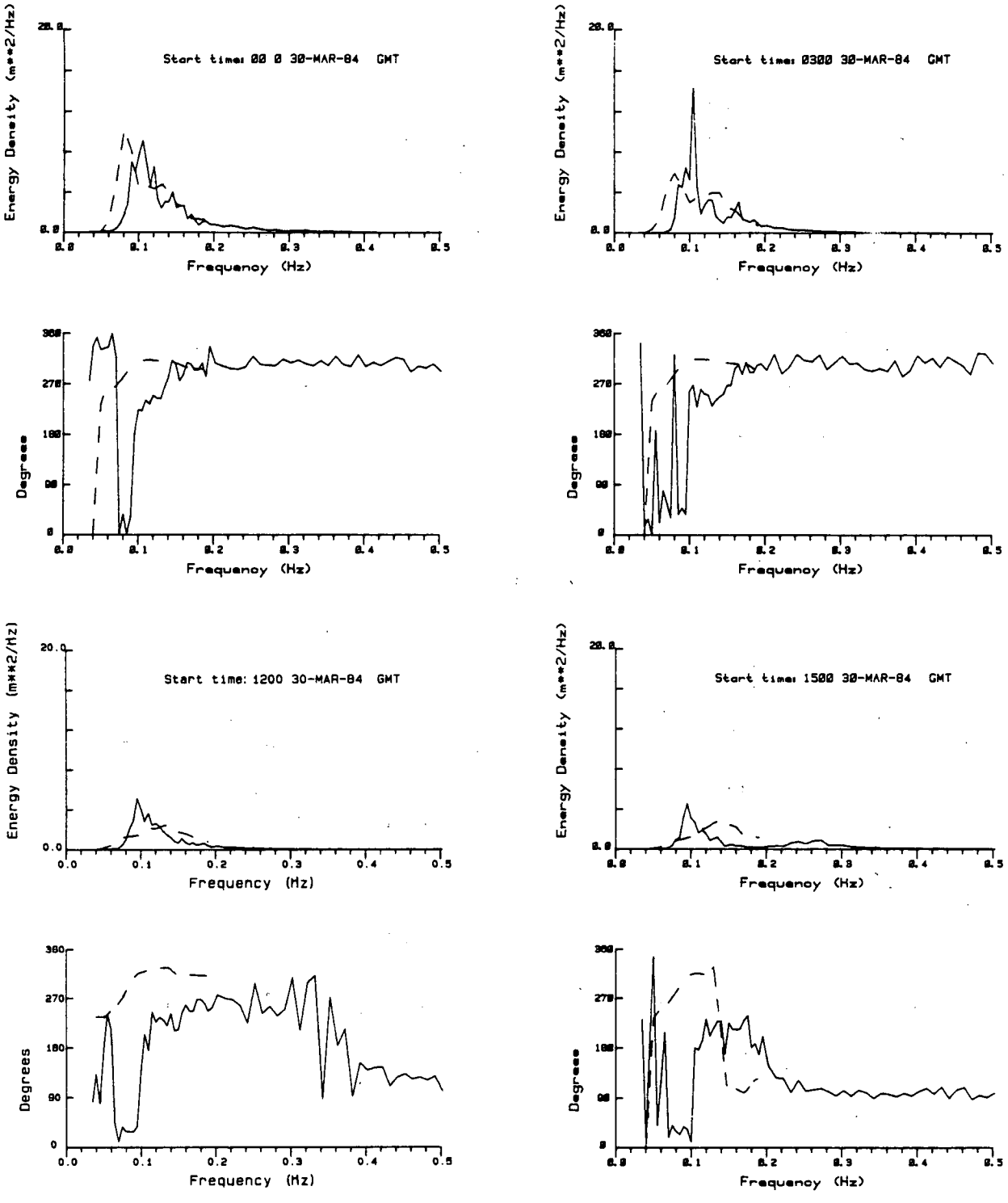

Figure 93. Overlayed heave spectra and mean direction Station 249 (solid) and model results (dashed) for records 0000/30, 0300/30, 1200/30, 1500/30.

storm and high frequency (> 0.2 Hz) easterly seas. Frequencies from 0.15 to 0.2 Hz appear to be in a transistion region. The energy between 0.2 and 0.3 Hz lies in the parametric domain of the hindcast model and could not be examined. Easterly winds continue to put energy into the mid-frequency band of the model spectra, which grows and shifts to lower frequencies. For the buoy, the low frequency energy stays relatively constant while that at higher frequencies grows as its position shifts to lower frequencies. Some nonlinear energy transfer can possibly explain the rise in energy between the two peaks (1800/30, 2100/30, 0000/31) (Figure 94), with a corresponding degradation of the southwesterly energy present previously in this region. During this period, the model is indicating low frequency energy (< 0.08 Hz), and it is possible that this is forerunner swell (due to the centre that has moved off) observed in the model before the buoy (seen at 0600/31 through to 1200/April 1). By 0600/31 (Figure 95), the long period (f < 0.1 Hz) southwesterly swell dominates the buoy spectrum. The buoy mid-frequencies (0.1 - 0.2 Hz) are showing a transistion between this swell and the easterly seas while modelled waves are aligned with the easterly winds and contain more energy (1200/31 - 1800/31) (Figure 95).

As the winds begin to rise on April 1 and turn from east, through north to northwest by 1200 April 2, the spectra show similar traits as observed earlier. The buoy measures north-northeasterly seas prior to the model with three direction regimes (0900/1, Figure 96). The model contains more low frequency energy and responds by 1200/1 (Figure 96). This response moves to lower frequencies by 1500/1 (Figure 96). All model frequencies greater than 0.1 Hz have the same direction. Though both spectra contain long period southwesterly swell, it is dominant in the model results. By 2100/1 (Figure 96), all frequencies greater than 0.06 Hz contain energy from the north. There is still significant south-southwesterly energy observed at the buoy site between 0.06 and 0.095 Hz (at higher frequencies than for the model). The higher frequency model directions and energy are preceeding those for the buoy. Through to the end of the modelling period, the buoy never shows the build-up of energy between 0.1 and 0.15 Hz as modelled.

The various observations can be summarized as follows. The model resulted in a more rapid development of the spectrum than observed. This may be reflecting the hindcast site (see Figure 1) which is east of the buoy location while

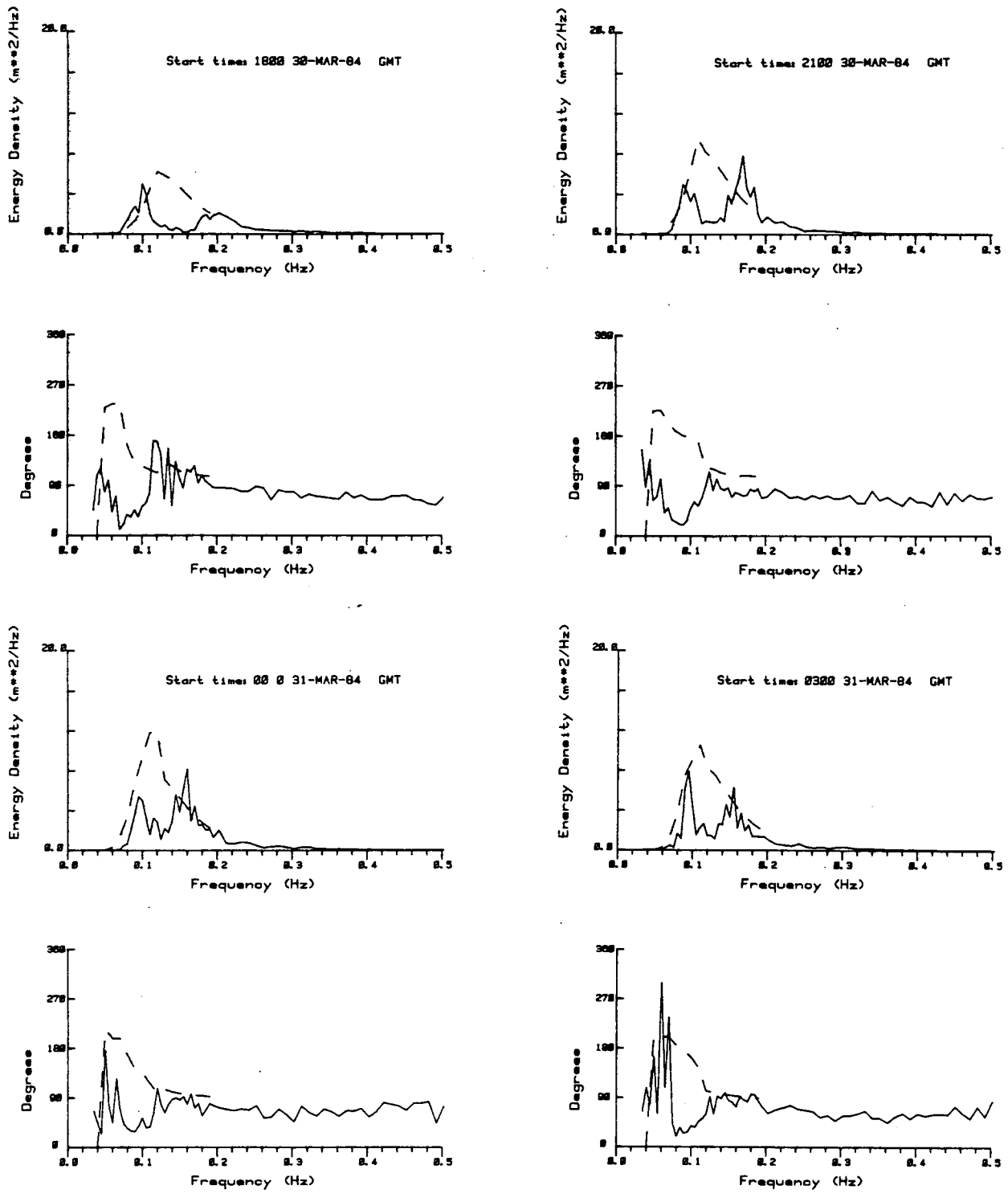

Figure 94. Overlayed heave spectra and mean direction Station 249 (solid) and model results (dashed) for records 1800/30, 2100/30, 0000/31, 0300/31.

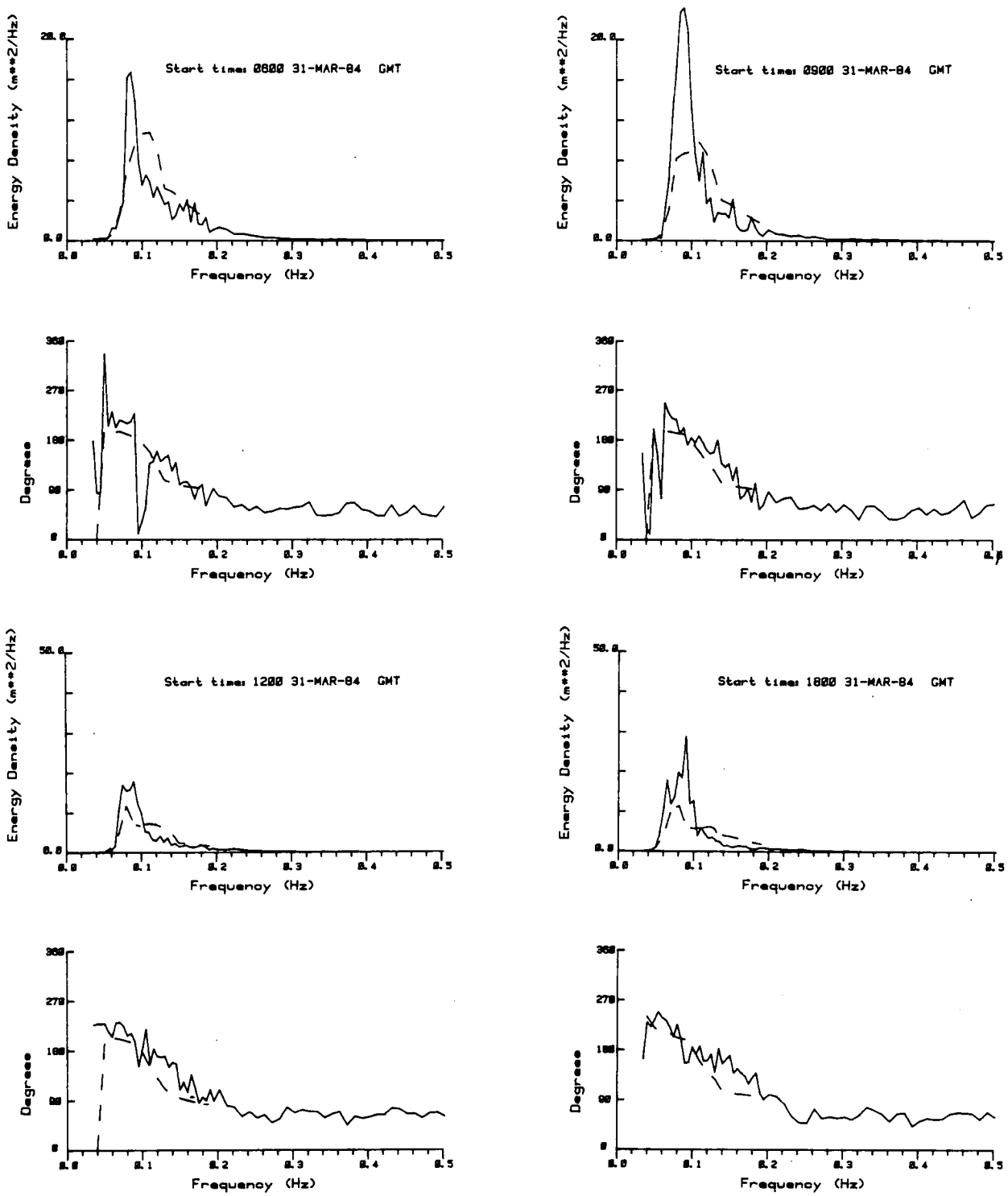

Figure 95. Overlayed heave spectra and mean direction Station 249 (solid) and model results (dashed) for records 0600/31, 0900/31, 1200/31, 1800/31.

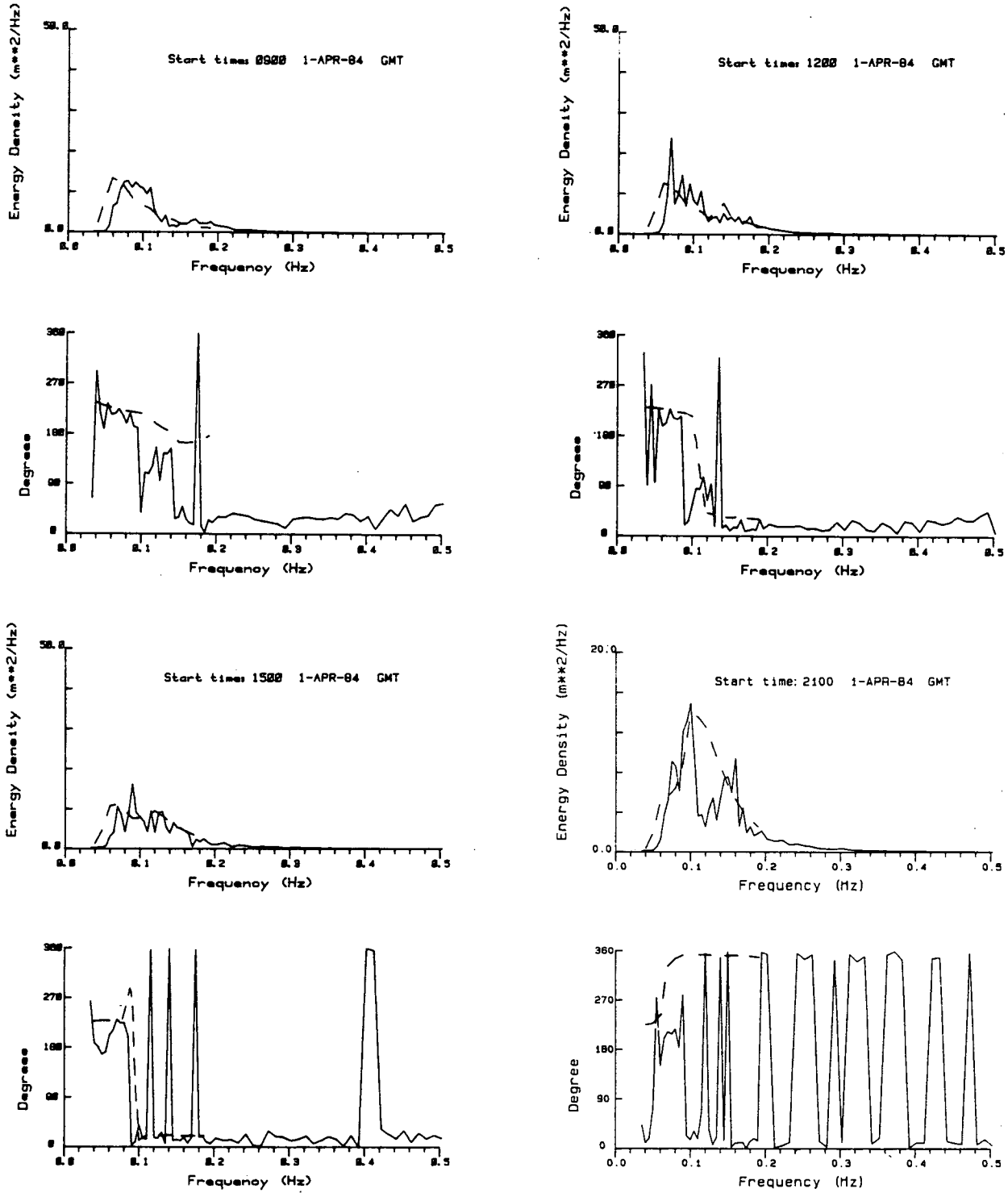

Figure 96. Overlayed heave spectra and mean direction Station 249 (solid) and model results (dashed) for records 0900/1, 1200/1, 1500/1, 2100/1.

winds during storm development were also from the east. It is possible that conditions were felt at the hindcast site before reaching the buoy. In a recent paper by Komen et al. (1984), too rapid development of the spectrum was shown to be consistent with a model lacking any energy dissipation at low frequencies with all the loss occurring at high frequencies assuming an f^{-5} dependence (such as Resio's model). To check that an f^{-5} assumption was appropriate in this application, sample spectra were plotted on log-log scale for the two storms (Figure 97). The agreement is good for frequencies greater than 0.3 Hz though possibly reduced between 0.2 and 0.3 Hz.

Komen et al. (1984) also indicated that if energy dissipation is occurring at the low frequencies, a shift of the frequency of minimum angular spread away from the peak frequency (to ~15% higher frequencies) occurs at equilibrium. Figure 98 shows a time series plot of the ratio (solid line) of peak frequency to the frequency of maximum cosine spread value (i.e. minimum angular spread) overlayed on wind speed and significant wave height. Though extremely noisy, there is some indication of a shift in the ratio (often at 1 from 1800/27 to 0300/28, storm build-up, less than 1 at 1500/28, saturated spectrum). This should be examined in future studies.

Without available information on energy in the parametric domain of the model, it is not clear whether the mid-frequency rise in energy observed, for example, on March 30 and April 1, results from energy above 0.19 Hz moving into the discrete spectral domain, as is the case during model spin-up or if winds are adding energy directly into this band, as is suspected given available information. The latter is not consistent with the observed spectral development. The hindcast spectra are generally broader in frequency though reduced in directional spread compared to buoy results. The directional spectra show characteristics dominated by the heave energy distribution, as expected. The truncation of the Fourier expansion to its first four components results in a broad peak in direction which is one of the major drawbacks of the Longuet-Higgins analysis. On at least three occasions, the model appeared to resolve two directional peaks, at a single frequency, not clear in the buoy data (e.g. 0300/28 and 1800/29 through 0300/30, and 0000/31) (Figures 92 and 99). The spread of energy in frequency of the model spectrum on the other hand is a drawback of this approach. The broader spectrum

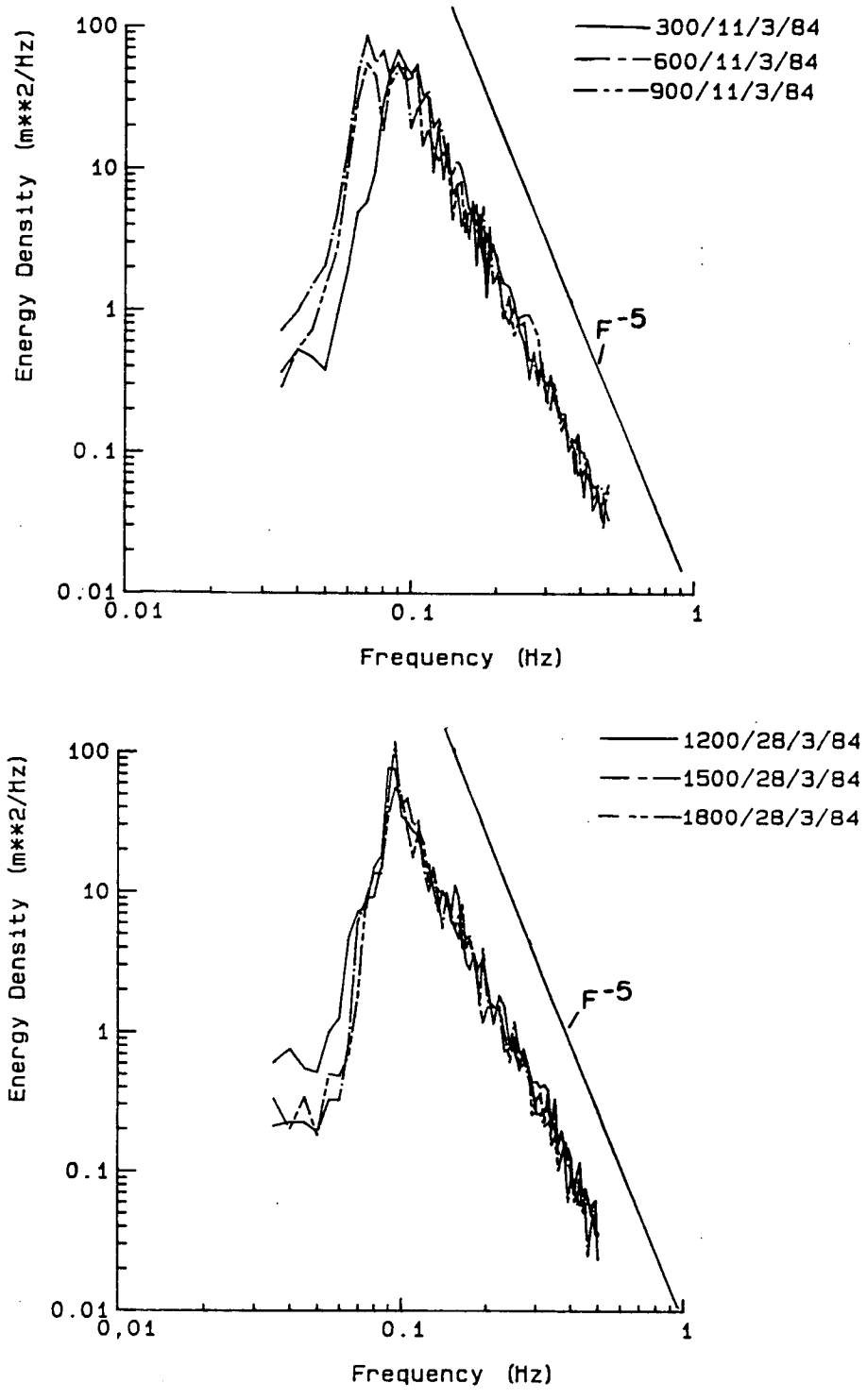

Figure 97. Sample spectra from Event 1 (upper) and Event 2 (lower) showing F-5 dependence.

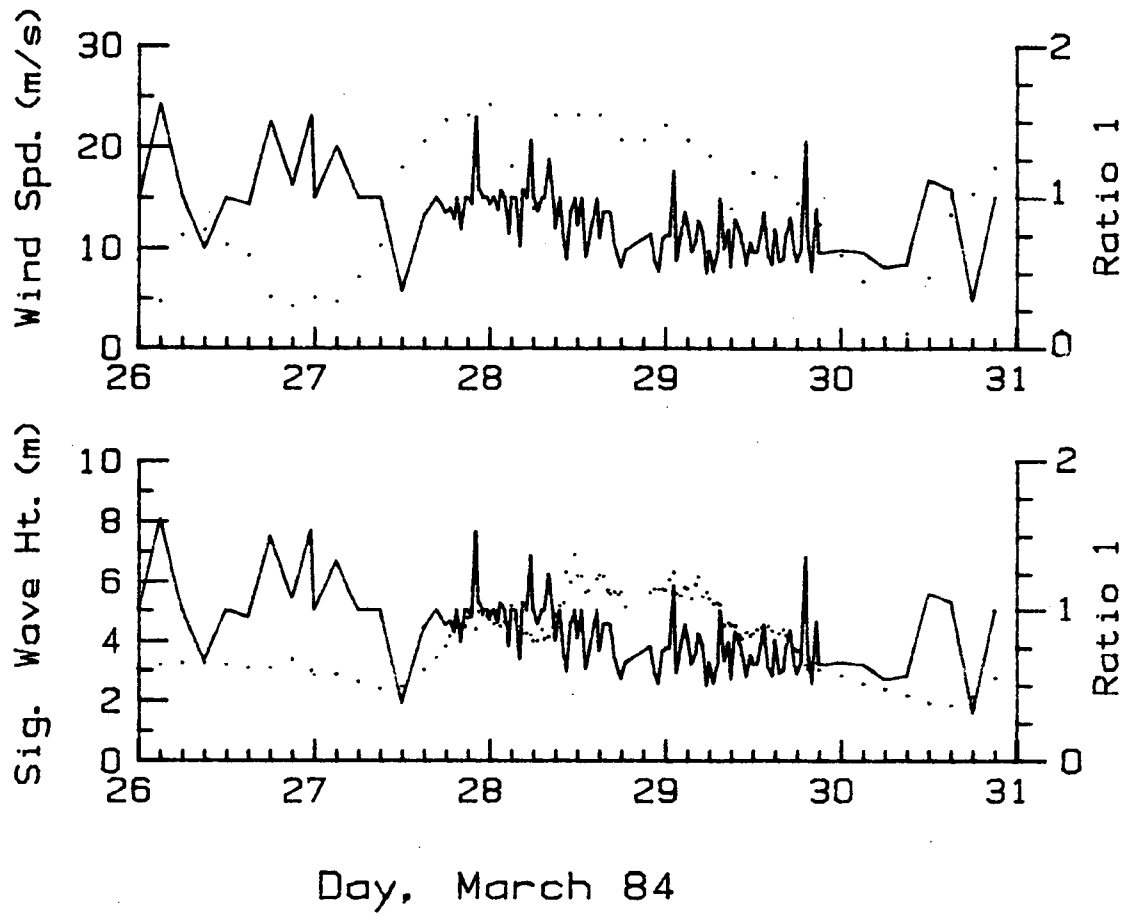

Figure 98. Time series of the ratio of peak frequency to the frequency of maximum value of cosine spread (solid line), in relation to significant wave height and wind speed (dotted line)

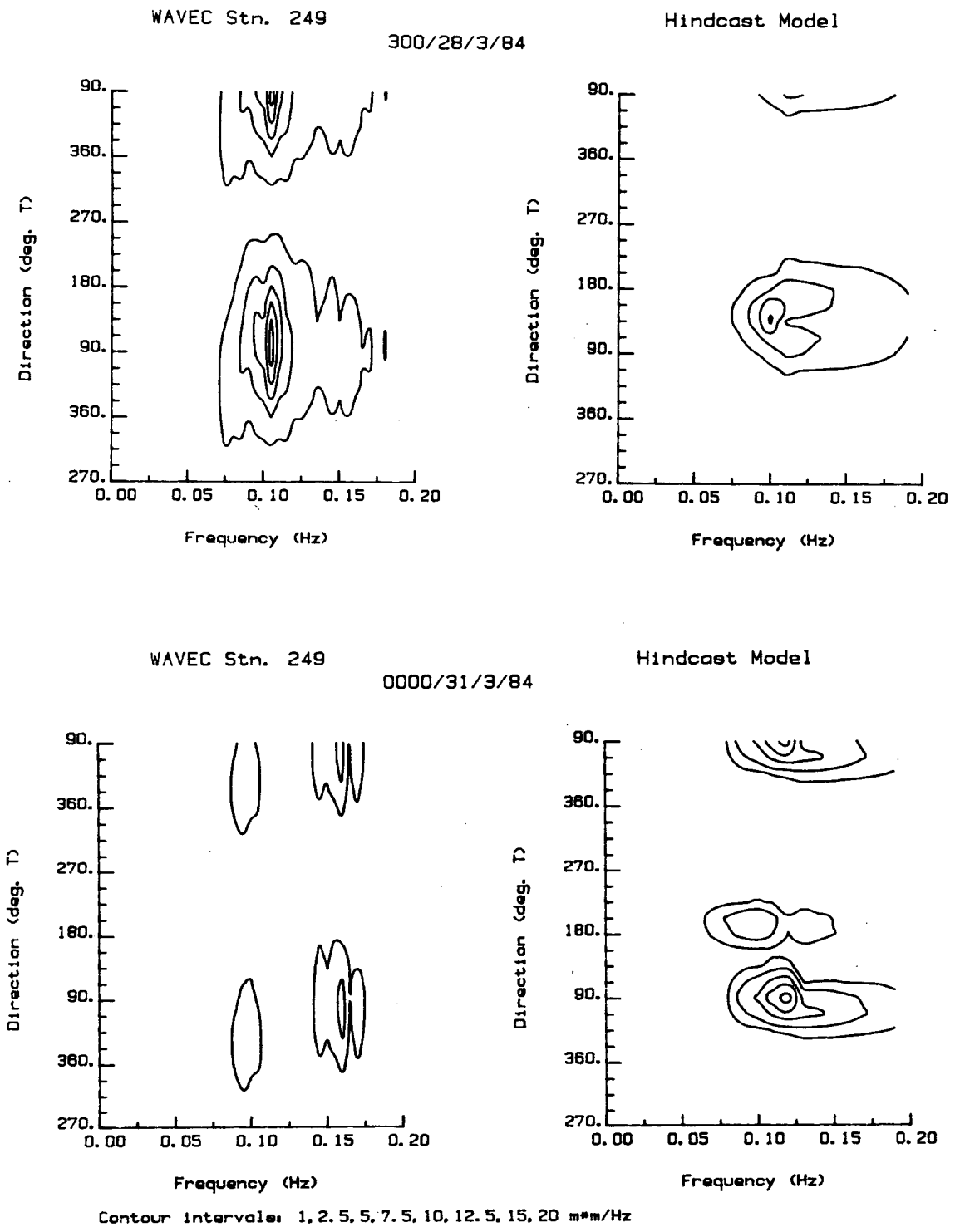

Figure 99. Contoured directional spectra Station 249 and model results for records 0300/28, 0000/31.

and lack of multiple peaks may be partially reflecting the poorer frequency resolution though it is potentially a result of too large a contribution of the nonlinear interaction terms. The latter could explain the tendency to dump too much energy into low frequencies during storm abatement, with a corresponding degradation of the earlier spectral peak (March 11) and the loss of remnant energy around 0.1 Hz. The model did predict long-period swell entering the area (March 29-30) though at a frequency lower than observed. As the study area was relatively shallow, around 80 metres, the development locally of low frequency energy < 0.06 Hz, or energy entering from other areas should be reduced. The model did not take water depth into account.

WAVE SLOPE STATISTICS

Development of Wave Profiles

As the WAVEC buoy offered the opportunity to examine wave slopes directly, unlike the "heave-only" buoy which requires some assumptions on wavelength and wave shape in order to calculate a surface slope, it was felt that a preliminary analysis of wave slope statistics was warranted.

Records from Station 249 were obtained for the two storm periods March 10-12 and March 27-31. These were corrected with the instrument specific amplitude and phase transfer functions. A zero upcrossing analysis was then performed on each record in order to locate the positions of preceding trough, zero upcrossing point and following crest for each wave. As the sampling rate was too coarse to allow for a wave-by-wave analysis of mean values, it was decided to average each statistic over the record to compare them with other average statistics such as significant wave height or spectral shape parameters. The resolved slopes (i.e. Square root $(S_1^2 + S_2^2)$) were summed to provide a record mean and maximum wave front slope (i.e. trough to crest), mean trough front slope (i.e. trough to first zero upcrossing), mean crest front slope (i.e. zero upcrossing to crest) and mean crest to mean trough slope ratio as an indicator of shape asymmetry. Figure 100 illustrates these definitions in light of the standard calculations based on wavelength and height (according to definitions of Kjeldsen and Myrhaug, 1979).

It is important to note at this stage that using different approaches to calculate the mean slope values, as well as the mean slope ratios, can provide significantly different results. A mean slope value can be obtained using either of the following equations.

$$\frac{1}{N}\sum^{N}\left[(S_1^2 + S_2^2)^{1/2}\right] \tag{8}$$

or

$$\left[\frac{1}{N}\sum^{N}(S_1^2 + S_2^2)\right]^{1/2} \tag{9}$$

Where S_1 and S_2 are the two slope components.

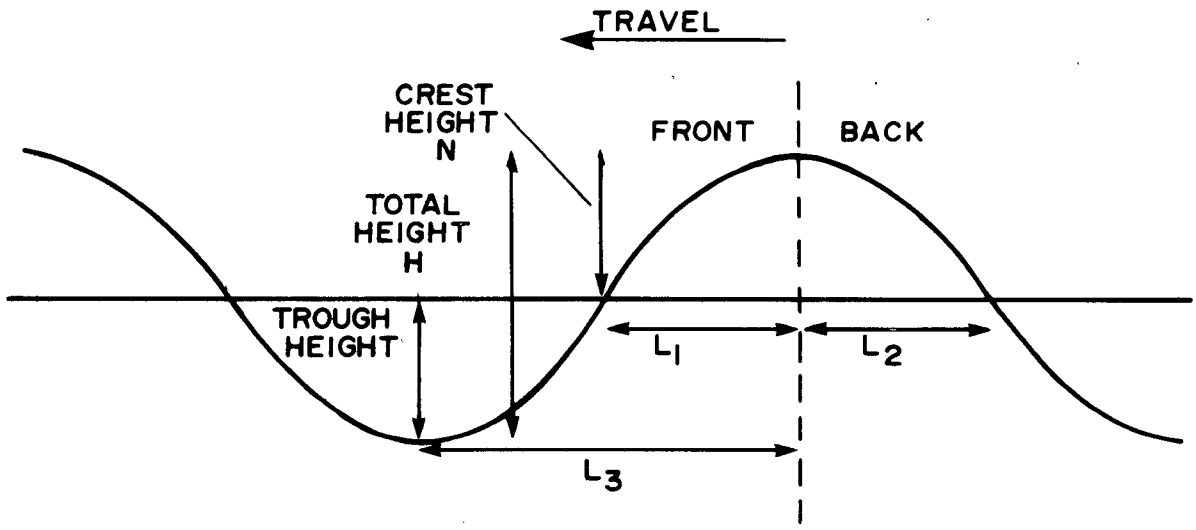

	COMPARED WITH
CREST FRONT STEEPNESS = N/L_1	MEAN CREST FRONT SLOPE
CREST BACK STEEPNESS = N/L_2	MEAN CREST BACK SLOPE
VERTICAL ASYMMETRY = L_2/L_1	$\frac{\text{MEAN CREST FRONT SLOPE}}{\text{MEAN CREST BACK SLOPE}}$
HORIZONTAL ASYMMETRY = N/H OR $\frac{(N/L_1)}{(H/L_3)}$	$\frac{\text{MEAN CREST FRONT SLOPE}}{\text{MEAN FRONT SLOPE}}$

Figure 100. Definition sketch of steepness parameters.

Equation 8 was used in this study as it was felt that the sum of the resolved slope is conceptually more desirable as we are interested in the properties of the slope magnitudes. Equation 9 has been used in the literature for calculation of the RMS slope. Figures 101 and 102 show regressions of the mean front and mean crest front slopes calculated using both equations. An approximately 18% increase is observed when using Equation 9. Similarly, significant differences are obtained if one calculates the mean of the ratio of crest slope over trough slope or the ratio of the mean crest slope over mean trough slope as indicators of asymmetry. This will be seen later in regressions against wind speed. Such differences must be kept in mind when comparing results of different studies.

Figure 103 shows the mean and maximum wave front slope (solid line) for the two storm periods compared against significant wave height. The maximums were initially examined to see if there was any upper slope resolution limit of the WAVEC buoy. In this experiment, there did not appear to be an upper limit although storm conditions were not that severe. These maximums were consistent with the experimental results of Kjeldsen and Myrhaug (1979)(as cited by LeBlond, 1982), who calculated a forward face steepness of 0.32 to 0.78. In Figure 103 there is an obvious co-variance with significant wave height though the rise in slope before the two storms and at the end needs to be explained. The mean crest front slope behaved similarly. The explanation for the rise can be seen if one plots mean wave front slope, or mean crest front slope, against wind speed and wind direction (Figures 104 and 105). The winds have not been corrected for anemometer height. The mean slopes (line) are responding to the wind field faster than the total heave variance given by the significant wave height. The respective lags are on the order of three hours or less for the slope (i.e. on the order of the wind sampling rate) and on the order of nine hours for significant wave height. This probably reflects an increase in wave slope at high frequencies, almost immediately with wind speed, while there is little contribution to the total variance at these frequencies. There was no obvious dependence on wind direction.

In order to quantify these observations, regression analyses were performed and shown in Figures 106, 107 and 108. Dashed lines indicate 95% confidence limits. Figure 108, showing the ratio of mean crest to mean trough slope, is an indication of slope asymmetry about mean sea level. Figure 109 shows a similar

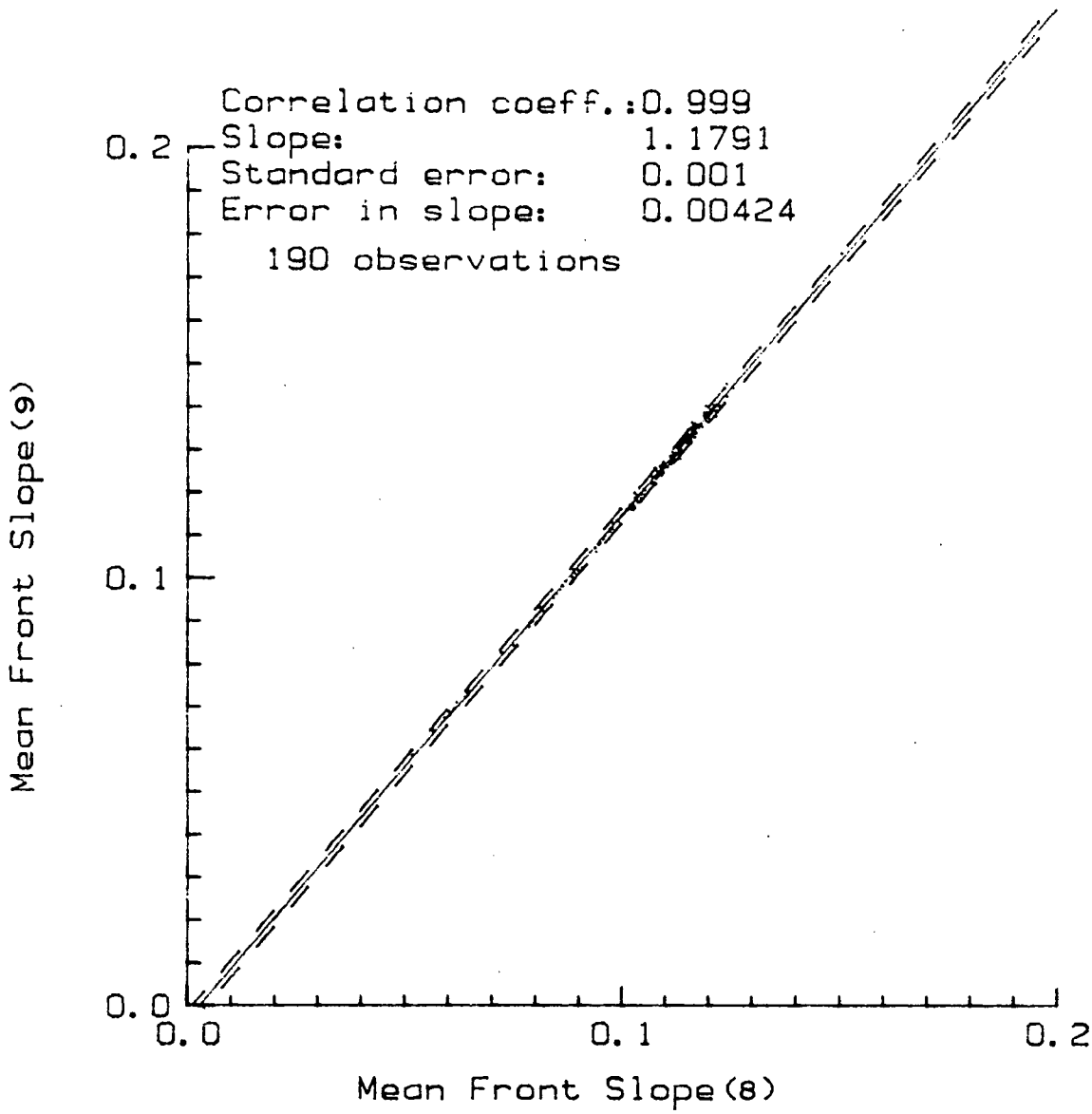

Figure 101. Regression of mean front slope calculated using Equation 9 vs. Equation 8.

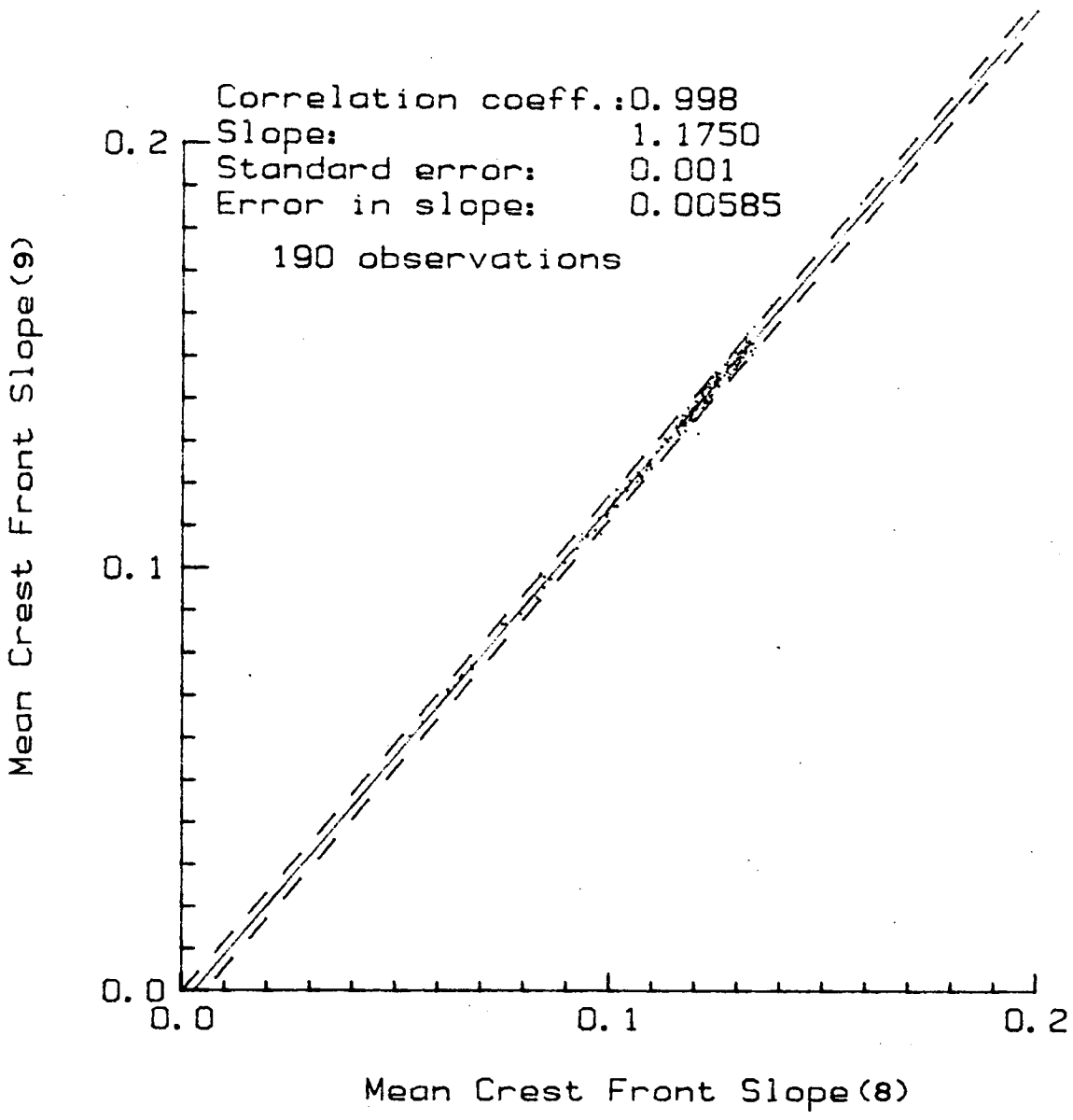

Figure 102. Regression of mean crest front slope calculated using Equation 9 vs. Equation 8.

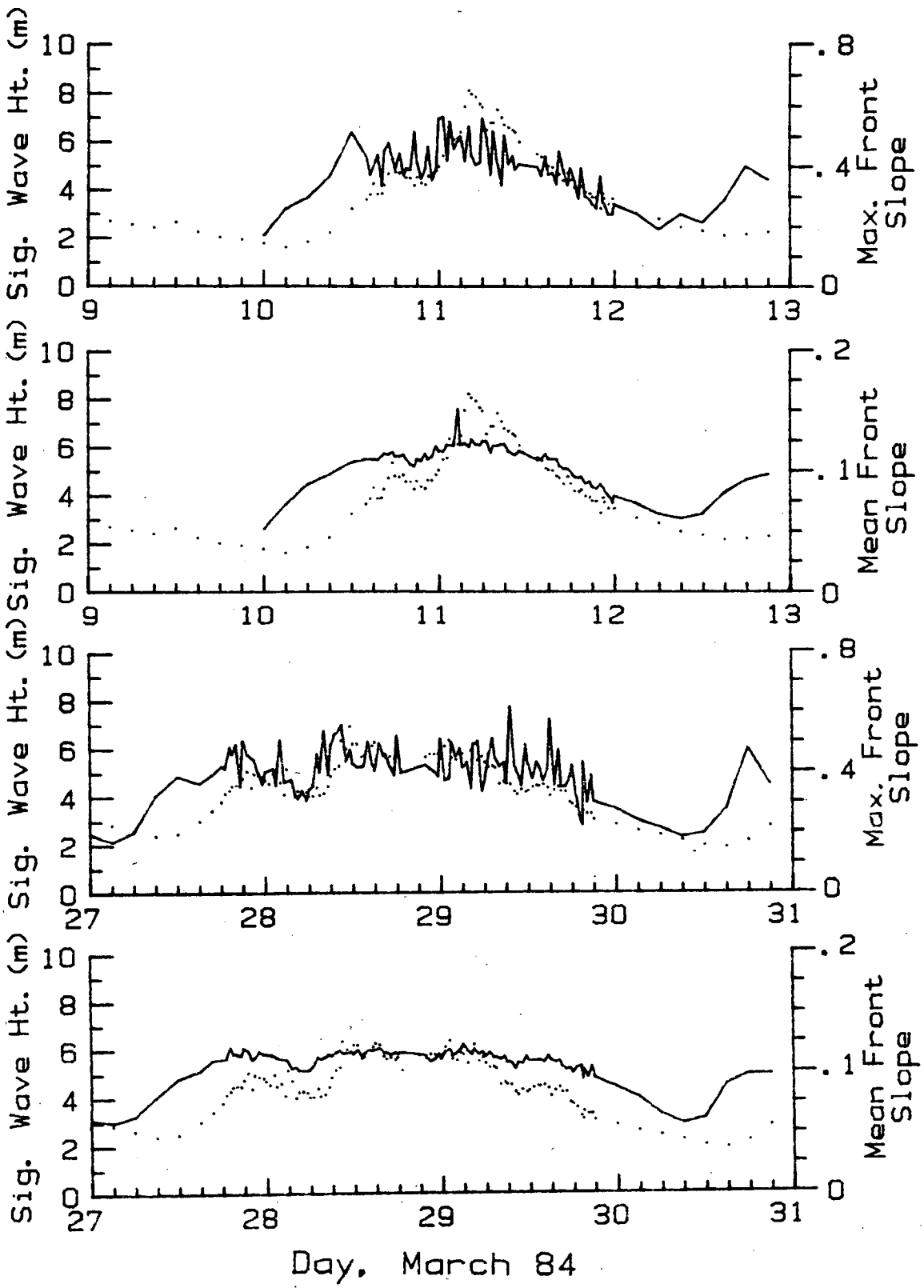

Figure 103. Mean and maximum wave front slope (solid) compared to significant wave height (dotted) during Event 1 and Event 2.

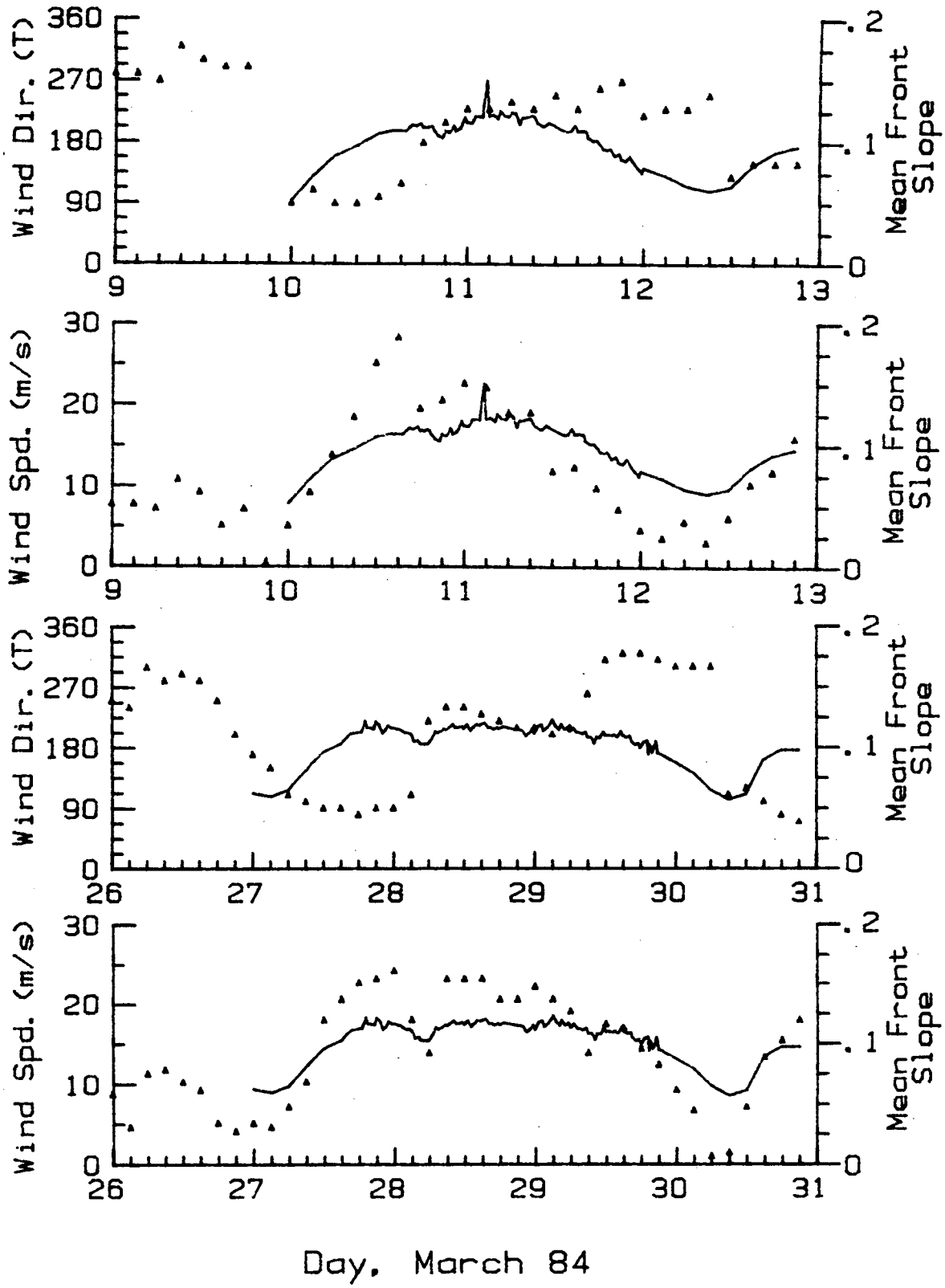

Figure 104. Mean wave front slope (solid) compared to wind speed and direction (triangle) during Event 1 and Event 2.

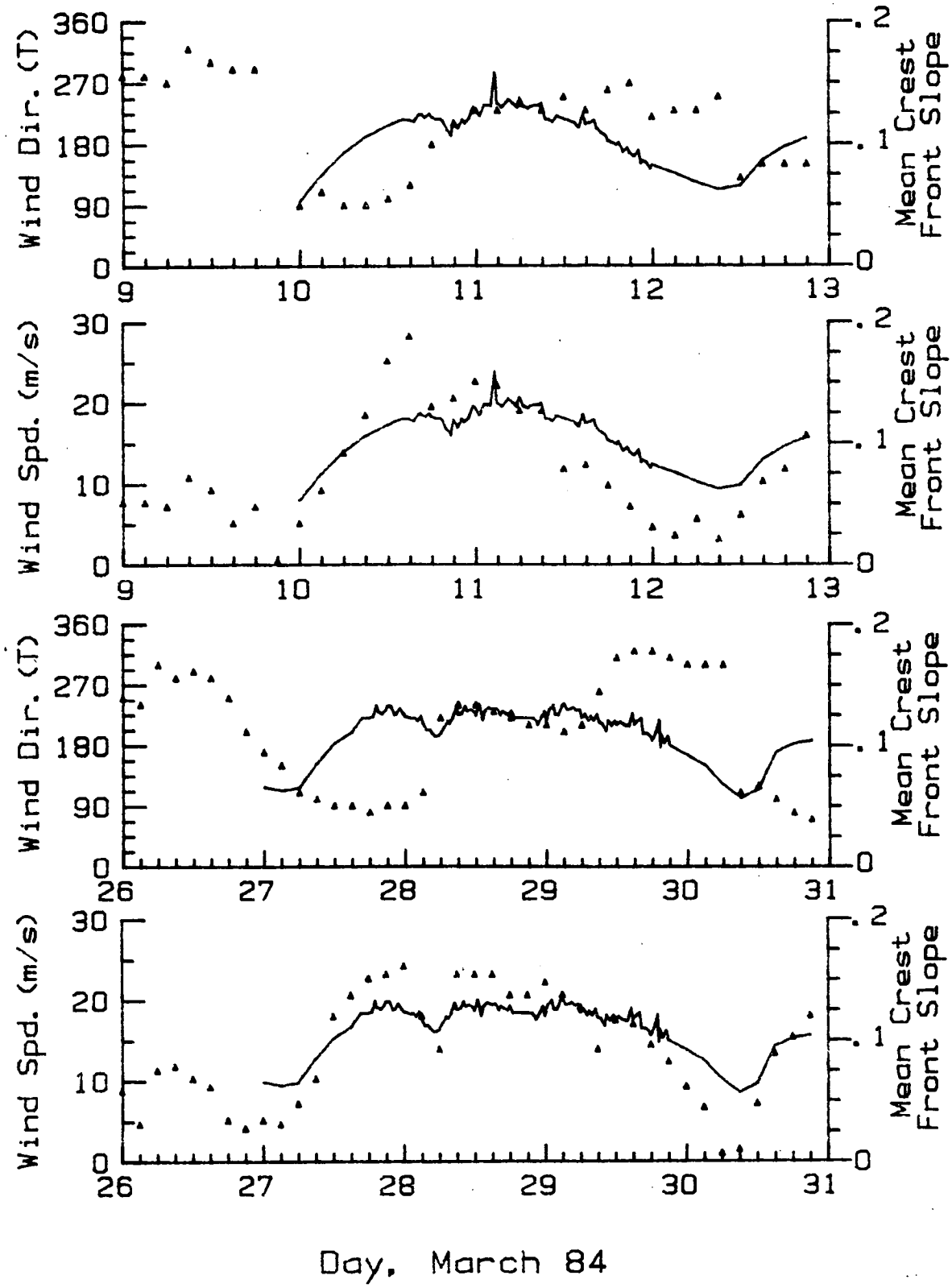

Figure 105. Mean crest front slope (solid) compared to wind speed and direction (triangle) during Event 1 and Event 2.

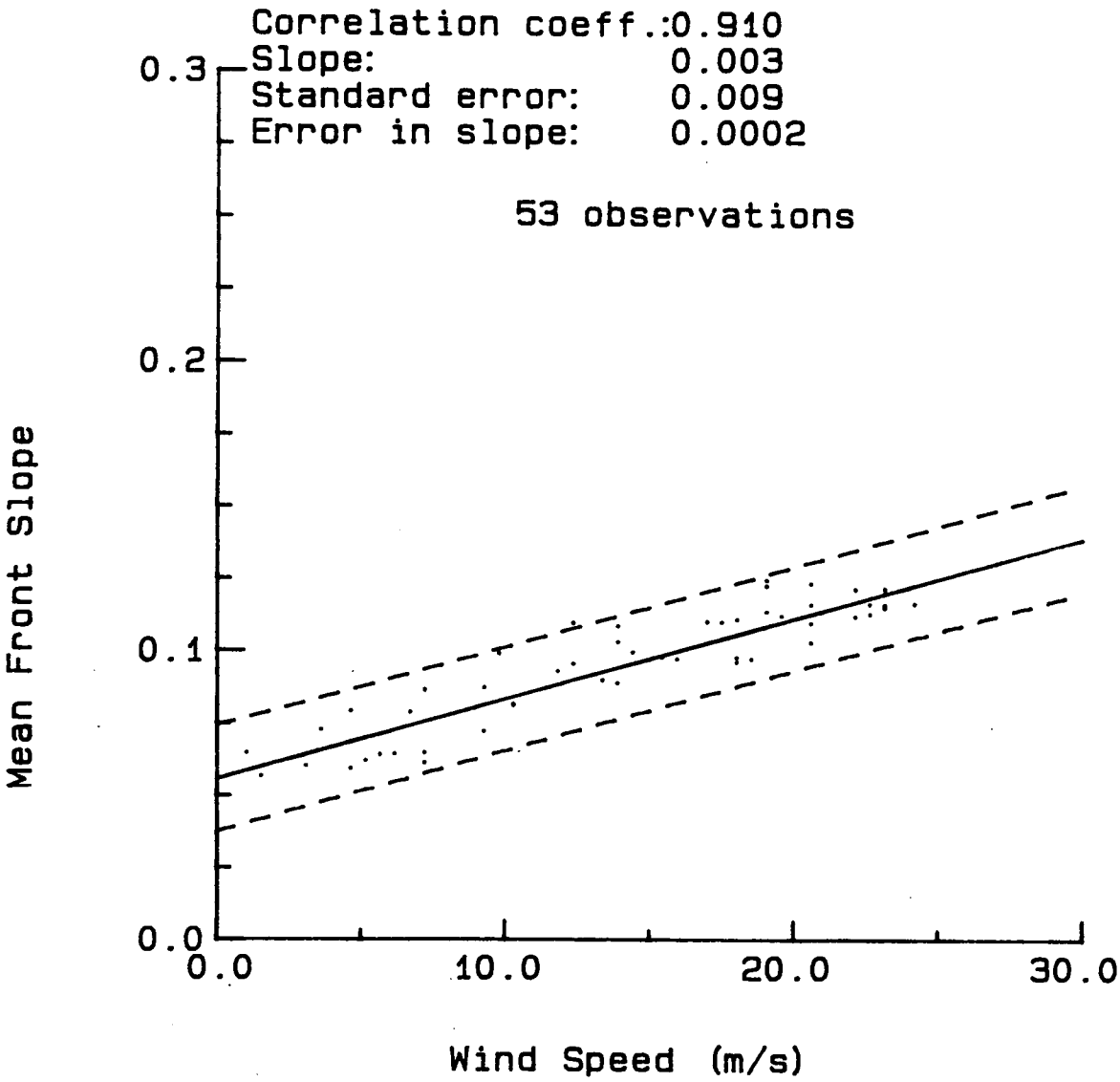

Figure 106. Regression of mean wave front slope against wind speed.

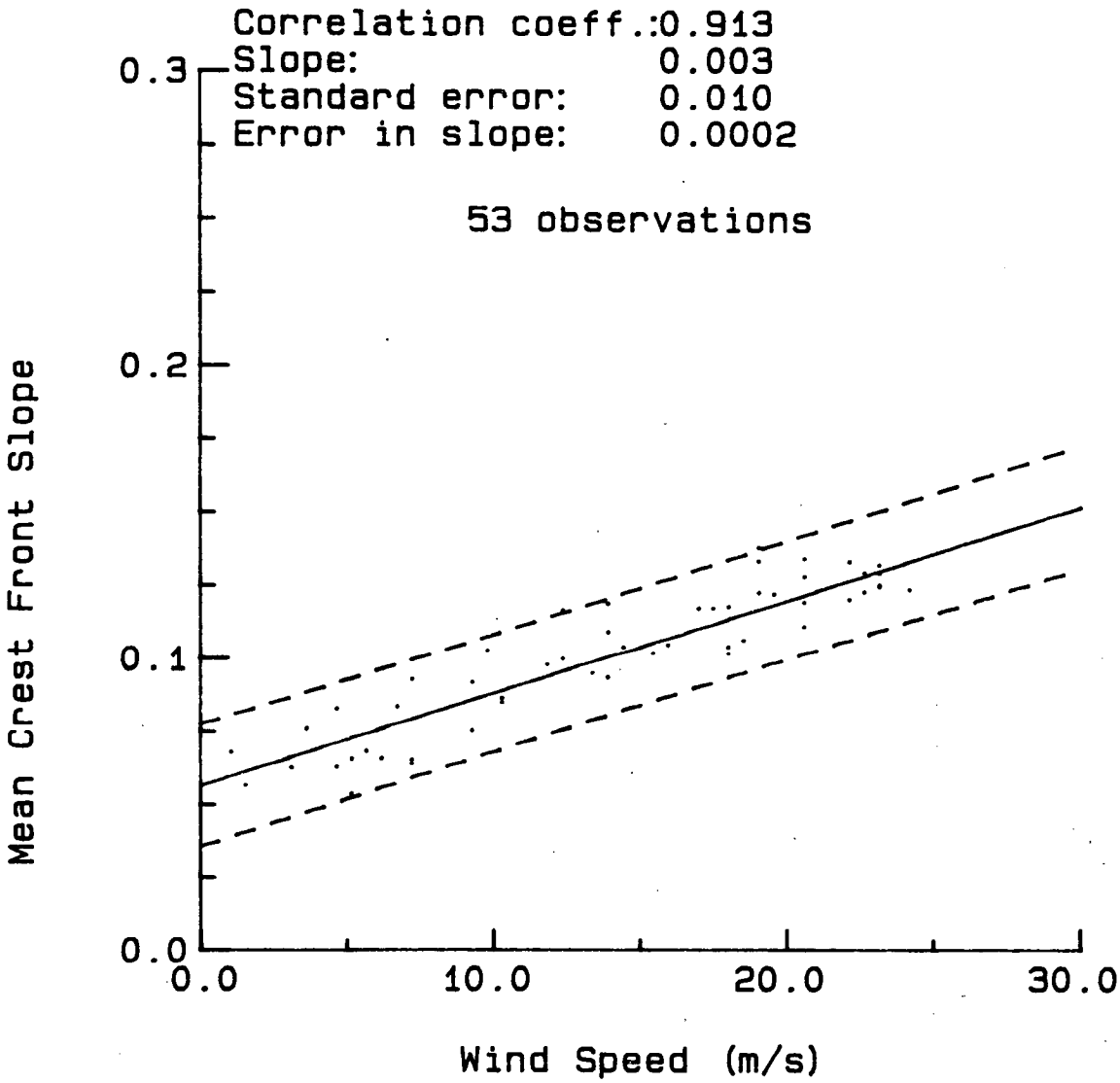

Figure 107. Regression of mean crest front slope against wind speed.

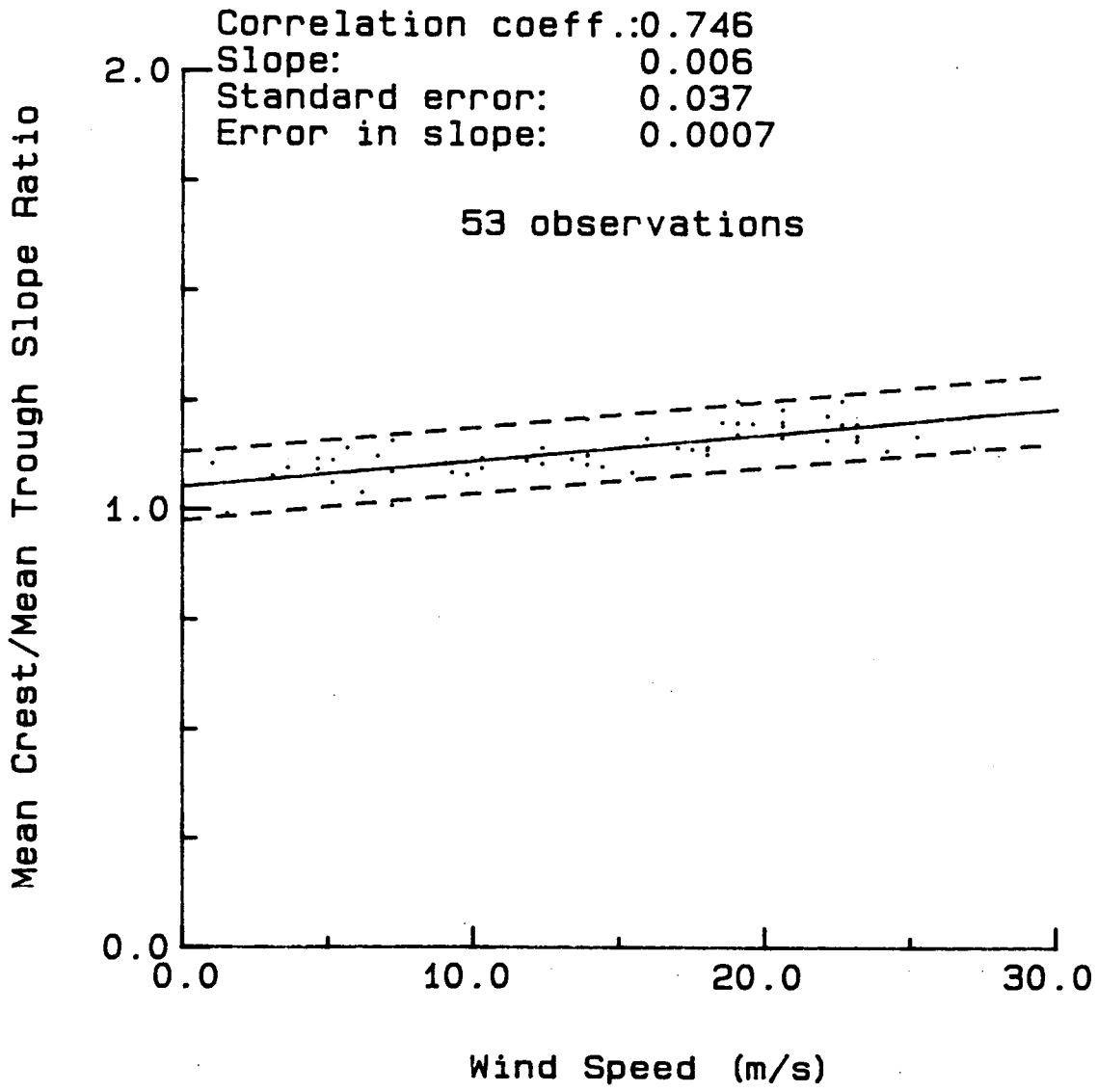

Figure 108. Regression of mean crest/mean trough slope ratio against wind speed

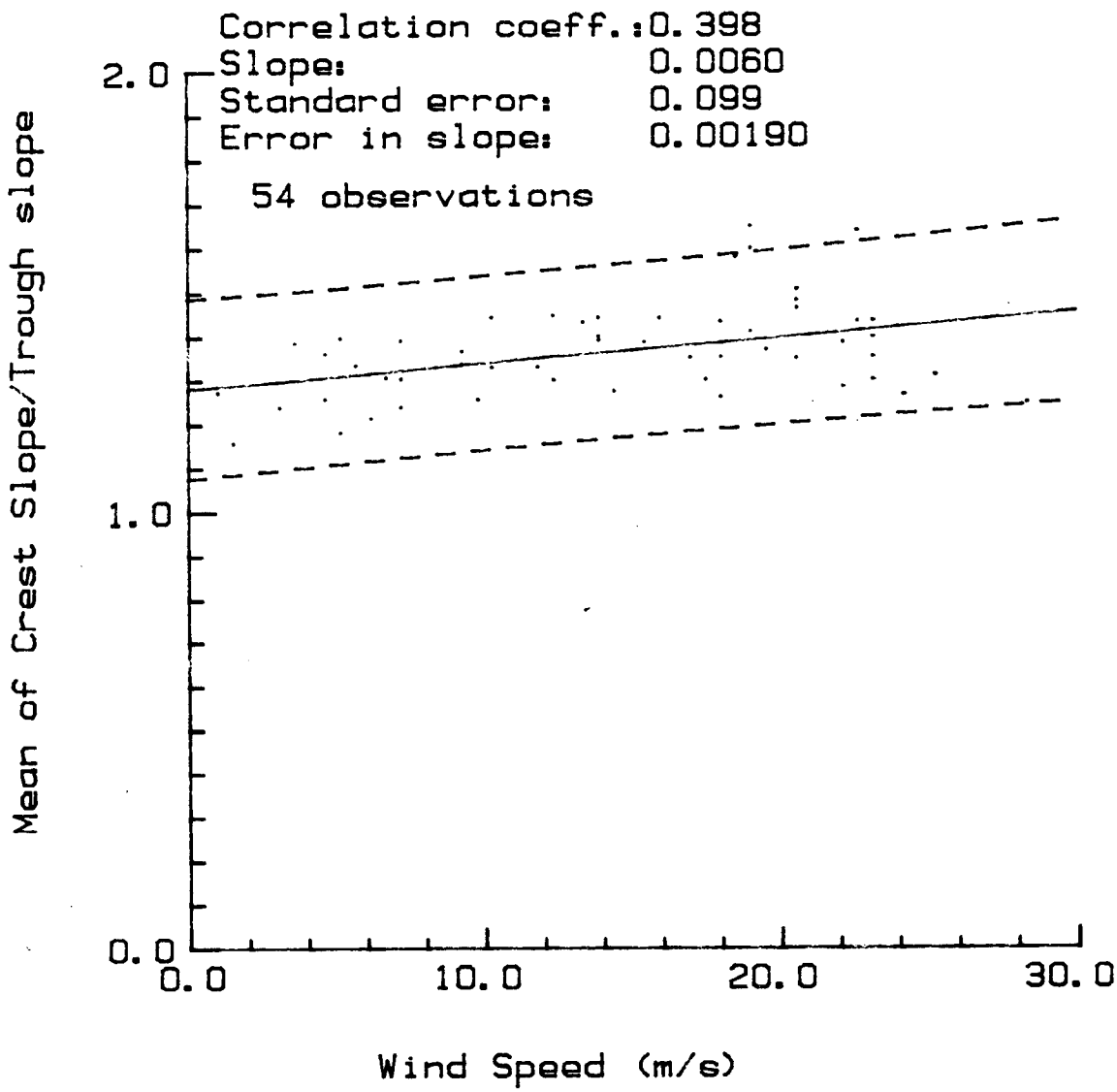

Figure 109. Regression of the mean of crest slope/trough slope ratio against wind speed

regression of the mean of the ratio of crest slope over trough slope. The increased scatter results from the necessary wave-by-wave ratio calculation required. What is important to note, as mentioned earlier, is that although the slopes of the regression lines are similar, the absolute values are different with those in Figure 109 being larger, hence indicating larger asymmetry. Conceptually, the means of the ratios (Figure 109) are the more acceptable parameter. The correlations with wind speed of the mean wave front slope, crest front slope and mean crest/mean trough slope ratio are 0.91, 0.913 and 0.746 respectively. The equivalent correlations with significant wave height were 0.83, 0.80 and 0.50. The rise in the crest/trough ratio implies an increase in wave asymmetry with wind speed and possibly an increase in nonlinear effects. The assumption of regular, symmetric waves, needed in estimates of wave steepness from a heave only buoy, therefore does not apply in higher energy conditions. Regressions of mean crest front slope and mean crest/trough slope ratios were also performed against wind stress (as wind speed x wind speed) and are included in Figures 110 and 111. The correlations are still good and only slightly less than for wind speed.

As winds should be acting on the back face of the waves, equivalent back slope statistics were calculated. This also allows for the opportunity to check for asymmetry about the wave crest. Figure 112 contains a plot of mean crest back slope for the two storms, overlayed on wind speed and direction. Again, a direct relationship can be seen with a lag of the slopes behind wind speed of less than 3 hours. Figures 113, 114 and 115 show the correlation between the mean back slope, mean crest back slope and mean crest/mean trough back slope ratio with wind speed. Figure 116 shows a similar regression using the mean of the ratio as was done for the forward face (Figure 109). The correlation is better for all of these statistics compared with the forward face ones. An indication of asymmetry about the wave peak can be given by the ratio of crest front and crest back slope. This statistic is plotted against wind speed in Figure 117. There appears to be little relative symmetry change about the crest with wind though the mean ratio is greater than 1.0, indicating a steeper front as would be expected. What these statistics are indicating is a wave profile which develops with wind speed in such a manner that the crests are steepening relative to the troughs and that the forward and back face crests are steepening proportionally at the same rate.

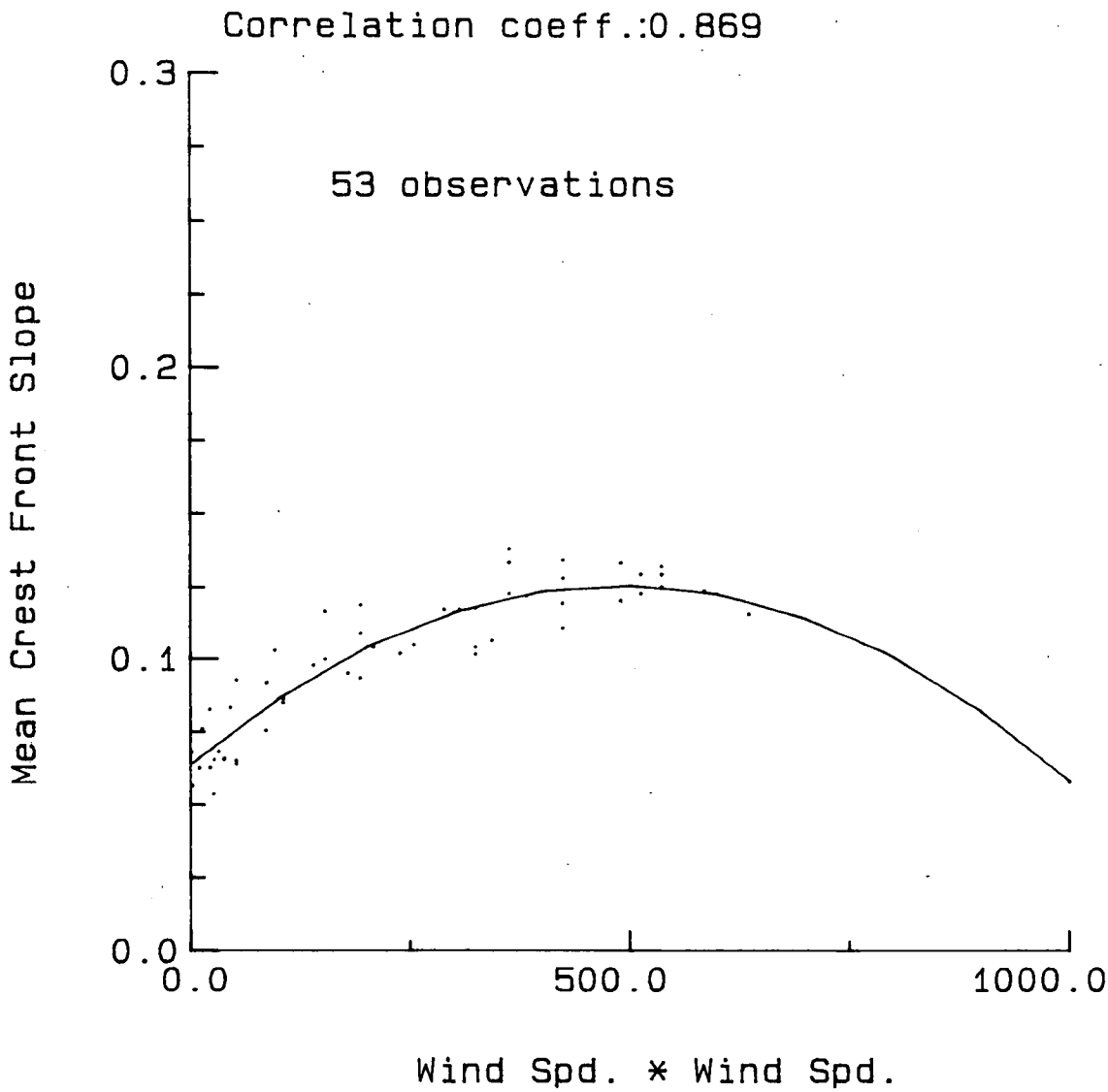

Figure 110. Regression of mean crest front slope against wind stress.

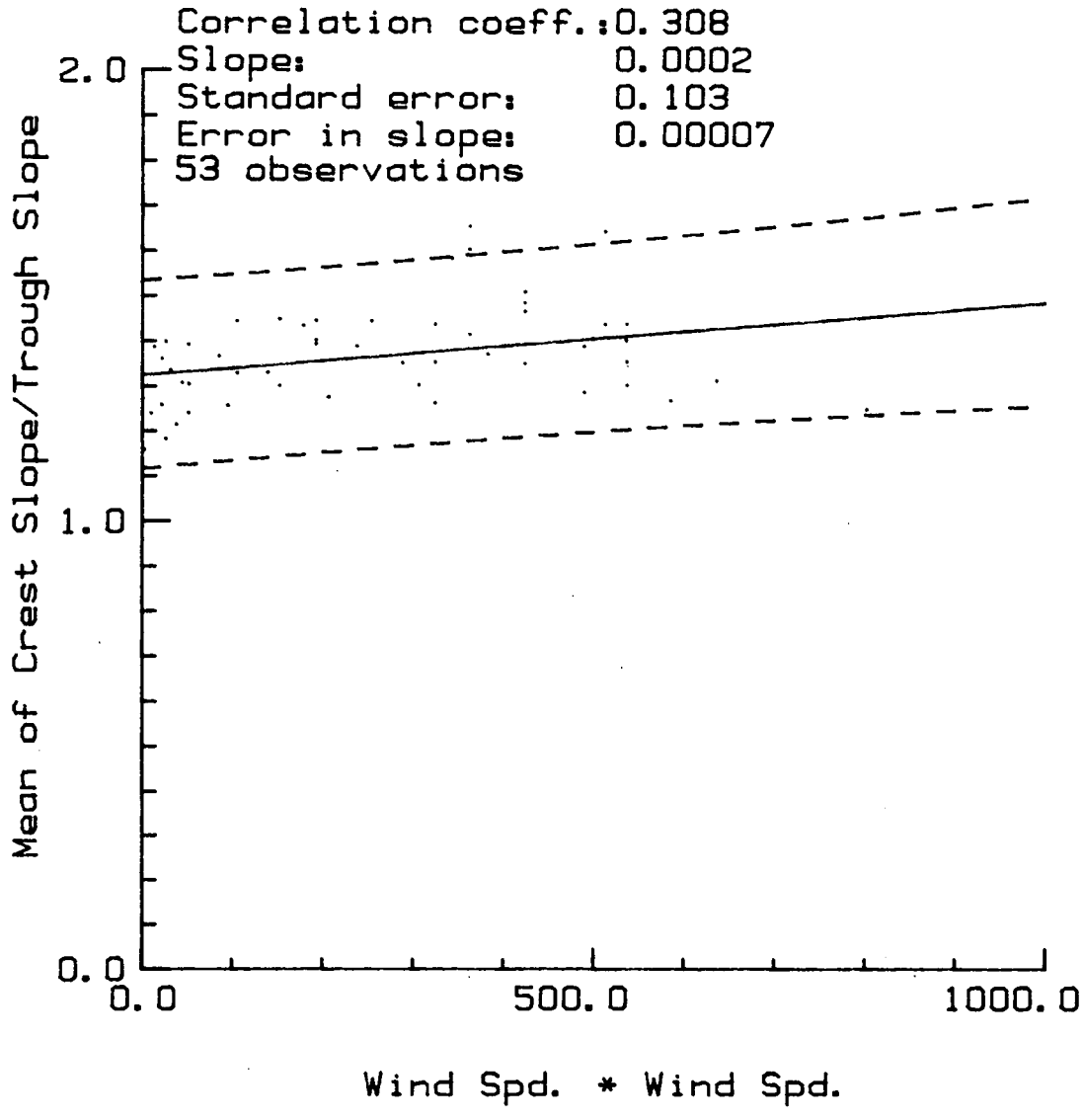

Figure 111. Regression of mean crest/trough slope ratio against wind stress.

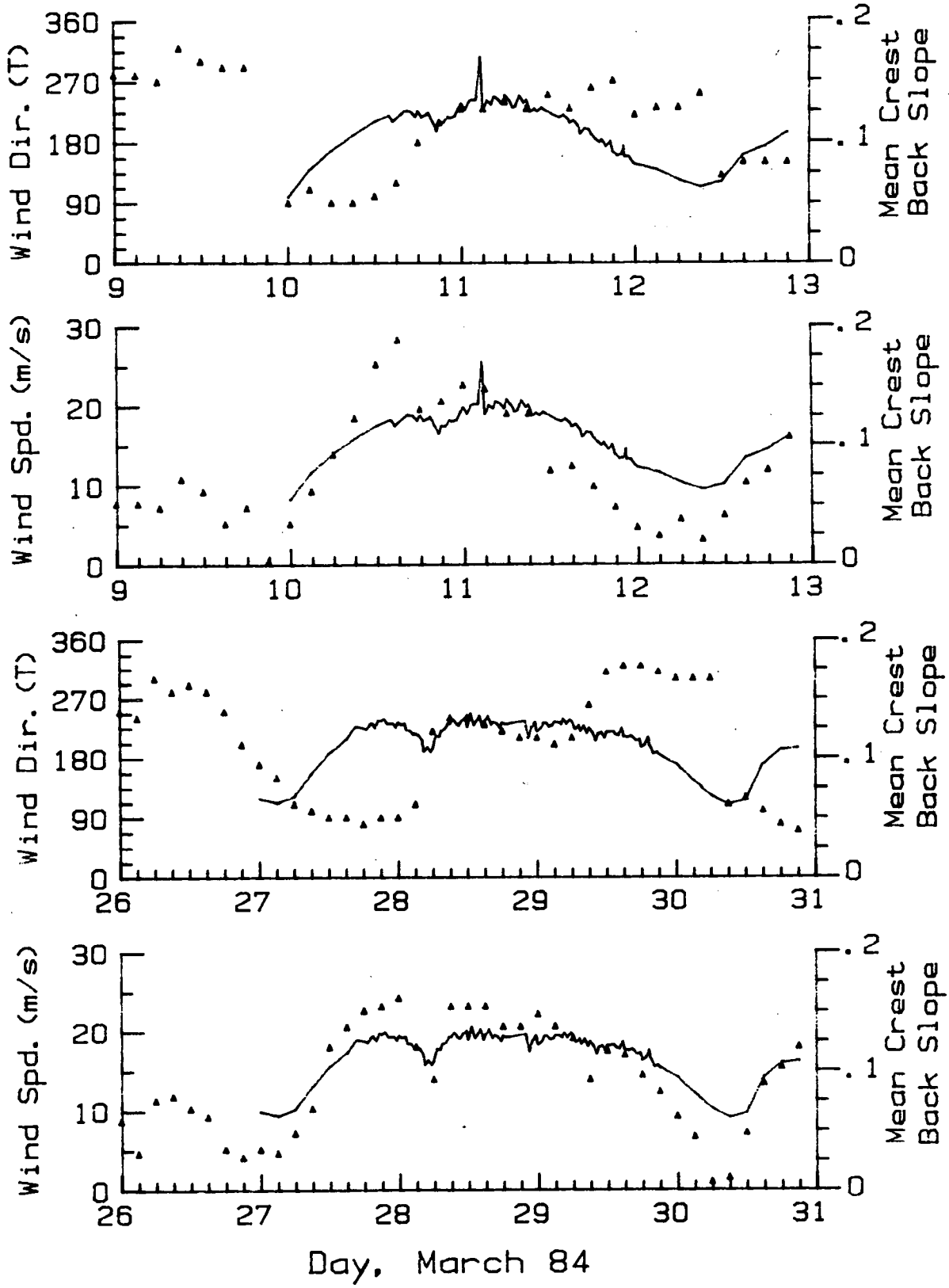

Figure 112. Mean crest back slope (solid) compared to wind speed and direction (dotted) during Event 1 and Event 2.

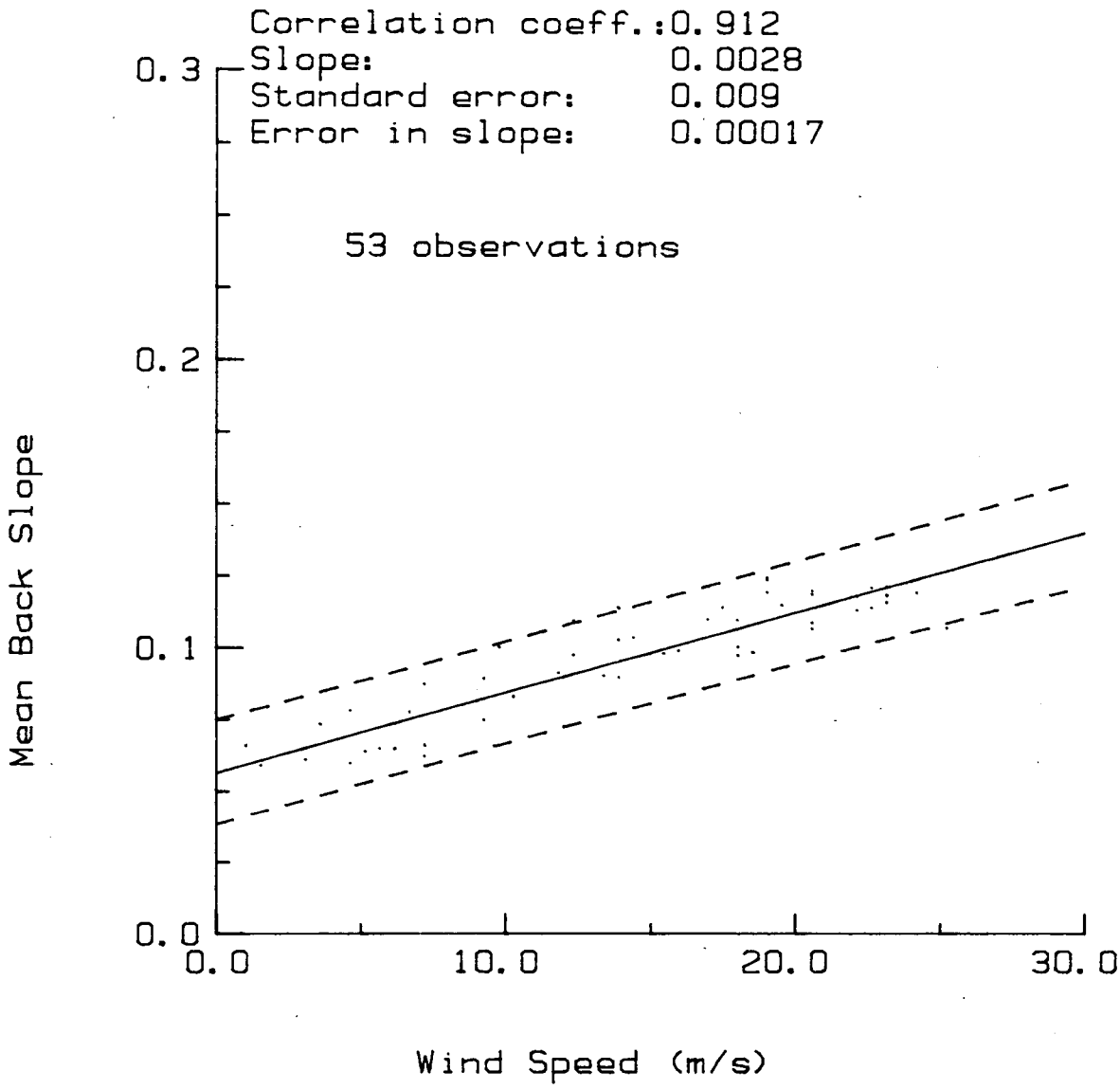

Figure 113. Regression of mean back slope against wind speed.

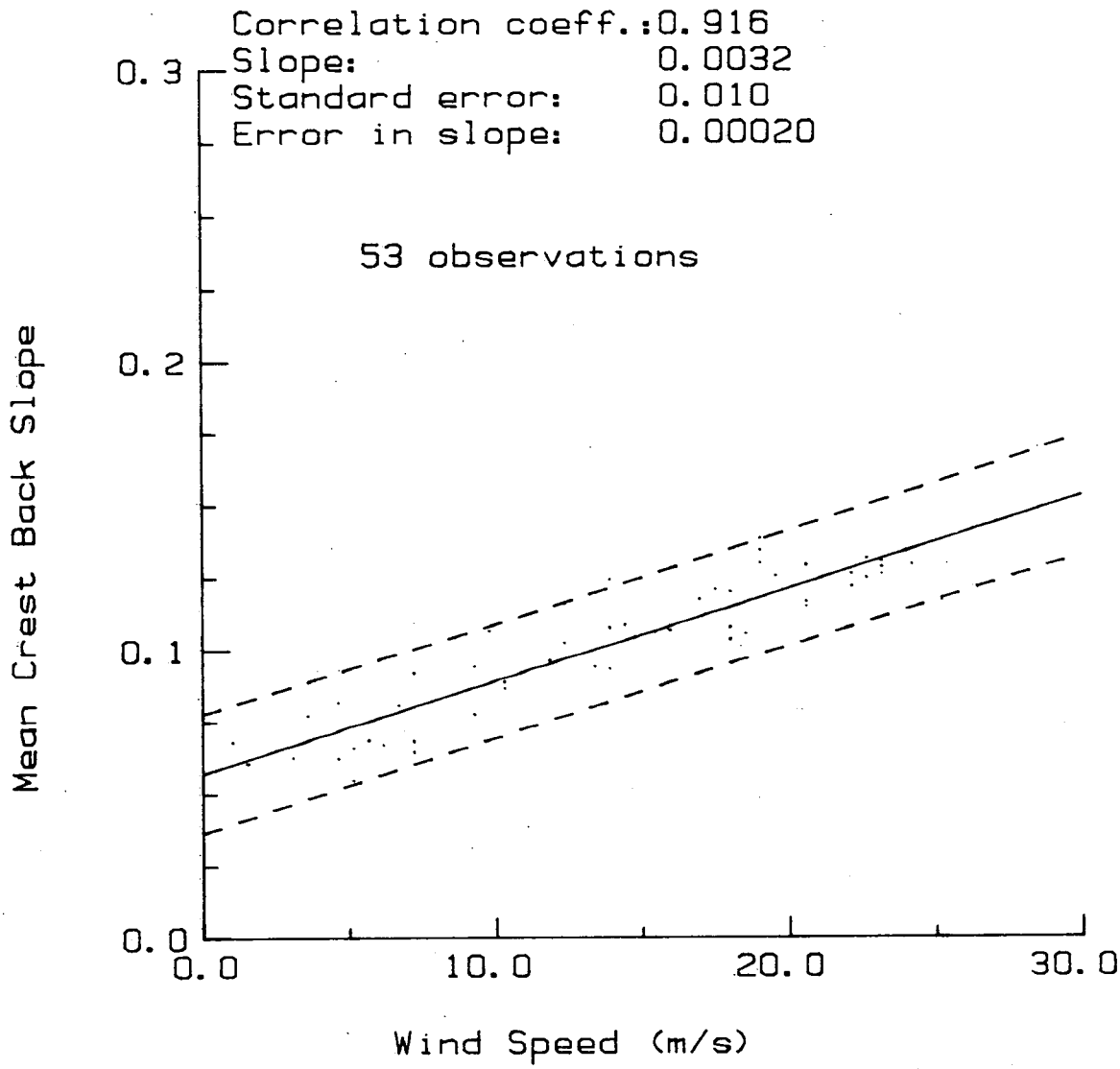

Figure 114. Regression of mean crest back slope against wind speed.

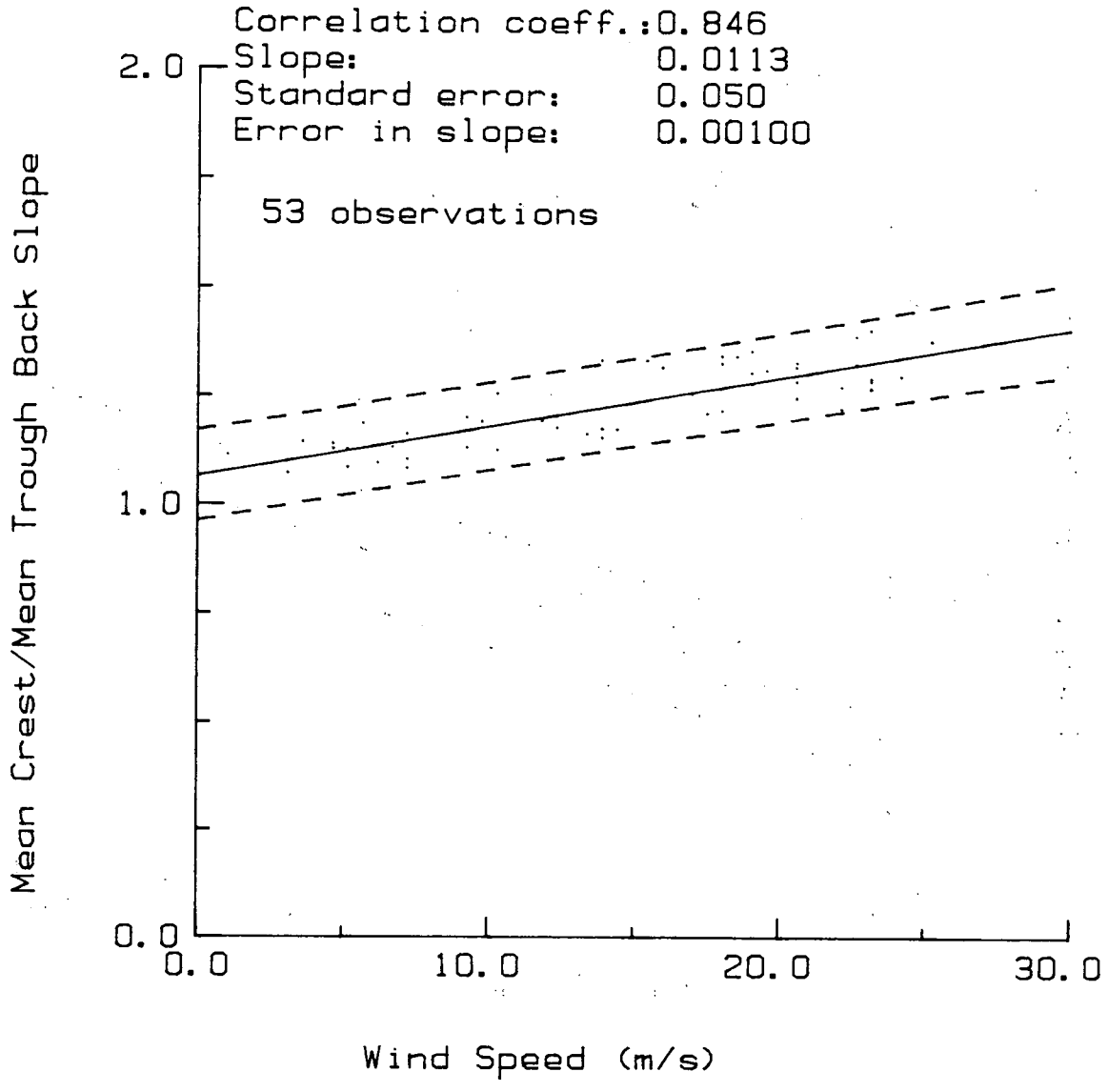

Figure 115. Regression of mean crest/mean trough back slope ratio against wind speed.

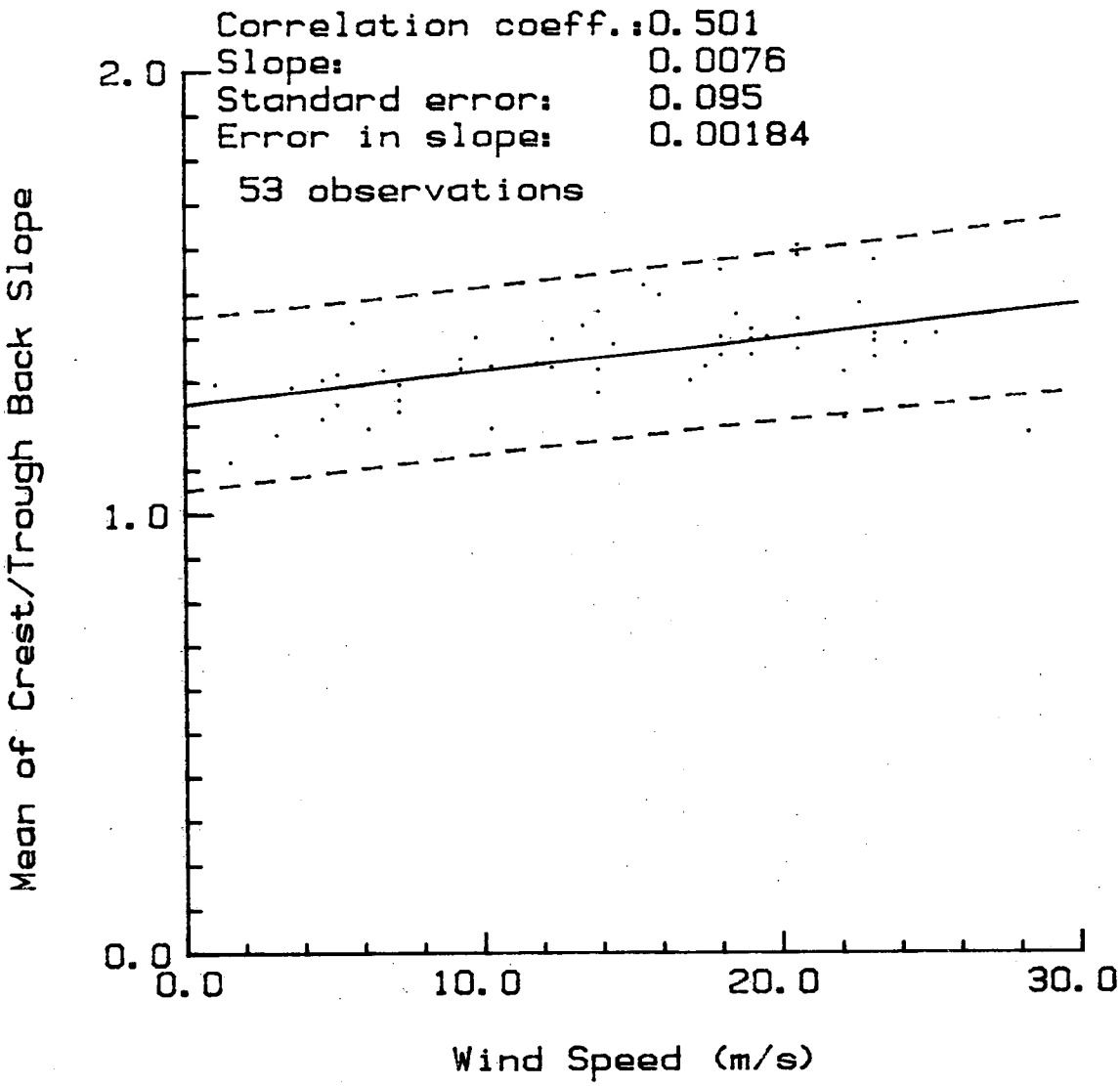

Figure 116. Regression of mean crest/trough back slope ratio against wind speed.

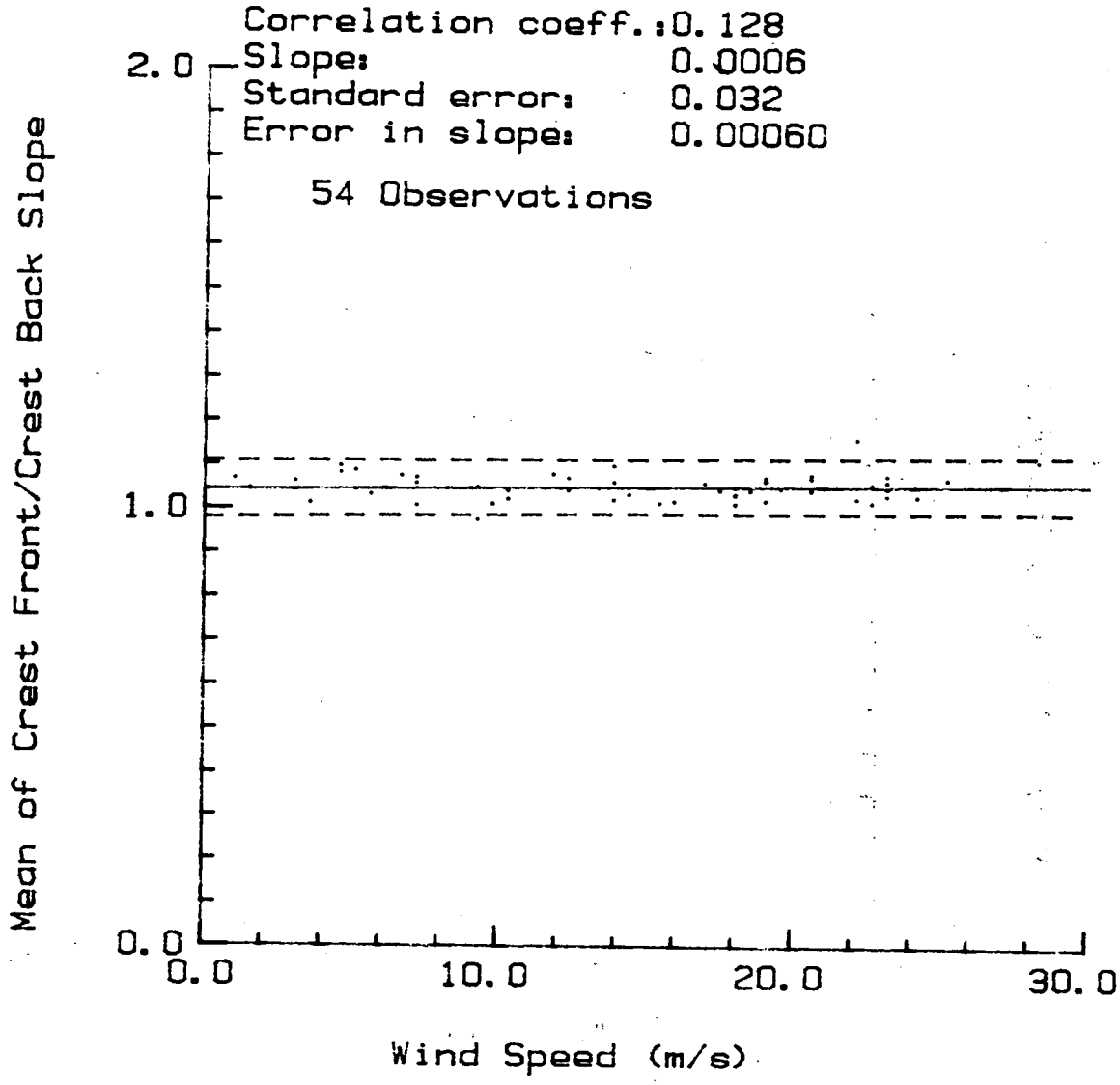

Figure 117. Regression of the mean of the crest front/crest back slope ratio against wind speed.

The mean crest front slope was also compared with information derived from the heave spectrum. Figures 118, 119 and 120 contain regressions against the three spectral shape parameters. The best correlation is with the spectral narrowness parameter (even better with the square root of this value where the correlation coefficient was 0.83). Again, this is not surprising as this parameter behaves similarly to significant wave height.

Cummins and Bales (1980) (as cited by LeBlond, 1982) and Komen et al. (1984), used an estimate of the mean slope parameter (α) or wave steepness parameter as

$$\alpha^2 = M_4/g^2$$

where M_4 is the fourth moment of the heave spectrum (i.e. kurtosis) and g is the acceleration due to gravity, in order to analyze hindcast spectra in relation to wave height and wind speed. This relationship follows directly from the linear wave dispersion equation and provides a test for its applicability. It was shown to be directly related with both wave height and wind speed (to be expected given earlier discussion). Figure 121 shows a regression of the mean crest front slope and this mean slope parameter. The correlation is extremely good.

The relationship of slope with wind speed as well as the ability to measure slopes directly have important consequences not only in estimates of non-spectral parameters but in the field of wave modelling. As wave models use energy source terms related to wind speed, while energy dissipation may be related to wave steepness, in turn a function of wind speed, the advent of slope following buoys may allow for better understanding of this inter-relationship.

Comparison with Heave Derived Steepness Values

Prior to the development of slope following buoys, wave shape statistics were determined using estimates of the wavelength in relation to crest and total wave height. There are obvious problems in estimating the wavelength from the time between zero crossings if there is any wave asymmetry or surface currents influencing wave speeds. It was thought that a comparison of heave derived steepness statistics with direct slope estimates was warranted.

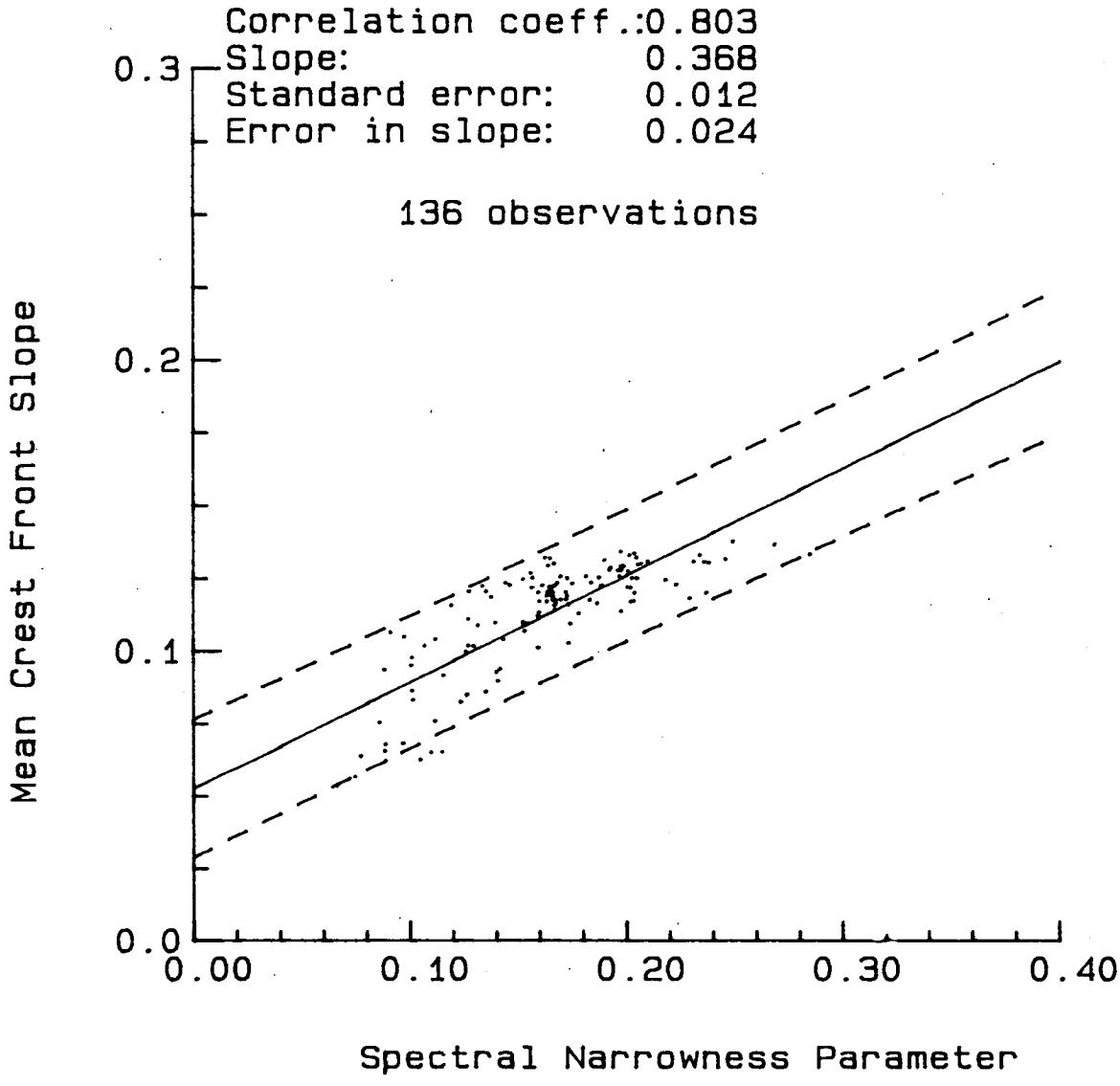

Figure 118. Regression of mean crest front slope against spectral narrowness parameter.

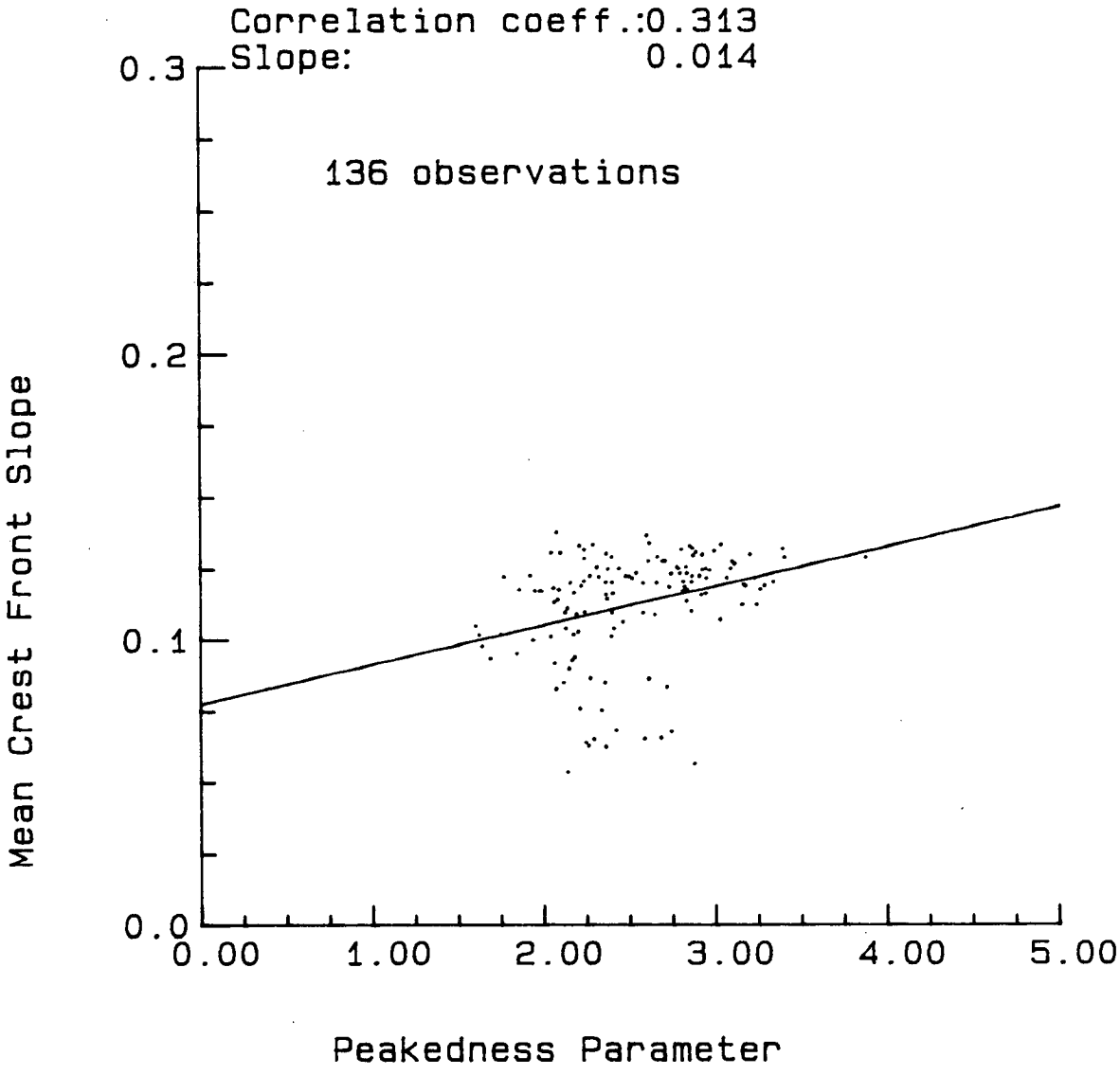

Figure 119. Regression of mean crest front slope against peakedness parameter.

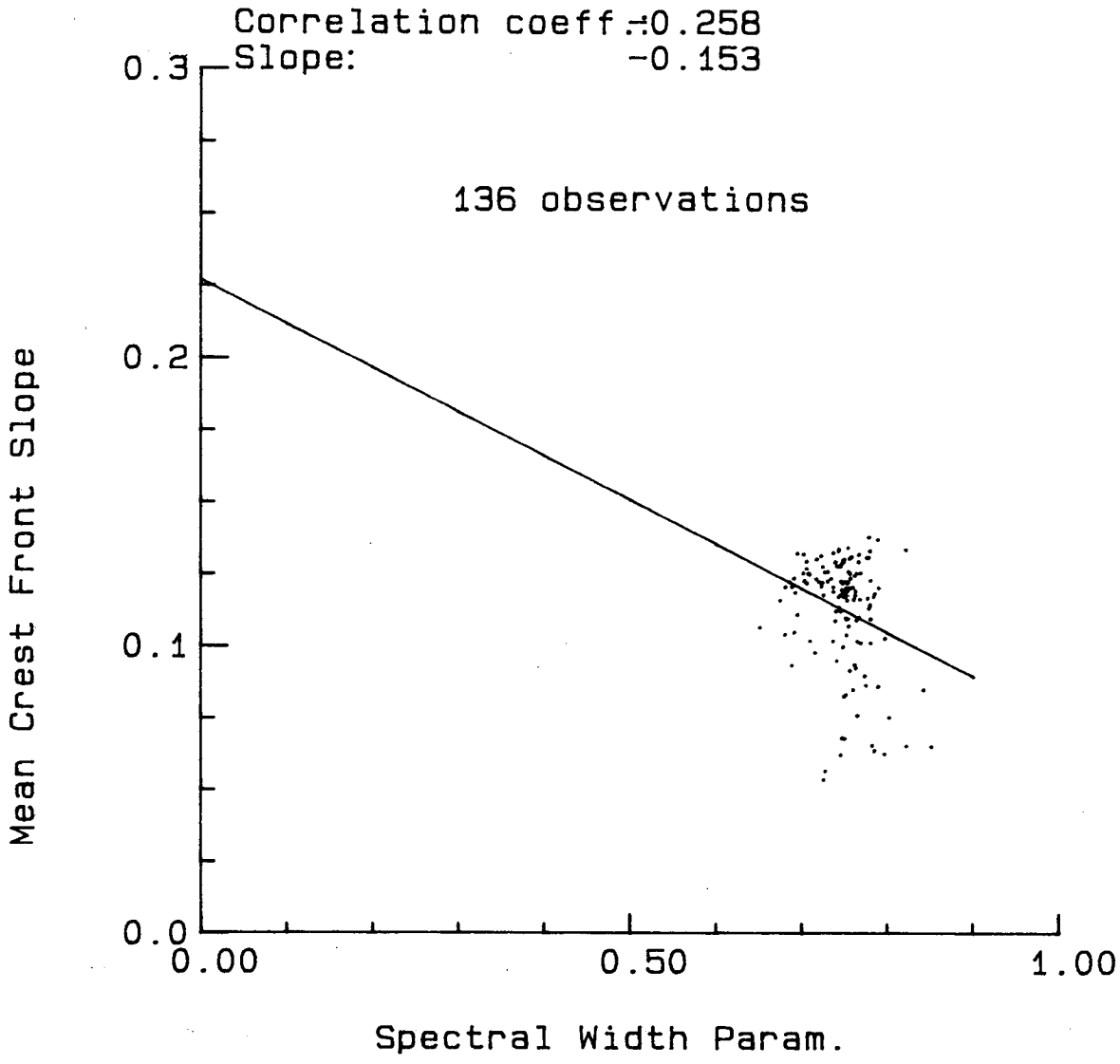

Figure 120. Regression of mean crest front slope against spectral width parameter.

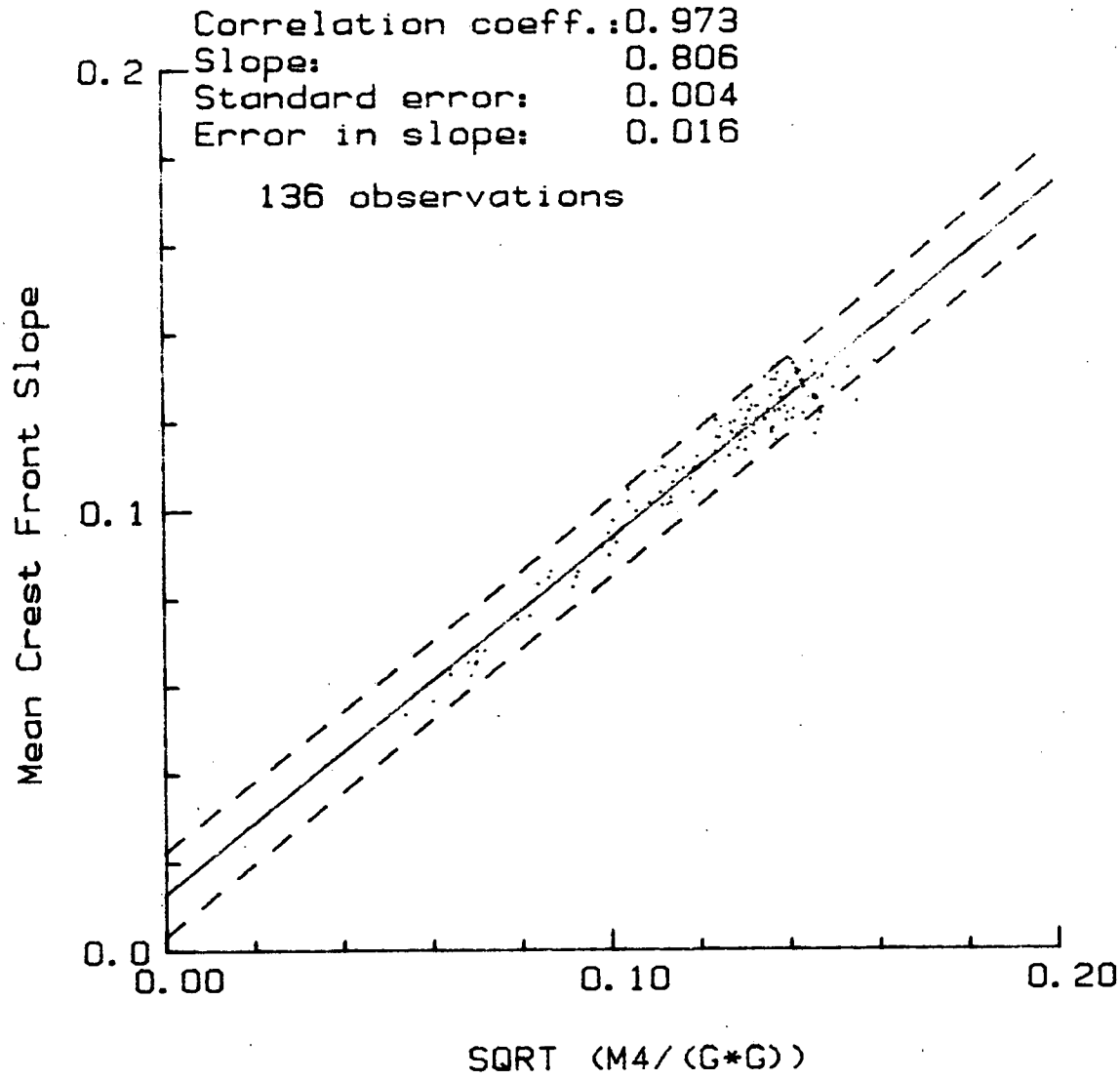

Figure 121. Regression of mean crest front slope against wave steepness parameter, $\sqrt{M_4/g^2}$.

The parameters described in Figure 100 were determined. In order to avoid calculating a wavelength, the two asymmetry components are examined, with the values for mean crest front and back slopes (L) replaced by the time passed between critical points on the wave profile. This requires only the assumption of constant phase speed across the wave which should be satisfied under non-wave breaking conditions. Figures 122 and 123 show the regressions between the horizontal and vertical asymmetry parameters. Both figures show considerable scatter with little agreement between the vertical asymmetry parameters. The heave derived horizontal asymmetry parameters (Figure 122) have numerous values less than 1.0 which would not be expected to occur frequently, though the upper range is similar to that for the direct slope estimates.

Wallops Spectrum

The Wallops spectrum, as discussed by Huang et al. (1981, 1983) defines the wave spectrum based solely on two parameters: the peak frequency and the significant wave slope. The significant wave slope is defined as the RMS elevation divided by the wavelength at the spectral peak. The Wallops spectrum is written as

$$E(\omega) = \frac{\beta_g^2}{\omega^m \omega_o^{5-m}} \quad \exp\left\{-\frac{m}{4}\left[\frac{\omega_o}{\omega}\right]^4\right\}$$

where ω = frequency

ω_o = peak frequency

g = acceleration due to gravity

$\beta = (2\pi S)^2 \, m^{(m-1)/4} \Big/ \left[4\left(\frac{m-5}{4}\right) \cdot \Gamma\left(\frac{m-1}{4}\right)\right]$

S = significant slope

$m = \left|\log\left(\sqrt{2}\,\pi S\right)2 \,/\, \log 2\right|$

Γ = Gamma function

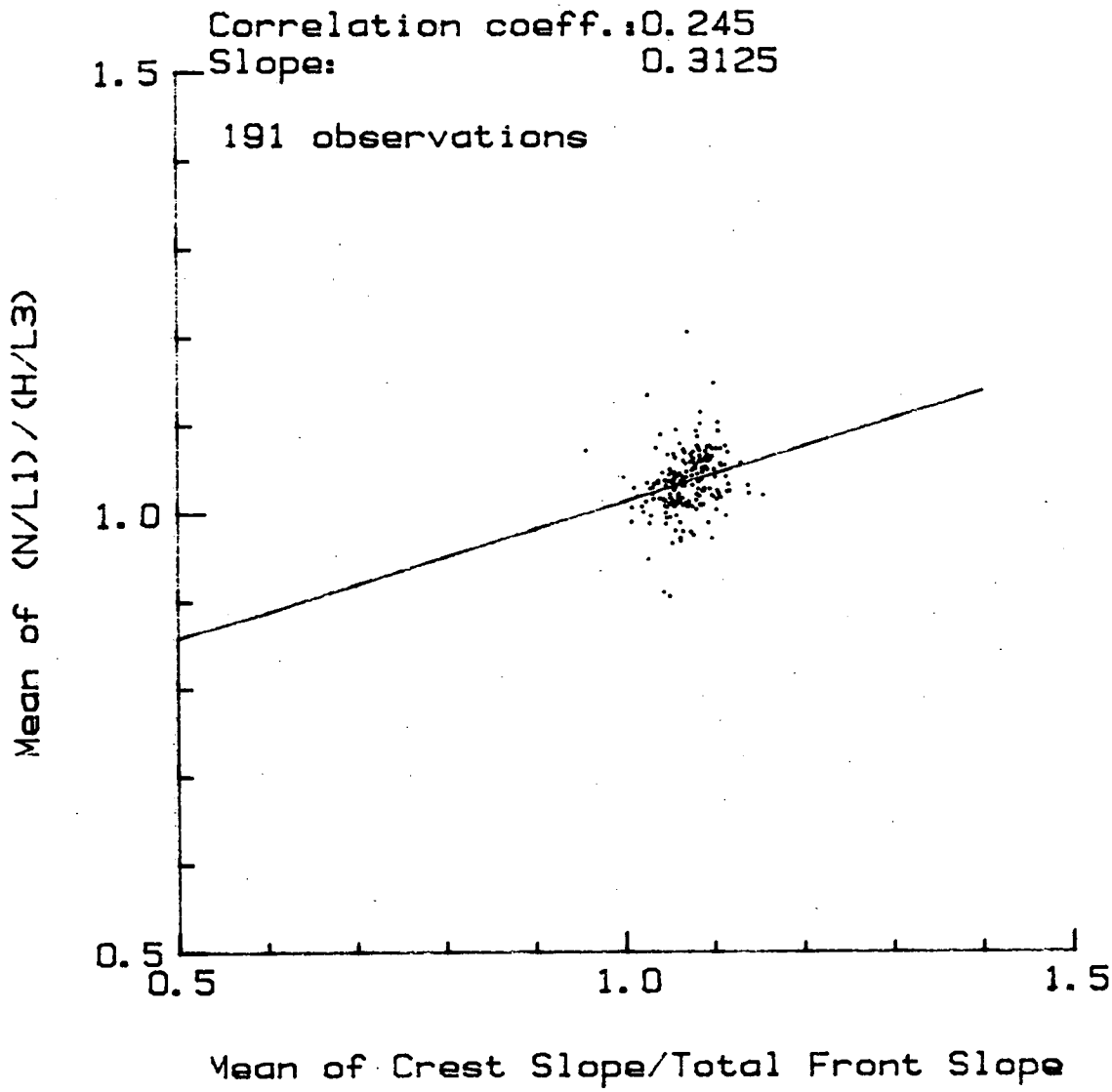

Figure 122. Regression between the horizontal asymmetry parameters and the mean of crest/total front slope.

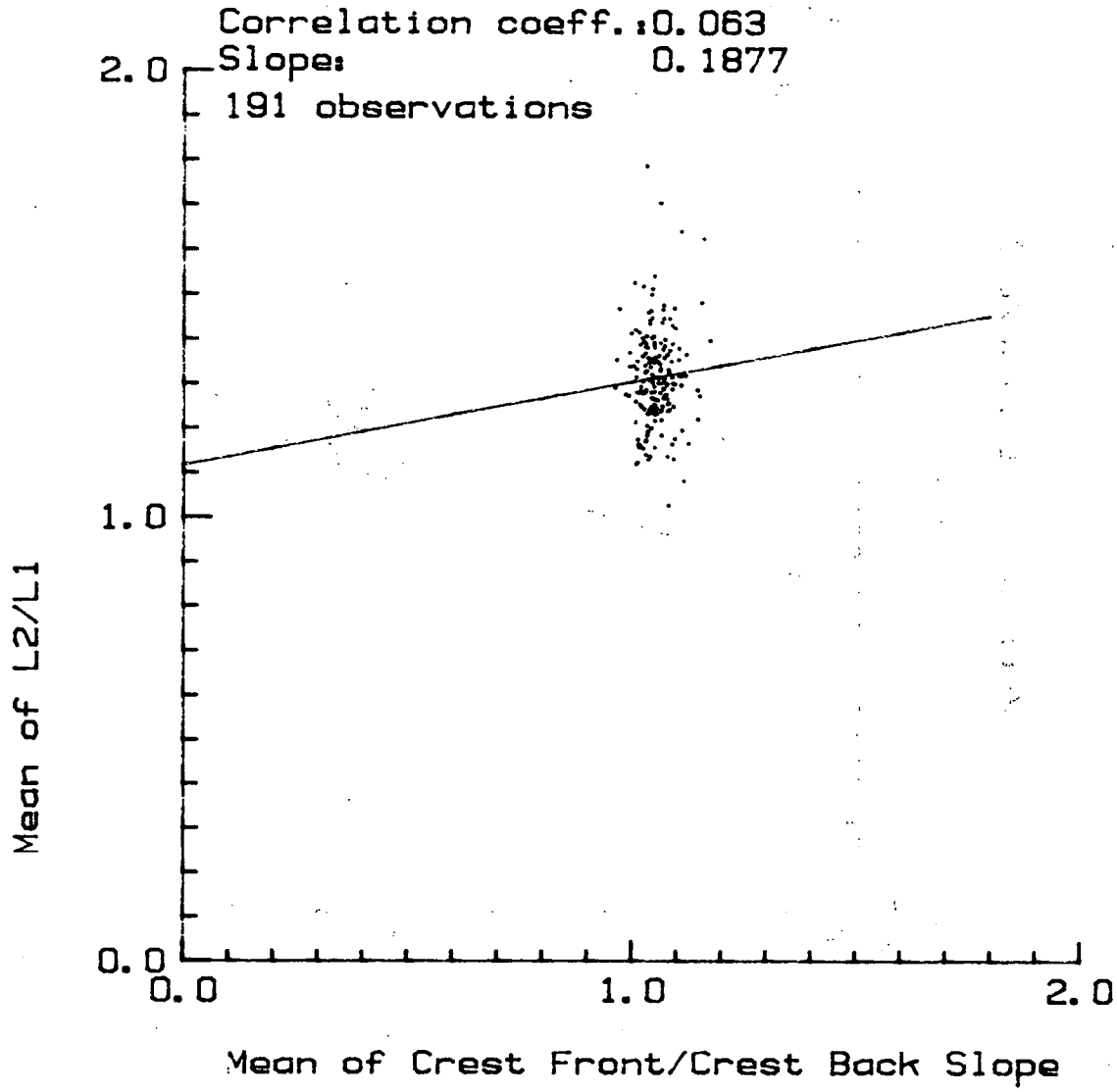

Figure 123. Regression of vertical asymmetry parameter and mean of crest front/crest back slope.

The significant slope can be compared with directly estimated slope statistics. Figure 124 shows a regression of significant slope against mean wave front slope. There appear to be two regimes, possibly indicating a separation between long wavelength swell and storm conditions. The significant slope was also compared against wind speed (Figure 125) and shows a direct relationship reflecting the increase in RMS elevation with wind.

In order to assess the applicability of Wallops spectrum modelling for the study site, the ratio of RMS slope/significant slope, given by Huang et al. (1981) and Hodgins et al. (1985) as

$$\frac{(\text{RMS Slope})^2}{(\text{Sig. Slope})^2} = m\pi^2 \quad \Gamma\left(\frac{m-5}{4}\right) \Big/ \Gamma\left(\frac{m-1}{4}\right)$$

can be compared with direct estimates. The RMS slope observed is calculated as

$$\frac{1}{N}\left[\sum^{N}(s_1^2 + s_2^2)^{1/2}\right]$$

Figure 126 shows the regression obtained. A high inverse correlation can be seen though there is considerably less spread in the model values. Some sample spectra are shown in Figures 127 a to e with the dashed line being the model results.

Direct Estimates of Direction from Slope data

If one considers the linearized equations of motion, then at the sea surface

$$\frac{\partial u}{\partial t} = -g\frac{\partial \eta}{\partial x} \qquad \text{and}$$

$$\frac{\partial v}{\partial t} = -g\frac{\partial \eta}{\partial y}$$

This indicates that the east-west slope is proportional to the x-component of acceleration and the north-south slope to the y-component of acceleration.

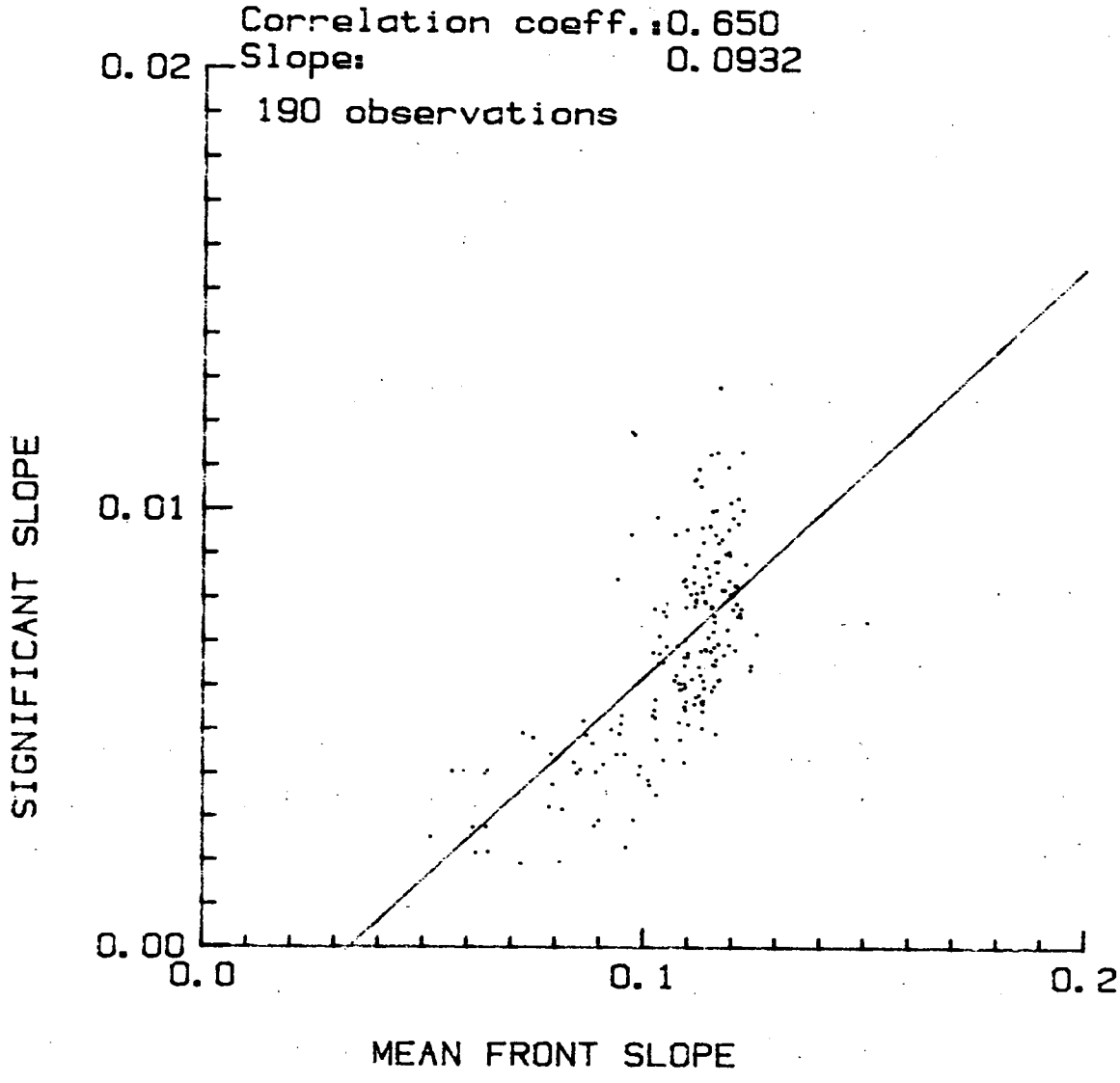

Figure 124. Regression of significant slope against mean wave front slope.

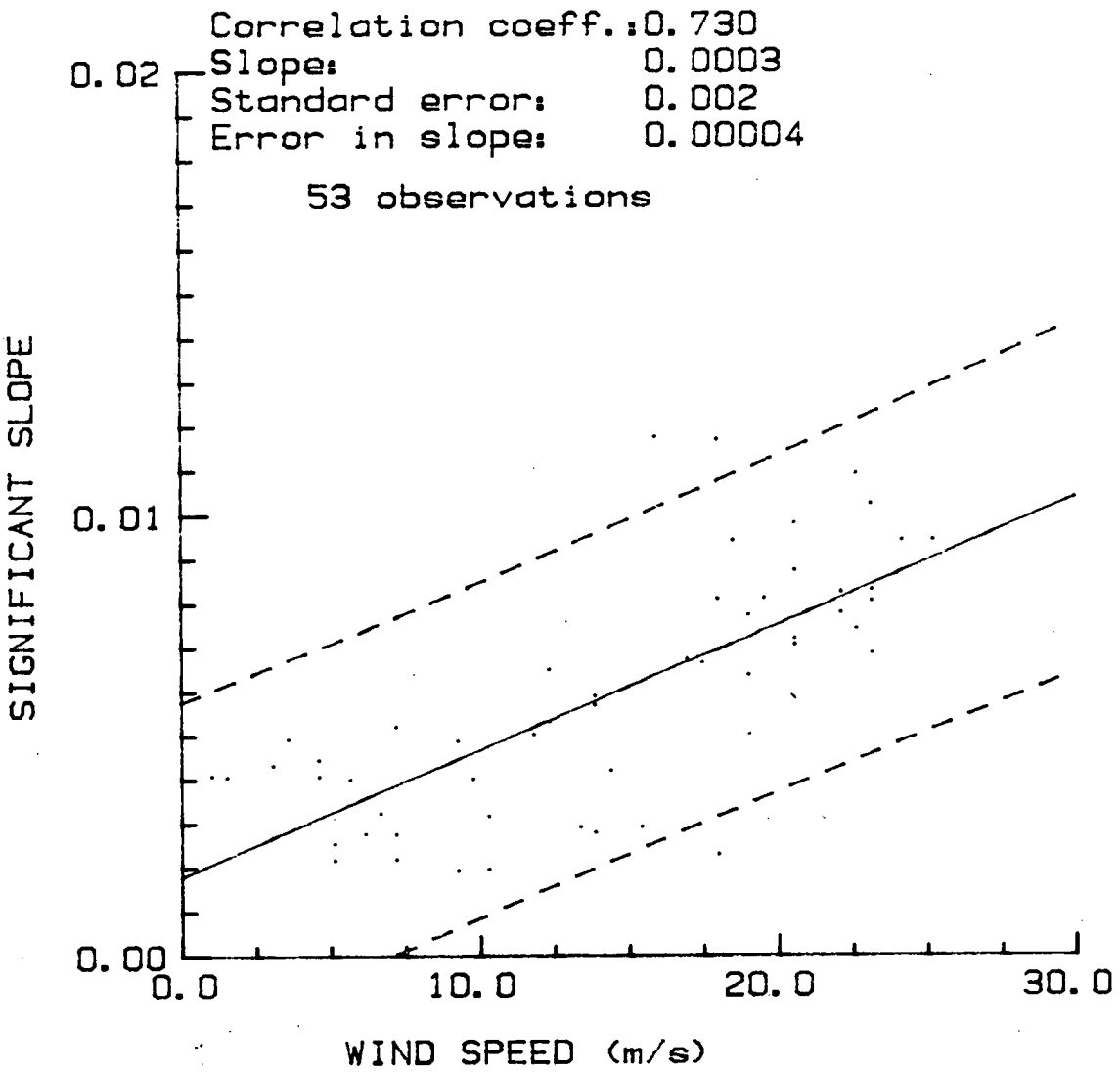

Figure 125. Regression of significant slope against wind speed.

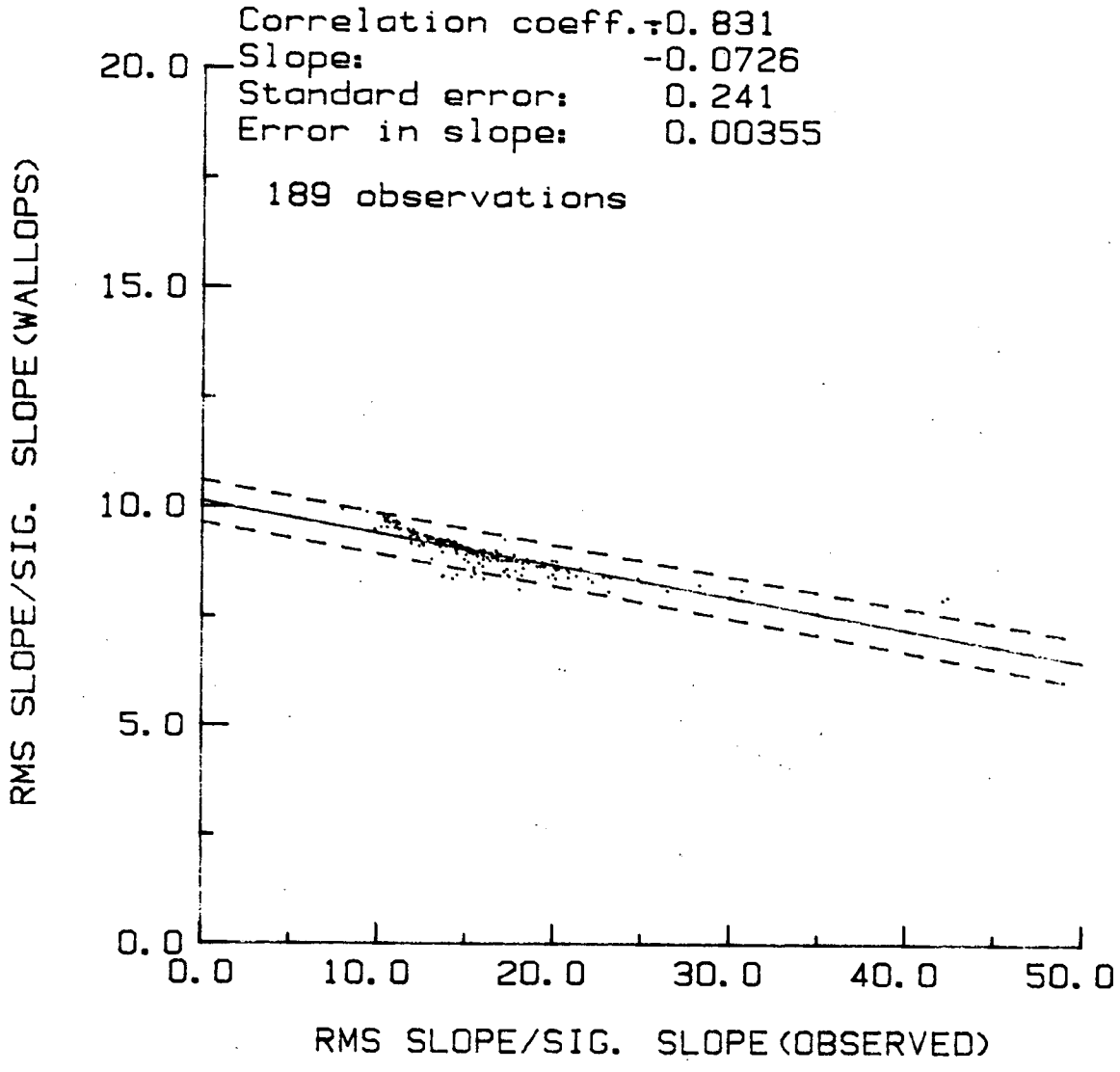

Figure 126. Regression of Wallops derived and observed ratio of RMS slope and significant slope.

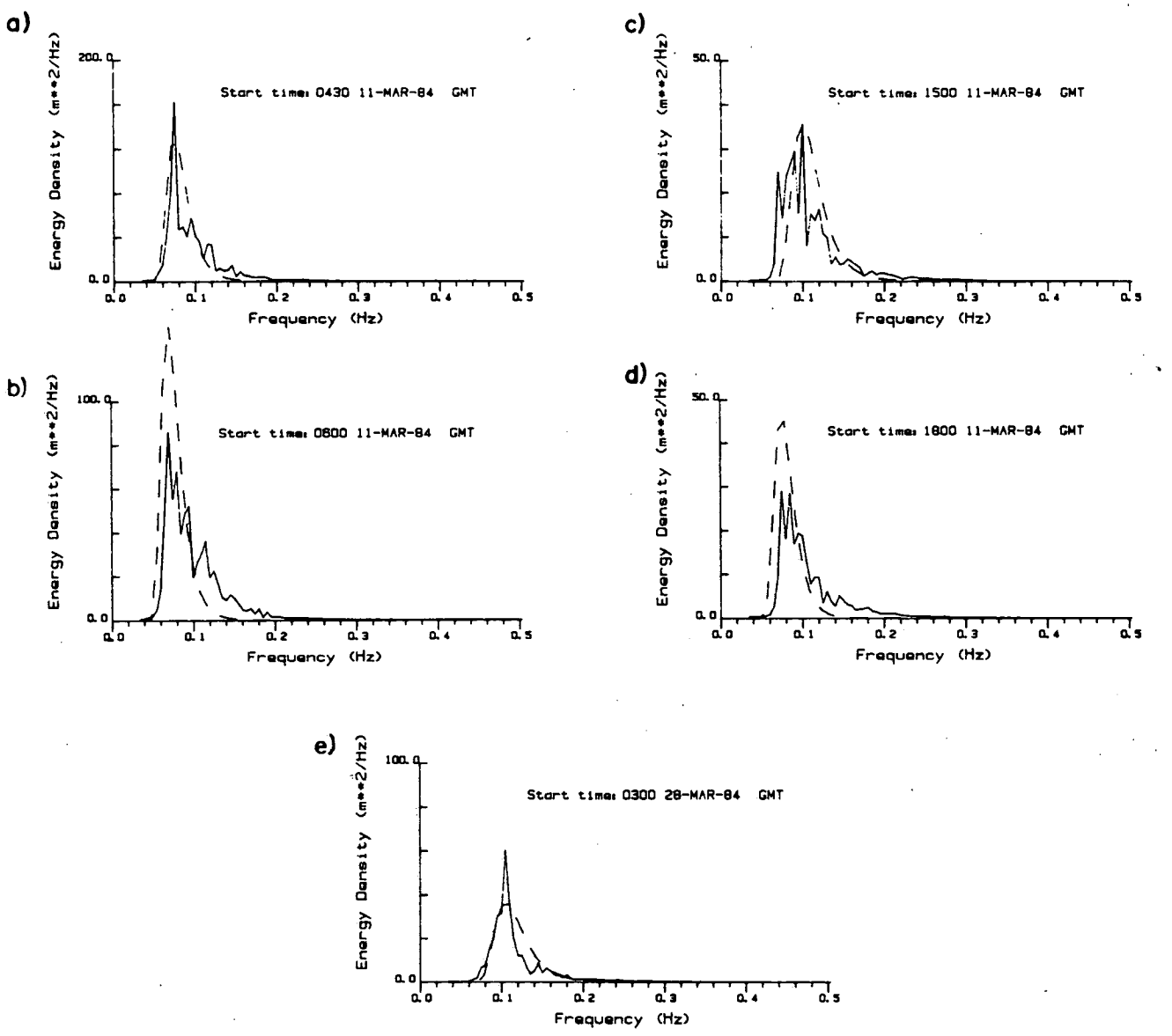

Figure 127. Sample overlayed WAVEC and Wallops spectra (a)0430/11/3/84, (b) 0600/11/3/84, (c) 1500/11/3/84, (d) 1800/11/3/84 and (e)0300/28/3/84.

If one considers a hodographic plane of accelerations, then the mean direction of the scatter ellipse is given by:

$$\text{Tan } 2\phi = \frac{2\,\overline{\frac{\partial \eta}{\partial x}\,\frac{\partial \eta}{\partial y}}}{\left(\overline{\frac{\partial \eta}{\partial y}}\right)^2 - \left(\overline{\frac{\partial \eta}{\partial x}}\right)^2}$$

(see Kundu et al., 1975 for example)

with ϕ also representing the mean direction of wave propagation and overbars indicating an averaging.

By rotating the coordinate axes to lie along ϕ , then

$$X_{maj} = \left[\overline{\left(\frac{\partial \eta'}{\partial x}\right)^2} - \left(\overline{\frac{\partial \eta'}{\partial x}}\right)^2\right]^{1/2}$$

is a measure of the scatter along the major axis of the ellipse and

$$X_{min} = \left[\overline{\left(\frac{\partial \eta'}{\partial y}\right)^2} - \left(\overline{\frac{\partial \eta'}{\partial y}}\right)^2\right]^{1/2}$$

is a measure of the scatter along the minor axis (rotation indicated by primes).

The ratio $R_X = X_{maj}/X_{min}$ provides a measure of spread in the direction. If $R_X = 1$ then there is no preferred direction and the scatter is spherically symmetric. If $R_X = \infty$, then the motion is a uniform wave in the direction ϕ.

Figures 128 and 129 show two sample hodographs for records having R values 1.4 and 1.1, respectively. There is considerable scatter in both figures though a distinct direction can be seen in Figure 128.

Figures 130 and 131 contain time series plots of the calculated direction ϕ and ratio R_X, for the two storm periods in March. In Figure 130, the directions are overlayed on the average direction obtained from the spectrum (weighted using the cosine spread) and in Figure 131 with the average sea direction. The

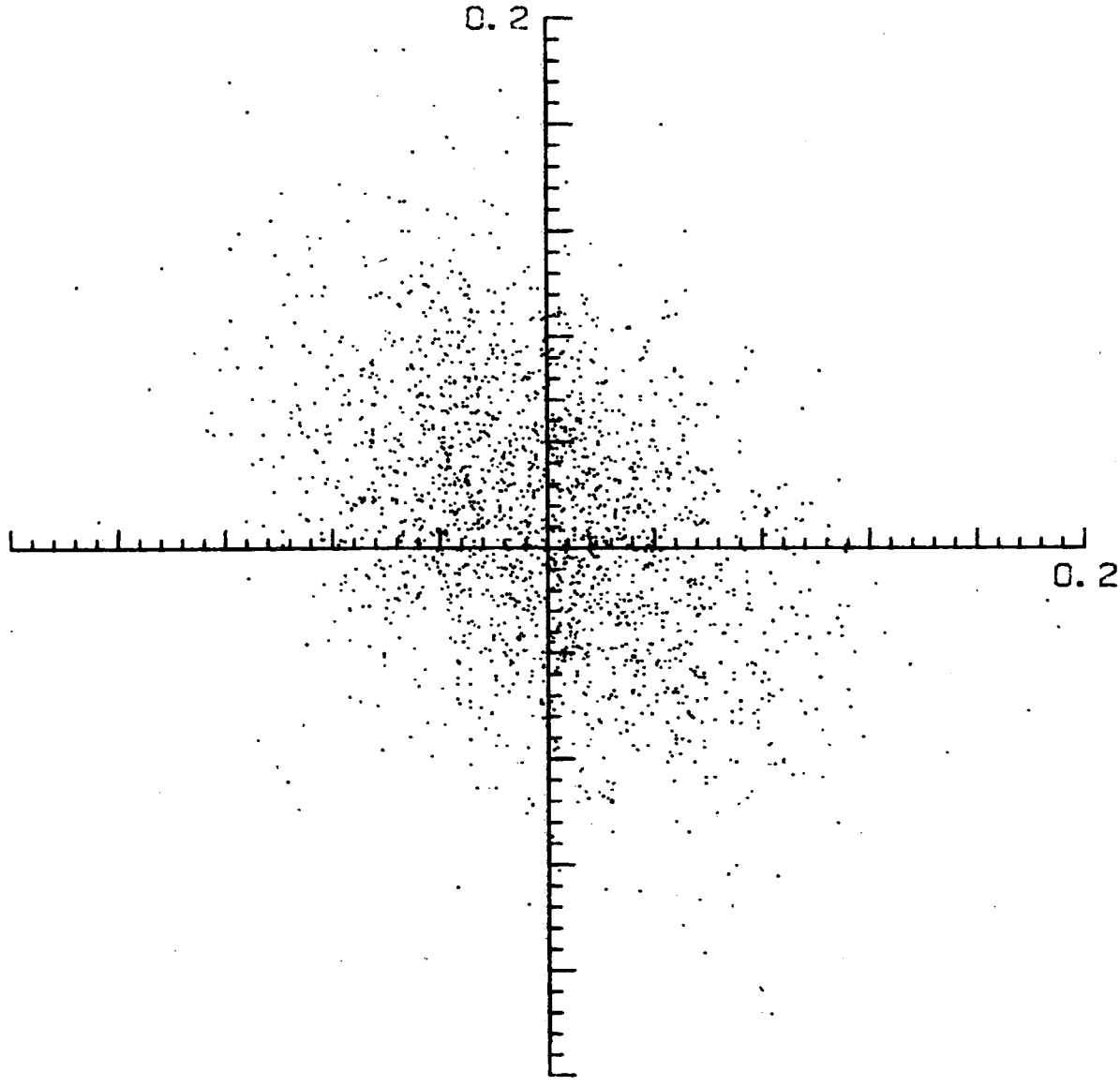

Figure 128. Hodograph of slope values for record 0300/10/3/84 ($R_x \sim 1.4$).

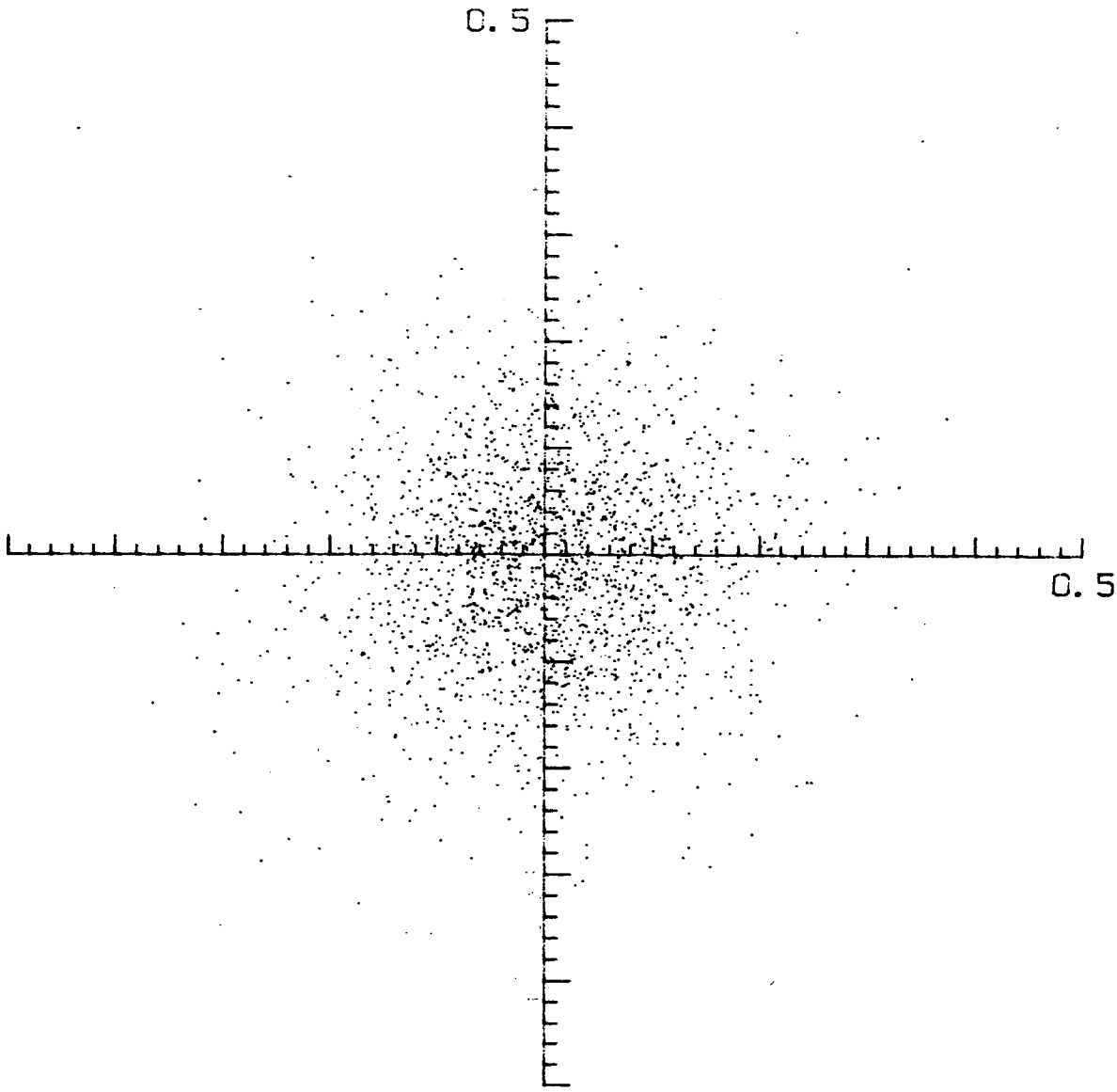

Figure 129. Hodograph of slope values for record 0430/11/3/84 (R_x ~ 1.1).

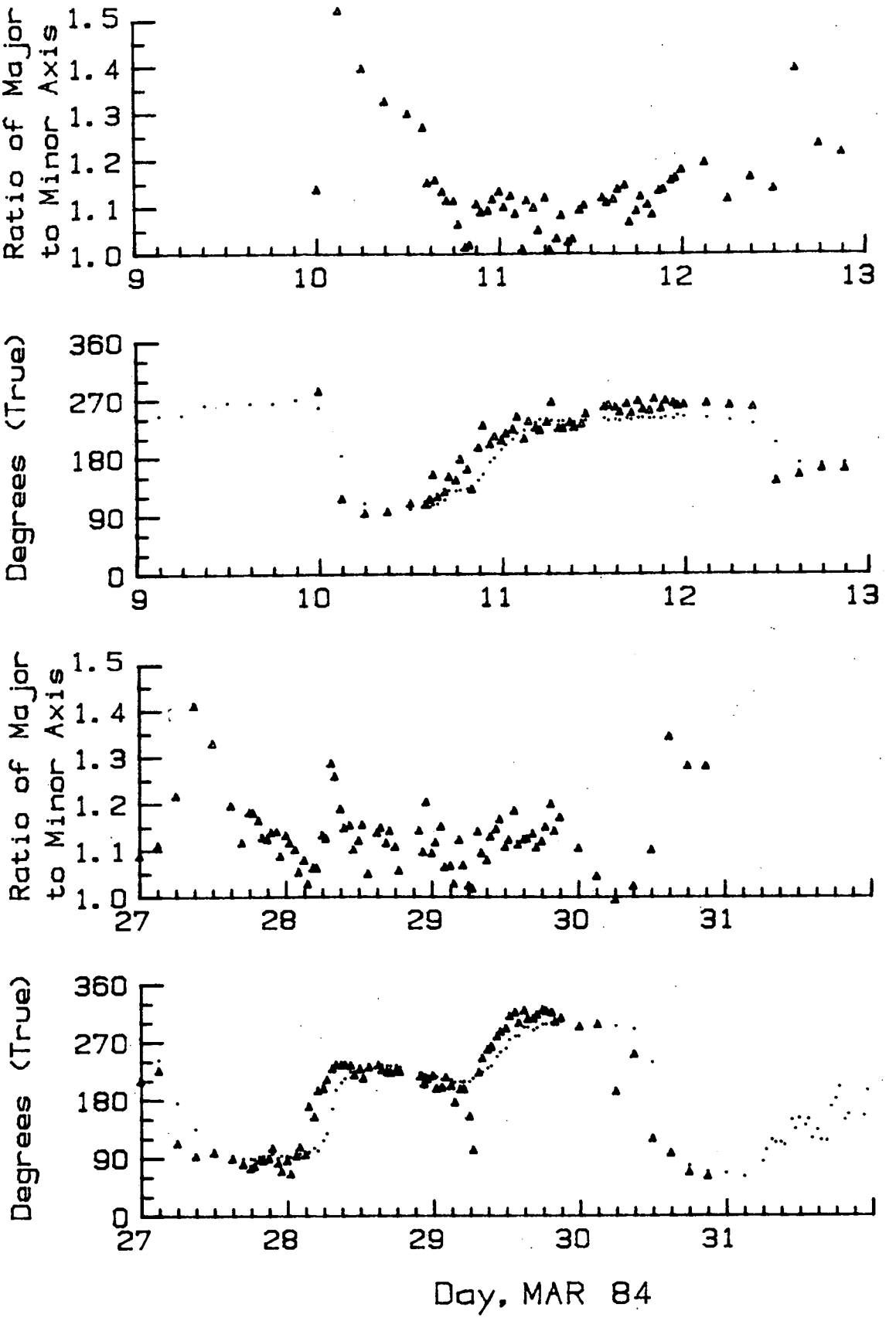

Figure 130. Time series of average wave direction calculated directly from the wave slopes (triangles) overlayed on average direction obtained from spectra (dots).

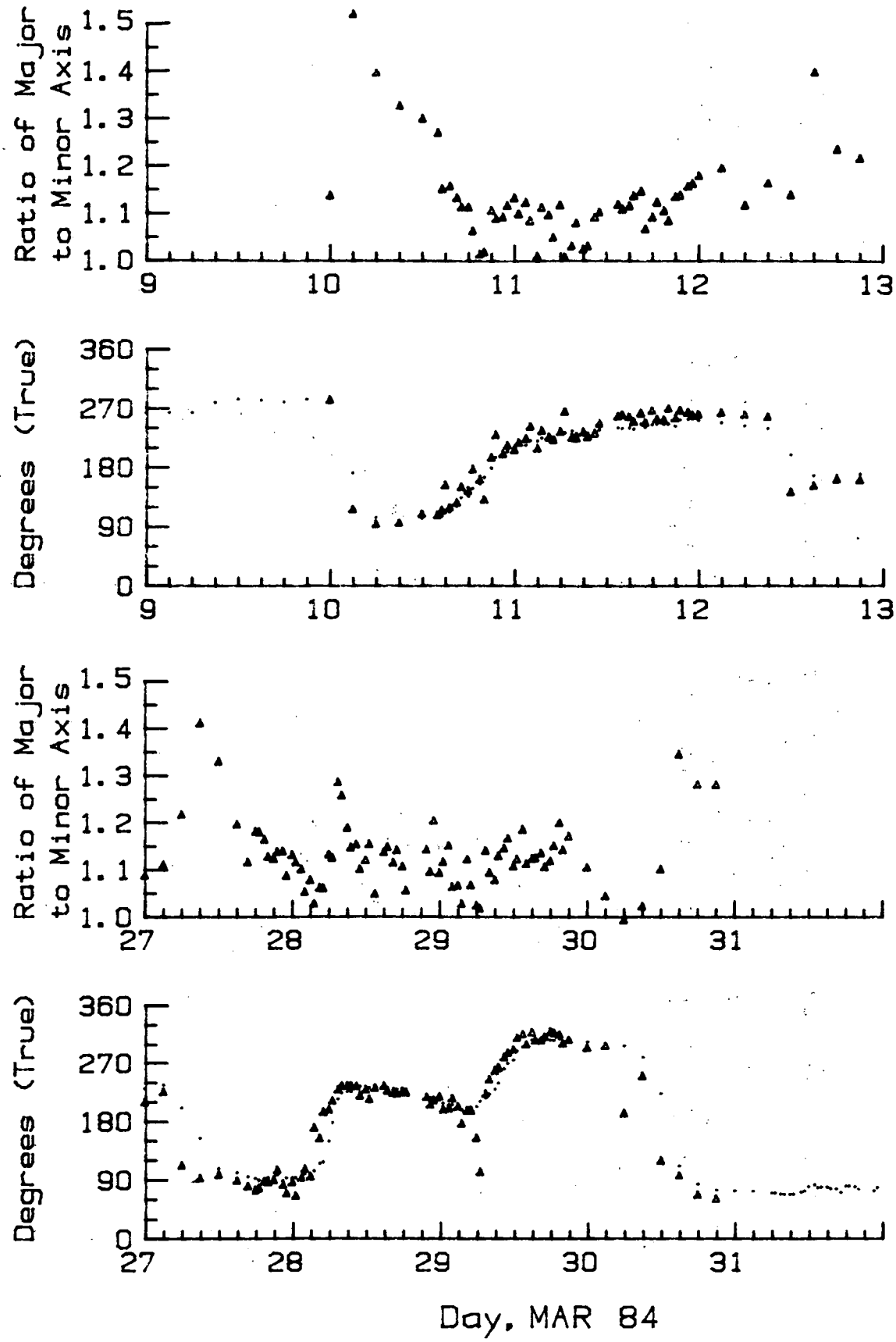

Figure 131. Time series of average wave direction calculated directly from the wave slopes (triangles) overlayed on average sea direction obtained from spectra (dots).

agreement, in both cases is extremely good with slightly better results when compared to the sea directions. This is to be expected due to the bias being introduced by the sampling. The larger values of R_x are associated with low energy conditions while the low values are seen during storms. The few poor direction estimates are associated with ratio values close to 1.

From these results, it can be seen that an average direction of wave travel can be obtained, with confidence, from the slope time series without resorting to a cross-spectral analysis. This is a quick method and can be used when only bulk values are required or for cross-checking directions calculated in a different manner. Other statistics can be calculated, such as the skewness of the scatter, which could provide information on the nonlinearity of the wave field.

GROUPINESS

On purely a mathematical basis, Longuet-Higgins (1957) developed expressions to characterize an average or principal direction of the directional energy distribution and principal direction of the wave envelope for a single, narrow peaked spectrum. The calculations are based on the moments of the directional spectrum given in his paper as (see reference for further details):

$$MD_{pq} = \int_{-\infty}^{\infty} \int_{-\infty}^{\infty} (u, v)\, u^p\, v^q\, du\, dv$$

where u and v are wavenumbers in two directions (i.e. $|k| \cos\theta$, $|k| \sin\theta$)

The principal direction, θ_p, can be obtained from:

$$\tan 2\theta_p = \frac{2MD_{11}}{MD_{20} - MD_{02}}$$

This expression gives two angles at 90° to each other associated with the minimum and maximum of the distribution (e.g. an ellipse).

An analogous expression for the direction of the envelope can be obtained using the moments of the energy distribution about the mean, i.e.

$$ME_{pq} = \int_{-\infty}^{\infty} \int_{-\infty}^{\infty} (u, v)\, (u - \bar{u})^p\, (v - \bar{v})^q\, du\, dv$$

and θ_E from $\tan 2\theta_E = \frac{2ME_{11}}{ME_{20} - ME_{02}}$

where $ME_{11} = (MD_{11}MD_{00} - MD_{10}MD_{01}) / MD_{00}$

$ME_{20} = (MD_{20}MD_{00} - MD_{10}^2) / MD_{00}$

$ME_{02} = (MD_{02}MD_{00} - MD_{01}^2) / MD_{00}$

The skewness of the waves, the angle β between the principal direction of the envelope and the principal direction of the waves, can be calculated from:

$$\tan 2\beta = \tan 2 (\theta_E - \theta_p)$$

To illustrate the results, four records with narrow spectrum were chosen and various direction parameters calculated. The wavenumbers needed for the calculation of the moments were obtained through the dispersion relationship. Table 10 contains the results which show consistent directions for all four definitions.

TABLE 10

GROUPINESS CHARACTERISTICS USING LONGUET-HIGGINS (1957) FORMULATION

RECORD TIME	SPECTRAL PEAK DIRECTION	SPECTRAL AVERAGE APPARENT DIRECTION	PRINCIPAL DIRECTION	ENVELOPE DIRECTION
Hr/ D/ M/ Yr (GMT)	(°T)	(°T)	(°T)	(°T)
1200/26/2/84	195	176	215	170
0300/11/3/84	206	221	241	218
0600/11/3/84	251	235	239	231
1500/28/3/84	235	233	239	232

DISCUSSION

Overall, the field operation, wave data collection and data processing aspects of the experiment were successful. The problems encountered with icing of the Endeco buoy and its receiver failures, and the loss of the Waverider, could not have been avoided. The difficulties encountered in processing the WAVE-TRACK data may have been reduced by using a different receiver and data logging system, however, the experiment was intended to test a complete instrument package as supplied by Endeco Inc.

Problems with the Station 248 WAVEC in February and early March may have been avoided by separating the station 247 and 248 receiver/antenna set-up as the two stations initially shared one antenna. The data loss, therefore, should not be a reflection on the instruments performance. The poor SAR results reflected a cost conserving measure by performing two experiments concurrently, the other being an ice survey, for which the necessary SAR parameters are considerably different.

The WAVEC systems were more reliable than the WAVE-TRACK reflecting similar experience with these instruments on the Pacific Coast (see Juszko et al. 1985). There were no obvious design problems in terms of durability for either of the buoys, however, again experience on the West Coast indicates potential problems with dislocation of flotation segments for the WAVEC. The small size of the WAVE-TRACK allows for easy assembly and deployment, however it also limits battery capacity and the reduced buoyancy complicates mooring design with the need for large amounts of subsurface buoyancy. The larger size of the WAVEC forces the use of a deployment vessel equipped with a crane which is often not available on supply vessels.

A standardized data processing system is available, currently using the Longuet-Higgins approach for directional calculations, and can be run efficiently with little operator interaction when no serious problems are encountered with data quality. Other analytical methods may be incorporated in the scheme if desired.

The amplitude and phase transfer functions, supplied by Endeco, were inadequate and the approach used by LeBlanc through a linearity analysis is necessary when analyzing WAVE-TRACK data. The band-pass directional analysis

was inefficient in computer time and gave mean directions different from the Longuet-Higgins analysis which, in turn, agreed with the mean directions measured by the WAVEC buoy. The WAVE-TRACK buoy did not resolve frequencies greater than 0.25 Hz very well as its design acts to damp high frequency "noise".

The WAVEC buoy was seen to operate well for all frequencies examined and provided statistics of the heave and directional spectra in agreement with buoy, visual, and wind observations. It had the option to record continuously, thereby resolving the maximum storm-wave heights which were missed by the three-hour sampling of the hindcast model. The Longuet-Higgins analysis did provide consistent mean directions, though with large angular spreads. Weighted directions, either by energy or angular spread, proved to be useful in describing the average sea state. As the major limitation of the direction analysis is the large angular spread for each frequency, different directional distributions should be tested.

The results of the hindcast model, though generally able to predict significant wave height, peak periods, and mean directions during all phases of the storm, exhibited obvious discrepancies with respect to individual spectra. For both storms, the model spectra developed too quickly at the onset and later appeared to be putting in energy at the mid-frequencies not observed in the buoy data. In fact, the buoy measurements showed response initiating at high frequencies which then shifted to lower ones. The model spectra were smoothed in frequency, possibly implying overestimates of the nonlinear interaction. Energy also appeared at frequencies much lower than observed. However, the model spectra can resolve two directions at a single frequency. In future, the modelling should take into account water depth considerations and should investigate the possibility of including low frequency energy dissipation and reduced nonlinear energy transfer. The hindcast model is a useful approach as it is the only method which provides long time series of data for analysis of extremes and was shown, in this case, to generally reproduce the average behaviour of the wave field (as indicated by significant wave height and mean directions) and to separate swell coming from a different direction than the peak wave energy. Depending on the accuracy required for a given application, the model may have to be modified.

The WAVEC system has considerable advantages over the standard Waverider or model results. Having both heave and slope signals allows for the

determination of the dispersion characteristics of the wave field, the possible influence of Doppler shifts due to currents (which would also be affecting Waverider data but, in this case, could not be quantified), and the ability to calculate directional spectrum independent of the dispersion relationship of the wave field. It is now possible to get estimates of wave groupiness and direction of group travel from a single buoy instead of an array. The buoy allows for direct measurement of surface steepness, without having to resort to assumptions on the wavelength and wave shape. Under the experimental conditions, there appeared to be no upper limit on the buoy's ability to resolve the surface slope. A direct relationship of mean surface slope and crest to trough asymmetry with wind speed was shown. This has important consequences in wave modelling and other air-sea interaction studies where knowledge of wind stress and drag coefficients are needed. The drag coefficient, Cd, has been shown by numerous authors (for example, Charnock (1975), Garrett (1977), Large and Pond (1981)) to be directly related to wind speed. This conceptually makes sense, if one also considers that the measured surface slopes increase with wind speed which results in a positive feedback mechanism (i.e. as the slope increases there is a greater surface area of the wave exposed perpendicularly to the wind, which may be observed experimentally as an increase in Cd, and in turn imparts more energy to the waves). This feedback should continue until significant wave breaking occurs. The measurement of surface slopes directly may provide an independent estimate of Cd. The slope values were shown capable of directly providing an estimate of the mean wave field direction of propagation without resorting to a cross-spectral analysis. This is a rapid and convenient method and can be used in standard processing schemes or for cross-checking the spectrally derived values.

Though the WAVEC buoy is more expensive than either the Datawell Waverider or Endeco WAVE-TRACK, its operational history and the significant increase in information it provides puts it at an advantage over both these systems. The standard Datawell WAVEC must be oeprated within line-of-sight of either a shore station or a manned platform. However, ARGOS and GOES satellite-reporting WAVEC and Waverider buoys have been developed by Seakem Oceanography Ltd. WAVEC's modified by Seakem can be deployed anywhere in the world covered by these satellites.

The synthetic aperture radar imagery could potentially provide high resolution directional spectra, however, it is operationally very expensive if one wants time series even over a limited number of days, due to aircraft charges and the image processing required. It may prove advantageous to use SAR in specific applications for offshore design requiring detailed knowledge of wave direction, and for further ground truthing of buoy estimates and model predictions (for example, refraction patterns around artificial islands). Compared with a field program, hindcast modelling is relatively inexpensive, once the model is established and calibrated. It is also the only method currently available for long-term extreme-wave predictions. As such, further effort is justified in improving existing models.

REFERENCES

Audunson, T., S.F. Barstow and H.E. Krogstad, 1982. Analysis of wave directionality from a heave, pitch and roll buoy operated offshore Norway. Ocean Sci. and Eng. 7(8), 291-319.

Barstow, S.F., and H.E. Krogstad, 1983. Directional wave spectra from heave/pitch/roll data buoy. IREE-9, 292-297.

Bayley, G.J., and J.M. Hammersley, 1946. The effective number of independent observations in an auto-correlated series. J. of Roy. Stat. Soc. Serial B8, 184-197.

Bell, W.H., 1977. Static analysis of single-point moorings. Unpub. Manus. Pacific Marine Science Report. 77-12. Institute of Ocean Sciences, Patricia Bay, Victoria, B.C. 63 pp.

Brainard, E.C., and W.T. Wang, 1981. Dynamic analysis of WAVE-TRACK™ slack mooring. Paper given at Oceans 81, Sept. 1981.

Cardone, V.J., A.J. Broccoli, C.V. Greenwood and J.A. Greenwood, 1979. Error characteristics of extratropical storm windfields specified from historical data. Proc. Offshore Tech. Conf., Paper No. OTC 3598, 2103-2110.

Charnock, H., 1955. Wind stress on a water surface. Quart. J. Roy. Meteor. Soc. 81, 639-640.

Corson, W.D., and D.T. Resio, 1981. Comparison of hindcast and measured deep-waters significant wave heights. U.S. Army Eng. Waterways Experiment Station, WES Report, 41 pp.

Cummins, W.E., and S.L. Bales, 1980. Extreme value and rare occurrence wave statistics for Northern Hemispheric Shipping Lanes. Society of Naval Architects and Marine Engineers, Spring, Meeting STAR - Symposium, Coronado, CA. June 4-6, 1980, 219-239.

Ezraty, R., and A. Cavanie, 1981. Evaluation of wave direction measurements using a pitch and roll buoy. Oceanol. Acta. 4. (2), 139-149.

Forristall, G.Z., E.G. Ward, L.E. Borgman and V.J. Cardine, 1978. Storm wave kinematics. Proceedings of the 10th Annual Offshore Technology Conference, Houston, May 8-11. OTC 3227, 1503-1514.

Garrett, J.R., 1977. Review of drag coefficients over oceans and continents. Mon. Wea. Review 105, 915-929.

Goda, Y., 1979. A review on statistical interpretation of wave data. Report, Port and Harbour Res. Inst., Japan 18(1), 5-32.

Hasselman, D.E., M. Dunckel and J.A. Ewing, 1980. Directional wave spectra observed during JONSWAP 1973. J. Phys. Ocean. 10, 1264:1280.

Hasselmann, K., T.P. Barnett, E. Bouws, H. Carlson, D.E. Cartwright, K. Enke, J.A. Ewing, H. Gienapp, D.E. Hasselmann, P. Kruseman, A. Meerburg, P. Muller, D.J. Olbers, K. Richter, W. Sell and H. Walden, 1973. Measurements of wind-wave growth and swell decay during the Joint North Sea Wave Project (JONSWAP). Deutsche Hydrographische Zeitschrift, Reihe A., Nr. 12, 96 pp.

Hodgins, D.O., P.H. LeBlond, D.S. Dunbar and C.T. Niwinski, 1985. A wave climate study of the Northern British Columbia Coast. Volume II - Wave properties and wave prediction. Prep. for Marine Environmental Data Service Branch, Fisheries and Oceans, Canada. 235 pp.

Huang, N.E., S.R. Long, C.-C. Tung, Y. Yuen and L.F. Bliven, 1981. A unified two-parameter wave spectral model for a general sea state. J. FLuid Mech. 112, 203-224.

Huang, N.R., P.H. Wang, H. Wang, S.R. Long and L.F. Bliven, 1983. A study on the spectral models for waves in finite water depth. J. Geophys. Res. 88 (C14), 9579-9587.

Intera Technology Ltd., 1984. SAR derived wave spectra over the West Venture, April 1984. R84-070. Report prep. for Seakem Oceanography Ltd., Victoria, B.C. by Intera Technology Ltd., Calgary, Alberta. 10 pp.

Juszko, B.A., R. Brown, B. de Lange Boom and D.R. Green, 1985. A wave climate study of the Northern British Columbia Coast. Volume I - Wave observations. Prep. for Marine Environmental Data Services Branch, Fisheries and Oceans, Canada. 164 pp. plus attachments.

Kjeldsen, S.P., and D. Myrhaug, 1979. Breaking waves in deep water and resulting wave forces. Offshore Technology Conference, Houston, 1979. Paper OTC-3646.

Komen, G.J., S. Hasselmann and K. Hasselmann, 1984. On the existence of a fully developed wind-sea spectrum. J. Phys. Ocean. Vol. 14, 1271-1285.

Kundu, P.K., J.A. Allen and R.L. Smith, 1975. Modal decomposition of the velocity field near the Oregon coast. J. Phys. Ocean. 5, 683-704.

Large, W.F., and S. Pond, 1981. Open ocean momentum flux measurements in moderate to strong winds. J. Phys. Ocean. 11, 324-336.

LeBlanc, L.R., and F.H. Middleton, 1982. Storm direction wave spectra measured with a single buoy. From Oceans 82 Conference Record, Washington, D.C. Sept. 20-22, 1982. pp. 885-892.

Le Blond, P.H., 1982. A preliminary review of nonspectral wave properties: Grouping, wave breaking, and "freak" waves. Canadian Contractor Report. Hydrogr. Ocean. Sci. 1,66 pp.

Long, R.B., 1980. The statistical evaluation of directional spectrum estimates derived from pitch/roll buoy data. J. Phys. Ocean. 10, 944-952.

Longuet-Higgins, M.S., 1957. The statistical analysis of a random, moving surface. Phil. Trans. Roy. Soc. A, 249, 321-387.

Longuet-Higgins, M.S., D.E. Cartwright and N.D. Smith, 1963. Observations of the directional spectrum of sea waves using the motions of a floating buoy. In: Ocean Wave Spectra, Englewood Cliffs, N.Y., Prentice-Hall, Inc., pp. 111-136.

Mitsuyasu, H., 1968. On the growth of wind-generated waves (I). Rep. Res. Inst. Appl. Mech., Kyushu Univ., 16, 459-482.

Penicka, F.X., D.T. Resio and R.D. Worsfold, 1985. Wave directional spectrum hindcasts for the ESRF Wave Direction Spectrum Intercomparison Study. Report to the Environmental Studies Revolving Fund.

Resio, D.T., 1981. The estimation of wind-wave generation in a discrete spectral model. J. Phys. Ocean. 11, 4, 510-525.

Resio, D.T., 1982. Assessment of wave hindcast methodologies in the Scotian Shelf, Grand Banks and Labrador Sea Areas. Marine Environmental Data Service, Canadian Contractor Report of Hydrography.

Resio, D.T., A.W. Garcia, and C.L. Vincent, 1978. Preliminary investigation of numerical wave models. Proc. Symp. on Tech. Env., Socioecon. and Regulatory Aspect of Coastal Zone Management, 2085-2104.

Resio, D.T., and C.L. Vincent, 1977. Estimation of winds over the Great Lakes. ASCE J. Waterway Port. Coast. Ocean Div., 103, 265-283.

Resio, D.T., and C.L. Vincent, 1979. A comparison of various numerical wave prediction techniques. Proc. Offshore Tech. Conf., Paper No. OTC 3642, 2471-2481.

Resio, D.T., C.L. Vincent and W.D. Corson, 1982. Objective specification of Atlantic Ocean wind fields from historical data. WIS Report 4. U.S. Army Waterways Experiment Station, 50 pp.

Rye, H., 1980. Wave parameter studies and wave groups. In: Sea Climatology. Conference Internationale Paris 3-4 Oct. 1979. Collection Colloques et Seminaires No. 34. Pub. by Editions Technip. Paris. pp. 89-122.

Snyder, R., and C.S. Cox, 1966. A field study of the wind generation of ocean waves. J. Mar. Res., 24, 141-177.

Szabados, M., 1982. Intercomparison of the offshore wave measurements during ARSLOE. Paper given at Oceans 82. pp 226.

Thompson, W.C., and J.R. Buckley, 1984. MINIMET buoy evaluation during the Directional Wave Spectrum Intercomparison Study. Unpub. Report. Petro-Canada Inc. Calgary, Alberta. 31 pp.

Vincent, C.L., and D.T. Resio, 1979. A discussion of wave prediction in the Northwest Atlantic Ocean. In: Marine Forecasting. J. Nihoul (Ed.). Elsevier Sci. Pub. Elsevier Ocean. Series No. 25, 1979.